Optical Emission and Mass Spectrometric Diagnostics of Laser-Induced Plasmas

John Stephen Cowpe

School of Computing, Science & Engineering (CSE)
Institute for Materials Research (IMR)

University of Salford, UK

Submitted in Partial Fulfilment of the Requirements of the Degree of Doctor of Philosophy, August 2008

Table of Contents

List of Tables and Illustrations

Acknowledgments

Firstly, I would like to thank my supervisor Richard Pilkington for securing the funding and equipment required for this work, and for his continued support, help and advice throughout its course; his knowledge of mass spectrometry, practical laboratory work and physics in general has been invaluable. I would also like to thank my co-supervisor Robin Hill for his advice and encouragement, especially during our hectic preparations for the LIBS 2006 conference in Montreal. I would like to thank Stuart Astin for teaching me about practical aspects of lasers and optics and for spending so much time working with me in the laboratory; without him I would not have been able to complete this work.

Many thanks to Dan Bull, who has advised me on many aspects of undertaking a PhD, and has been kind enough to spend many hours proof-reading (and criticising) my work. Thanks also to Garry Rowsell for his advice on all matters, and his creative thinking. Heartfelt thanks must be extended to Bruce Lewis for providing the copious amounts of coffee required to keep me going during this work, and a roof over my head. I would like to thank Wayne Lawson for introducing me to the RSM technique and for helping me to remain focussed on my work. Many thanks also to Jay Smith for fixing our ailing laser and his expert advice on all matters electronic, and to Steve Hurst and Mike Clegg for their machining expertise and engineering know-how.

I would like to thank John Wilkinson and Nigel Murphy of Photometrics UK for their invaluable continued support and maintenance of the LIBS imaging

apparatus, and also for the kind loan of their PTG and camera controller when ours were malfunctioning. Thanks also to Mark Longson of MKS Spectra Instruments for reconfiguring the RGA employed in this work and explaining the subtle intricacies of ion optics to me, and to Tim Robinson of MKS Spectra Instruments for kindly donating said RGA.

Finally I should very much like to thank my mother for her continued support over the years, and my fiancée Gill for putting up with me during the finishing stages of this work. My apologies and thanks to those who I may have forgotten.

Declaration

The RSM measurements presented in Chapter 5 were performed in conjunction with Stuart Astin, and analysed with the help of Wayne Lawson. A peer-reviewed publication regarding these RSM results was composed (Cowpe et al. 2007) and forms the basis of Chapter 5, Sections 5.1 – 5.5.

The description of the fibre-optic feed-through system given in Section 5.4.1 is taken from a peer-reviewed publication by the author and Richard Pilkington (Cowpe and Pilkington 2008), which was kindly proof read and corrected by Dan Bull. Richard Pilkington rendered Figures 5-4 and 5-5.

Abstract

Optical Emission Spectroscopy (OES) and Mass Spectrometry (MS) were employed in tandem for diagnostic studies of Nd:YAG (532 nm) laser induced plasma plumes. OES measurements of laser-induced silicon plasmas were performed through a range of ambient pressure regimes from atmospheric pressure down to ~10^{-4} mbar. The temporal evolution of the plasmas was characterised in terms of electron excitation temperature T_e, ionisation temperature T_i, and electron density N_e. Electron densities were determined in the range 2.86×10^{16} to 5.53×10^{19} cm^{-3}, electron temperatures were calculated in the range 8794 to 21229 K, and ionic species temperatures calculated in the range 13658 to 22551K. The requirements for OES analysis based on the assumption of Local Thermal Equilibrium (LTE) conditions existing within the plasmas are discussed. The plasma morphology and expansion dynamics with respect to pressure are described.

Response Surface Methodology (RSM) was employed to optimise Laser-Induced Breakdown Spectroscopy (LIBS) analyses of silicon at atmospheric pressure and under vacuum conditions. Multivariate analysis software was used to design and analyse several multi-level, full factorial RSM experiments. A Quality Factor (QF) was conceived as the response parameter for the experiments, representing the quality of the LIBS spectrum captured for a given hardware configuration. A full parametric study of the LIBS hardware configuration was performed to determine the true response of the system; the outcome of which compares favourably with the results yielded from the RSM investigation.

MS analyses of silicon and copper laser-induced plasma plumes were performed using a commercially available Residual Gas Analyser (RGA). The RGA sampling configuration was investigated in order to maximise neutral and ionic species detection from the laser-induced plasmas.

Abbreviations, Definitions and Nomenclature

Abbreviation	Description
CCD	Charge Coupled Device
CE	Coronal Equilibrium plasma model
CF-LIBS	Calibration-Free Laser-Induced Breakdown Spectroscopy
CRSS	Collisional Radiative Steady State plasma model
EDX	Energy Dispersive X-ray analysis
EI	Electron Ionisation
FWHM	Full With at Half Maximum peak height
ICCD	Intensified Charge Coupled Device
ICP	Inductively Coupled Plasma
LA-ICP-MS	Laser Ablation Inductively Coupled Plasma Mass Spectrometry
LAMS	Laser Ablation Mass Spectrometry
LIBS	Laser-Induced Breakdown Spectroscopy
LIMS	Laser Ionisation Mass Spectrometry
LI-ToF-MS	Laser Ionisation – Time of Flight – Mass Spectrometry
LODS	Limit Of Detectable Signal
LTE	Local Thermal Equilibrium
MALDI	Matrix Assisted Laser Desorption Ionisation
MCP	Multi Channel Plate
MS	Mass Spectrometry / Mass Spectrometer
ND	Neutral Density (opacity of a given neutral density filter)
Nd:YAG	Neodymium doped Yttrium Aluminium Garnet
OES	Optical Emission Spectroscopy
PMT	Photo-Multiplier Tube

QF	Quality Factor
RGA	Residual Gas Analyser
RSD	Relative Standard Deviation
RSM	Response Surface Methodology
SEM/EDX	Scanning Electron Microscopy with Energy Dispersive X-ray microanalysis
ToF-MS	Time of Flight Mass Spectrometry
XRF	X-Ray Fluorescence

Symbol	**Meaning**
a	Diffraction grating groove spacing
A	Ion broadening parameter
A_{kl}	Transition probability between two states, e.g. k and l
c	Speed of light in vacuum (2.9979×10^{8} ms^{-1})
C_r	2.005×10^{-5} (s K)
D	Relative electron impact shift
e	Electron charge (1.60×10^{-19} C)
E	Energy
$E_{i,j,k,l}$	Energy of a given level $i,j,k,l,$ etc.
f	Frequency of R.F. field applied to quadrupole rods
$g_{i,j,k,l}$	Statistical weight of a given energy level $i,j,k,l,$ etc.
G	Free-free Gaunt factor [assumed to be unity (Liu et al. 1999)]
h	Planck's constant (6.6261×10^{-34} Js)
$\hbar$	Planck's constant divided by 2π

I	Intensity of a given emission line
i	Electron current
k	Boltzmann's constant (1.3807×10^{-23} JK^{-1})
L	Mean free path
m	Mass
$\tilde{m}$	Diffraction order; may take positive or negative integer values
M	Atomic mass
n_i	Ion density
N	Normal to diffraction grating
N'	Normal to individual blazed diffraction grating groove face
N_D	Number of particles in the Debye sphere
N_e	Electron density (generally given per cm^3)
$N_{i,j,k,l}$	Relative population of energy levels *i,j,k,l,*etc.
N_0	Total species population
p_a	Ambient pressure
q	Number of ions produced in EI source
Q	Partition function
r_0	Radius of quadrupole mass analyser rod arrangement
R	Resolution of mass spectrometer = $m/\delta m$
R_i	Radius of the ion sphere
R^2	Coefficient of determination
t	Time
t_d	Gate delay time between laser firing and data acquisition
t_w	Gate width, the integration time of data acquisition
T	Absolute temperature

T_e	Electron excitation temperature
T_i	Ionic species temperature
T_0	Neutral species temperature
U	Direct potential applied to quadrupole rods
v	Velocity
V	Zero-to-peak amplitude of radio frequency voltage applied to quadrupole rods
V^+	Ionisation potential
V_i	Volume of the ion sphere
w	Electron impact line broadening parameter
$w_{1/2}$	Alternative notation for FWHM / Γ
z	Charge state of a given ion: z = 1 refers to a singly ionised ion, z = 2 a doubly ionised ion etc.
Z	Atomic number
$\overline{Z}$	Average ionisation state
Δ	Path length difference between two equivalent light rays
ΔV^+	Lowering of the ionisation potential of atoms in the presence of a field of ions
ε_0	Permittivity of free space (8.85×10^{-12} Fm^{-1})
ε_c	Continuum emission coefficient
ε_l	Spectral line emission coefficient
Γ	Full Width at Half Maximum (FWHM) height of a spectral line
κ	Constant proportionality coefficient
λ	Wavelength
η_i	Number of ions within the Debye sphere

ν	Frequency
ω	Angular frequency = $2\pi f$
ρ_D	Debye shielding distance, the radius of the Debye sphere
σ	Wave number
θ_b	Blaze angle of a blazed diffraction grating
θ_i	Angle of incident light ray on diffraction grating
θ_m	Angle of diffraction
Φ_0	Potential applied to rods of quadrupolar mass analyser
ξ	Free-bound continuum correction factor
ζ	Charge of a given ion

Spectroscopic notation is employed in this work, following the convention of labelling ionisation states with upper case Roman numerals; I refers to neutral atoms, II to singly ionised species, III to doubly ionised species etc. Thus Si (I) 288.16 nm refers to a certain emission line arising from emission by excited neutral silicon atoms, Si (II) 413.09 nm refers to a spectral line arising from the emission of excited singly ionised silicon ions.

Introduction

The aim of this work was to perform Optical Emission Spectroscopy (OES) and Mass Spectrometry (MS) diagnostics of laser-induced plasmas. OES and MS measurements of plasma plumes induced by nano-second pulsed Nd:YAG (532 nm) laser radiation were performed through a range of ambient pressure regimes. The two diagnostic techniques were found to be complementary, permitting a detailed study of the temporal evolution of laser-induced plasma plumes. Employing OES and MS in tandem, the laser-induced plasmas were characterised in terms of excitation and ionisation temperature, electron density, and neutral to ionic species ratio with respect to time and ambient pressure.

To perform temporally resolved OES and MS plasma diagnostics through a range of ambient pressures, a rig was conceived, designed, constructed, tested and validated. The Response Surface Methodology (RSM) was successfully applied to the optimisation of this apparatus. This thesis presents a thorough literature review, an overview of the relevant theory, an account of the system design, the results obtained with the tandem OES/MS apparatus and the conclusions drawn.

Chapter 1 contains a thorough literature review encompassing to the disciplines of OES and MS. A history of MS and Laser-Induced Breakdown Spectroscopy (LIBS) is presented, as well as a survey of past and present applications of LIBS and MS.

Chapter 2 provides a background to basic plasma analysis. The requirements of plasma charge neutrality and collective effects are described, alongside a summary of plasma various regimes and theoretical models. OES diagnostics of plasmas are described, and the measurement of excitation temperature, ionisation temperature and electron density explained.

Chapter 3 presents a review of the LIBS technique. Laser ablation mechanisms and plasma plume evolution are discussed. Practical considerations of concern when performing LIBS are considered, including a description of the major factors affecting the accuracy and reproducibility of the technique.

Chapter 4 details the design and construction of a LIBS apparatus capable of characterising laser-induced plasma plumes through a range of ambient pressures from atmosphere down to ~10^{-6} mbar. LIBS measurements of excitation temperature, ionisation temperature, electron density and fractional ionisation are presented. High speed photography provides non-dispersed images of the plasma plume with respect to time, yielding information regarding the plasma morphology at various pressures.

Chapter 5 describes the application of RSM to the optimisation of the LIBS system. A Quality Factor for the output of the LIBS apparatus was defined and employed in modelling the response of the system to changes in hardware configuration, specifically: gate width and delay, spectrometer input slit-width, ICCD gain, and focussing lens position relative to the sample. Multivariate statistical analysis software was used to design and subsequently optimise several

experiments in order to fully describe the response of the LIBS system. A full parametric investigation of the LIBS hardware configuration was performed to validate the accuracy of the RSM model.

Chapter 6 describes the principle of MS and the construction and testing of two systems designed to perform mass spectrometric plasma analyses. The principles and theory governing MS are described, focussing predominantly on the quadrupolar mass analyser as employed in this study. The design and construction of a direct line-of-sight and a 'sniffing' MS plasma diagnostic tool are detailed, and the results obtained from each presented.

Chapter 7 presents the general conclusions drawn from OES and MS diagnostics of the laser-induced plasmas, and lists potential avenues of further research and the proposed reasons for these. References to the thesis are contained in **Chapter 8**, with appendices and publications listed as **Chapter 9**.

1 Literature Review

The following literature review outlines the development and selected applications of the techniques employed in this work; it does not describe their operating principles which may be found in Chapters 2, 3, 4, 5 and 6.

1.1 Laser-Induced Breakdown Spectroscopy

Laser-Induced Breakdown Spectroscopy (LIBS) is a powerful Optical Emission Spectroscopy (OES) analytical tool capable of sampling solids, liquids and gases for research and industrial applications (Cremers and Radziemski 2006, Vadillo and Laserna 2004, Amoruso et al. 1999, Yueh et al. 2000, Russo et al. 2004, Rusak et al. 1998, Tognoni et al. 2002). A pulsed laser source is employed to vaporise and excite the analyte forming a transient plasma which subsequently expands away from the sample surface. The optical emission from the relaxation of excited species within the plasma yields information regarding the composition of the material under test. LIBS has historically been a qualitative technique but over recent years it has developed into a pseudo-quantitative materials micro-analysis technique, capable of determining the elemental composition of solids, liquids and gases, providing a suitable calibration has been conducted beforehand (Vadillo and Laserna 2004).

The basis of the LIBS technique requires the formation of a short lived plasma from the material under test. High intensity pulsed laser radiation is focussed onto the sample under investigation and if the laser fluence exceeds a material specific threshold value, typically 10^{9} – 10^{14} Wm^{-2} (Cremers and Radziemski 2006), then the analyte is ablated forming a plume propagating from the surface.

The ablated material is composed of neutral particles, free electrons and ionic species, and expands as a high temperature plasma, approximately 10^3 - 10^5 K (Rusak 1998, Cremers and Radziemski 2006, Amoruso et al. 1999). Spectroscopic analysis of the optical emission from the excited species enables identification of the material under test, assuming that the stoichiometry of the plume is identical to that of the sample. Typically the optical emission from the expanding plasma is dispersed using a spectrograph and subsequently captured and analysed. The captured emission spectrum provides information regarding the elemental composition of the sample, the temperature and particle density of the plasma itself, and the degree of plasma fractional ionisation. Suitably delayed gated capture of the emission spectra from laser-induced plasmas enables temporal investigation of plasma characteristics and expansion dynamics (Amoruso et al. 1999, Tognoni et al. 2002).

Several excellent review articles (Amoruso et al. 1999, Tognoni et al. 2002, Russo et al. 2004, Rusak et al. 1998, Vadillo and Laserna 2004, Radziemski 2002, Mauchien 2007) regarding LIBS fundamentals, applications and experimental approaches have been published.

The versatility of LIBS has seen it employed in numerous industrial (Noll et al. 2005, Noll et al. 2001, Barrette and Turmel 2001, St.-Onge et al. 2004), environmental (Harmon et al. 2005, N.Rai and A. Rai 2008, Gondal and Hussain 2007) and archaeological (Kaminska et al. 2007, Brysbaert et al. 2006, Fortes et al. 2005) applications, to give but a few examples.

LIBS possesses several attractive features as an elemental analysis technique; it may be conducted at atmospheric pressure, and can provide rapid, real-time analysis; generally LIBS can produce useful results in less than 60 seconds (Yueh et al. 2000). LIBS requires no pre-treatment of the analyte (Tognoni et al. 2002) thus reducing overall preparation and analysis time, and facilitating measurements *in-situ*. LIBS is a virtually non-destructive technique, with typically micro-grams of material removed from the sample during analysis (Nogar and Estler 1990). Perhaps the most attractive feature of the LIBS technique is the ability to provide remote stand-off measurements, with materials analysis having been successfully conducted at distances of up to 180 m (Bogue 2005). Stand-off measurements permit materials analysis in potentially hazardous environments such as nuclear power stations (Whitehouse et al. 2001) and in the effective detection of explosives (Singh 2007).

Although displaying many advantages, LIBS suffers several severe limitations. Preferential ablation of elements from a complex sample and matrix effects can lead to non-linearity in emission spectra and thus disrupt quantitative compositional determination (Cremers and Radziemski 2006, Bulajic et al. 2002, Russo et al. 2004). A further disadvantage of LIBS is the poor shot-to-shot reproducibility of the plasmas (Rusak et al. 1998); this may be due to laser power fluctuations, changes in ambient temperature and pressure, sample in-homogeneity etc.

The phenomenon of the laser-induced plasma was first reported and published by Brech and Cross in 1962 (Brech and Cross 1962), not long after Theodore

Maiman engineered the first ruby laser in 1960 (Radziemski 2002). In 1963 Debras-Guédon and Liodec published the first analytical use of the laser-induced plasma for spectrochemical analysis of surfaces (Debras-Guédon and Liodec 1963); this was the birth of the LIBS technique (Cremers and Radziemski 2006). In 1963 Maker et al. reported the first laser-induced breakdown in a gas, and the first investigations concerning LIBS of liquids were performed (Cremers and Radziemski 2006). As an analytical technique in its infancy LIBS faltered and not a great deal of interest was devoted to this emerging technology. LIBS was fundamentally limited by the hardware and data manipulation processing available at the time, and could not compete with the accuracy, reproducibility and precision of established spectroscopy and materials analysis techniques (Cremers and Radziemski 2006). With recent improvements in computer processing and data-handling speed, the development of smaller and more powerful lasers and improved optical apparatus, LIBS has undergone somewhat of a resurgence since the mid 1990s (Tognoni et al. 2002). The number of papers published relating to LIBS research is still increasing year on year.

1.1.1 LIBS of Solid Samples

The capability to sample solids, liquids and gasses has seen LIBS applied to a diverse multitude of applications. Carmona et al. have employed LIBS in order to determine the lead content of several different types of glass (Carmona et al 2007), finding a linear correlation between the intensity of selected Pb peaks in the LIBS spectra and the PbO content of the glasses as determined by X-ray fluorescence (XRF) and scanning electron microscopy with energy dispersive X-ray microanalysis (SEM/EDX). Amador-Hernandez et al. have successfully

exploited LIBS to characterise thin-film multilayer screen-printed electrodes with high lateral spatial resolution (Amador-Hernandez et al. 2001). Garcia-Ayuso et al. were able to characterise jewellery products using LIBS, employing multivariate analysis and calibration to permit the identification of the component metals (Garcia-Ayuso et al. 2002). Caneve and co-workers have analysed asbestos using LIBS; by analysing selected Mg, Si and Fe emission lines in the LIBS spectra they were able to accurately discern the differences between asbestos and cements (Caneve et al. 2005).

1.1.2 LIBS Involving Liquids

De Giacomo et al. have applied the LIBS technique to marine archaeology to ascertain the composition of metallic artefacts in sea water. Preliminary analysis of bronze samples shows promise in expanding the technique to other submerged alloys for use in underwater in-situ materials identification (De Giacomo et al 2004). Gruber at al. have performed in-situ analysis of liquid steel, using a variable focussing system that takes account of the variations in height of the molten steel surface (Gruber et al 2001). With suitable calibration the measurement of elemental composition takes as little as 7 seconds, and the system is sensitive enough to respond in real-time to the addition of admixtures. Yaroschyk et al. performed quantitative determination of wear metal concentrations in engine oil (Yaroschyk et al. 2005). LIBS measurements of metal contamination in used engine oils agreed well with inductively-coupled plasma atomic emission spectroscopy analysis, and the LIBS limits of detection were seen to be four times lower on average when analysing oil jets rather than static surfaces, typically in the range 0.4 - 47 ppm.

1.1.3 LIBS of Gaseous Samples

Carranza and co-workers developed a LIBS instrument to analyse aerosols in ambient air (Carranza et al. 2001); the instrument was sensitive enough to detect a rise in Al, Na, Ca and Mg-based aerosol concentrations in the atmosphere caused by fireworks discharged during the July 4th holiday period. Molina et al. evaluated the aerosol concentration in the exhaust of an oxygen/natural gas furnace using LIBS (Molina et al. 2005); they found that an increase in the furnace temperature from 300 to 700 K produced a rise in the plasma continuum emission level, which was ascribed to the increased number of free electrons in the plasma vicinity. Glumac and Elliott performed a thorough investigation of the effects of ambient pressure on LIBS analyses in air (Glumac and Elliott 2007). They reported that in the range 1 – 0.1 atm as the ambient pressure was reduced the size of the plasma, the electron density and the peak emission were found to diminish significantly.

1.1.4 LIBS for Archaeology and Art Restoration

LIBS has flourished in recent years with a concerted drive to develop it as a tool for the preservation of cultural heritage, focussed predominantly on archaeological investigations and art restorations. Fortes et al. discussed the capability of LIBS to characterise bronze and iron-age metallic artefacts (Fortes et al. 2005). Arsenic content in the artefacts was found to provide a distinguishing factor between bronze and iron-age specimens, enabling LIBS to facilitate a chronological sorting of the objects that agreed well with established dating methods. After suitable calibration curves for copper, tin, lead, iron and

arsenic were established a semi-quantitative elemental evaluation of the artefacts was performed.

Suliyanti et al. analysed the carbon content in various fossil specimens, ranging from 400 000 to 1 000 000 years old (Suliyanti et al. 2005). Carbon emission was seen to diminish with the degree of fossilisation, allowing a crude method of age estimation. Acquaviva et al. performed compositional investigations using LIBS whilst conducting restoration of a bust of St. Gregory the Armenian; their investigation revealed that the bust was covered in calcium-rich pollution deposits and that certain decorative pieces were coated with gold rather than brass as previously supposed (Acquaviva et al. 2005).

Kaminska et al. have successfully applied LIBS to the preservation of historical paper documents, used as an online tool during laser ablation cleaning of the works (Kaminska et al. 2007). By monitoring the decrease in intensity of emission lines ascribed to the surface contamination (Ca, Na, K, Al, Fe) the surface layer was safely removed by laser ablation with no damage to the substrate. Salimbeni et al. have conducted preliminary investigations into optimising the restoration of artworks by employing LIBS as a monitoring tool during laser ablation cleaning (Salimbeni et al. 2001), the results of which indicate that LIBS has the potential to aid online and offline process control.

1.1.5 LIBS in Geological Studies

LIBS is being applied in the field of geology, for prospecting and ore analysis. Yoon et al. applied LIBS to elemental mapping of the surfaces of polished rock

samples, and found that although LIBS shows promise as a sensitive, rapid analysis tool, it is hindered by calibration problems and provided at best a semi-quantitative determination of ore composition (Yoon et al. 1997). Rosenwasser et al. evaluated a commercially available LIBS system, the TRACER™ 2100, as a method of performing on-line quantitative sorting of ores (Rosenwasser et al. 2001). The instrument was capable of analysing the elemental composition of phosphate ore samples with 2% to 4% relative standard deviation after extensive calibration. Vadillo and Laserna report the LIBS analysis of silicate, vanadate and sulphide rocks, and performed successful qualitative characterisation of similar mineral species by time-resolved emission spectroscopy (Vadillo and Laserna 1996). Asimellis et al. found that the phosphorous to silica line intensities in LIBS spectra of phosphate ore may be used as an indicator of ore quality (Asimellis et al. 2006).

1.1.6 LIBS as a Potential Extra-Terrestrial Analysis Technique

The use of LIBS as an analytical tool onboard extra-planetary exploration missions is being investigated by a number of groups due to its potential to provide stand-off measurements, lack of sample preparation requirements and the comparatively light weight of the apparatus. The development of a LIBS instrument design named ChemCam has been approved for the 2009 Mars Science Laboratory rover mission (Cremers and Radziemski 2006). Salle et al. have investigated the effect of ambient pressure and gas composition on the calibration curves obtained from clay samples, simulating the Martian atmosphere with an ambient atmosphere of 7 Torr of CO_2 and roughly approximating the atmosphere of the moon with 50 mTorr of air (Salle et al.

2005). Reproducible results were obtained in the simulated Martian atmosphere, but the free expansion of the laser-induced plasmas in the low pressure regime simulating the atmosphere of the moon led to reduced plasma emission intensity, indicating a need for enhanced light collection systems for low pressure LIBS analyses; their results showed less interference from matrix effects at reduced pressures. Radziemski and his co-workers investigated the use of the vacuum ultra violet spectral region for LIBS based geological analysis in a Martian atmosphere, again simulated by 7 Torr of CO_2 (Radziemski et al. 2005), finding that the ambient CO_2 led to significant absorption of emission lines in the range 130-160 nm, thereby reducing the effective sensitivity of the technique; at lower ambient pressures ~ 0.02 Torr this line absorption was found to decrease. Lazic et al. studied the LIBS signal behaviour as a function of ambient temperature in a simulated Martian atmosphere (Lazic et al. 2007) concluding that the plasma parameters are sensitive to ambient temperature in the range -60°C to +25°C, with electron density varying by an order of magnitude.

LIBS studies in simulated extra-planetary atmospheres are not limited solely to Mars; Arp et al. have conducted a feasibility study of performing LIBS in a high pressure environment to simulate the atmosphere of Venus (Arp et al. 2004). Useful emission spectra were obtained from laser ablation of basalt samples in 9.1 MPa of N_2, suggesting that LIBS may prove to be a suitable analytical technique for use on Venus.

1.1.7 LIBS Applied to Environmental Monitoring

LIBS has shown promise as an environmental monitoring technique. Harmon and his co-workers (Harmon et al. 2006) have applied LIBS to the detection of lead in contaminated soils, obtaining reasonable determination of lead content when compared to X-ray fluorescence measurements. Gondal and Hussain developed a LIBS system for the detection of poisonous metal pollutants in the waste water from a paint factory (Gondal and Hussain 2007). Quantitative analysis of elemental concentrations compared well with that performed by Inductively Coupled Plasma Mass Spectrometry (ICP-MS), and limits of detection for pollutants such as Pb, Cr, Al, Ba, Cu, Fe, P and Zn were found to be in the range 0.2 – 14 mg kg^{-1}. Rai and Rai used LIBS to evaluate the amount of Cr present in the waste water from an electroplating plant, finding that concentration of Cr was 1500 ppm; their results have led to remedial action taking place (Rai and Rai 2008).

1.1.8 LIBS Applied to Forensic Analysis

Dockery and Goode have investigated the possibility of using LIBS to detect traces of gunshot residue on the hands of suspected shooters (Dockery and Goode 2003). Although in the early stages of investigation, and with an un-optimised system, Dockery and Goode's findings indicate that LIBS may be suitable for accurate detection of gunshot residue and other particulate matter in sample swabs taken from human skin, indicating a promising forensic analysis tool. Almirall et al. evaluated the performance of a LIBS system as a forensic analysis tool for glass, paint, metals and gun shot residue; concluding that the

ease of operation and almost non-destructive nature of the technique make it a viable option for rapid qualitative forensic analysis (Almirall et al. 2005).

1.1.9 LIBS in Medical Research

LIBS has been applied to the fields of medicine and dentistry. Kumar et al. attempted to characterise malignant tissue cells by LIBS (Kumar et al. 2004), their results indicating a clear difference between spectra obtained from healthy and malignant tissue. Samek et al. performed in-vivo and in-vitro LIBS analysis to identify carious teeth (Samek et al. 2001). In their study Nd:YAG (1064 nm) laser radiation was focussed onto the teeth via a fibre delivery system which also served to collect the optical emission from the laser-induced plasmas. By monitoring the calcium emission lines in the spectra, and by comparing against a database of known spectra, unambiguous real-time discrimination of healthy and carious tooth sections was achieved with high spatial resolution. Corsi et al. considered the application of LIBS to hair tissue mineral analysis (Corsi et al. 2003). The preliminary results of their study indicated the feasibility of using LIBS as a relatively inexpensive method of detecting heavy metal poisoning by analysis of human hair samples.

1.1.10 LIBS Used to Detect Potential Biological Hazards

With the current climate of fear regarding terrorist threats, techniques for the rapid, accurate identification of potentially hazardous substances are receiving heavy funding. Kim et al. proved the potential for using LIBS as an in-situ technique for the detection and recognition of non-pathogenic bacterial strains,

which were identified and clearly distinguished according to their respective calcium and phosphate components (Kim et al. 2004). Morel et al. investigated the possibility of employing LIBS to identify biological matter as a means of detecting and identifying micro-biological hazards (Moreal et al. 2003). The major inorganic components of the bacteria were easily identified from the breakdown emission spectra, and were subsequently used as a fingerprint to rapidly identify individual strains with low false-positive result instances.

1.1.11 LIBS Applied to the Analysis of Steel

LIBS has been employed extensively in the analysis of steel products. Cabalin and co-workers investigated the effect of surface roughness when performing Nd:YAG (532 nm) LIBS of steel; at low laser fluences the superficial surface finish greatly influenced the LIBS analyses, but at higher laser fluences the effect of the surface roughness was reduced (Cabalin et al. 1999). LIBS has been proven to be capable of analysing materials very quickly in comparison to other, established analysis techniques. Boué-Bigne applied LIBS to the quantification of oxide inclusions in steel (Boué-Bigne 2007); LIBS was compared favourably to automated scanning electron microscopy with energy dispersive x-ray analysis (SEM/EDX), being able to detect sub-μm diameter inclusions with a much faster scan speed.

1.1.12 Remote LIBS Measurements

LIBS may be implemented to achieve remote samples analysis; De Lucia and his co-workers at the U.S. Army Research Laboratory are conducting preliminary

investigations into the potential for using LIBS as a tool for the detection and discrimination of explosives (De Lucia et al. 2007). Stand-off LIBS measurements of the nitrogen and oxygen components of the explosives are complicated by the contribution to the LIBS signal by atmospheric gases, but initial studies using a double-pulse laser configuration show promise. Salle et al. have evaluated the suitability of LIBS to perform remote analyses of rock and metals in a simulated Martian atmosphere (Salle et al. 2004) at distances of 3 – 12 metres, with limits of detection for Cr, Mg and Si comparable to those obtained from more conventional set-ups. Palanco et al. describe the design, construction and testing of a remote LIBS instrument capable of performing stand-off analyses at distances up to 100 metres (Palanco et al. 2006). Palanco et al. found that signal intensity drops off rapidly with increased range, the ambient atmosphere has no influence on the LIBS signal in the range studied, and that careful consideration must be given to laser focussing in order to minimise interference from pre-ablation breakdown in the air.

1.1.13 LIBS Material Depth Profiling

A prominent advantage of LIBS as an analytical technique is its ability to not only perform surface analyses of materials, but also to conduct depth-resolved material profiling as well. A small amount of material, typically of the order of micrograms (Nogar and Estler 1990), is ablated from the sample by each laser pulse, equating to an average ablation depth of 20 – 30 nm per laser pulse (Garcia et al. 2001). By repeatedly pulsing the laser at the same spot on the target surface it is possible to drill through the sample, in this way compositional changes in the bulk structure of a given sample may be determined by

successively monitoring the resultant plasmas. The use of LIBS as a depth profiling tool has been employed as a diagnostic technique for thin film elemental composition (Caneve et al. 2005a), to measure the thickness of protective coatings applied to archaeological artefacts (Pouli et al. 2005), to investigate the properties of paper coatings (Hakkanen et al. 2005) and to examine the doping of phosphorous in photonic-grade silicon (Milan et al. 1998).

Nano- and femto-second depth resolved LIBS has been conducted to determine the thickness of protective coatings on historical artefacts (Puli et al. 2005), yielding well resolved depth profiles and providing a reliable method of analysing various organic coatings on metallic archaeological items. Depth resolved LIBS has also been applied to the analysis of the archaeological artefacts themselves (Lopez et al. 2005) with complementary SEM/EDX analyses correlating well with LIBS depth profiles of Al, Si, Fe and Ca. LIBS was able to discern trace amounts of Mg and Ti which were below the detection threshold of the SEM/EDX. A comparative study of LIBS and Laser-Ionisation Time of Flight Mass Spectrometry (LI-ToF-MS) showed the advantages of LIBS in terms of negligible sample preparation and speed of analysis when performing depth characterisation of Zn coatings on steel (Garcia et al. 2001).

LIBS has been applied to online depth characterisation of Zn coated steel; the achieved thickness resolution is estimated to about 400 nm for coating thicknesses of electrolytic galvanized sheet steel in the range of 3.2 to11.2 μm (Balzer et al. 2005). Calibrated quantitative depth profile analysis of Zn coated steel has been performed; quantitative depth profiles of three elements: Al, Fe

and Zn were obtained for two galvannealed samples. The iron profiles are found to be in broad agreement with those obtained by transmission electron microscopy energy dispersive X-ray spectrometry (St.-Onge and Sabsabi 2000).

LIBS has been applied to depth-resolved characterisation of paper, with variations in Ca emission used to determine variations in pigment and filler depth on a microscopic scale (Hakkanen et al. 2001). Laser induced breakdown spectroscopy (LIBS) was used for the analysis of Ca during a depth profile in Patagonian soil, using a CO_2 laser for environmental contamination monitoring (Bustamante 2002). LIBS has been applied to determine depth resolved quantitative characterisation of sulphur and chloride concentrations (Wilsch et al. 2005) in concrete structures. Application of LIBS to rapid at-line analysis of coating thickness and uniformity on tablets has been conducted. The results indicate that a change in coating application of less than 2 wt.% on a 100 mg tablet can be easily detected (Mowery et al. 2002). Depth-resolved zinc analysis in human skin by laser induced-breakdown spectroscopy as been performed (Sun et al. 2000). The results indicate that LIBS is a useful tool for accurate trace elemental analysis in human skin.

1.1.14 Portable LIBS Apparatus

Much work has been conducted regarding the development of portable LIBS systems (Milan et al. 1998, Bogue 2005, Palanco et al. 2003) for general in-the-field analysis, and specifically for archaeological (Melessanaki et al. 2005) and geochemical environmental analysis (Harmon et al. 2006). These instruments are portable in so far as they are transportable by a vehicle to the site of interest,

they are not compact and lightweight enough to carry; rather they are mobile laboratory devices.

A briefcase-sized portable LIBS system has been developed (Pierce et al. 2004) and is currently being tested to detect environmental pollutants in the field. The US Army Research Laboratory has reported development of a LIBS based system capable of detecting and classifying buried landmines (Harmon et al. 2003); this is the only system to utilise a sensing 'wand' to probe the target in-situ. This device has undergone laboratory testing and in-the-field trials show some promise.

1.1.15 LIBS as a Plasma Diagnostic Technique

Aside from materials analysis, the LIBS technique may be used as a plasma diagnostic tool. Spectroscopic analysis of laser-induced plasmas can lead to the determination of electron number densities from the Stark broadening of emission line profiles (Shaikh et al. 2006, El Sherbini et al. 2006); plasma temperatures may be determined from the 2 line ratio method (Shaikh et al. 2006), Boltzmann plot method (Le Drogoff et al. 2001, Lee et al. 1997) and line-to-continuum ratio method (Liu et al. 1999, Griem 1997). Milàn and Laserna (Milan and Laserna 2001) performed diagnostics of silicon plasmas produced by 532 nm Nd:YAG nanosecond pulses, in air at atmospheric pressure. Plasma temperatures determined using the Boltzmann plot method tended to remain constant with increasing delay, in the range of 6000 - 9000 K. This behaviour, contrary to their expectations, was ascribed to difficulties in finding silicon lines fulfilling the requirements of the Boltzmann plot method. Electron densities of

the order 10^{18} cm^{-3} were determined from the Stark broadening of the Si (I) 250.65 nm line. Liu et al. (Liu et al. 1999) performed spectroscopic analyses of silicon plasmas induced by nanosecond Nd:YAG 266 nm pulses, in air at atmospheric pressure. Plasma temperatures were determined from the line-to-continuum ratio method in the range 20000 – 70000 K during the early phase (<300 ns) of plasma expansion. Electron densities in the range of 10^{18} -10^{19} cm^{-3} were determined from the Stark broadening of the Si (I) 288.16 nm line.

The electron densities and temperatures reported by Milàn and Laserna and Liu et al. for silicon plasmas are comparable to those calculated for other solid analytes in air at atmospheric pressure. Shaikh et al. report electron temperatures in Nd:YAG (532 nm) ns pulse induced zinc plasmas of approximately 9000 K determined by the 2-line method, and electron densities of the order 10^{16} cm^{-3} (Shaikh et al. 2006). Le Drogoff et al. report electron densities of the order 10^{16} – 10^{18} cm^{-3}, and electron temperatures in the range 5500 -11000 K in Nd:YAG (1064 nm) nanosecond pulse laser induced aluminium plasmas (Le Drogoff et al. 2001). Harilal et al. performed electron density and temperature measurements in Nd:YAG (1064 nm) laser induced plasmas at an ambient pressure of ~10^{-4} mbar; electron densities of the order 10^{17} cm^{-3} and temperatures in the range 17000 – 40000 K were determined (Harilal et al. 1997). Radziemski et al. conducted LIBS of geological samples in a simulated Martian atmosphere, and reported that the appearance and characteristics of the induced plasma plumes were strongly pressure dependent (Radziemski et al. 2005). Harilal et al. applied 2 ns gated ICCD photography to characterise the morphology of laser-induced aluminium plumes through a range of ambient pressures from ~10^{-6} to 100 mbar,

confirming the general agreement of plume front expansion with various models (Harilal et al. 2003).

1.2 Mass Spectrometry

Mass spectrometry (MS) is a versatile materials analysis method, providing unequalled detection limits and sensitivity (de Hofmann and Stroobant 2003). Mass spectrometric analysis operates on a very simple principle; charged ions produced from the analyte are separated according to their mass to charge ratios, *m/z*. Mass discrimination may be performed either by exploiting the different trajectories of ions in electric or magnetic fields, or by the variation in time of flight (ToF) for ions of different *m/z* (Farmer 1963). The electrostatic quadrupolar mass analyser, as employed in this work, is described fully in Chapter 6. MS may be employed to directly analyse ionic species generated in plasmas, flames, spark discharges etc., but may equally well be applied to the analysis of electrically neutral substances provided that an ion source is used to produce gas-phase ions from the analyte beforehand. Ionisation may take place due to a variety of mechanisms; electron ionisation, chemical ionisation, matrix-assisted laser desorption/ionisation (MALDI), electrospray ionisation etc (de Hoffmann and Stroobant 2003, Elliott 1963). The electron ionisation source, as employed in this work, is described in Chapter 6.

The birth of Mass Spectrometry (MS) may be traced back to J.J. Thomson's first pioneering investigations into the properties of cathode rays in the late 19th century. In 1897 Thomson discovered the electron and subsequently determined its mass to charge ratio (Budzikiewicz and Grigsby 2006). In 1912 Thomson constructed the first magnetic mass spectrometer, then dubbed a *parabola*

spectrograph, and employed this to obtain mass spectra of O_2, N_2, CO and CO_2 (Thomson 1913). Since these early days a range of instruments has been developed, and is still being developed, and the mass spectrometer has become an invaluable analytical tool.

MS is employed in many diverse disciplines such as materials analysis (Garcia et al. 2001), monitoring of environmental pollutants (Steen et al. 1997), the pharmaceuticals industry (Rubakhin et al. 2005), forensic science (Wood et al. 2006), and radiocarbon dating of archaeological artefacts (Ingalls et al. 2004), to name but a few. There are many variants of the MS technique, and to cover all would be beyond the scope of this literature review; rather, we shall focus on MS variants that utilise lasers for sampling purposes and as ionisation sources, and MS performed with the quadrupole mass analyser.

The potential for using lasers in conjunction with MS was first noticed in 1963, when Honig et al. and Linlor independently demonstrated that charged and neutral particles may be sputtered from solids by absorption of pulsed ruby laser radiation (Lazare et al. 1996). Since then, developments in both laser and MS technology have seen laser ablation-based MS flourish into one of the most widely used analytical techniques in the world. Common laser-based MS variants include Laser Ablation Mass Spectrometry (LAMS), Laser Ionisation Mass Spectrometry (LIMS), Laser Ablation Inductively Coupled Plasma Mass Spectrometry (LA-ICP-MS) and Matrix Assisted Laser Desorption/Ionisation Mass Spectrometry (MALDI MS) (de Hoffmann and Stroobant 2003).

In the LAMS variant, neutral species sputtered from samples are subject to a secondary post-ionisation technique, such as electron impact ionisation, and subsequently mass analysed. When performing LIMS the laser is used to both volatilise the analyte into the gas phase, and ionise this sampled material prior to mass analysis. The most commonly encountered form of LAMS is LA-ICP-MS. LA-ICP-MS may be considered as a simple three-stage process (Alexander et al. 1998): electrically neutral particulates are formed by laser ablation of the sample in argon gas at atmospheric pressure; the analyte particulates are transported to an ICP torch by a stream of argon gas; the sample particulates are atomised and ionised in the ICP torch and subsequently mass-analysed, generally by a quadrupole mass analyser.

1.2.1 Laser Ablation Inductively-Coupled Mass Spectrometry

A review article by Becker (Becker 2002) highlights some of the most attractive features of LA-ICP-MS and several of the avenues of research in which it is currently employed. Becker states that LA-ICP-MS is the most frequently used variant of MS for fast, sensitive multi-elemental determination of trace and ultra-trace concentrations, employed in water pollution monitoring, geological, biological and medical applications, as well as the characterisation of high-purity materials. LA-ICP-MS requires little or no sample preparation and features a low contamination risk. Bi et al. profiled patterned metal layers on silicon and polymer substrates using LA-ICP-MS (Bi et al. 2000), obtaining a lateral spatial resolution of 45 microns, and greater sensitivity as compared to analysis by laser-ablation optical emission spectroscopy.

Bugoi et al. have applied LA-ICP-MS to the analysis of Transylvanian obsidian artefacts, concluding that it is a rapid, sensitive method for complete chemical determination, with detection limits in the ppb to ppm range (Bugoi et al 2004). Alexander and his co-workers at the Pacific Northwest Laboratory employed LA-ICP-MS for the analysis of nuclear waste materials, comparing the results obtained from Nd:YAG ablation at wavelengths of 266, 355, 532 and 1064 nm (Alexander et al. 1998). UV laser ablation was found to provide greater precision and accuracy, showing less signal dependence on matrix effects and minimal fractionation. Kylander et al. performed quadrupole LA-ICP-MS of peat and lichens, determining the relative concentrations of lead isotopes as a measure of environmental contamination (Kylander et al. 2007).

1.2.2 Laser Ionisation Mass Spectrometry

Numerous LIMS studies been carried out directly analysing positive ionic species emanating from laser-induced plasmas. Kimura et al. (Kimura et al. 2001) performed Nd:YAG ablation of silicon carbide targets at 266, 355, 532 and 1064 nm (Kimura et al. 2001). ToF mass analysis of the plume constituents revealed that silicon carbide clusters were observed when using 355, 532 and 1064 nm laser ablation/ionisation, but not when the 266 nm wavelength was employed as the $Si_xC^+_y$ clusters were photo-electrically excited above their dissociation limit at this wavelength. Wang et al. probed borocarbide targets using an XeF (351 nm) excimer laser and performed analysis of the ionic species generated using ToF MS (Wang et al. 2003). Spatially resolved studies of the plasma plumes revealed that heavier ions were found closer to the centre of the plumes and lighter ions towards the edges, on an axis normal to the target

sample. Dimov and Chryssoulis attempted to optimise and standardise a ToF LIMS instrument to perform reproducible quantitative analysis of mineral surfaces, and found that matrix effects were dramatically reduced if a secondary laser pulse is used to post-ionise neutral species ablated by a primary pulse (Dimov and Chryssoulis 1998).

1.2.3 Matrix Assisted Laser Desorption/Ionisation

Matrix Assisted Laser Desorption/Ionisation (MALDI) was developed in the latter part of the 80s (Griesser et al. 2004), and requires the analyte to be potted in an acid/solvent matrix prior to analysis. The matrix has strong absorbance at the laser wavelength, typically nitrogen lasers (337 nm) are used (de Hoffmann and Stroobant 2003). When the matrix is ablated by the laser, it expands into the gas phase carrying the analyte molecules with it; the matrix absorbs most of the incident laser energy and so protects the sample from fragmentation. The matrix is then thought to transfer part of its charge to the analyte creating positively charged sample ions that may then be mass analysed; the desorption and ionisation mechanisms of MALDI are not fully understood on a molecular level (Griesser et al. 2004).

MALDI allows for the desorption and ionisation of molecular masses in excess of 100 000 amu without fragmentation (de Hoffmann and Stroobant 2003). Angelatti et al. have applied MALDI MS to the detection of fraudulently produced buffalo mozzarella cheese (Angelatti et al. 1998). The detection of bovine milk used to dilute the water buffalo milk during cheese manufacture was performed by employing MALDI MS to hunt for certain tell-tale milk protein

signatures. MALDI MS is widely employed in pharmaceutical research and development. Escoubas et al. have developed MALDI MS as a technique to investigate animal venoms and toxins in the search for new analgesic drugs (Escoubas et al. 2008). Reyzer et al. validated MALDI MS as a technique to directly analyse and image an anti-tumour drug in intact tissue, concluding that the MALDI MS response was proportional to the concentration of drug in the tissue (Reyzer et al 2003).

1.2.4 Quadrupole Mass Spectrometry

The quadrupolar mass analyser was first described by Paul and Steinwedel in 1953 (de Hoffmann and Stroobant 2003), and recent developments associated with this design offer the potential for this small, relatively inexpensive instrument to be used as a flexible analytical tool. Quadrupole based MS has been performed in many varying disciplines. Quadrupole mass analysers have been used in medical applications such as respiratory and blood gas analysis, drug detection and analysis and the discrimination of bacteria (Lawson 1976). Quadrupole MS has been exploited to quantify the concentration of pharmaceutical contaminants in waste water (Tosjek et al. 2007), for the measurements of anaesthetic agents in respiratory gases at a veterinary clinic (Turner et al. 2007), to determine residual pesticide contamination levels in food (Soler et al. 2005), and for real-time monitoring of air contaminants during a chemical fire (Karellas et al. 2003).

Quadrupole mass analysers coupled with electron impact ionisation sources are found in Residual Gas Analysers (RGA) which are commonly employed as

vacuum process monitoring and leak detection apparatus (O'Hanlon 2003, Todd 1976). Bennett and his co-workers at the Rutherford Appleton Laboratories used a calibrated RGA to accurately measure the outgassing of hydrogen, methane, water, CO and CO_2 from carefully prepared 316L stainless steel, concluding that only hydrogen is outgassed from the steel surface (Bennett et al. 2004).

Neutral species generated from laser ablation of polymers have been investigated (Lazare et al. 1996) using quadrupole mass spectrometry. UV excimer laser ablation (ArF 193 nm, KrF 248 nm) of polymers was performed in high vacuum conditions, and the sputtered neutral species subsequently ionised by a 100 eV electron ionisation source and subject to quadrupole mass analysis. The sensitivity of this method proved to be high, permitting 100 ng of sample to be probed. Ion energetics of ZnTe laser ablation plumes were measured using both ToF and quadrupole MS; the two techniques yielding comparable results (Kelly et al. 1998).

Several groups have applied a quadrupole mass filter to LIMS with varying degrees of success. Kuzuya et al. (Kuzuya et al. 1998) employed a quadrupole mass filter to monitor the ion signals produced from laser ablation of metals, metal alloys and ceramics, obtaining reproducible spectra with less than 1% standard deviation in ion signal. Torrisi and co-workers characterised laser-induced silicon plasmas using a commercially available instrument, the Hiden Analytical EQP 300 which combines quadrupolar mass analysis of neutral and ionic species with electrostatic deflection to determine ion energetics (Hiden Analytical 2007). The Hiden EQP may analyse ionic species directly from the

laser-induced plasmas, and is equipped with an electron impact ionisation source for the ionisation and subsequent analysis of neutral species sputtered from the silicon target. The post ionisation of the neutrals does not corrupt their energy distribution, as the energy of the electrons emitted from the source is set just above the first ionisation potential of silicon, 8.15 eV (Torrisi et al. 2008). Laser ablation of silicon was performed at an ambient pressure of ~10^{-6} mbar using the second harmonic of a Nd:YAG; electron densities of 1.47×10^{17} cm^{-3} and plasma temperatures of the order 10^5 K were reported (Torrisi et al. 2008).

1.2.5 Portable Mass Spectrometers

There is a recognised need for capable *in-situ* mass spectrometers which are reliable, portable and compact. Mass spectrometry is an excellent candidate for a field analytical technique owing to its speed of sample acquisition and analysis, potential to analyse solids, liquids and gases, its high sensitivity and ability to continuously monitor analytes in real time. So called "field portable" miniature mass spectrometers may be employed to identify unknown substances on site; thereby minimising sample preparation and transportation requirements, thus reducing analysis time and cost. Of particular interest is the capability of such a system to provide fast, accurate determination of unknown substances in situations where a rapid response to a potential environmental/biological hazard is required.

Much work has been conducted investigating the suitability of various mass spectrometer systems for field analytical chemistry whilst attempting to retain the performance of laboratory based instruments (Sparkman 2001, Diaz et al. 2004,

Sillon and Baptist 2002, Makas et al. 2004, Blain et al. 2004, Boumsellek and Ferran 2001). Mass analysers of all types have been miniaturised with varying degrees of success, and an inevitable compromise of performance (Diaz et al. 2004, Sillon and Baptist 2002, Makas et al. 2004, Blain et al. 2004, Boumsellek and Ferran 2001). The major obstacle to miniaturisation of an integrated mass spectrometry system lies not in reducing the size of the mass spectrometer itself; rather it is the reducing in bulk of the necessary ancillary devices such as the associated vacuum system and power supplies.

Numerous reviews of the difficulties associated with mass spectrometer miniaturisation have been conducted. Badman and Crooks state (Badman and Crooks 2000),

"Currently, the limiting factor for cost, power, size and mass of the miniature spectrometer is the availability of appropriate pumping systems".

C.M. Henry sums up the general consensus of those attending a symposium devoted to miniature mass spectrometers in 2002 (Henry 2002),

"One after another, the speakers reiterated that, until the ancillary parts of the system are also reduced in size, it won't do much good to continue to shrink the mass analyser".

Short et al. have successfully designed and constructed two portable mass spectrometry systems capable of real-time adaptive in-water analyses (Short et

al. 2001). The two systems, one utilising a quadrupole mass filter and one a quadrupole ion trap filter, incorporate a membrane inlet system and have been tested to a depth of 30 metres. Both systems were tested off the coast of Florida and were found to provide accurate ppb and sub-ppb detection of natural and anthropogenic substances, and battery life sufficient for 12 days operation. Work is underway to strengthen the apparatus in order to function at greater depths, with a view to creating a worldwide network of marine monitoring devices.

1.3 Simultaneous LIBS and MS Analyses

A small amount of literature has been published concerning research combining results from simultaneous LIBS and MS analysis. Song et al. constructed a system capable of performing simultaneous LIBS and ToF-MS analysis of Gd plate at an ambient pressure of ~ 10^{-6} Torr (Song et al. 2004). The high vacuum conditions were necessary for successful ToF-MS analysis, but this low ambient pressure was found to be detrimental to the LIBS analyses. The increased rate of free plasma expansion under vacuum led to a reduction in plasma emission intensity, which in turn reduced the potential sensitivity of the LIBS analysis. An increase in the laser power density led to an increase in the LIBS sensitivity to the detriment of the MS signal.

Garcia et al. performed a comparative analysis of zinc coated steel using LIBS and laser-ionisation ToF-MS (Garcia et al. 2001). Laser ablation was conducted at an ambient pressure of ~ 2×10^{-6} mbar using the fundamental harmonic of a Nd:YAG laser, giving an average ablation rate of approximately 20 – 30 nm per pulse. The LI-ToF-MS was found to provide greater sensitivity, with the

continuum background emission dominating the LIBS signal. Due to the use of a non-gated CCD detector, with a minimum integration time of 17 ms, the LIBS background could not be reduced by gated spectrum capture. A comparison of the LIBS spectra captured at atmospheric pressure and a pressure of ~ 2×10^{-6} indicated an improvement of the instrumental resolution, with the FWHM of the Zn (I) 334.5 nm decreasing from 1.1 nm at atmosphere to 0.2 nm under vacuum.

Pettke and co-workers compared the limits of detection for LA-ICP-MS and OES of ArF Excimer ablation of NIST standard glass (Pettke et al. 2000). LA-ICP-MS was found to provide lower limits of detection and more representative analysis than LA-OES, but it was noted that OES has the advantage of simultaneously monitoring emission from all elements in the sample, whereas quadrupole based MS is subject to data skew when performing a mass scan of over ten elements or more.

The preceding literature review is by no means exhaustive, but aims to promote the wide spread of disciplines throughout which LIBS and MS variants are employed, highlighting the versatility of the two techniques.

2 Plasmas: an Overview of Plasma Properties and Optical Plasma Analysis Techniques

2.1 Introduction

To perform LIBS or mass spectrometric plasma diagnostics a sufficient knowledge of basic plasma parameters, models and analysis is required. This chapter aims to describe such basic plasma properties and analysis in sufficient detail that later chapters may be understood. The concepts of charge neutrality, the ion sphere, collective effects and the Debye sphere, as applied to all plasmas in general, are introduced. Various plasma regimes shall be described, characterised in terms of their electron density N_e and temperature T_e, with a focus on the concept of Local Thermal Equilibrium (LTE) conditions existing within plasmas. Optical emission from plasmas is described in terms of continuum and line emission, and Optical Emission Spectroscopy (OES) techniques of determining plasma temperature and density are explained.

2.2 The Plasma

Plasmas are often described as a fourth state of matter (Salzmann 1998). Plasma is a term encompassing many plasma regimes, characterised according to the plasma temperature and particle density. Plasma behaviour is highly complex and difficult to describe, with different models applied to analyse plasmas of differing temperature and density; the properties of any given plasma dictate the method of modelling and analysis. Figure 2-1 illustrates the broad range of density and temperature values which plasmas may exhibit, where plasma electron density N_e is plotted against absolute temperature T. It can be seen that plasma electron densities may extend from the order of 10^0 cm^{-3} as encountered

in the solar wind and the earth plasma sheet, up to 10^{23} cm^{-3} in some laser generated plasmas. Plasma temperatures may span the range 10^{-2} to 10^{5} eV (~10^{2} to ~10^{9} K).

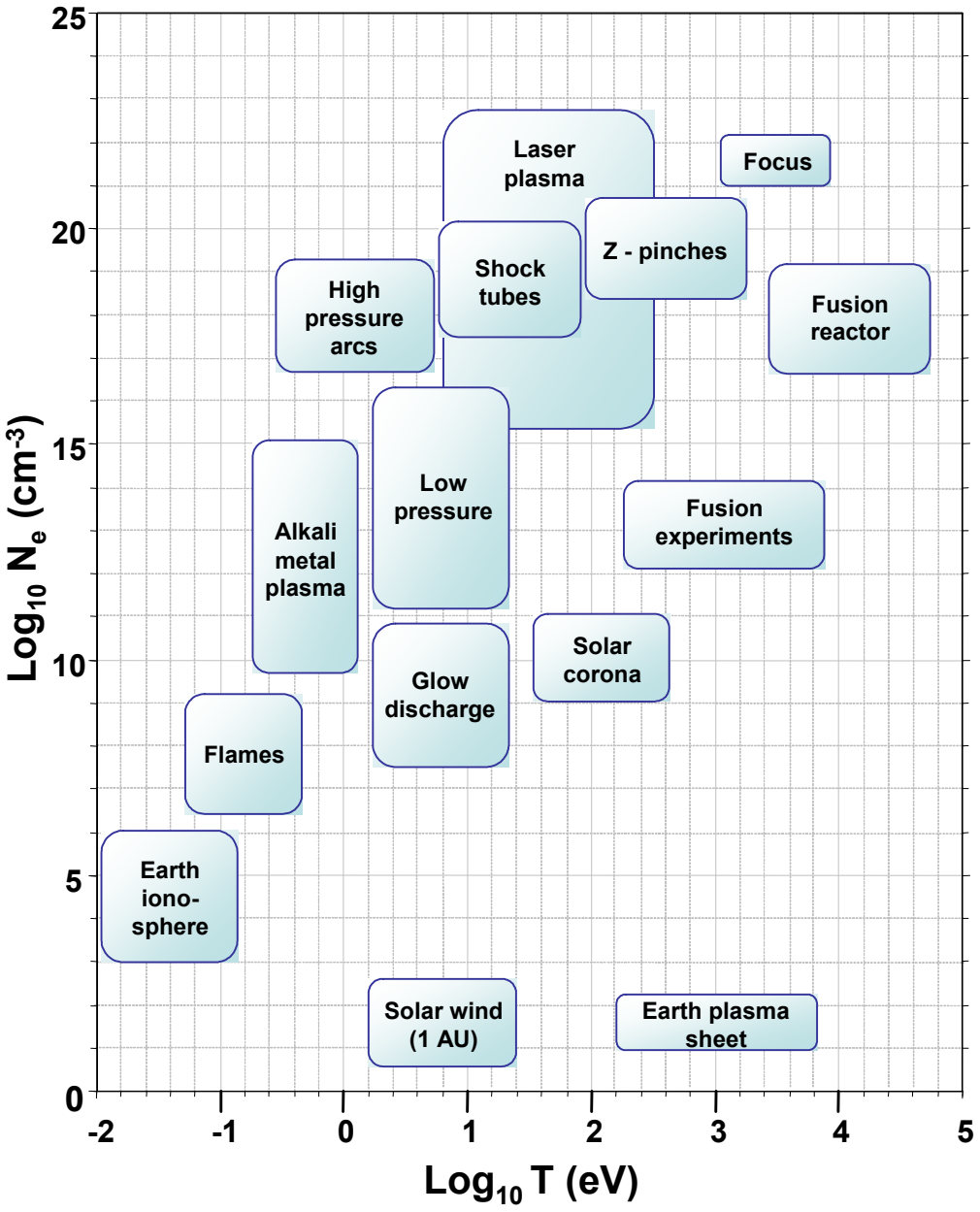

Figure 2-1 Plasma regimes (redrawn from Huba 2007): *T* here represents plasma temperature, N_e represents plasma electron density

A plasma consists of atoms, molecules, ions and electrons and may be treated statistically as a whole as being electrically neutral. The electrons may be separated into *bound electrons*, electrons that occupy negative-energy quantum states bound to a single ion, and *free electrons*, positive energy electrons moving freely in the plasma (Salzmann 1998). The total ionic charge equals the number of free electrons. Considering a homogeneous plasma containing positive ions of atomic number Z, the average charge of the nuclei is therefore Z and the ion density may be denoted by n_i. The ions will in general be of different ionisation or charge states depending on how many electrons have been stripped from them. The charge state of a given ion is denoted by ζ and is equal to the number of electrons missing from the atom. The number density of ions having a given charge state ζ is denoted N_ζ, giving (Salzmann 1998):

$$\sum_{\zeta=0}^{Z} N_\zeta = n_i \tag{2.1}$$

The summation in Equation 2.1 includes, in principle, all of the possible ionisation states from neutral ($\zeta = 0$) up to fully ionised ($\zeta = Z$). Ions with a given ionisation state ζ contribute ζ electrons to the population of free electrons in the plasma. The plasma electron density is given (Salzmann 1998):

$$N_e = \sum_{\zeta=0}^{Z} \zeta N_\zeta \tag{2.2}$$

this is equivalent to the requirement of charge neutrality within the plasma. The relationship in the above equation is only valid over the whole population of the plasma. The electron density may not be homogeneous throughout the plasma

(Salzmann 1998). The average ionisation state of positive ions within the plasma is denoted as $\overline{Z}$ and is defined by (Salzmann 1998):

$$\overline{Z} = \frac{\sum_{\zeta=0}^{Z} \zeta N_\zeta}{\sum_{\zeta=0}^{Z} N_\zeta} = \frac{N_e}{n_i} \tag{2.3}$$

or:

$$N_e = \overline{Z} n_i \tag{2.4}$$

The ionisation state distribution and $\overline{Z}$ depend on both the plasma temperature and density (Salzmann 1998).

2.2.1 The Ion Sphere

In a plasma of ion density n_i the average volume available for each ion is $V_i=1/n_i$. The ion sphere is a sphere with this volume V_i and radius R_i (Salzmann 1998).

$$V_i = \frac{4\pi}{3} R_i^3 = \frac{1}{n_i} \tag{2.5}$$

R_i is called the ion sphere radius,

$$R_i = \left(\frac{3}{4\pi n_i} \right)^{1/3} \tag{2.6}$$

and referred to as the *Wigner-Seitz radius* (Salzmann 1998). The Wigner-Seitz radius is defined as the radius of a sphere having the same volume as the volume per ion. On average, each ion sphere contains one ion of average charge $\overline{Z}$, and thus the requirement of charge neutrality dictates that it must also contain $\overline{Z}$ free

electrons. This statement is only true as an average, and in real plasmas there may be significant local fluctuation around this average.

2.2.2 The Debye Sphere

The long range of electrostatic forces between charged particles means that each charged particle may interact with an appreciable number of other particles at any time; the motion of the charged particles is thus correlated and termed *collective*. Plasmas are distinguished from hot gases by the dominance of collective effects (Thorne 1974). The *Debye shielding distance* (also known as the *Debye length*), $\rho_{D,}$ measures the distance to which the electric field of an electron or ion extends before it is effectively shielded or screened by oppositely charged particles (Thorne 1974). Interactions between individual charged particles dominate over distances < ρ_D, whereas collective effects dominate at distances > ρ_D (Thorne 1974). The criterion for plasma existence i.e. the dominance of collective effects) requires that ρ_D must be appreciably smaller than the dimensions of the plasma. The Debye shielding distance is given:

$$\rho_D = \left(\frac{\varepsilon_0 kT}{e^2 N_e} \right)^{1/2} \tag{2.7}$$

inserting numerical values in Equation 2.7 one can approximate:

$$\rho_D \approx 50 \sqrt{\left(\frac{T}{N_e} \right)} \tag{2.8}$$

where T is in K, N_e is in m^{-3}, ρ_D is in m, ε_0 is the permittivity of free space, e is the electron charge and k is Boltzmann's constant (Thorne 1974). The Debye

radius decreases as the ion density rises (Salzmann 1998). Considering a typical laser-induced plasma of $T \sim 7000$ K and $N_e \sim 2 \times 10^{24}$ m^{-1} then Equation 2.8 yields ρ_D as approximately 2.96×10^{-9} m, which is considerably smaller than the dimensions of such a plasma, generally of the order of millimetres.

The *Debye sphere* is a sphere of radius ρ_D where ρ_D is the Debye length, or the Debye shielding distance. The number of ions η_i inside the Debye sphere is given by (Salzmann 1998):

$$\eta_i = \frac{4\pi}{3} n_i \rho_D^3 = \left(\frac{\rho_D}{R_i} \right)^3 \tag{2.9}$$

2.3 Plasma Models

Plasmas are generally separated into two main classifications, Local Thermal Equilibrium (LTE) plasmas and Coronal Equilibrium (CE) plasmas (Thorne 1974). LTE plasmas are characterised by a single temperature, and generally have electron densities greater than $\sim 10^{15}$ cm^{-3}. Coronal Equilibrium plasmas (Griem 1964, Thorne 1974), named after the corona of the sun, are characterised by high temperatures (typically of the order 10^6 K), but low electron densities (of the order $\sim 10^8$ cm^{-3}).

The Collisional Radiative Steady State (CRSS) model is a third, less commonly encountered, plasma model describing plasmas that fall between the LTE and CE regimes (Salzmann 1998). Traditionally it is assumed that the plasmas induced by pulsed laser radiation generally fall into the regime of LTE (Thorne 1974,

Griem 1997, Cremers and Radziemski 2006); as such CE and CRSS plasmas will not be encountered during this work and so will not be described here.

2.3.1 Local Thermal Equilibrium Plasmas

LIBS plasmas are traditionally modelled as being in Local Thermal Equilibrium (LTE), wherein the plasma may be treated as having a single temperature, i.e. the free electrons, ions and neutral species comprising the plasma are at the same temperature. For the plasma to exhibit LTE, atomic and ionic states must be populated and de-populated predominantly by collisional rather than radiative processes (Le Drogoff et al. 2001); this requirement dictates that the electron density is sufficiently rich to maintain a high collision rate. The corresponding necessary condition for LTE is that:

$$N_e \ (\mathrm{cm}^{-3}) \geq 1.6 \times 10^{12} \ T^{1/2} \ \Delta E^3 \qquad (2.10)$$

where ΔE (in eV) is the energy difference between the upper and lower states, T (in eV) is the temperature (Russo et al. 1999, Milan and Laserna 2001, Shaikh et al. 2006). N_e is the lower limit for the electron number density to collisionally maintain the energy level populations of LTE while competing with radiative processes. If LTE exists, then the distribution of electron speeds and populations of energy levels or ion stages are dependent on temperature alone. The Maxwellian velocity distribution function f_M is given by (Cremers and Radziemski 2006):

$$f_M = \left(\frac{m}{2\pi kT}\right)^{3/2} \exp\left(\frac{-mv^2}{2kT}\right) \tag{2.11}$$

where m is the electron mass and v the electron speed. Boltzmann's formula for the ratio of populations of two energy levels E_1 and E_2 is given by (Thorne 1974):

$$\frac{N_2}{N_1} = \left(\frac{g_2}{g_1}\right)\exp\left(\frac{-(E_2 - E_1)}{kT}\right) \tag{2.12}$$

where g is the statistical weight of that level. The statistical weight of a state is equal to its degeneracy, which is the number of distinct sub-states having the same energy (Thorne 1974). Sometimes it is required to express the population of a given state N_j in terms of the total number density N of a particular species. If N_0 represents the population of the ground state, N_1 the population of the first excited level etc. then:

$$\begin{aligned} N &= N_0 + N_1 + N_2 + \cdots \\ &= \frac{N_0}{g_0}\left[g_0 + g_1 \exp\left(\frac{-E_1}{kT}\right) + g_2 \exp\left(\frac{-E_2}{kT}\right) + \cdots\right] \\ &= \frac{N_0}{g_0}\sum_{j=0}^{\infty} g_j \exp\left(\frac{-E_j}{kT}\right) = \frac{N_0}{g_0} Q(T) \end{aligned} \tag{2.13}$$

where $Q(T)$ is the partition function, and is defined by (Thorne 1974):

$$Q(T) = \sum_{j=0}^{\infty} g_j \exp\left(\frac{-E_j}{kT}\right) \tag{2.14}$$

The partition function is usually taken as the ground state statistical weight (Cremers and Radziemski 2006). From Equation 2.13 we can see that $N_0 = g_0N/Q(T)$. The population of the level j is given by (Thorne 1974):

$$N_j = \frac{N}{Q(T)} g_j \exp\left(\frac{-E_j}{kT}\right) \tag{2.15}$$

It is well known that the assumption of LTE within typical LIBS plasmas is tenuous, with spectroscopic analyses yielding different electron and ion temperatures for a given plasma (Milan and Laserna 2001, Le Drogoff et al. 2001). As the electron densities in such plasmas may satisfy the condition in Equation 2.10 the LTE model is still applied, but with caution. It should be noted that the criterion outlined in Equation 2.10 is a necessary, but not entirely sufficient, requirement for the assumption of LTE within a given plasma.

The main obstacle to LTE conditions existing within LIBS plasmas is their transient nature, with lifetimes in the nanosecond to microsecond range. Typically it will take approximately 1 μs for full LTE conditions to stabilise in a static plasma at $T \sim 10\ 000$ K and $N_e \sim 10^{16}$ cm^3 (Thorne 1974); however, the expanding nature of laser-induced plasmas dictates that LTE conditions may never hold in the lifetime of the plasma.

2.4 Optical Plasma Emission

Analysis of the optical emission from plasmas is perhaps the most important diagnostic tool for characterising their properties, and has the benefit of remote measurement without perturbing the plasma during the process. The emitted

spectrum yields important information regarding the neutral and ionic species within the plasma, as well as instantaneous information concerning the plasma density, temperature and degree of fractional ionisation.

Plasma emission spectra may be considered as two parts: line emission and continuum emission. Spectral line emission occurs when a bound electron in an excited state relaxes to a lower energy state, emitting a photon of a specific wavelength in the process. The continuum emission is due to free-free transitions (also called 'brehmstrahlung' radiation) and free-bound transitions (also called recombination radiation). Figure 2-2 shows typical transitions in an atom or ion; E_g refers to the ground state of the atom or ion, E_1 and E_2 to two excited states, and $E_{ionisation}$ to the ionisation potential of the atom. If E is given in Joules, the transition frequency $\nu = \Delta E/h$, the wave number $\sigma=\nu/c$ and the wavelength $\lambda=1/\sigma$ where ΔE is the energy difference between two states, c is the speed of light in vacuum and h is Planck's constant (Cremers and Radziemski 2006).

The bound-bound transition refers to a bound electron in an excited state relaxing to a lower energy level. The photon emitted during such a transition has a frequency $\nu = (E_1 - E_0)/h$ where E_1 and E_0 are the energies of the upper and lower states respectively and h is Planck's constant (Lee et al. 1997). The free-bound radiation is emitted during the recombination of a free electron into an ionic or atomic energy level, where the electron gives up its excess kinetic energy in the form of a photon.

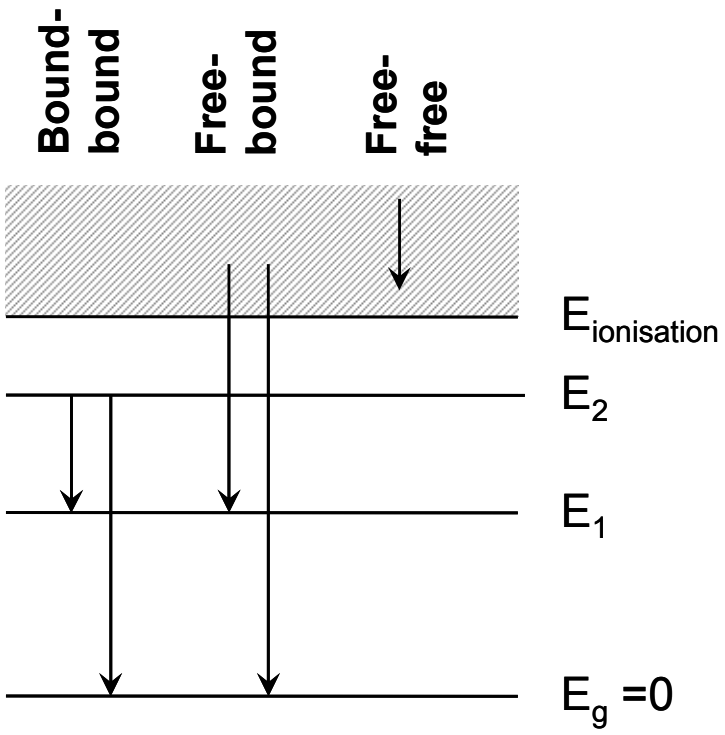

Figure 2-2 Typical transitions in an atom or ion giving rise to optical emission

In the free-free brehmstrahlung process photons are emitted by electrons which are accelerated or decelerated by the influence of surrounding ions.

2.4.1 Emission Line Profiles

The ideal monochromatic emission line does not exist; any atomic or molecular transition is associated with a finite spread of energy and hence of frequency (Thorne 1974); this is known as natural line broadening. Physical processes occurring within the plasma perturb the emitting species and also lead to a broadening of the emission lines. Line broadening due to the Stark effect and Doppler broadening (Section 2.8.1) is frequently encountered in LIBS plasmas, as is resonance broadening (Section 2.8.2). Pure Doppler broadening will lead to a Gaussian line profile (Cremers and Radziemski, 2006) as described by:

$$I(\sigma) = \left(\frac{4\ln 2}{\pi\Gamma^2}\right)\exp\left[\frac{-4\ln 2(\sigma-\sigma_0)^2}{\Gamma^2}\right] \tag{2.16}$$

where Γ is the peak Full Width at Half Maximum height (FWHM), given by:

$$\Gamma = \left(\frac{8kT\ln 2}{Mc^2}\right)^{1/2}\sigma_0 \tag{2.17}$$

where M is the atomic mass of the emitting species and σ_0 the central wave number of the transition. Natural line broadening and Stark broadening lead to a Lorentzian line profile:

$$I(\sigma) = \frac{(\Gamma/2\pi)}{(\sigma-\sigma_0)^2 + (\Gamma/2)^2} \tag{2.18}$$

The convolution of the Gaussian and Lorentzian line profiles leads to a Voigt profile (Cremers and Radziemski 2006, Thorne 1974, Bulajic et al. 2002); either the Gaussian or Lorentzian contribution may dominate depending upon the primary line broadening mechanism.

2.4.2 Plasma Opacity and Emission Line Self Absorption

Plasmas are described as being optically thin, so the radiation is emitted from the plasma without significant absorption or scattering (Cremers and Radziemski 2006).

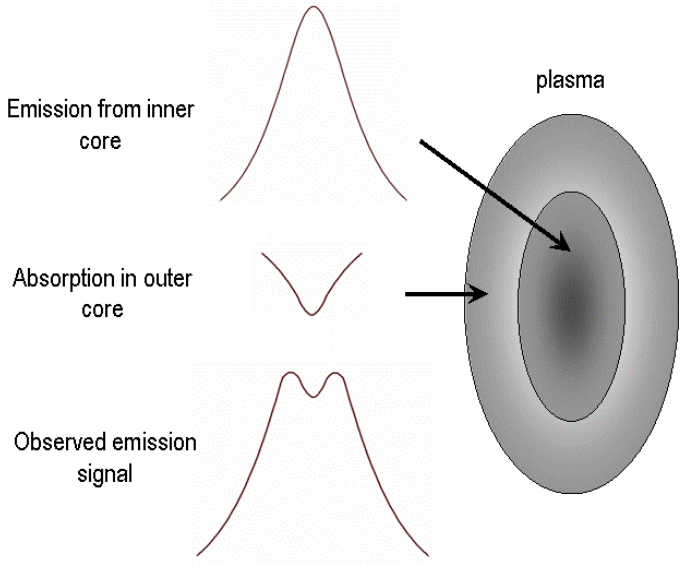

Figure 2-3 Origin of self-absorption of emission lines (Redrawn from Cremers and Radziemski 2006)

If a plasma is optically thick then self-absorption, and in extreme cases reversal, of emission lines can occur; this self absorption leads to a lower perceived emission line intensity which will corrupt spectroscopic plasma diagnostics. Figure 2-3 illustrates the origin of emission line self absorption. The outer layer of the plasma is comprised of cooler species than those radiating in the core. The cooler species absorb the radiation emitted from the core of the plasma, leading to an observed drop in line intensity. Self absorption is generally encountered in emission lines where the lower energy level of the transition is the ground state, or close to the ground state (Liu et al. 1999). As transitions are element specific, emitting photons of a specific wavelength, a given species has the highest probability of reabsorbing a photon from the same species (Cremers and Radziemski 2006).

An emission line that is not self absorbed will best fit a Lorentzian curve profile, whereas a self absorbed line will display a Gaussian profile (Liu et al. 1999, Bulajic et al. 2002); the profile of a spectral line may thus be employed as a diagnostic tool to determine the opacity of a plasma.

2.5 Optical Emission Spectroscopy

Optical Emission Spectroscopy (OES) is a spectroscopic technique exploiting the optical emission from a plasma. Generally a spectrograph or monochromator is used to disperse the optical emission, which is then subsequently captured using a CCD array, or a photo-multiplier tube etc., and analysed. The dispersed emission spectrum can yield information regarding the elemental composition of the plasma, the fractional ionisation of the plasma, electron and ionic species temperatures and electron density. Gated capture of the spectra allows temporal resolution of the plasma.

The main advantage of OES plasma analysis is that the measurements are performed remotely; the plasma is not disturbed during the measurement process. The major disadvantage of OES plasma analysis is that the technique relies on the assumption of LTE conditions within the plasma, which is seldom the case where LIBS is concerned.

2.6 OES Measurements of Electron Temperature

If a plasma is assumed to be in LTE, then it is described by a single temperature, the electron, or electron excitation, temperature T_e. The three most commonly

employed OES techniques for determining T_e are the 2-line-ratio method, the Boltzmann plot and the line-to-continuum ratio method.

2.6.1 The 2-Line-Ratio Method

The radiant spectral intensity of a line is related to N_j the population of a given state *j* by (Cremers and Radziemski 2006):

$$I = \frac{h\nu A N_j}{4\pi} \tag{2.19}$$

where I is in units if W/sr, ν is the line frequency and A is the transition probability. Recalling Equation 2.15, giving the population N_j of a level j, Equation 2.19 may be rewritten:

$$I = \left(\frac{hcNg_j A}{4\pi\lambda Q}\right)\exp\left(\frac{-E_j}{kT}\right) \tag{2.20}$$

The ratio of the intensities of two lines is thus:

$$\frac{I_1}{I_2} = \frac{g_1}{g_2}\frac{A_1}{A_2}\frac{\lambda_2}{\lambda_1}\exp\left[-\left(\frac{E_1 - E_2}{kT}\right)\right] \tag{2.21}$$

In Equation 2.21 the subscripts *1* and *2* refer to two spectral lines of the same element and ionisation state. The spectroscopic constants *I, λ, g, A* and *E*, represent the line intensity, wavelength, statistical weight, transition probability

and energy of the excited state, respectively. Therefore if the intensities of two lines are accurately known, as are the values of g, A and E, then one may calculate T. Since the difference between E_1 and E_2 may be small the accuracy of this method is limited. To overcome this problem one can resort to the determination of relative intensities of lines from the same element but of successive ionisation states (Amoruso et al. 1999), which by definition will have a greater energy difference. The line intensities used in Equation 2.21 may be either the peak heights or integrated areas of the peaks so long as either one or the other is adhered to consistently throughout.

2.6.2 The Boltzmann Plot

Relative intensities of emission lines are not always easy to measure precisely, and the accuracy of the two-line-ratio method may be poor if the lines chosen have the same or similar upper energy levels. A more accurate method of temperature determination uses the Boltzmann plot (Sneddon et al. Eds 1997), which is a graphical method of analysing several emission lines simultaneously. Equation 2.20 describing the intensity of a given emission line may be rearranged:

$$\frac{I\lambda}{gA}\frac{4\pi Q}{hcN_0} = \exp\left(\frac{-E}{kT}\right) \tag{2.22}$$

taking logarithms we obtain:

$$\ln\left(\frac{I\lambda}{gA}\right) + \ln\left(\frac{4\pi Q}{hcN_0}\right) = \frac{-E}{kT} \qquad \text{or:}$$

$$\ln\left(\frac{I\lambda}{gA}\right) = \frac{-E}{kT} - \ln\left(\frac{4\pi Q}{hcN_0}\right) \qquad (2.23)$$

which is the equation of a straight line with a gradient -1/*kT*. If one plots a graph of *ln(Iλ/gA)* versus *E* for several simultaneously measured emission lines, the plasma temperature can be determined (Sneddon et al. Eds 1997, Cremers and Radziemski 2006).

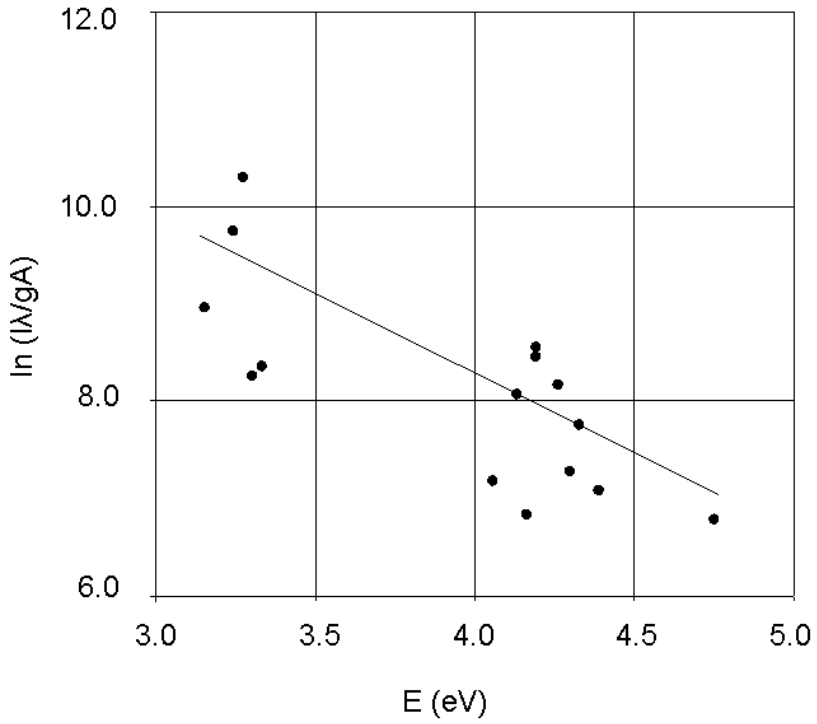

Figure 2-4 Example of a Boltzmann Plot derived from LIBS of iron ore (redrawn from Cremers and Radziemski 2006)

Figure 2-4 is an example Boltzmann plot of several Fe (I) lines used in electron temperature determination of a LIBS plasma from basalt; from the slope of the line of best fit $T \sim 7500$ K (Cremers and Radziemski 2006).

2.6.3 The Line-to-Continuum Ratio Method

The ratio of the integrated peak intensity of an emission line to the continuum emission level may be used to determine the plasma electron excitation temperature. To employ the line-to-continuum ratio method a Lorentzian curve is fitted to the captured emission spectrum.

An example of a Lorenztian curve fitted to the 288.16 nm Si (I) emission line is shown in Figure 2-5; the captured spectrum is plotted in grey, the fitted Lorentz curve in black. The Lorentzian curve fit enables the continuum background level and the integrated line area to be calculated.

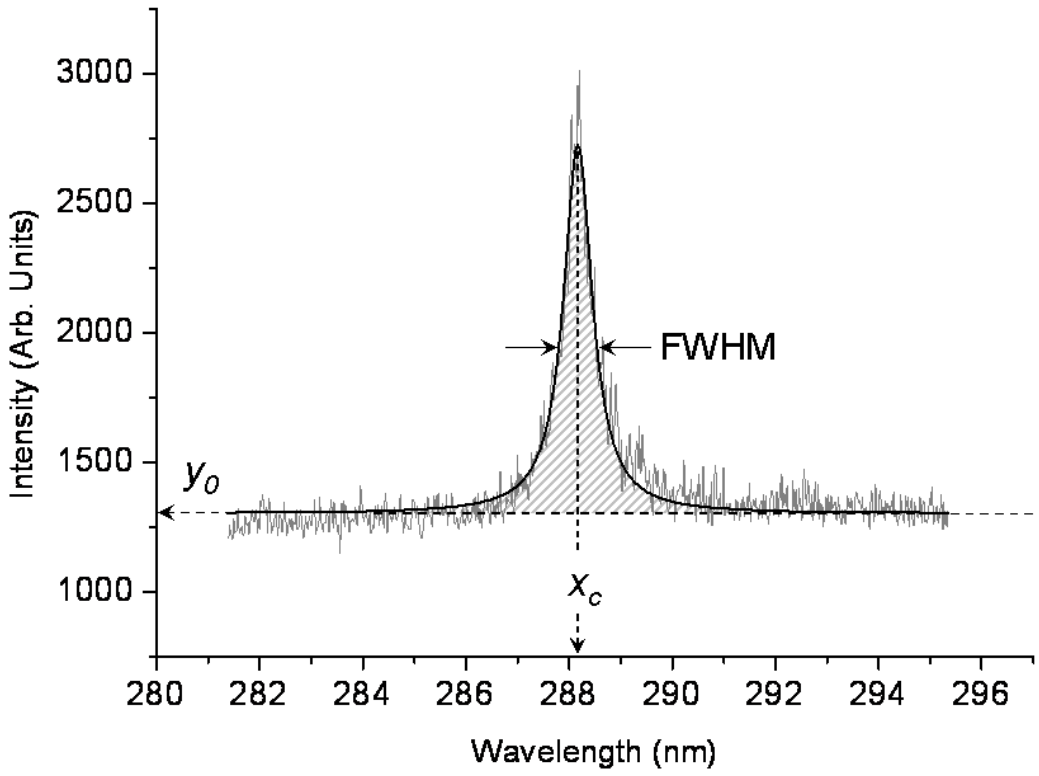

Figure 2-5 Example of a Lorentzian curve fitted to the Si (I) 288.16 nm emission line

The Lorentz curve is expressed by Equation 2.24:

$$y = y_0 + \frac{2A}{\pi}\frac{w}{4(x - x_c)^2 + w^2} \tag{2.24}$$

where y_0 is the baseline offset, which represents the plasma continuum level. A represents the integrated peak emission (the shaded area bounded by the dotted line y_0 and the Lorentz fit), x_c is the centre wavelength of the peak, and w the peak full width at half maximum height (FWHM).

Using the parameters resulting from the Lorentz fit to the emission line the electron temperature T_e may be calculated using Equation 2.25 (Liu et al., 1999).

$$\frac{\varepsilon_l}{\varepsilon_c}(\lambda) = C_r \frac{A_{21} g_2}{Q_i} \frac{\lambda_c^2}{\lambda_l T_e} \frac{\exp\left(\frac{E_i - E_2 - \Delta E_i}{kT_e}\right)}{\left[\xi\left(1 - \exp\frac{-hc}{\lambda k T_e}\right) + G\left(\exp\frac{-hc}{\lambda k T_e}\right)\right]} \tag{2.25}$$

In Equation 2.25 ε_c is the continuum emission coefficient and is equal to y_0 obtained from the Lorentz fit; ε_l is the integrated emission coefficient over the line spectral profile, and is given by the integrated area of the fitted Lorentz curve, A. λ_c and λ_l are the continuum wavelength and line wavelength respectively; from the Lorentz curve fit: $\lambda_c = \lambda_l = x_c$. $C_r = 2.005 \times 10^{-5}$ (s K), A_{21} is the transition probability, E_i is the ionisation potential, E_2 is the upper state energy level, and g_2 the upper state statistical weight. ΔE_i is the lowering of the

ionisation potential of atoms in the presence of a field of ions and is small enough to be deemed insignificant (Liu et al 1999). Q_i is the partition function for a singly ionised silicon ion, and G is the free-free Gaunt factor, which is assumed to be unity (Liu et al. 1999). ξ is the free-bound continuum correction factor, and was calculated for Si vapour by Liu et al. as 1.4 (Liu et al. 1999). Considering the 288.16 nm Si (I) line as an example, the parameters used for plasma temperature determination by the line-to-continuum method are summarised in Table 2-1.

Table 2-1 Parameters used for plasma temperature determination using the Si (I) 288.16 nm emission line-to-continuum method (Liu et al. 1999, CRC Press 1987)

λ (nm)	A_{21} (10^8 s^{-1})	g_2	E_2 (eV)	E_i (eV)	Q_i (eV)	ξ	G	C_r (sK)
Si (I) 288.16	1.9	3	5.028	8.151	6.159	1.4	1	2.005×10^{-5}

There is no simple analytical solution to Equation 2.25 so it is solved for T_e by a process of successive iteration (Appendix 10.4).

2.7 OES Measurements of Ionic Species Temperature

If a plasma is considered to be in LTE, the ionisation equilibrium temperature, often known simply as the ion or ionic species temperature, may be determined through the use of the Saha-Eggert formula (Le Drogoff et al 2001, Keszler and Nemes 2003). This formula is usually applied to singly ionised ions to neutral species equilibrium but may be applied equally well to any two successive ionisation states z and $z + 1$ provided all relevant spectroscopic constants are known. In general, if an appreciable number of ions have reached an ionisation state $z + 1$ then there will be a negligible number of state $z - 1$ present and it is

therefore sufficient to only consider two successive ionisation states at once (Thorne 1974).

2.7.1 The Saha-Eggert Equation

Equation 2.26 is the Saha-Eggert equation relating plasma ionisation equilibrium temperature to the ratio of population of two successive ionisation states z and $z + 1$, and may be written for a neutral atom and singly ionised ion of the same element as (Le Drogoff et al. 2001, Keszler and Nemes 2004):

$$\frac{I_{ion}}{I_{atom}} = \frac{4.83\times10^{15}}{N_e}\left(\frac{gA}{\lambda}\right)_{ion}\left(\frac{\lambda}{gA}\right)_{atom} T_{ion}^{3/2} \exp\left[\frac{-\left(V^{+} + E_{ion} - E_{atom} - \Delta V^{+}\right)}{kT_{ion}}\right] \quad (2.26)$$

The suffixes *ion* and *atom* in Equation 2.26 refer to the spectral lines of an ion and atom respectively, but the equation may be employed between any two successive ionisation states of the same element if the required spectroscopic constants are known. V^{+} represents the ionisation potential of the lower ionisation stage; all other symbols have their usual meaning. There is a small correction to the final term, $-\Delta V^{+}$ which is a correction to the ionisation potential V^{+} of the lower ionisation stage due to plasma interactions (Harilal et al. 1997). ΔV^{+} is usually considered to be negligible for $z = 1$, but for higher ionisation states should be taken into account, and may be determined from (Keszler and Nemes 2004, Harilal et al. 1997):

$$\Delta V^{+} = \frac{ze^2}{4\pi\varepsilon_0\rho_D} \quad (2.27)$$

where z is the ionisation charge state, e the electron charge, ε_0 the permittivity of free space and ρ_D the Debye shielding distance as defined in Equation 2.7.

The spectroscopic constants for example silicon (I) and (II) emission lines suitable for use with the Saha-Eggert equation are given in Table 2-2; the need for simultaneous detection of the two lines requires a spectral capture window with a wide wavelength range.

Table 2-2 Spectroscopic constants of Si emission lines suitable for use in ionic temperature determination by the Saha-Eggert equation (Milan and Laserna 2001)

Ionisation State	Wavelength [λ (nm)]	Transition probability [A] ($\times 10^8$ s^{-1})	Upper state statistical weights [g_k]	Upper state energy level [E_k (cm^{-1})]	Ionisation potential [V (eV)]
Si (I)	390.552	0.118	3	40992	8.152
Si (II)	413.089	1.42	8	103556	16.346

2.8 OES Measurement of Electron Density and Emission Line Broadening Mechanisms

The emission lines from plasmas may be broadened from their theoretical widths due to processes occurring within the plasma. The major cause of line broadening for neutral and singly ionised emitting species in LIBS plasmas is the Stark effect (Thorne 1974, Shaikh et al. 2006, Liu et al. 1999, Milan and Laserna 2001). The magnitude of the Stark line broadening can be used to determine the plasma electron density. The contribution of other major types of line broadening; Doppler broadening, natural broadening and resonance broadening; may be neglected in LIBS plasmas where relatively low temperatures and high densities are observed (Milan and Laserna 2001).

2.8.1 Stark Line Broadening

The Stark effect causes a broadening of emission lines which is proportional to the electron density of the plasma; the higher the electron density, the greater the Stark broadening; accurate measurement of this broadening enables determination of plasma electron density. The Stark effect also produces a shift of the emission line central wavelength, which can also be exploited to calculate the plasma electron density (Amoruso et al. 1999, Griem 1997); this is of limited use for LIBS plasma diagnostics as the resolution of typical LIBS spectrometers is generally too coarse to measure the small shift accurately.

The broadening and shift of emission lines due to the Stark effect arises from the perturbation of emitting species by nearby charged particles (Griem 1964). In the presence of an external electric field, energy levels for a given transition are split into separate degenerate sub-levels, identified by the quantum number m_J (the z component of the total angular momentum J), which causes a corresponding broadening and wavelength shift in the emission line of that transition (Thorne 1974, Cremers and Radziemski 2006, Shaikh et al. 2006, Amoruso et al 1999). The electric field that produces the Stark effect in LIBS plasmas arises primarily from collisions with electrons, with a small contribution from ion collisions (Cremers and Radziemski 2006, Thorne 1974). Doppler broadening effects tend to dominate in the case of highly ionised species due to their small Stark shift, so the inference of electron density from Stark broadening is only suited to lines from neutral or singly ionised emitters (Amoruso et al.1999).

The Stark broadening, $\Delta\lambda_{1/2}$, of emission lines is related to the electron density of the plasma by Equation 2.28 (Milan and Laserna 2001):

$$\Delta\lambda_{1/2} = 2w\left(\frac{N_e}{10^{16}}\right) + \left[3.5A\left(\frac{N_e}{10^{16}}\right)^{1/4}\left(1 - 1.2N_D^{-1/3}\right)w\left(\frac{N_e}{10^{16}}\right)\right] \tag{2.28}$$

The coefficients w and A, both independent of density and weak functions of temperature, are the electron impact width parameter and the ion broadening parameter, respectively. These values are interpolated for the appropriate temperatures from the tables of Griem (Griem 1964). $\Delta\lambda_{1/2}$ is the FWHM of the emitted line in nm. N_D is the number of particles in the Debye sphere, given by Equation 2.29 (Liu et al. 1999):

$$N_D = 1.72 \times 10^9 \frac{T^{3/2}}{N_e^{1/2}} \tag{2.29}$$

Due to the small ionic contribution to line broadening Equation (2.28) may be reduced to (Milan and Laserna 2001, Shaikh 2006):

$$\Delta\lambda_{1/2} = 2w\left(\frac{N_e}{10^{16}}\right) \tag{2.30}$$

To justify this simplification, taking typical values from laser ablation of silicon, $T_e \sim 10\,000$ K and $N_e \sim 2 \times 10^{18}$ cm^{-1}, yields $w = 9 \times 10^{-4}$ nm and $A = 0.0036$ nm (Griem 1964). Using these values the total line broadening is calculated from Equation 2.29 as 0.3684 nm; the ionic contribution to this broadening is 0.0084nm, which is only 2.2 % of the total.

Before performing any line width based measurements the observed line shape must be corrected by subtracting the broadening contribution from the instrumental width (Shaikh et al. 2006, Charfia and Harith 2002):

$$\Delta\lambda_{true} = \Delta\lambda_{observed} - \Delta\lambda_{instrument} \quad (2.31)$$

The instrumental broadening contribution may be determined by spectroscopic analysis of a narrow line width emitter such as a hollow cathode lamp (see Appendix 10.2).

2.8.2 Doppler Line Broadening

Doppler line broadening arises from the apparent shift of wavelength of a signal moving relative to the observer (Thorne 1974). In typical LIBS plasmas there is a large spread of particle velocities, leading to a spread of emitted wavelengths and giving rise to the broadened line shape. The Doppler component of the line width depends only on absolute temperature and the atomic mass of the emitter. The Doppler effect will cause a broadening in line width for Si (I) 288.16 nm of less than 0.0123 nm, even if the plasma is assumed to be ~ 100 000 K (Liu et al. 1999). This value is estimated from:

$$w_{1/2} = 7.19 \times 10^{-10}\ \lambda\ (T/M)^{1/2} \quad (2.32)$$

where M is the atomic mass number, T is the plasma temperature in Kelvin and λ is the line wavelength in nm (Liu et al. 1999, Cremers and Radziemski 2006).

Equation 2.32 is obtained from Equation 2.14 and converting to wavelength units for FWHM (Cremers and Radziemski 2006).

2.8.3 Natural Line Broadening

Natural line widths are related to energy level widths by $\sim \Delta E \Delta t > \hbar$, where ΔE is the width of the level and Δt its lifetime (Thorne 1974). For a transition between two levels with natural lifetimes of approximately 10 ns, the natural spectral line width is about $\sqrt{2}$ times the level width, or 7×10^{-4} cm^{-1} (Cremers and Radziemski 2006). At 500 nm the line width in the example amounts to 0.002 nm, which is not observable at the spectrometer resolutions typically used in LIBS (Cremers and Radziemski 2006).

2.8.4 Resonance Line Broadening

Resonance interactions only occur between identical atoms, and lead to symmetrically broadened, un-shifted lines (Thorne 1974). Resonance line broadening is negligible if the emission line in question is not connected to the ground state of the emitter (Liu et al. 1999, Thorne 1974).

The above discussion of the complex behaviour of plasmas reveals the difficulties inherent in plasma analysis. Much of the work reported by the author goes someway to furthering an understanding of the mechanisms associated with the transient short-lived plasmas that lie at the heart of the LIBS process.

3 Laser-Induced Breakdown Spectroscopy

3.1 Introduction

This chapter provides a summary of the Laser-Induced Breakdown Spectroscopy (LIBS) technique, presenting its advantages and limitations as a compositional analysis tool. A brief overview of laser ablation and plasma plume evolution is followed by a discussion of practical considerations, matrix effects, quantitative problems, and factors limiting the reproducibility of LIBS.

There are many advantages to LIBS over other established elemental analysis techniques; for instance the ability to perform stand-off measurements (Bogue 2005, Whitehouse et al. 2001) and relatively little sample preparation is required (Tognoni et al. 2002, Amoruso et al. 1999); but there are several major disadvantages too. Some of the disadvantages of the LIBS technique are due to current hardware and software restrictions; others are due to the fundamental physical processes occurring during the generation of the plasma plumes, and the inadequacies of the inappropriate LTE-based analyses currently applied to these plasma plumes.

The goal of LIBS is to generate an optically thin plasma that is in LTE and is compositionally representative of the target sample. In fact, such a plasma is seldom generated by pulsed laser radiation; laser-induced plasmas are frequently optically thick (Cremers and Radziemski 2006), such transient plasmas do not entirely fulfil the requirements of LTE (Thorne 1974), and preferential ablation and matrix effects lead to the plume possessing a different composition to that of the sample (Tognoni et al. 2002). Thus any optical emission collected from the

plasma is not necessarily representative of the species comprising the plasma, and the plasma is in turn not necessarily representative of the analyte composition.

LIBS suffers from lack of sensitivity when compared to other materials quantitative analysis techniques, displaying lower limits of detection and generally poor accuracy when determining elemental ratios (Cremers and Radziemski 2006). Free-free and free-bound electronic processes lead to the plasma continuum emission, which imposes a fundamental background limit upon the elemental emission line radiation; this non-specific spectral background radiation severely disrupts the effective sensitivity of the LIBS technique (Garcia et al. 2001). The problems outlined above fundamentally limit the use of LIBS as a quantitative elemental analysis technique, and are the focus of much current work in the LIBS research community.

3.2 LIBS

The principle underlying LIBS is a simple one: the analyte composition may be inferred by spectroscopic analysis of the optical emissions from a laser-induced plasma, generated by focussing high-power, pulsed laser radiation on the sample. LIBS materials analysis requires the following steps:

1.) Laser ablation of the sample and subsequent plasma generation

2.) Collection of the optical emissions from the laser-induced plasma

3.) Dispersion of the captured polychromatic plasma emission

4.) Detection of the dispersed emission spectra

3.3 Laser Ablation

The work contained in this thesis is concerned only with post-breakdown phenomena; it is sufficient to recognise only that laser ablation does occur and is used as a tool to generate the transient plasmas of interest in this study. Due to the complexity of the laser-material interactions occurring, and the short timescales involved in plasma formation and evolution, currently there does not exist a satisfactory model that entirely describes laser-induced plasma formation (Cremers and Radziemski 2006).

The following description of laser ablation is merely an overview of the major processes occurring and does not seek to describe the complex interactions. For a more in-depth discussion of laser ablation mechanisms the reader is directed to (Vadillo and Laserna 2004, Amoruso et al 1999, Cremers and Radziemski 2006, Ready 1971).

Figure 3-1 describes the main processes in laser-induced breakdown of a solid sample; it should be stressed that this is a highly simplified, macroscopic description. Laser ablation is a complex process dependent on the properties of both the sample material and the laser used (Tognoni et al. 2002); the following discussion is valid for laser pulses in the nanosecond regime incident on a solid sample.

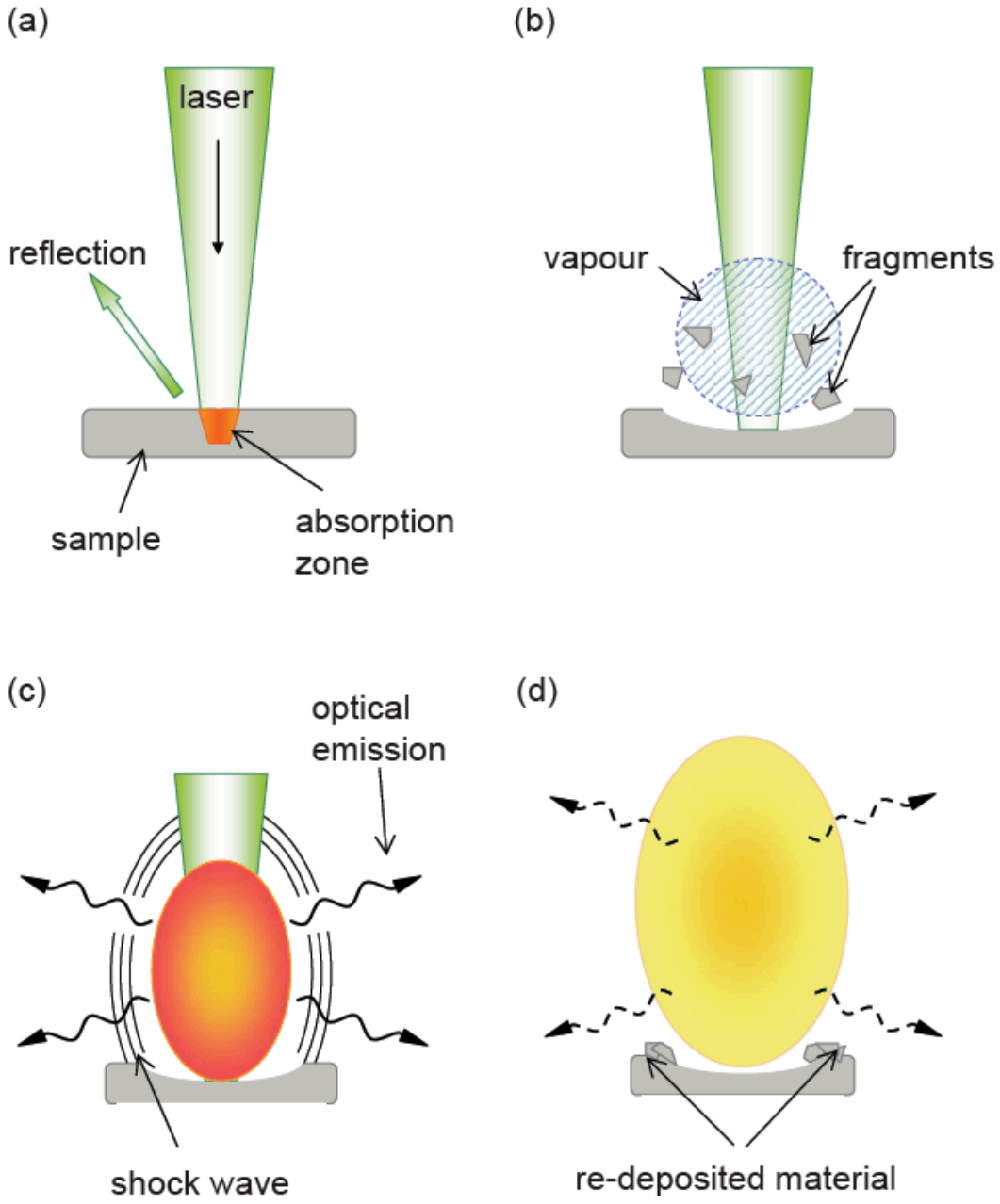

Figure 3-1 Laser ablation and laser-induced plasma formation.

Figure 3-1 (a) represents the laser pulse incident on the sample surface; the amount of energy absorbed depends on reflection losses (Vadillo and Laserna 2004), the laser wavelength, and pulse duration (Shaikh et al. 2006). The absorbed energy is converted into heat, causing analyte vaporisation as the local temperature exceeds boiling point of the sample material; the timescale of this

interaction is so small that it has been considered that the optical energy is converted into heat instantaneously at the point of absorption (Ready 1971).

Figure 3-1 (b) illustrates analyte vaporisation and ejection of particulate matter from the sample, which gives rise to a small volume of vapour immediately above the sample surface. This vapour interacts with the tail end of the incoming laser pulse, scattering and absorbing laser radiation which leads to heating, ionisation and plasma formation. The absorption of laser radiation by the plasma leads to *plasma shielding* wherein the laser energy may not reach the sample surface to initiate further material ablation (Liu et al. 1999, Milan and Laserna 2001).

Figure 3-1 (c) shows breakdown occurring as the plasma expands causing further material to be removed from the sample surface, which feeds the reaction. The plasma expands rapidly producing an audible shockwave (Amoruso et al. 1999). Visible radiation is emitted by the expanding plasma; the plasma is comprised of excited neutral and ionic species giving rise to emission line radiation, and free electrons that contribute to the plasma continuum emission. Re-combination of ionic species with free electrons creates electrically neutral species, which in turn may aggregate to form polyatomic clusters and larger particles (Vadillo and Laserna 2004). The power density required for laser-induced plasma formation is typically 10^8 to 10^{11} Wcm^{-2} for solids at atmospheric pressure (Cremers and Radziemski 2006).

Figure 3-1 (d) illustrates the plasma expanding and cooling. The net intensity of the optical emission diminishes as the emitting species within the plasma relax and recombine. Ablated particulate matter is re-deposited on the crater walls and around the crater surface.

3.3.1 Temporal Evolution of a Typical Laser-Induced Plasma

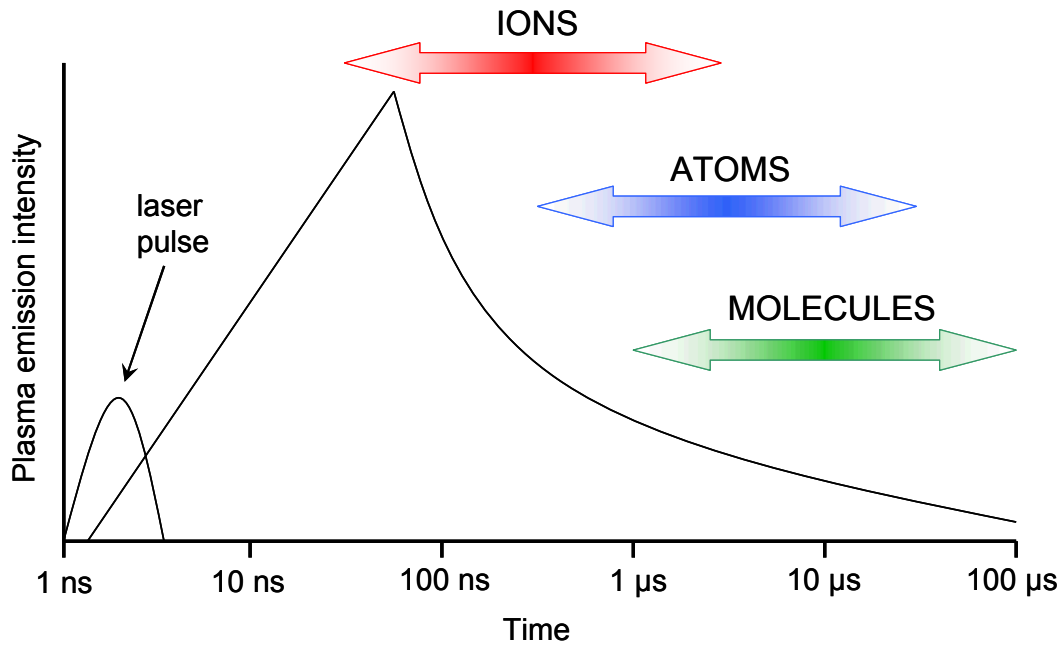

Figure 3-2 The optical emission intensity of a typical laser-induced plasma with respect to time (redrawn from Lee et al. 1997)

The behaviour of laser-induced plasmas is very complex; the temperature, density, fractional ionisation and net emission signal intensity vary as the plasma expands (Vadillo and Laserna 2004). Figure 3-2 depicts the variation in the broadband visible emission intensity of a typical ns-pulsed laser-induced plasma with respect to time. The initiating laser pulse is represented on the figure; this is not drawn to the same intensity scale as the plasma emission. The emission intensity is seen to rise rapidly during and immediately after the laser pulse

irradiates the target material, achieving a maximum at approximately 100 ns after plume formation. The signal intensity in this early phase of the plasma is dominated by the continuum emission; as the plasma expands and cools, line emission becomes the dominant characteristic feature of the optical signal.

Ionic species emissions are the predominant contribution to signal intensity in the early stages of plasma evolution; as the ionic species re-combine with free electrons the neutral atomic species emission intensity rises and the ionic species emissions diminish. In the latter stages of plasma expansion there is a contribution to the signal intensity from molecular transitions due to the agglomeration of atoms. These three emission regimes are marked on Figure 3-2, where an overlap is evident; at certain times the three states may co-exist in the plasma, their ratio a function of temperature (Liu et al. 1999). The timescales indicated in Figure 3-2 may alter depending on laser wavelength and pulse width, sample composition, ambient gas pressure and composition; but all laser-induced plasmas display a similar emission trend (Lee et al. 1997).

Figure 3-3 shows the temporal evolution of the optical emission from typical laser-induced silicon plasmas (Milan and Laserna 2001). LIBS of semiconductor grade silicon wafers was performed in air at atmospheric pressure, induced by the second harmonic of a ns pulsed Nd:YAG laser. The plasma emission was imaged 1:1 onto the entrance slit of a 0.5 metre spectrograph, and the dispersed spectra captured with a gated system enabling temporal resolution of the plumes; the spectra shown in Figure 3-3 are not corrected for the instrument's spectral response.

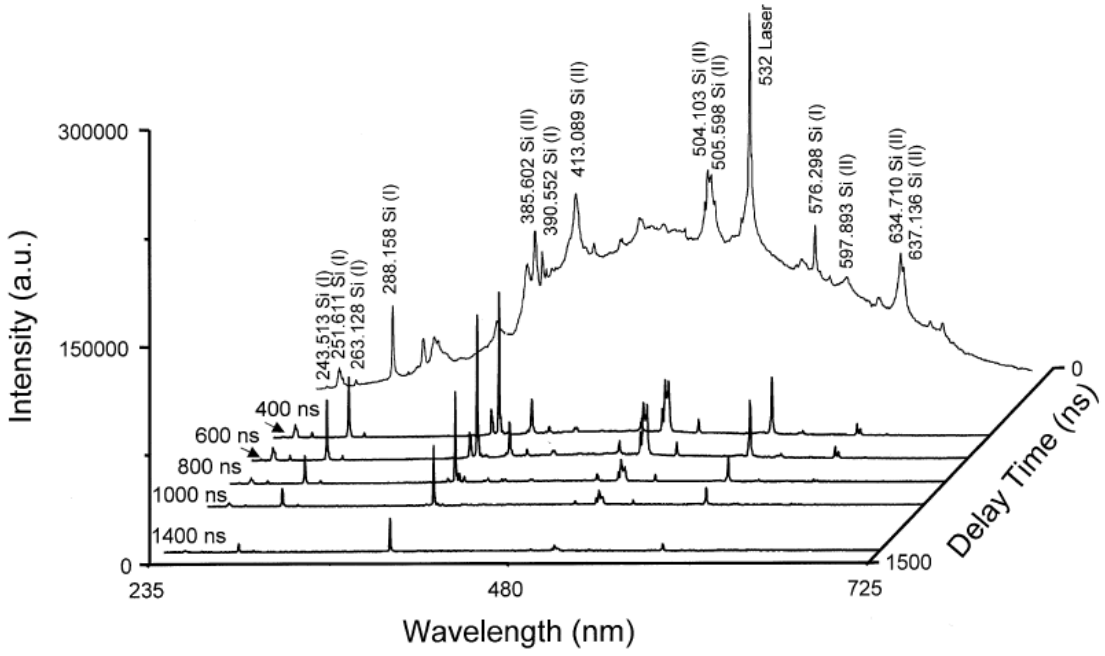

Figure 3-3 Temporally resolved LIBS emission spectra of silicon (Milan and Laserna 2001)

In the early phases of plume expansion (indicated as a delay of 0 ns) the emission spectrum is dominated by the characteristic continuum radiation profile, which arises from brehmstrahlung and recombination events in the electron-rich plumes. Several neutral and ionic emission lines are resolvable above the continuum background; the Stark line-broadening due to the abundance of free electrons early in the plume development is evident in the line profiles.

At later stages of plasma evolution (400 – 1000 ns) the continuum background has diminished, and the Si (I) and (II) emission lines appear sharp and clearly resolvable; the peak intensity of the emission lines decreases as the plasma expands and cools. The emission line profiles display narrower FWHM; this is due to a decreased Stark effect as electron-ion recombination events have reduced the electron density of the plasma. At delay times of approximately 1400 ns the emission line peak intensities have decreased to levels just resolvable

above the instrument background, with the ionic Si (II) emission line barely evident. The emission spectra for all elements share similar characteristics to those displayed by silicon in Figure 3-3, with the emission timescale expanded or contracted according to changes in the specific laser wavelength, energy, pulse duration, material ablation threshold etc. The optical emission from typical LIBS plasmas may have a lifetime of 300 ns to 40μs (Tognoni et al. 2002).

3.4 Collection and Analysis of LIBS Optical Emissions

Prior to spectroscopic analysis, the polychromatic optical emissions from the laser-induced plasma must be collected. By far the most commonly employed system of light collection uses one or more lenses to image the plasma onto the entrance slit of a spectrograph (Milan and Laserna 2001, Liu et al. 2006). Lenses are readily available and inexpensive, offering a versatile system provided that one is careful to choose lenses that transmit light in the wavelength ranges of interest.

To achieve greater flexibility in sample positioning, many groups opt to collect plasma emissions via a fibre-optic cable (Keszler and Nemes 2004, Harmon et al. 2006, Amador-Hernandez et al. 2001) or a combination of collimating lenses and fibre-optic means (Shaikh et al. 2006, Balzer et al. 2005). The use of a fibre-optic cable allows for rapid alteration of sampling geometry, but does introduce complexity to the collection optics system. As is the case with lenses, one must ensure that the fibre-optic efficiently transmits light in the required wavelength range, and when using fibres one must be wary of compatibility with the ambient environment, and interface transmission losses (Cowpe and Pilkington 2008). In

terms of limits of detection and signal-to-noise levels, there is very little difference in the performance of lens versus fibre-optic based systems (Tognoni et al. 2002).

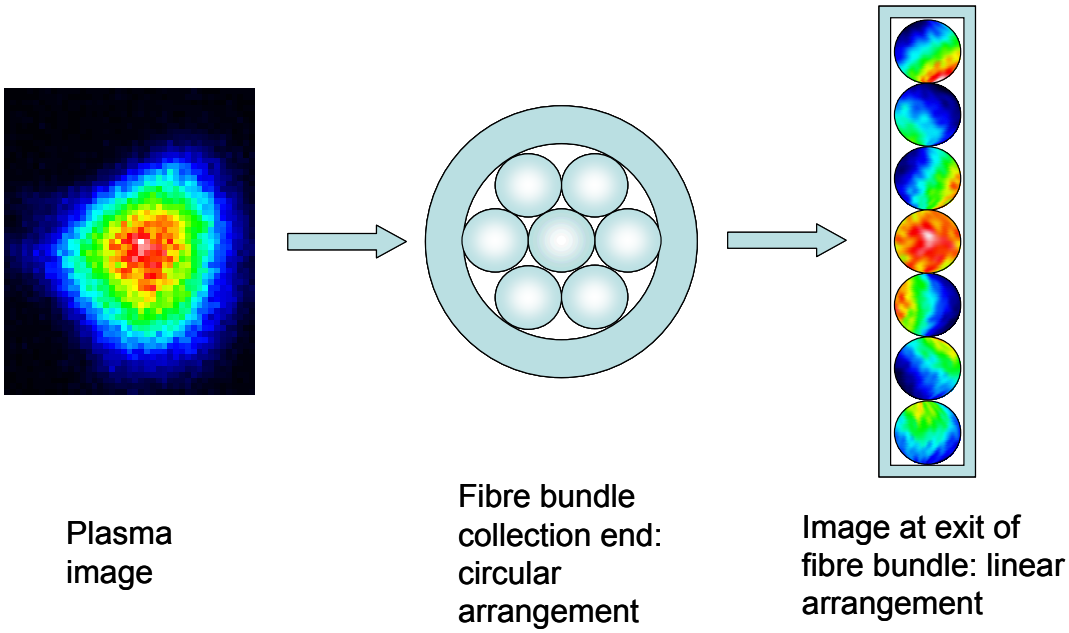

Figure 3-4 Circular to linear optical fibre bundle arrangement; only 7 fibre cores are illustrated for clarity

To maximise the flux collected from the plasma, thus increasing sensitivity, it is typical to employ a multimode bundle of optical fibres, thereby sampling a larger cross sectional area of the plume. Such bundles may consist of tens of individual fibres, each of the order of microns in diameter (Cremers and Radziemski 2006). Fibre bundles have been developed specifically to couple with the narrow input slits of spectrographs, possessing different fibre geometry at either end as shown in Figure 3-4. The collection head of the bundle has fibres arranged in a circular pattern to collect as much light as possible, whereas the end coupled to the spectrometer input has the bundles aligned in a strip, ensuring that all the collected light enters the spectrograph. The major drawback of such an

arrangement, clearly apparent from Figure 3-4, is that spatial resolution of the plasma is corrupted.

3.5 Dispersal of Polychromatic Light

To glean useful analytical information from the plasma emissions, the collected polychromatic light must be dispersed into its component wavelengths, each wavelength being specific to a particular excited elemental transition. Polychromatic light may typically be dispersed by a prism or diffraction grating (Pedrotti and Pedrotti 1993), or by a combination of the two as in the Echelle configuration spectrometer (Cremers and Radziemski 2006). The most commonly encountered dispersing device in LIBS analyses is the Czerny-Turner type spectrograph, which is generally equipped with one or more reflection diffraction gratings (Tognoni et al 2002).

3.5.1 The Diffraction Grating

The diffraction grating disperses polychromatic light by exploiting the sensitivity of its diffraction pattern to the wavelength of the incident light (Pedrotti and Pedrotti 1993). The reflection diffraction grating is most commonly employed in research applications (Pedrotti and Pedrotti 1993), and comprises a periodic array of non-reflecting grooves ruled in a polished, highly reflective surface; a high resolution grating will typically feature a groove density of several thousand grooves per mm (Cremers and Radziemski 2006).

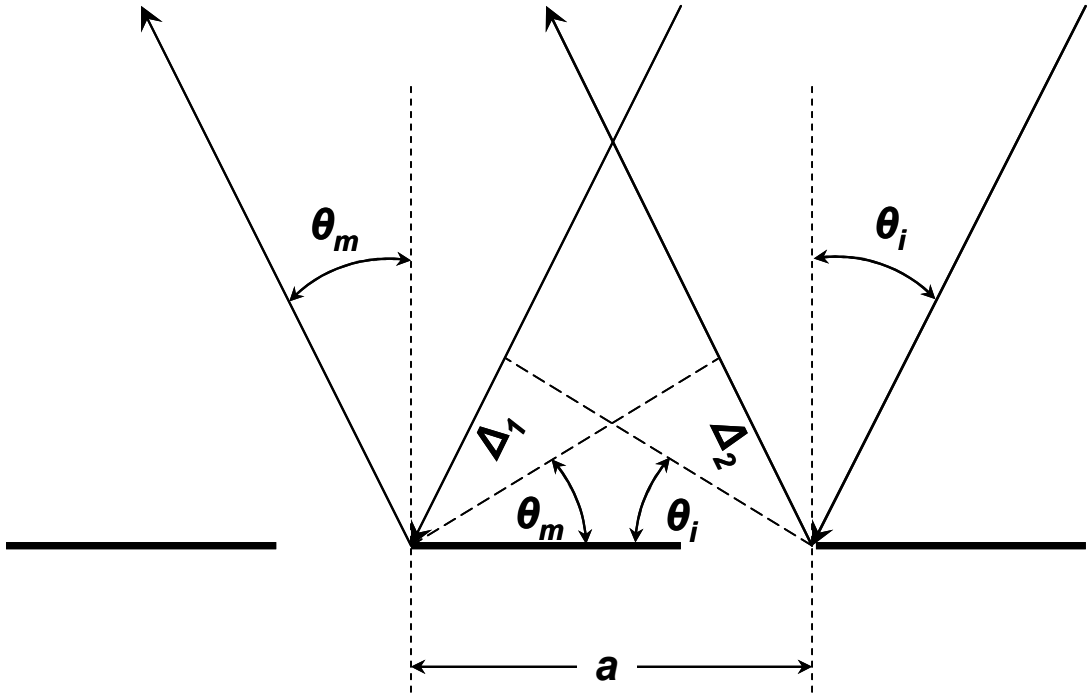

Figure 3-5 Neighbouring reflection grating grooves illuminated by light incident at an angle θ_i with the grating normal (redrawn from Pedrotti and Pedrotti 1993)

A schematic representation of a reflection diffraction grating is given in Figure 3-5, in which a represents the groove spacing, θ_i is the angle of incidence that the incoming light makes with the grating face, and θ_m is the angle of diffraction. The path difference Δ between two equivalent rays of light reflected from successive groove faces is given by (Pedrotti and Pedrotti 1993):

$$\Delta = \Delta_1 - \Delta_2 = a\sin\theta_i - a\sin\theta_m \qquad (3.1)$$

If $\tilde{m}$ represents the order of diffraction, then a principal interference maximum occurs at $\Delta = \tilde{m}\lambda$ and the grating equation follows from Equation 3.1:

$$\tilde{m}\lambda = a\sin\theta_i - a\sin\theta_m \qquad (3.2)$$

with $\tilde{m} = 0, \pm 1, \pm 2$, etc. (Pedrotti and Pedrotti 1993). For $\tilde{m} = 0$, the so-called *zeroth order*, specular reflection at the angle of incidence occurs for all wavelengths. For $\tilde{m} \neq 0$ spectral lines are produced either side of the zeroth order. For a fixed angle of incidence θ_i, the direction θ_m of diffraction depends on wavelength; therefore the grating acts as a dispersing element, separating wavelengths of light.

The efficiency of a grating for a given wavelength and diffraction order is the ratio of the diffracted light intensity to that of the incident light. The efficiency of a grating may be improved by controlling the geometry of the grooves, known as *blazing* the grating. The blazed grating features grooves shaped with a right-angled triangle cross-section, making an angle θ_b, the blaze angle, to the grating body.

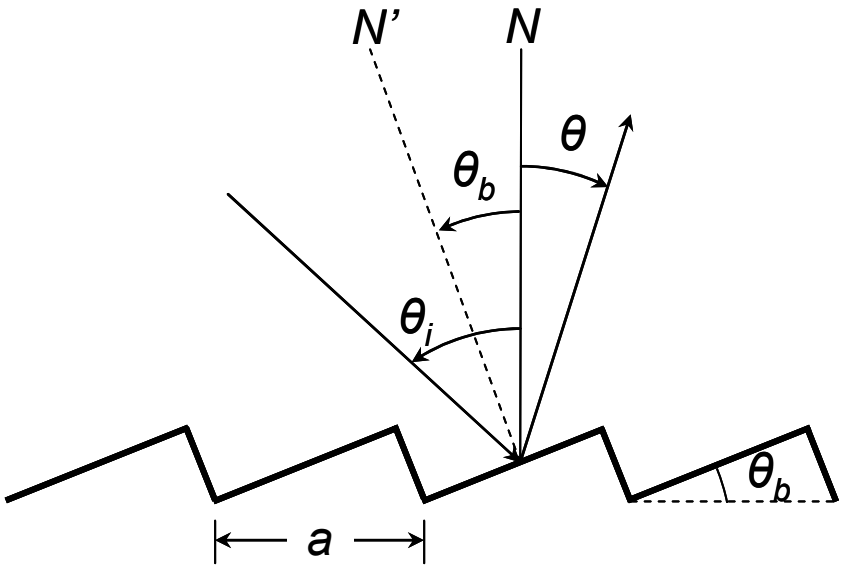

Figure 3-6 Cross section of a blazed reflection diffraction grating (redrawn from Pedrotti and Pedrotti 1993)

A blazed grating is illustrated in Figure 3-6, where N represents a normal to the grating body, N' a normal to an individual groove face, a is the groove spacing, θ_i is the angle of light incidence relative to N, θ_b is the blaze angle of the grating, and θ is the angle of diffraction relative to N. The effect of blazing a grating is that the principle maximum diffraction envelope of the zeroth order is shifted into a different order $\neq 0$, and the efficiency of the grating is improved over a certain wavelength range dependent on the blaze angle. For a blazed grating the grating equation becomes (Pedrotti and Pedrotti 1993):

$$\tilde{m}\lambda = a[\sin\theta + \sin(2\theta_b - \theta_i)] \tag{3.3}$$

3.5.2 The Czerny-Turner Spectrograph

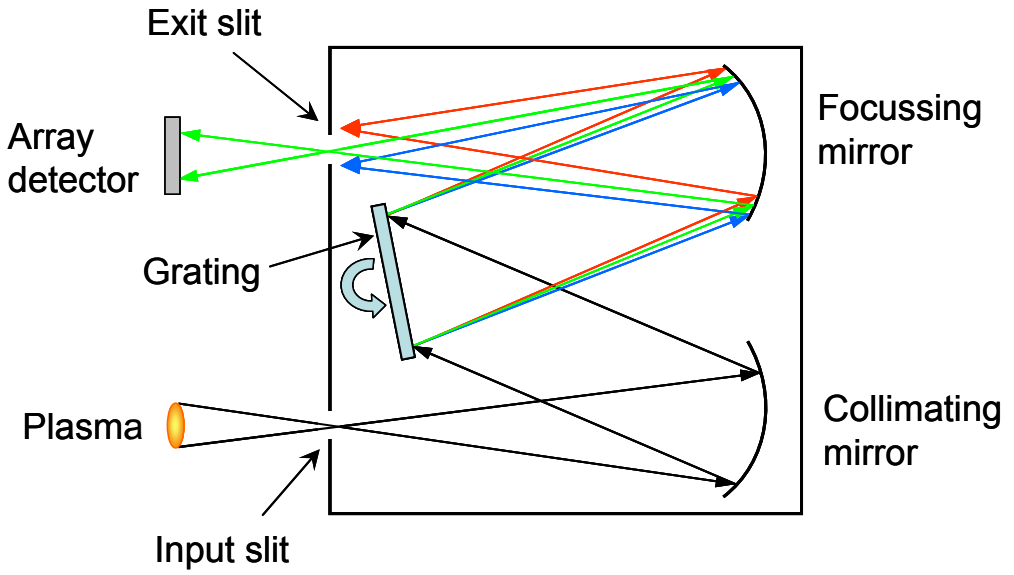

Figure 3-7 Schematic diagram of a Czerny-Turner type spectrograph

There are many types of spectrograph, each defined by a particular configuration of entrance and exit slits, diffraction gratings and mirrors, but they all share a

common principle of operation (Cremers and Radziemski 2006). Polychromatic broadband radiation is dispersed into discrete wavelengths by a diffraction grating; the angle of the grating relative to the incident light determines the wavelength range that propagates through to the exit slit. Figure 3-7 depicts the layout of a typical Czerny-Turner imaging spectrograph with the diffraction grating oriented such that light in the green wavelength range may propagate through the device.

The optical emission from the plasma is imaged onto the entrance slit of the spectrograph, collimated by a curved mirror, and directed onto the diffraction grating; the diffraction grating is mounted such that it may rotate about its centre on an axis perpendicular to the page. The incident light is reflected from the diffraction grating, dispersed according to wavelength, and focussed at the plane of the spectrograph exit slit forming a wavelength-dispersed series of images of the input slit signal. The lateral position of each image depends on the angle through which the diffraction grating diffracts each given wavelength of light; thus the linear dispersion of the images correlates directly to wavelength. Narrowing the input slit of the spectrometer in turn narrows the slit image propagating through the device, thereby reducing overlap of the resultant dispersed images in the plane of the exit slit and hence improving wavelength resolution.

A detector situated at the exit slit of the spectrograph records the relative intensity of each component wavelength, generating an emission spectrum of the broadband input source (Cremers and Radziemski 2006). An array detector,

such as a Charge-Coupled Device (CCD) Intensified-Charge-Coupled Device (ICCD) or Photo-Diode Array (PDA) captures a range of wavelengths simultaneously; if the spectrograph is employed to simultaneously record the relative intensities of a range of wavelengths using such an array detector, it is referred to as a *spectrometer*.

If one replaces the array detector with a single channel device such as a photo-multiplier tube (PMT), then a very narrow spectral range is recorded at any given time and the spectrograph acts as a *monochromator*. Using the spectrograph as a monochromator requires the diffraction grating to be swept through successive angles to derive an emission spectrum, presenting each wavelength in turn to the detector. Several single channel detectors may be employed simultaneously to monitor specific emission lines of interest; this hybrid configuration of monochromator and spectrometer is known as a *polychromator* (Pedrotti and Pedrotti 1993).

When performing spectroscopic measurements using a spectrometer the entrance slit is set to its minimum width, typically tens of microns, in order to achieve the highest possible wavelength resolution. The array detector equipped spectrometer may be exploited to produce non-dispersed images (Milan and Laserna 2001). By positioning the diffraction grating such that the zeroth order propagates through to the detector, maximising the input slit width, and ensuring that the plasma image is de-magnified sufficiently that it does not over-fill the entrance slit, the array detector may capture a ‘conventional’ photographic image of the plasma. Although this method of image capture is complicated, it provides

the benefits of employing the same imaging apparatus and optical collection set-up for both dispersed and non-dispersed plasma image capture.

3.6 Detection of Emission

The most common OES photo-detector is the photomultiplier tube (PMT). The PMT is a single channel detector consisting of a photocathode and a series of dynodes to provide light amplification; they are rugged, relatively inexpensive and provide response times of < 1 ns (Cremers and Radziemski 2006). Although offering only single channel detection, PMTs have been employed in LIBS. Noll et al. (Noll et al. 2005) coupled a spectrometer to 12 PMTs to identify more than 30 high alloy steel grades and prevent material mismatches on a production line. Boue-Bigne employed a spectrometer coupled with 41 PMTs when analysing oxide inclusions in steel, and found that the LIBS system compared favourably with SEM-EDX analysis (Boue-Bigne 2007).

The Charge-Coupled Device (CCD) is an array detector providing two or three-dimensional spatial information about light intensity. If the vertical columns of pixels are binned, that is their intensities integrated, then signal to noise ratio may be improved when capturing a wavelength range of a spectrum. Generally the gating time of a CCD array is long compared to the lifetime of the typical laser-induced plasma (Garcia et al. 2001), so temporal resolution is poor. Despite the lack of temporal resolution, the relatively inexpensive CCD has found application in LIBS analyses. Keszler and Nemes used a CCD equipped spectrometer to study time-averaged emission spectra of Nd:YAG induced carbon plasmas (Keszler and Nemes 2004). Garcia et al. performed LIBS

analyses of zinc using a CCD equipped imaging system, concluding that the long CCD integration time (17 ms) was detrimental to the LIBS signal (Garcia et al. 2001).

To provide temporal resolution and two-dimensional spatial information an Intensified CCD (ICCD) must be used. The ICCD couples a fast-gated photocathode with a CCD array to provide integration times as short as nanoseconds (Cremers and Radziemski 2006). Milan and Laserna performed LIBS analysis of silicon using an ICCD and a gate width of 200 ns to provide accurate temporal resolution of the plasmas (Milan and Laserna 2001). Harilal et al. used a 2 ns gate width on an ICCD equipped LIBS system to image laser-induced aluminium plasmas and chart their evolution under various ambient pressures (Harilal et al. 2003).

3.7 Practical Considerations

There exists no 'default' LIBS setup. Various groups around the world use different lasers, sampling geometries, collection optics, spectrographs and detection systems, giving rise to enormous problems when reproducing results (Tognoni et al. 2002). Ambient factors such as temperature, atmospheric composition and pressure, humidity and particulate matter in the air can also affect LIBS analyses (Cremers and Radziemski 2006). The experimental parameters having perhaps the greatest impact on plasma formation and evolution are the laser wavelength and pulse duration, and the ambient gas pressure (Lee et al. 1997).

3.7.1 Effects of Laser Properties on LIBS Analyses

The wavelength and pulse duration of the laser have a great impact on both the laser-material and laser-plasma interactions, and therefore on the formation and subsequent evolution of the plasma (Lee et al. 1997). Shaikh et al. performed electron density and temperature measurements of Nd:YAG-induced zinc plasmas, operating the laser at 1064, 532 and 355 nm, using the same laser power density of 4×10^{10} Wcm^{-2} for each wavelength (Shaikh et al. 2005). It was found that the plasma electron excitation temperature increases at longer laser wavelengths, which was ascribed to a more efficient laser-plasma interaction and energy transfer. It was also observed that the plasma electron density decreases with longer wavelengths, owing to the increased amount of target material ablated at shorter wavelengths due to reduced plasma shielding.

Le Drogoff et al. report comparative analyses of laser-induced aluminium alloy plasmas, generated by a 8 ns-pulsed Nd:YAG versus a 100 fs-pulsed Ti:Sapphire laser (Le Drogoff et al. 2001). Spatially averaged measurements of plasma electron density and temperature were performed. It was found that the plasmas induced by 8 ns pulses were, in general, 1000 K hotter than those induced by the 100 fs pulses, due to the greater amount of interaction of the ns pulse with the plasma. The plasmas induced by 8 ns pulses displayed electron densities of approximately an order of magnitude greater than those induced by 100 fs pulses; this was explained by the lower temperature of the fs-induced plasmas promoting re-combination of free electrons and more rapid plasma thermalisation.

3.7.2 Effects of Ambient Gas Pressure

The ambient atmosphere plays an important role in dictating the morphology and evolution of laser-induced plasmas (Cremers and Radziemski 2006, Lee et al. 1997). The ambient gas confines the plasma and in some cases may react with it. The behaviour of plasma emission intensity dependence on ambient gas pressure and composition is too complex for a unique interpretation, although several independent studies have been conducted (Tognoni et al. 2002). It is generally recognised that as the ambient pressure decreases so too does the plasma emission intensity and lifetime due to a lack of external ambient confinement (Cremers and Radziemski 2006, Lee et al. 1997, Radziemski et al. 2005) and that the signal to background ratio is improved due to a lack of continuum radiation at lower plasma densities (Garcia et al. 2001, Cowpe et al. 2007).

3.8 Matrix Effects and Calibration

Relatively poor sensitivity and complex matrix effects have hindered the quantitative application of LIBS (Vrenegor et al. 2005). The optical thickness of plasmas generated by laser ablation results in self-absorption of certain resonant emission lines, leading to non-linearity in the spectra produced (El Sherbini 2005). Self absorbed spectral lines will display measured intensities lower than those expected for a given elemental concentration; the observed spectra may therefore not accurately represent the actual composition of the analyte. For environmental monitoring, forensic applications and process control etc. this inaccuracy is unacceptable. Numerous calibration methods have been developed to counteract and correct for this effect (Lazic et al. 2001), and several iterative calibration-free studies have and are being conducted (Bulajic et al. 2002).

Construction of accurate calibration curves from standard samples (Salle et al. 2005, Stavropoulos et al. 2004) requires a large number of reference, which in the case of complex, multi-elemental substances can be impractical and expensive. It can prove to be extremely difficult, if not impossible, to confidently perform quantitative analysis of unknown samples if a suitable calibration has not been previously undertaken. Bulajic et al. (Bulajic et al. 2002) and Yaroschyk et al. (Yaroschyk et al. 2006) have shown that calibration-free methods require complex algorithms to accurately generate predicted spectra.

Systematic errors in the LIBS hardware may also limit the accuracy with which elemental determinations may be performed. Identification of emission lines in complicated spectra can be problematic, resulting in inaccurate spectral interpretation, which in turn can lead to errors in compositional analysis.

The greatest barrier to accurate, quantitative LIBS materials analyses lies in the lack of understanding regarding the complex mechanisms governing plume formation and evolution. With various the LIBS research groups across the globe utilising different experimental apparatus, ambient conditions, sample materials and sampling geometries, there is consequently a dearth of accurate, reproducible results on which to base accurate transient plasma models. The following chapters present the author's initial steps in providing the data required to produce such a model.

4 Experimental: LIBS Silicon Plasma Diagnostics

4.1 Introduction

The thrust of this investigation was to ascertain the validity of models based on LTE when applied to short lived transient laser induced plasmas. During the course of this investigation a number of interesting results were obtained, many of which require further investigations.

Laser-Induced Breakdown Spectroscopy of single crystal silicon was performed using a 5 nanosecond pulsed frequency doubled Nd:YAG (532 nm) laser. The temporal evolution of the laser ablation plumes of silicon in air at atmospheric pressure and through a range of ambient pressures down to ~10^{-4} mbar is presented. Time resolved dispersed emission spectra are discussed in terms of emission line self absorption, relative intensities of neutral and ionic species emission lines, the integrated area and FWHM of the Si (I) 288.16 nm emission line, and the spectrum continuum level.

Plasma plumes were characterised in terms of electron excitation temperature T_e, ionisation temperature T_i, and electron density N_e with respect to time at each pressure considered. The Boltzmann plot and 2-line-ratio methods of plasma temperature determination were found to breakdown, giving clearly erroneous results; the possible causes of this are discussed. Electron excitation temperatures were obtained from the line to continuum ratio of the Si (I) 288.16 nm line, which yielded temperatures in the range 8000 – 22000 K. Ionic species temperatures were determined from an iterative solution of the Saha-Eggert equation yielding temperatures in the range 13000 – 23000 K. Electron number

densities were determined from the Stark broadening of the Si (I) 288.16 nm emission line; number densities in the range of 2.9×10^{16} to 5.5×10^{19} cm^{-3} were observed.

Electron excitation and plasma ionisation temperatures are compared and the validity of the LTE model, as applied to the plasmas under the conditions of this study, is discussed The assumption that LTE conditions exist within the plasmas is also discussed in terms of minimum electron number density requirements.

Non-dispersed gated images reveal information regarding the morphology of the laser-induced plasmas in each pressure regime, and the plume propagation front position is charted with respect to time. Plume stagnation, splitting and free expansion were observed at different ambient pressures. Spectroscopic notation is employed in this work, following the convention of labelling ionisation states with upper case Roman numerals; I refers to neutral atoms, II to singly ionised species, III to doubly ionised species etc. Thus Si (I) 288.16 nm refers to a certain emission line arising from emission from excited neutral silicon atoms, Si (II) 413.09 nm refers to a spectral line arising from the emission from excited singly ionised silicon ions.

Work carried out under various ambient pressure, consistently produced results that indicated 3 pressure regimes in which the characteristic behaviour of the plasma expansion dynamics and spectroscopic measurements were markedly different. These results have been linked to the changes in the mean free path of the ambient gas with changing pressure.

4.2 Experimental Set-up

The apparatus shown in Figure 4-1 was designed to allow LIBS material analysis and plasma plume characterisation through a range of pressure regimes, from atmospheric pressure down to a minimum ambient pressure, p_a, $<10^{-6}$ mbar. The set-up includes a Nd:YAG laser (Continuum, Surelite), frequency doubled to produce an output at 532 nm, with a 5 ns pulse length and a peak energy of 200 mJ. For this investigation the laser was operated at its maximum repetition rate of 10 Hz. Laser radiation was focussed onto the sample surface using a 150 mm focal length plano-convex glass lens, producing a spot size at the sample estimated as ~ 400 μm when using full laser power.

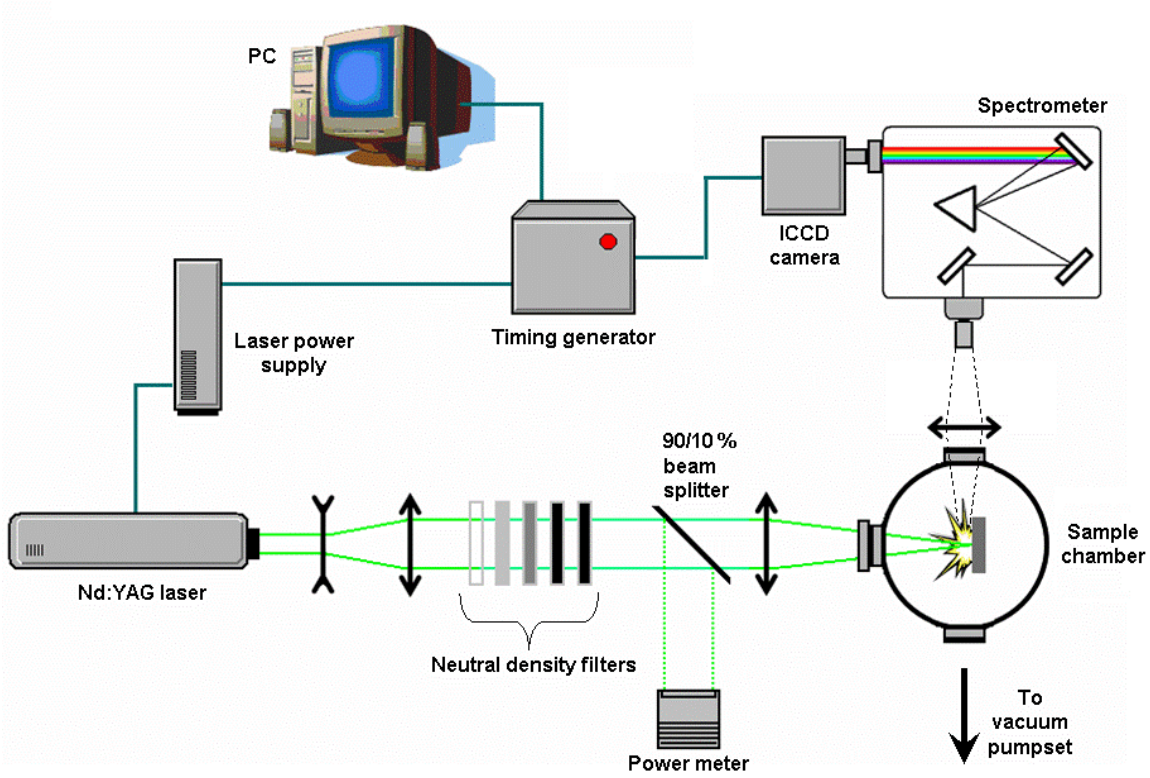

Figure 4-1 Schematic diagram of the LIBS experimental set-up

Samples were placed perpendicular to the axis of laser beam propagation,

mounted on a rotating stage such that each LIBS analysis was performed on a new area of the sample. Ten 'cleaning shots' were performed before data collection, to remove any surface contamination present.

A schematic diagram of the vacuum pump-set and measurement apparatus is presented in Figure 4-2. The chamber is a stainless steel 6-way CF flanged cross piece, with an approximate volume of 1.5 litres. A Varian 301 NavigaTorr 280 ls^{-1} turbomolecular pump was used to evacuate the chamber to pressures $<10^{-6}$ mbar, and was controlled via a Varian Turbo-V301 control unit.

The turbomolecular pump was backed by a Varian DS302 dual stage rotary pump that was also used to reduce the chamber to rough pressures ~ 10^{-3} mbar prior to engaging the turbomolecular pump. A molecular sieve foreline trap was installed to reduce pump oil back-streaming and subsequent chamber contamination.

Chamber pressures in the range from atmospheric to 1.33×10^{-3} mbar were measured using a Varian TC0531 thermocouple gauge operated using a Varian MultiGauge controller. Chamber pressures below 10^{-3} mbar were measured using a Varian CC252 cold cathode gauge, again controlled by the MultiGauge controller. The backing pressure of the turbomolecular pump was continuously monitored with a second TC0531 gauge mounted at the pump exhaust.

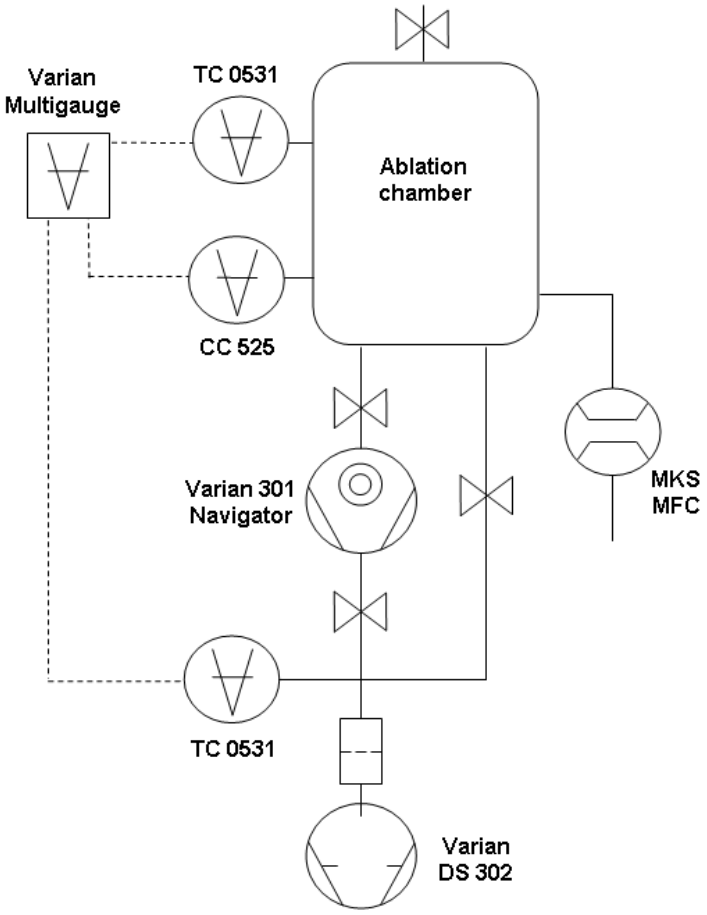

Figure 4-2 Schematic diagram depicting the laser-ablation chamber vacuum apparatus

Pressure control within the chamber was facilitated by an MKS 0 – 200 sccm Mass Flow Controller (MFC) controlled by an MKS 147B MultiGas controller, calibrated for nitrogen. The MFC allowed a controlled volumetric flow of ambient gas into the chamber in order to achieve the desired set-point chamber pressure, and was operated with an inlet filter to reduce particulate contamination. Using this set up, chamber pressure could be maintained at any value from atmospheric pressure down to ~ 10^{-6} mbar. A high vacuum valve was situated above the inlet to the turbomolecular pump enabling the isolated turbo to remain at full speed operation whilst the chamber was vented to atmospheric pressure for sample changing. The chamber was vented to atmospheric pressure

by means of a ball valve, the inlet of which was covered with a filter to reduce contamination.

Optical emission from the plasma plumes was collected at 90° to the direction of laser beam propagation, through a quartz window mounted in a CF carrier. The plasma plumes were imaged using a plano-convex quartz lens (focal length 100 mm, diameter 50 mm) onto the entrance slit of an Acton Research Spectra Pro 500i 0.5 metre imaging triple grating (150, 600, 2400 grooves mm^{-1}) spectrometer. Table 4-1 lists the important properties of the three reflection diffraction gratings with which the spectrometer is equipped. The spectral range of a given grating is here defined as the wavelength range over which the grating efficiency is at least 40 %, the capture window refers to the wavelength range which may be recorded during an individual capture using that particular grating, and the resolution in this case refers to the wavelength range covered by a single ICCD column using this particular imaging apparatus.

Table 4-1 Spectrometer diffraction grating properties

Groove Density (mm^{-1})	Spectral Range (nm)	Capture Window (nm)	Blaze Wavelength (nm)	Resolution (nm $pixel^{-1}$)
2400	190 – 700	11	240	0.02
600	650 – 2000	44	1000	0.09
150	170 - 700	250	300	0.36

Dispersed images of the plasma were captured with the spectrometer input slit-width set to 10 μm, its minimum value. Non-dispersed images were captured employing the maximum slit-width of 3 mm. The spectrometer input slit was orientated to capture images along the entire length of the plume in the direction

of plume propagation; all measurements taken were thus spatially integrated along the length of the plume.

The output of the spectrometer was coupled to a Princeton Instruments PI-MAX ICCD camera that utilised a proximity-focussed multi-channel plate intensifier connected via a fibre-optic coupling to the CCD array. The 1024 × 256 pixel CCD array was thermoelectrically cooled to -20°C to minimise the dark charge current. The laser power supply, camera and PC were connected to a Princeton Instruments ST-133A Programmable Timing Generator (denoted PTG in Figure 4-1), allowing for temporal resolution of the plasma plumes. A 1ns increment in both the gate capture delay and integration width was possible with a resolution of 40 ps. Roper Scientific's WinSpec/32 spectrum capture and manipulation software allowed for both capture of optical emission and the subsequent identification of any prominent spectral lines present.

Standard semiconductor grade polished silicon [111] wafers were used throughout this study. Electron temperature and number density measurements were performed with the 2400 grooves mm^{-1} grating, centred on the neutral Silicon (I) 288.16 nm emission line. Ionic species measurements were performed using the 150 grooves mm^{-1} grating, simultaneously monitoring the neutral Si (I) 288.16 nm and the ionic Si (II) 413.09 nm emission lines. Non-dispersed images of the laser-induced plasmas were collected with the 2400 grooves mm^{-1} grating positioned so as to allow the zeroth order to propagate to the ICCD.

4.3 Results

In the following sections all spectra were corrected for the spectral response of the instrument, and the ICCD dark charge subtracted. Each data set is the software accumulation of ten individual spectra. Lines drawn connecting data points on the Figures are not meant to represent interpolation between points, rather they are merely aids to the eye to display the general *trend* of the data on what would otherwise be very confusing plots.

4.3.1 Discussion of the Si (I) 288.16 nm Emission Line Profile

The profile and longevity of the Si (I) 288.16 nm emission line both differ as a function of ambient pressure. In general, the FWHM of plasma emission lines decreases with decreasing ambient pressure, and the line intensity with respect to time drops more rapidly at lower pressures. As an example, Figures 4-3 and 4-4 show the temporal evolution of the Si (I) 288.16 nm emission line intensity at atmospheric pressure and at an ambient pressure of ~10^{-4} mbar, respectively.

The gate delay was swept from 10 to 4010 ns after laser firing, in 200 ns increments. The capture gate width fixed at 200 ns to avoid overlapping information, and the ICCD gain was set to 200. When comparing Figures 4-3 and 4-4 it is evident that the FWHM of the emission line is considerably narrower at p_a ~10^{-4} mbar due to free plasma expansion and a subsequent lack of pressure broadening effects.

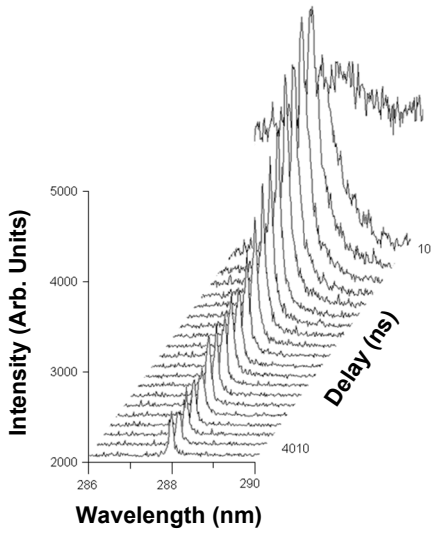

Figure 4-3 Temporal evolution of the Si (I) 288.16 nm emission line at atmospheric pressure

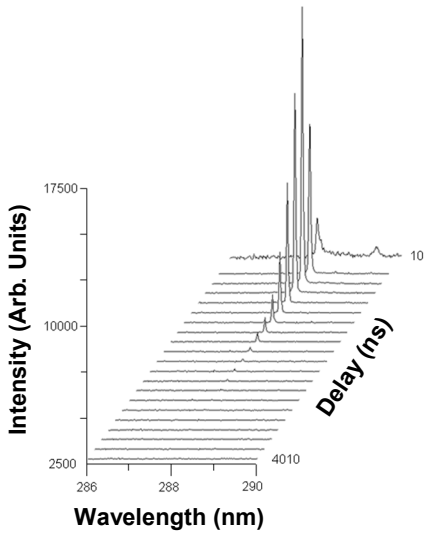

Figure 4-4 Temporal evolution of the Si (I) 288.16 nm emission line at a pressure of 10^{-4} mbar

In Figures 4-3 and 4-4 the maximum line intensity recorded under vacuum is approximately 3 times greater than at atmospheric pressure; but is observed to diminish more rapidly. The emission line and the plasma continuum radiation are clearly seen to decay more rapidly under vacuum.

4.3.2 Si (I) 288.16 nm Self Absorption Considerations

The temporal evolution of the Si (I) 288.16 nm line was monitored using the 2400 grooves mm^{-1} grating to provide the maximum system resolving power, and thus enabling the maximum possible accuracy in FWHM determination. The vacuum pump and MFC configuration described in Section 4.2 enabled eight stable ambient pressures to be maintained during laser ablation of the silicon sample. Pressures were maintained at atmospheric pressure, then at each decade from 1×10^{2} down to 1×10^{-4} mbar. The emission spectra captured under each ambient pressure were analysed and compared.

Gated spectra were captured with a swept delay to provide temporal resolution of the plasma emission. The integration width was set to 50 ns for each acquisition; this value was chosen to provide fine temporal resolution. Using this short gate width, dictates that less flux will be collected from the plasma, leading to a decreased emission line signal above the background noise. Using this integration width, the emission from the Si (I) 288.16 nm is longest lived at atmospheric pressure, clearly resolvable above the background level up to delay times of approximately 1400 ns.

The Si (I) 288.16 nm spectral line emission was observed to decrease most rapidly at the lowest ambient pressure considered here, $p_a = 1 \times 10^{-4}$ mbar, and is barely resolvable above the instrument background at a delay time of 1400 ns; as such this value was chosen as the maximum delay to be considered in this study. The plasma emission was particularly intense in the first few nanoseconds of

plume formation; therefore to prevent damage to the LIBS imaging apparatus the earliest delay considered here was chosen as 10 ns after plume formation.

To provide greater information regarding the early phases of plasma expansion, gated emission spectra were captured over 10 to 510 ns in 50 ns intervals. In the latter stages of plume evolution, spectra were captured from 510 to 1410 ns in 100 ns intervals. The main hardware parameters chosen for this investigation are summarised in Table 4.2.

Table 4-2 Hardware parameter space chosen for LIBS plasma diagnostics of silicon

Parameter	Setting
Pressure	1×10^{3} to 1×10^{-4} mbar in 10^{1} mbar increments
Gate delay	10 – 510 ns in 50 ns increments
	510 – 1410 ns in 100 ns increments
Gate width	50 ns
ICCD gain	200
Accumulations	10

In order to analyse the raw spectroscopic data produced by the Roper Scientific WinSpec software, a Lorentzian curve was fitted to each captured spectrum as detailed in Section 2.6.3. (Page 49). Using the software package OriginPro v.7.5, such a Lorentzian curve was fitted to each captured Si (I) 288.16 nm emission line, providing a calculated line area, peak intensity, FWHM and the baseline offset representing the continuum emission level of the plasma.

The accuracy of the Lorentz curve fit is expressed by a coefficient of determination, R^2, which may vary from 0 to 1; the higher this value the more

accurately the fit represents the captured data. Where a given emission line exhibits negligible self-absorption, the Lorentz curve should fit the captured data more accurately (Liu et al. 1999) and as such the measured R^2 value will be greater.

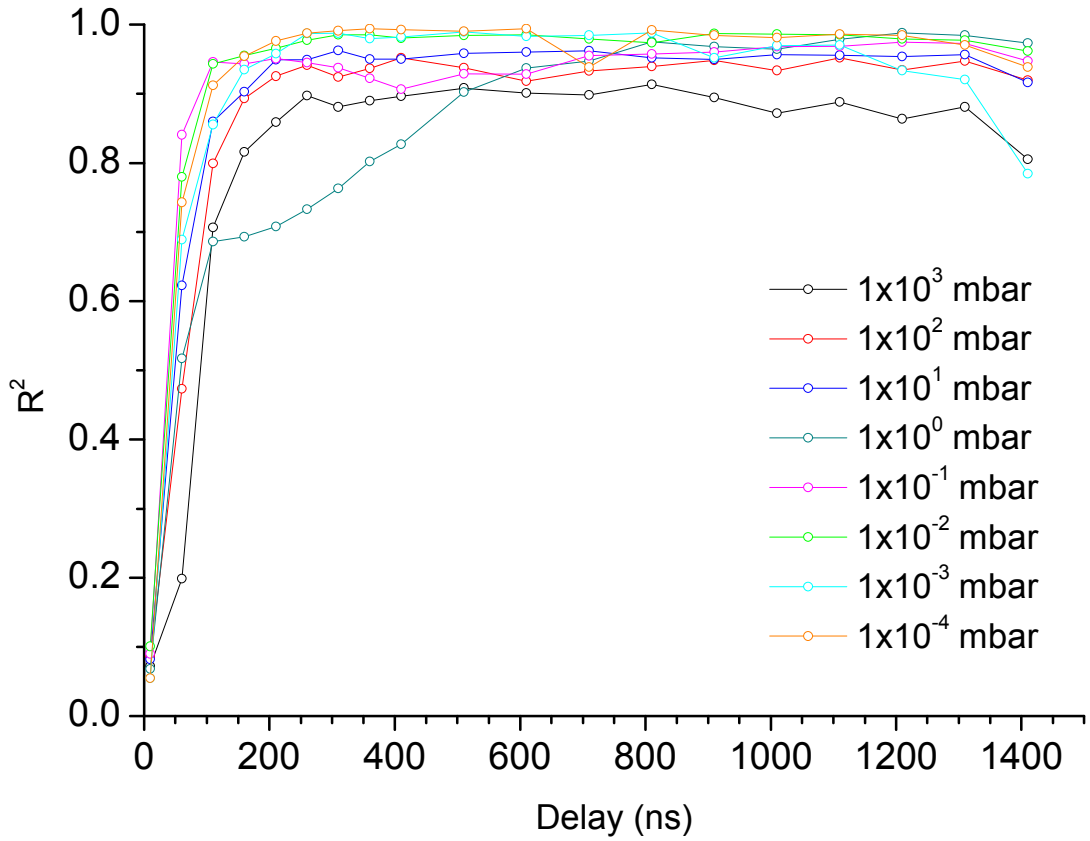

Figure 4-5 Temporal dependence of the Si (I) 288.16 nm line Lorentz fit R^2 value

Figure 4-5 presents the R^2 values obtained from a fit to each data-set captured in this study; the temporal change of the R^2 value is plotted for each pressure. It can be seen that for delay times > 200 ns the Lorentz curve fits the spectra very well at all pressures indicating negligible self-absorption; the poor fit at early delay times is due to the dominance of the continuum radiation in the early phases of plasma expansion. As a general trend there is less self-absorption with

decreasing pressure, with the exception of the spectra captured at 1×10^0 mbar which display moderate self absorption until delay times of ~ 600 ns; this was seen to be a reproducible result.

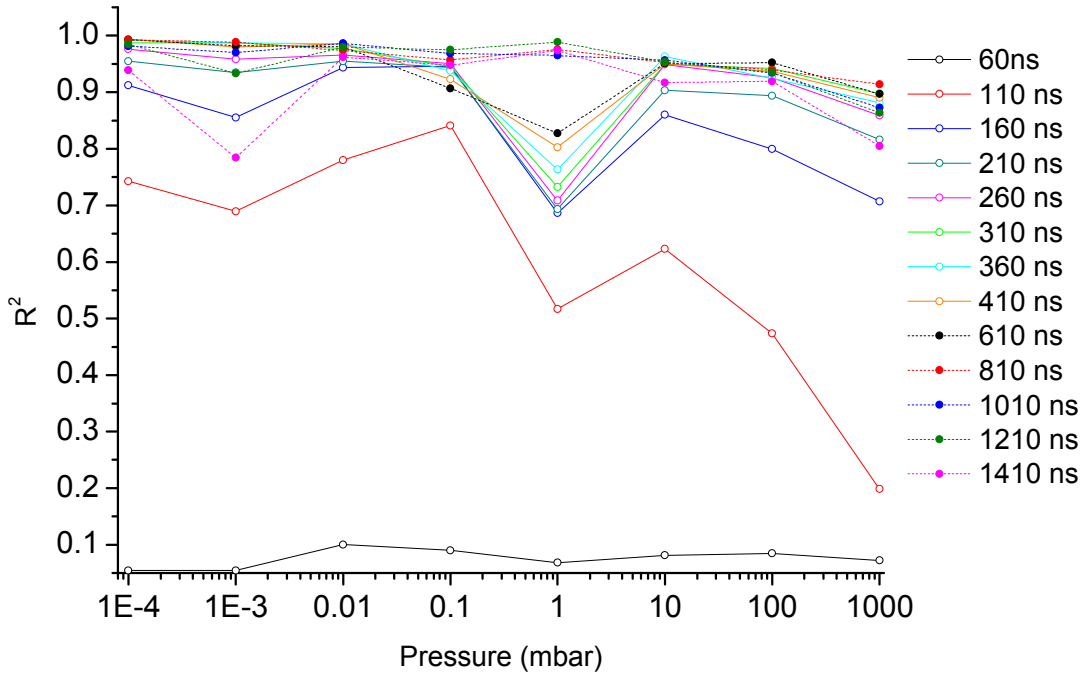

Figure 4-6 Pressure dependence on the Si (I) 288.16 nm line Lorentz fit R-squared value

Figure 4-6 illustrates more clearly the pressure dependence of the Lorentz fit R^2 value and hence the inferred level of self absorption exhibited by the Si (I) 288.16 nm emission line. Again it is evident that the Lorentz fit to the spectra is poor at early delay times, and that there is clearly a marked drop in R^2 and by inference a greater self absorption, at a pressure of 1×10^0 mbar. As a general trend the coefficient of determination R^2 increases as the ambient chamber pressure decreases, indicating less emission line self-absorption at lower pressures.

4.3.3 Peak Intensity of the Si (I) 288.16 nm Emission Line

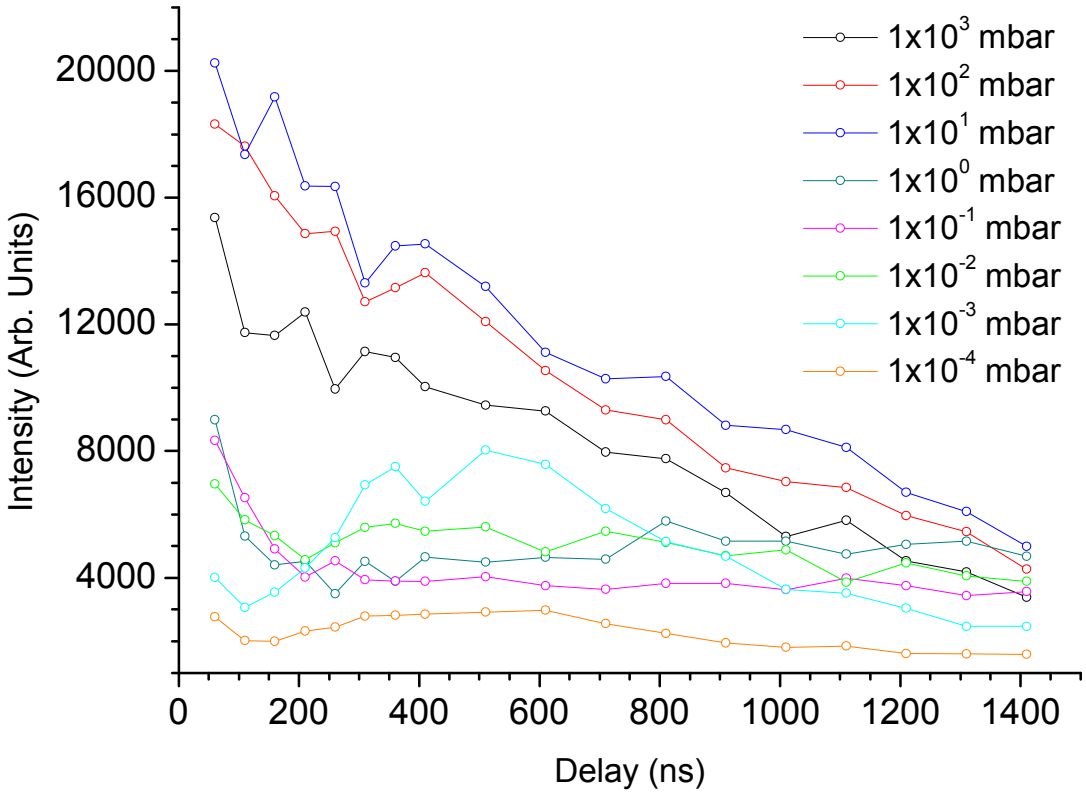

Figure 4-7 Temporal evolution of the Si (I) 288.16 nm peak intensity

Figure 4-7 presents the change in the measured 288.16 nm Si (I) emission line intensity with respect to time at each pressure considered. The 150 grooves mm^{-1} diffraction grating was employed to simultaneously monitor the Si (I) 288.16 nm and Si (II) 413.09 nm lines in order to directly compare their magnitudes. The 2400 and 1200 grooves mm^{-1} diffraction gratings do not provide a sufficiently wide wavelength capture window to simultaneously monitor the above mentioned emission lines. The coarser resolution of the 150 grooves mm^{-1} grating does not impose a limit in this instance as both the lines monitored are isolated, and as such well resolved within the resolution of the grating.

There is a general decrease of intensity with time at all pressures except 1×10^{-2}, 1×10^{-3} and 1×10^{-4} mbar, at which pressures the intensity reaches a maximum between delays of 400 – 600 ns then subsequently decays. It should be noted that the intensity of the Si (I) 288.16 nm emission line is greater at pressures of 1×10^{2} mbar and 1×10^{1} mbar than at atmospheric pressure.

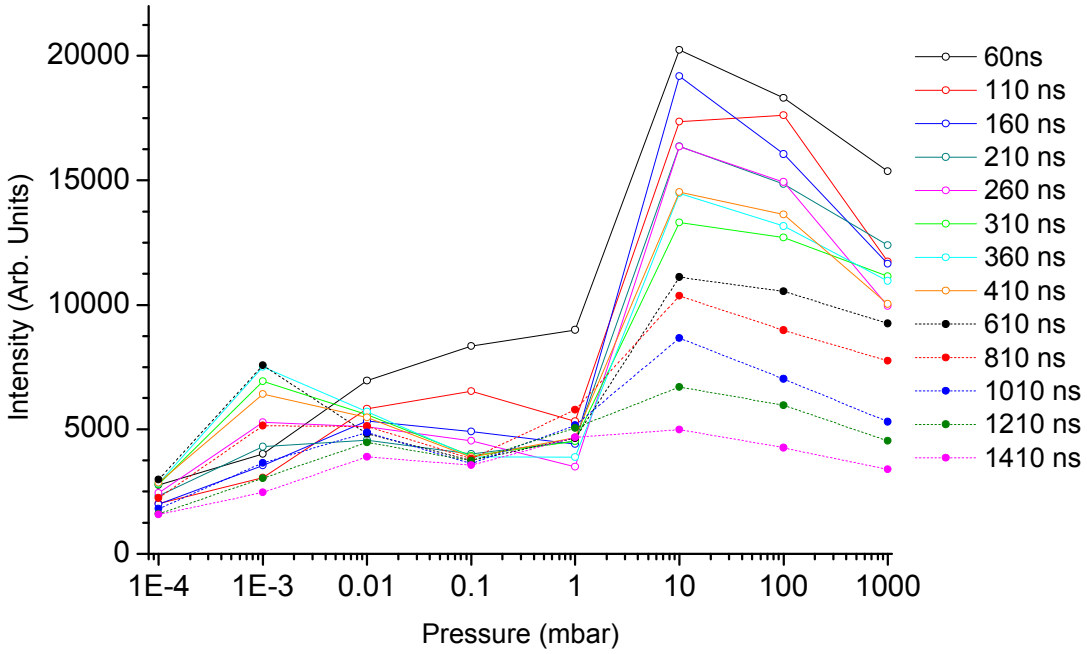

Figure 4-8 Pressure dependence of the Si (I) 288.26 nm peak intensity

Figure 4-8 illustrates the pressure dependence on the intensity of the Si (I) 288.16 nm emission line; it can clearly be seen that the greatest emission line intensities are observed at a chamber pressure of 1×10^{1} mbar.

4.3.4 Intensity of the Si (II) 413.09 nm Emission Line

Figure 4-9 shows the intensity of the singly ionised Si (II) 413.09 nm emission line with respect to time at each pressure. As in Section 4.3.3 the spectra were captured using the coarse 150 grooves mm^{-1} grating. There is a general trend of

intensity decay with respect to time at most pressures, except 1×10^{0} mbar and 1×10^{-1} mbar at which pressures the line intensity displays first a rise and then subsequent fall of intensity.

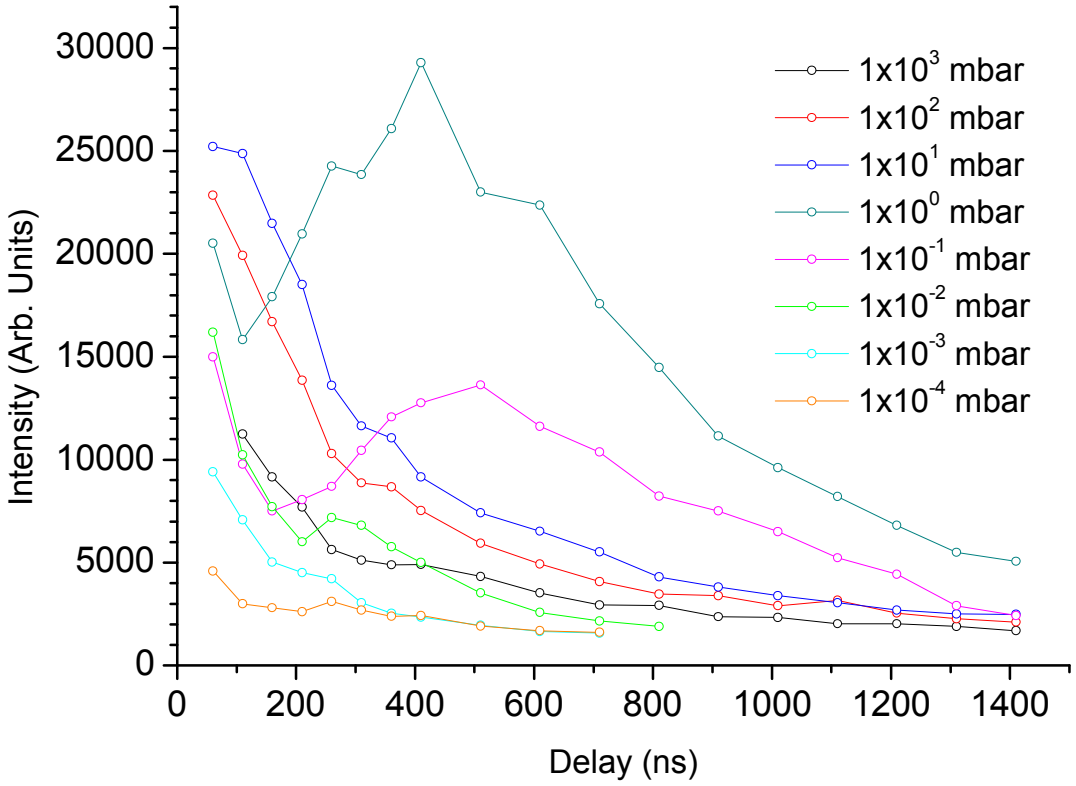

Figure 4-9 Si (II) 413.09 nm peak intensity versus delay

The maximum emission line intensity is recorded at 1×10^{0} mbar at a delay time ~ 400 – 500 ns. At lower pressures, $p_a \leq 1 \times 10^{-2}$ mbar, the Si (II) 413.09 nm emission line decays below the background noise level more rapidly due to a reduced amount of plasma confinement by the ambient atmosphere, and the resulting more rapid plasma expansion. It should be noted that the peak intensities observed at 1×10^{2} mbar and 1×10^{1} mbar are greater than those recorded at atmospheric pressure.

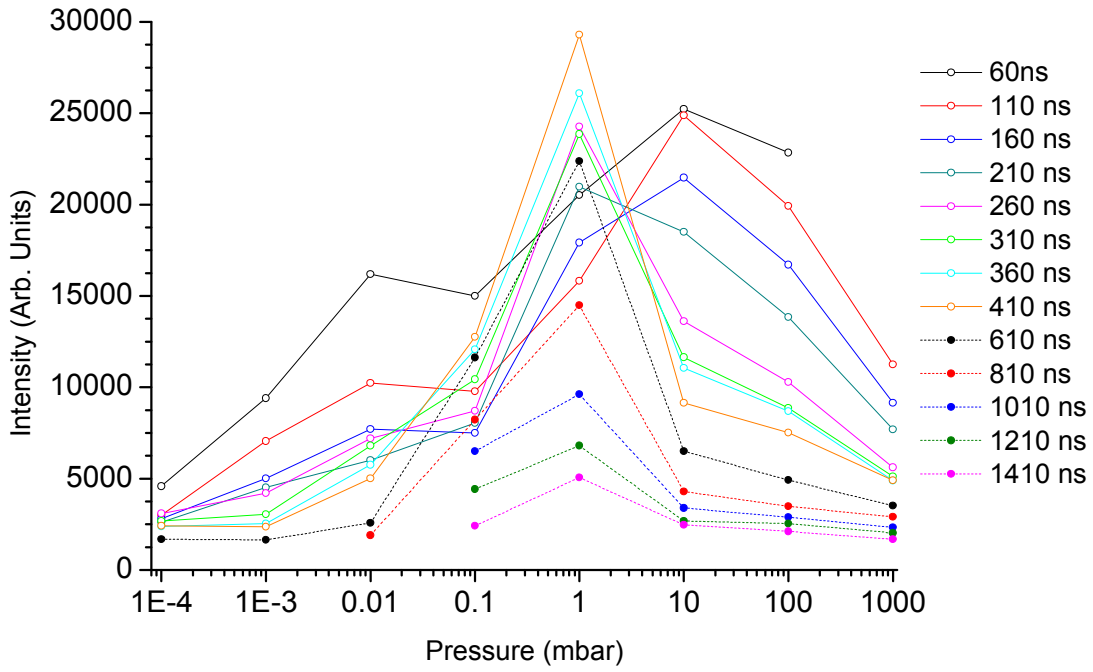

Figure 4-10 Pressure dependence of the Si (II) 413.09 nm emission line peak intensity

Figure 4-10 illustrates the ambient pressure dependence on the Si (II) 413.09 nm emission line intensity. A maximum is displayed for most delay times at a chamber pressure $p_a = 1 \times 10^0$ mbar which is in agreement with the results given in figure 4-9.

4.3.5 Integrated Area of the Si (I) 288.16 nm Emission Line

The integrated area of a given emission line displays complex temporal behaviour, being a function of both peak intensity and FWHM. The integrated area of the Si (I) 288.16 nm emission line is used to calculate the electron excitation temperature of the laser-induced plasmas, by employing the line-to-continuum ratio technique, Equation 2.25.

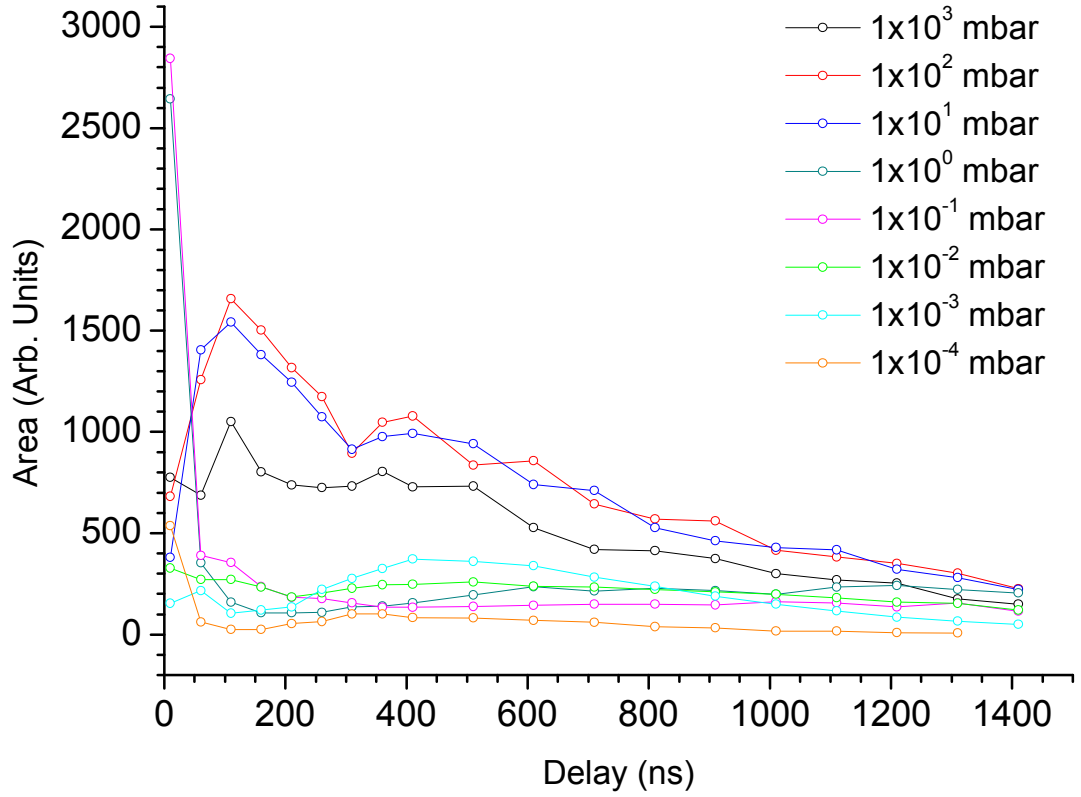

Figure 4-11 Si (I) 288.16 nm line integrated area versus delay

Figure 4-11 indicates the existence of two distinct regimes in which the temporal behaviour of the integrated emission line area differs. For $p_a \geq 1 \times 10^1$ mbar the line areas are seen to increase to a maximum at delays of ~ 100 ns then decay over time. When considering $p_a \leq 1 \times 10^0$ mbar the line area is seen to be of much grater magnitude in the early phases of plasma expansion and then decay with increasing delay. From analysing Figure 4-5 we recall that the Lorentz curve coefficient of determination R^2 indicates a poor fit at delays earlier than approximately 100 ns; as such the peak areas measured at short gate delays should be treated with caution.

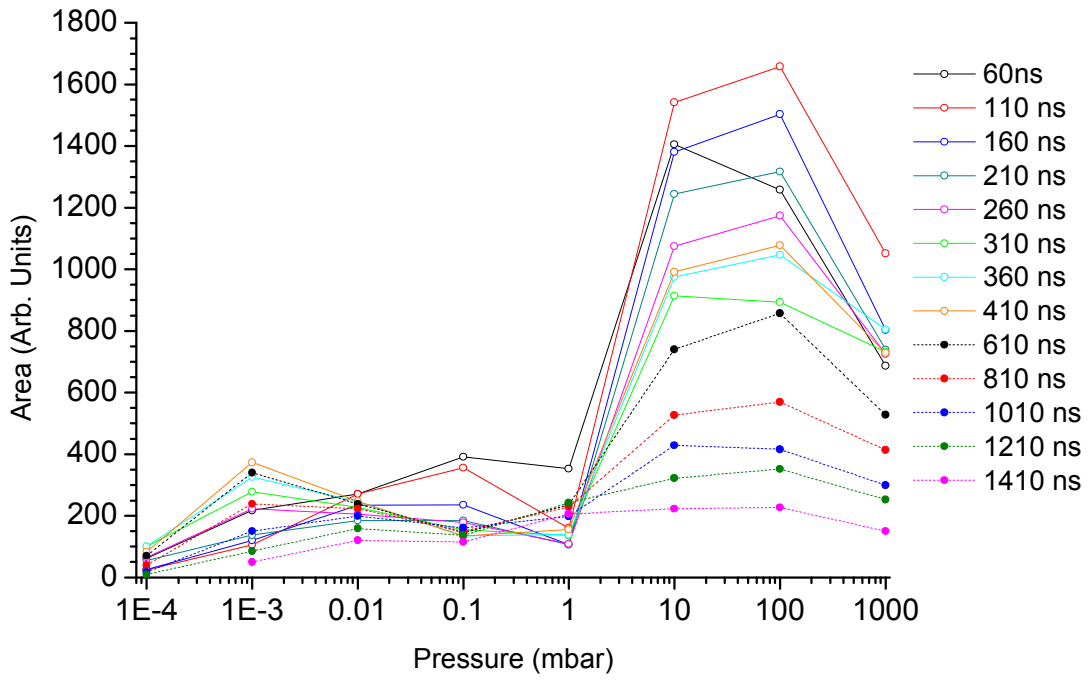

Figure 4-12 Si (I) 288.16 nm emission line integrated area versus pressure

Figure 4-12 shows the Si (I) 288.16 nm emission line areas as a function of varying pressure. It can be seen that the line areas display the greatest values at p_a of 1×10^2 and 1×10^1 mbar, and there is very little difference in the line areas captured at chamber pressures of 1 mbar and below.

4.3.6 Plasma Continuum Emission Level

The Lorentz curve fit for each captured Si (I) 288.16 nm emission line yields an offset value, y_0 as described in Equation 2.24 (Page 50). The plasma continuum radiation may be obtained by subtracting the ICCD dark charge, as determined in Appendix 10.3, from this y_0 value. The plasma continuum intensity with respect to time at each pressure is plotted in Figure 4-13. The decay of the continuum emission level at every pressure considered here is found to best fit a second-order exponential decay of the form:

$$y = y_0 + A_1 \exp\left(\frac{-x}{t_1}\right) + A_2 \exp\left(\frac{-x}{t_2}\right) \qquad (4.1)$$

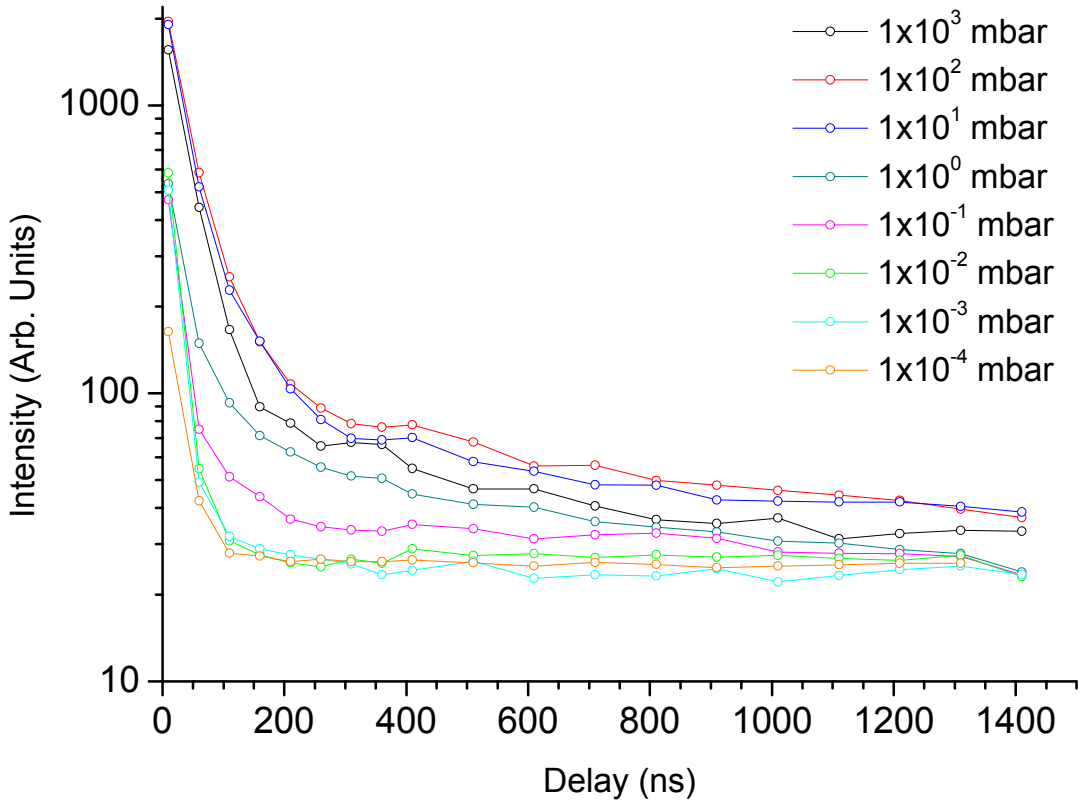

Figure 4-13 Plasma continuum emission level versus delay

The coefficients of determination for the fits to the continuum emission are presented in Table 4-3, and it may be seen from the high R^2 values that the second order exponential model describes the decay of the plasma continuum very accurately indeed. From Figure 4-13, the plasma continuum emission is observed to be clearly resolvable above the dark charge of the ICCD for long delay times at every ambient pressure considered in this particular study.

Table 4-3 Coefficients of determination R^2 for plasma continuum emission intensity versus delay, derived from the data presented in Figure 4-13

Pressure (mbar)	R^2	Pressure (mbar)	R^2
1×10^3	0.99992	1×10^{-1}	0.99943
1×10^2	0.99987	1×10^{-2}	0.99989
1×10^1	0.99987	1×10^{-3}	0.99962
1×10^0	0.99964	1×10^{-4}	0.99975

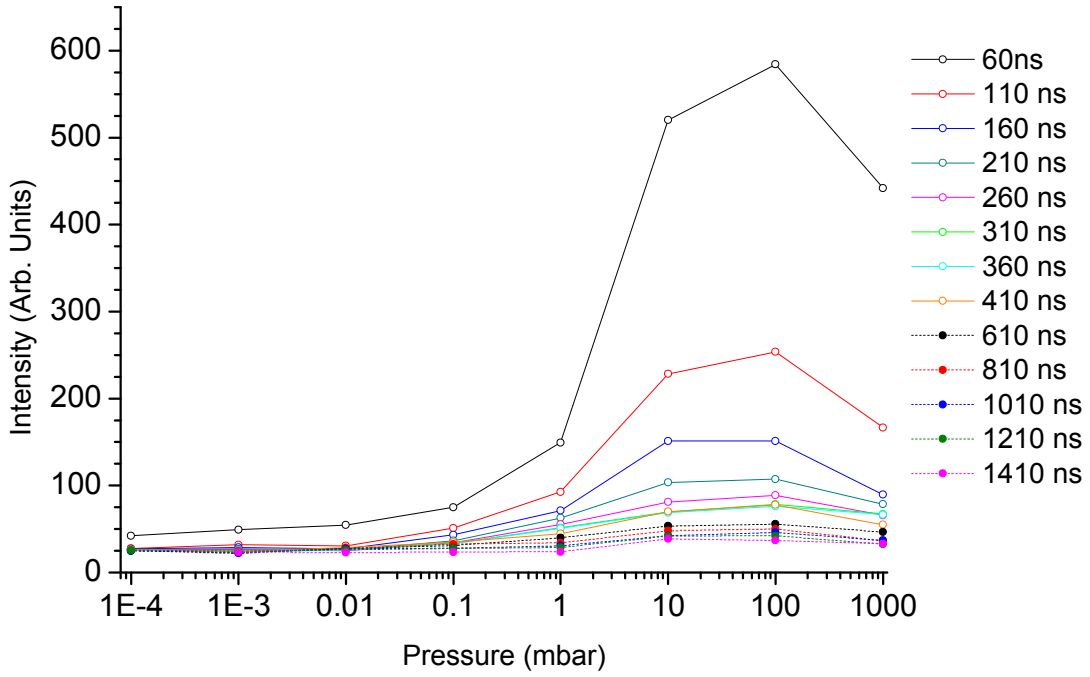

Figure 4-14 Plasma continuum emission level versus pressure

Figure 4-14 plots the change in continuum emission intensity as a function of ambient chamber pressure. It is evident that the plasma continuum emission is most intense at p_a of 1×10^2 and 1×10^1 mbar, at which pressures the plasma continuum emission levels are greater than those recorded at atmospheric pressure. For delay times greater than 610 ns there is little difference in the plasma continuum level with respect to ambient pressure; the largest variation in

continuum emission with respect to pressure is predominant in the early stages of plume formation and evolution.

4.3.7 FWHM of the Si (I) 288.16 nm Emission Line

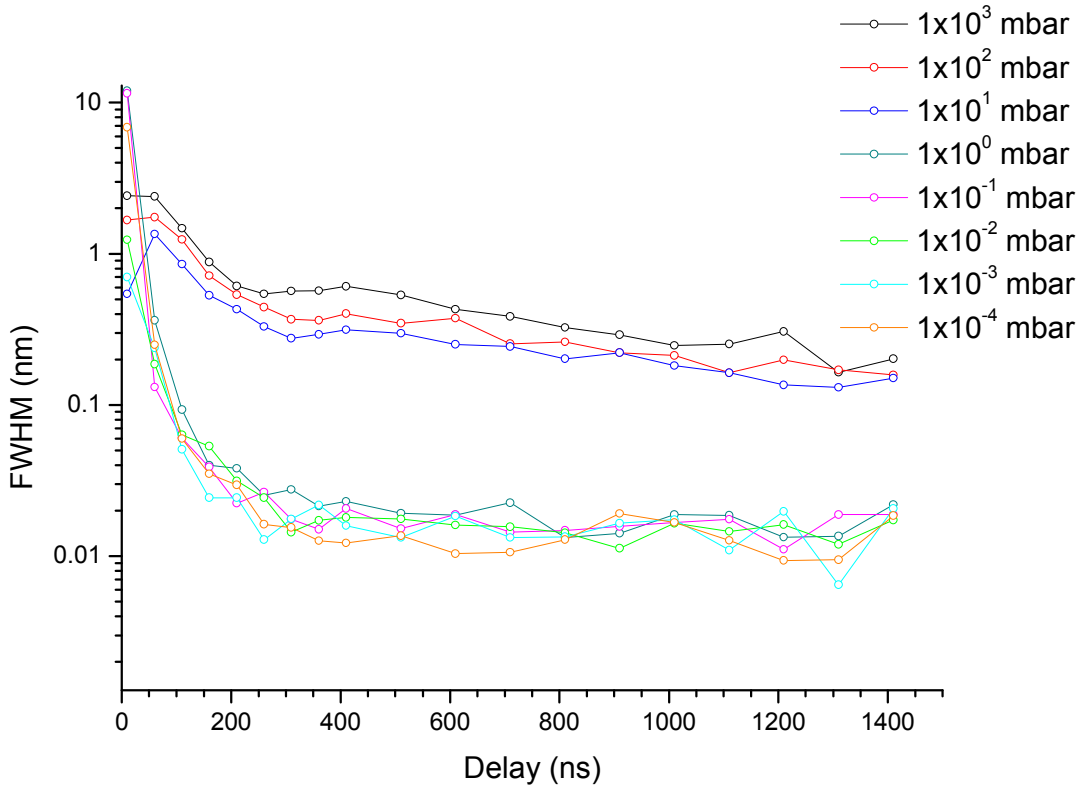

Figure 4-15 Si (I) 288.16 nm emission line FWHM versus delay

The FWHM of the Si (I) 288.16 nm emission line was determined from the Lorentzian fit to the peak, as described in Section 2.6.3 (Page 49). Figure 4-15 shows the change in the FWHM of the Si (I) 288.16 nm emission line at each pressure. The most striking feature of Figure 4-15 is the apparent difference in FWHM evolution according to two distinct ambient pressure regimes. For $p_a \geq 1 \times 10^1$ mbar the FWHM drops steadily from an initial value in the range 0.8 – 2.5 nm and follows a second order exponential, as given in Equation 4.1, to values in the range of 0.15 – 0.2 nm after 1410 ns. For $p_a \leq 1 \times 10^0$ mbar the FWHM

decreases rapidly following the same form of exponential relationship as given in Equation 4.1 to values in the range 0.015 – 0.02 nm after 1410 ns. For delay times greater than approximately 200 ns the FWHM at $p_a \geq 1 \times 10^1$ is generally an order of magnitude greater than that for $p_a \leq 1 \times 10^0$ mbar. The values of R^2 for the exponential fit to the FWHM behaviour at each pressure are tabulated in Table 4-4, and indicate that the exponential model accurately describes the captured data. It should be noted that for pressures greater than 10^1 mbar the accuracy of the fit falls to 93% as atmospheric pressure is approached.

Table 4-4 Coefficient of determination R^2 for Si (I) 288.16 nm emission line FWHM versus delay (Figure 4-15)

Pressure (mbar)	R^2	Pressure (mbar)	R^2
1×10^3	0.93786	1×10^{-1}	0.99998
1×10^2	0.93894	1×10^{-2}	0.99875
1×10^1	0.96629	1×10^{-3}	0.99734
1×10^0	0.99997	1×10^{-4}	0.99996

The large values of FWHM observed for $p_a \geq 1 \times 10^1$ at 10 ns after plume formation are due to the dominance of the continuum emission and the inaccuracy of the Lorentzian fit to spectra captured at these times.

Figure 4-16 illustrates the variation of the FWHM with respect to the ambient pressure for the Si (I) 288.16 nm emission line, demonstrating the step change in FWHM observed between 1×10^1 and 1×10^0 mbar. The boundary between the two behaviour regimes is clearly evident.

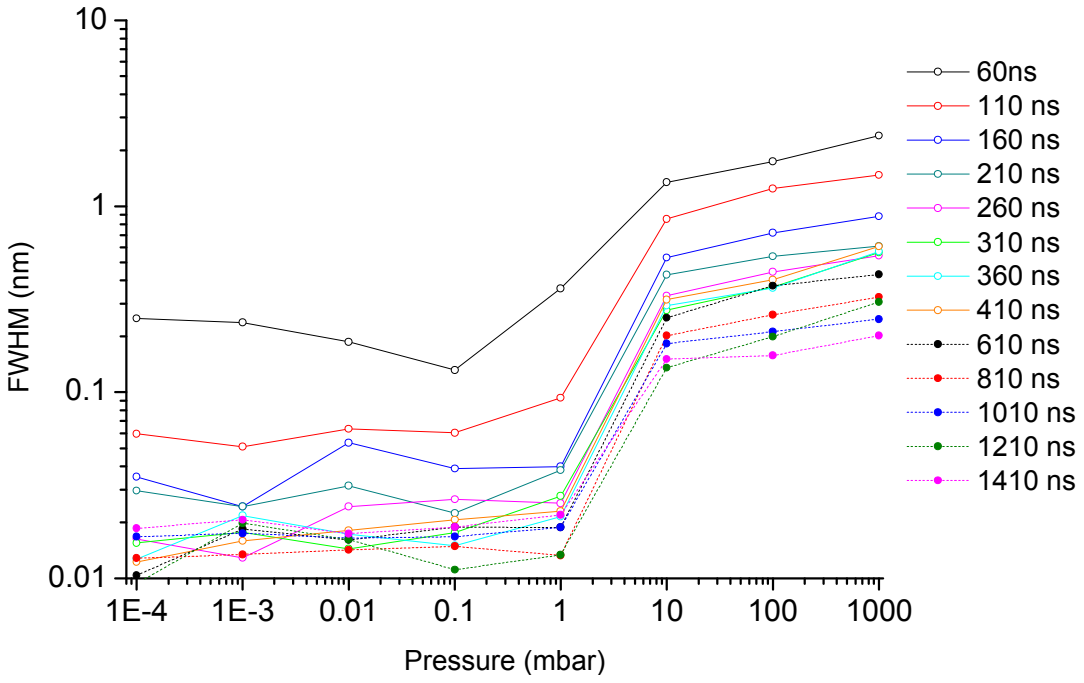

Figure 4-16 Si (I) 288.16 nm emission line FWHM versus pressure

4.3.8 Breakdown of the Boltzmann Plot and 2-Line-Ratio Methods of Plasma Temperature Determination

Perhaps the simplest method of plasma temperature determination is to employ the 2-line-ratio method to calculate the electron temperature, T_e, as described in Equation 2.21. (Page 46). In order to successfully perform the 2-line-ratio method spectroscopic emission lines must first be chosen that:

1. have known spectroscopic constants: the statistical weight g of the upper level, the transition probability A, and E the energy difference between the two levels
2. are clearly observable above the background level
3. are relatively long lived
4. are resolvable within the resolution of the imaging apparatus

5. may be captured simultaneously in the spectral window for direct comparison.

Bearing in mind the constraints listed above, two neutral Si (I) emission lines at 263.13 and 288.16 nm were chosen to perform the 2-line-ratio temperature determination method; their spectroscopic constants are given in Table 4-5.

Table 4-5 Spectroscopic constants of two silicon emission lines employed for the 2-line-ratio method of plasma temperature determination (CRC Press, 1988)

Wavelength (nm)	g	A ($\times 10^8$ s^{-1})	E (cm^{-1})
263.13	3	0.97	53960
288.16	3	1.90	40991

In table 4-5 g represents the statistical weight of the upper energy level, A the transition probability and E the energy difference between the upper and lower energy levels. The 150 grooves mm^{-1} grating was used to provide the required spectral coverage. The lack of resolution for this grating does not pose a problem as the line profile FWHM is not of interest here, only the peak intensity.

Figure 4-17 displays the measured intensities of the chosen emission lines versus time, and the resulting temperatures as calculated from these intensities and Equation 2.21 (Page 46). It can be seen that the temperatures calculated by this method are clearly erroneous, alleging an *increase* in plasma temperature over time, which is obviously not the case.

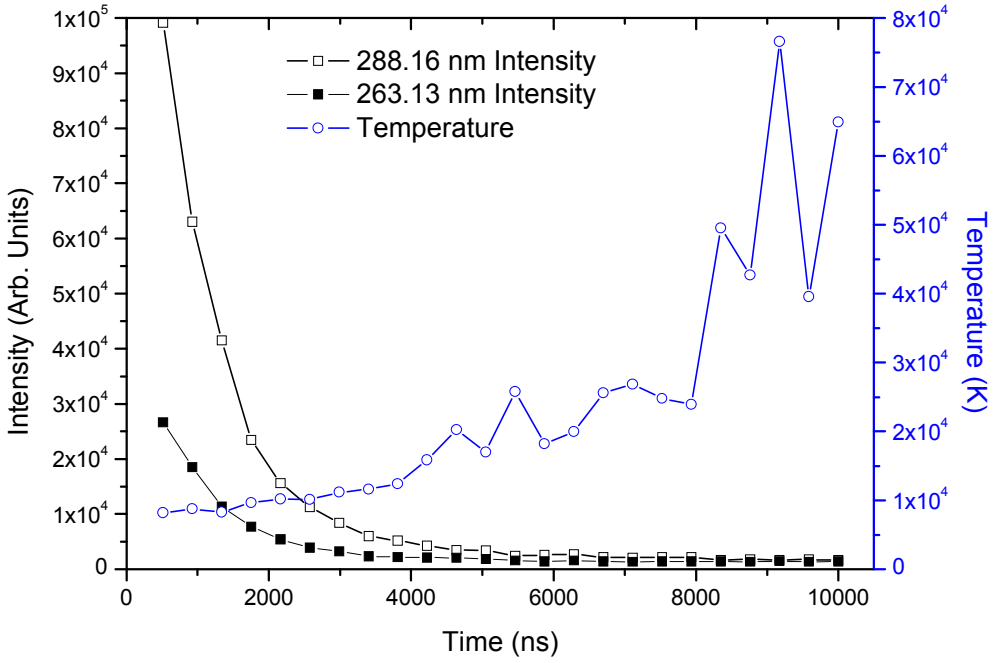

Figure 4-17 Laser-induced silicon plasma temperature as calculated by the 2-line-ratio method using the Si (I) 263.13 nm and Si (I) 288.16 nm emission lines

The reason for the breakdown of the 2-line-ratio method is the fact that there are so few suitable silicon emission lines, fulfilling the criteria outlined above, that it was necessary to use emission lines having only a small difference in their upper state energies. Further errors in the two-line-ratio method are due to inaccuracies in the determination of the transition probabilities, *A*, as recorded in the literature (CRC Press 1987, Milan and Laserna 2001).

After the failure of the two-line-ratio method, the Boltzmann plot method of plasma temperature determination, Section 2.6.2 (Page 48), was subsequently applied to the laser-induced silicon plasmas, and was also found to produce erroneous results. Again, the major obstacle to accurate plasma temperature determination proved to be the lack of suitable silicon emission lines; the spectroscopic constants of the lines chosen are listed in Table 4-6.

Table 4-6 Spectroscopic constants of selected Si (I) emission lines used in the Boltzmann plot method of plasma determination (CRC Press 1988)

λ (nm)	A ($\times 10^8$ s^{-1})	g_k	E_k (cm^{-1})
250.690	0.4666	5	39955
251.611	1.21	5	39955
251.920	0.456	3	39760
252.411	1.81	1	39683
252.851	0.77	3	39760
253.238	0.26	3	54871

Figure 4-18 shows an example of a typical Boltzmann plot obtained from LIBS of silicon, derived from the relative intensities of the Si (I) emission lines as listed in Table 4-6. When using the Boltzmann plot method, a plot of *ln(Iλ/gA)* versus *E* should yield a straight line graph of the form $y = mx + c$, where the gradient m is equal to $-1/kT$.

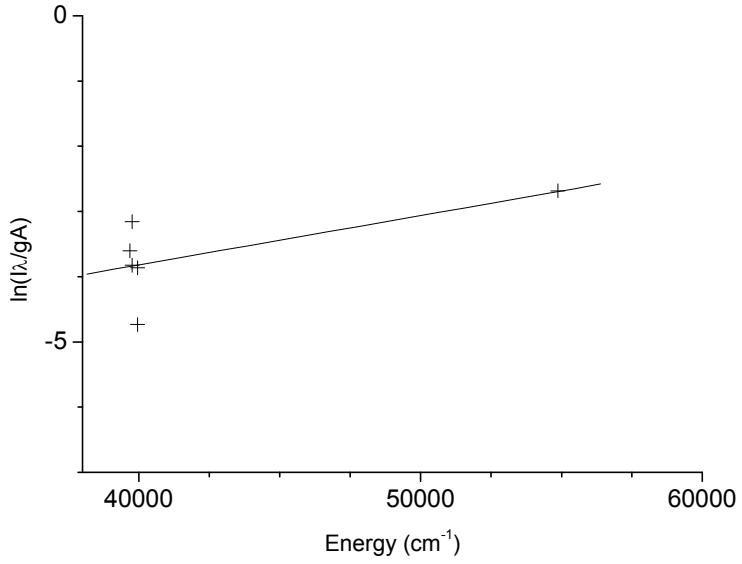

Figure 4-18 Example of a typical Boltzmann plot derived from LIBS of silicon

The slope of the line of best fit in Figure 4-18 is found here to be positive, which will lead to a negative value of temperature, which is of course nonsense. Milan and Laserna report similar difficulties when applying the Boltzmann plot method to laser-induced silicon plasma diagnostics, their results indicating an erroneous rise in plasma temperature over the first two microseconds of plume evolution (Milan and Laserna 2001). Every spectrum captured in this study yielded Boltzmann plots having a positive slope, indicating a flaw in the method rather than an isolated erroneous data-set.

4.3.9 Plasma Electron Temperature

As the two-line-ratio and Boltzmann plot methods of temperature determination were found to be unsuitable for LIBS of silicon with this particular imaging apparatus, the line-to-continuum method (Section 2.6.3 Page 50) was investigated. This method was successfully applied to the neutral Si (I) 288.16 nm emission line; the spectroscopic constants used are given in Table 4.7.

Table 4-7 Parameters used for plasma temperature determination by the line-to-continuum method for the Si (I) 288.16 nm emission line (Liu et al. 1999, CRC Press 1988)

λ (nm)	A_{21} (10^8 s^{-1})	g_2	E_2 (eV)	E_i (eV)	Q_i (eV)	ξ	G	C_r (sK)
Si (I) 288.16	1.9	3	5.028	8.151	6.159	1.4	1	2.005 x 10^{-5}

In Table 4-7, λ represents the wavelength of the emission line, A_{21} the transition probability between two energy levels E_1 and E_2, g_2 the statistical weight of the upper energy level, and E_2 the energy of the upper level. E_i is the ionisation potential of a neutral silicon atom, Q_i is the partition function for a singly ionised silicon ion, and G is the free-free Gaunt factor, which is assumed to be unity (Liu

et al. 1999). ξ is the free-bound continuum correction factor, and was calculated for Si vapour by Liu et al. as 1.4 (Liu et al. 1999).

Figure 4-19 shows the plasma electron temperatures, T_e, obtained by the line-to-continuum ratio method at each pressure. The values determined at atmospheric pressure are similar to those observed by Milan and Laserna (Milan and Laserna 2001) and Liu et al. (Liu et al. 1999).

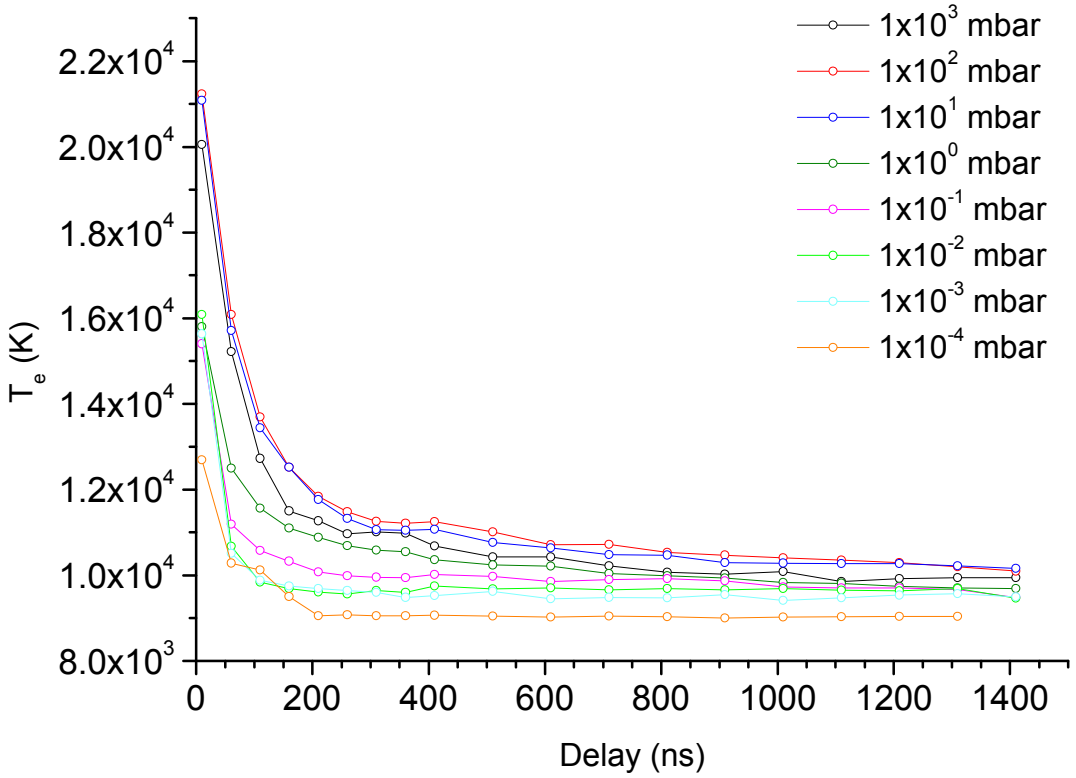

Figure 4-19 Electron excitation temperature versus delay as derived from the line-to-continuum ratio method for the Si (I) 288.16 nm emission line

The plasma temperatures are seen to follow a second-order exponential decay at all pressures; the values of the coefficient of determination R^2 for such fits are listed in Table 4-8, and indicate a very accurate fit at each pressure.

Table 4-8 Coefficients of determination, R^2, for a second order exponential decay as fitted to the electron temperature data presented in Figure 4-21

Pressure (mbar)	R^2	Pressure (mbar)	R^2
1×10^3	0.99763	1×10^{-1}	0.99577
1×10^2	0.99956	1×10^{-2}	0.99832
1×10^1	0.99913	1×10^{-3}	0.99899
1×10^0	0.99933	1×10^{-4}	0.98738

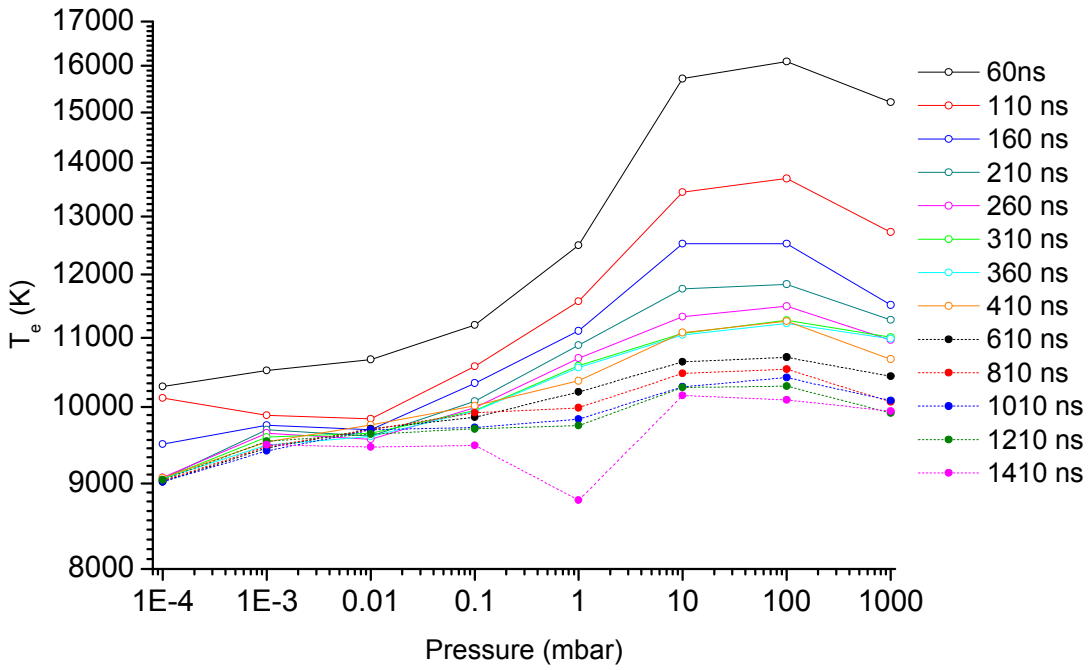

Figure 4-20 Electron temperature versus pressure as derived from the line-to-continuum ratio method for the Si (I) 288.16 nm emission line

Figure 4-20 clearly shows that the electron temperatures calculated at ambient pressures of 1×10^2 and 1×10^1 mbar are greater than those observed at atmospheric pressure. The maximum calculated electron temperature T_e was 21229 K, the minimum was 8794 K.

4.3.10 Singly Ionised Species Temperature

The Saha-Eggert equation, Equation 2.26, was used to determine the Si (II) singly ionised species temperature. In order to calculate the ionic species temperature using the Saha-Eggert equation, two selected silicon emission lines from successive ionisation states I and II were monitored; the spectroscopic constants for these lines are tabulated in Table 4-9.

The Si (I) 288.16 nm and Si(II) 413.09 nm emission lines were chosen for this purpose as they have known spectroscopic constants (CRC Press 1988, Milan and Laserna 2001), they are intense and relatively long lived, and their wavelengths may be monitored simultaneously in the same spectral capture window, using the 150 grooves mm^{-1} diffraction grating. The calculated ionic species temperatures are plotted with respect to gate delay in Figure 4-21.

Table 4-9 Spectroscopic constants of Si (I) and Si (II) emission lines used in ionic temperature determination by the Saha-Eggert equation (Milan and Laserna 2001, CRC Press 1988)

Ionisation State	Wavelength [λ (nm)]	Transition probability [A] ($\times 10^8$ s^{-1})	Upper state statistical weights [g_k]	Upper state energy level [E_k (cm^{-1})]	Ionisation potential [V (eV)]
Si (I)	288.16	1.90	3	40991	8.152
Si (II)	413.09	1.42	8	103556	16.346

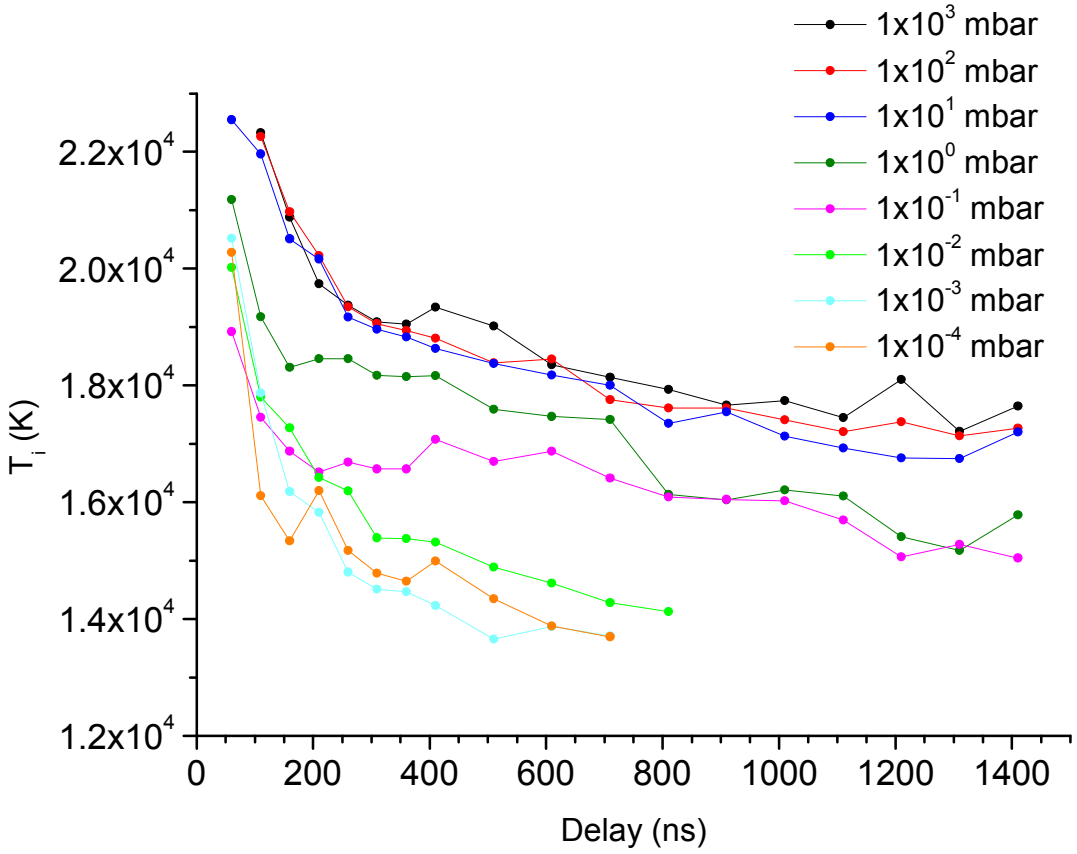

Figure 4-21 Ionic species temperature versus delay using the Saha-Eggert equation

It may be seen from Figure 4-21 that the singly ionised species temperature decreases with time at all pressures. This temperature drop was found to follow a second-order exponential fit; the coefficients of determination for such fits are listed in Table 4-10, and indicate an accurate fit at each pressure.

Table 4-10 Coefficient of determination R^2 for second-order exponential fits applied to the data presented in Figure 4-21

Pressure (mbar)	R^2	Pressure (mbar)	R^2
1×10^3	0.96577	1×10^{-1}	0.92019
1×10^2	0.99108	1×10^{-2}	0.99300
1×10^1	0.98193	1×10^{-3}	0.99420
1×10^0	0.96312	1×10^{-4}	0.97236

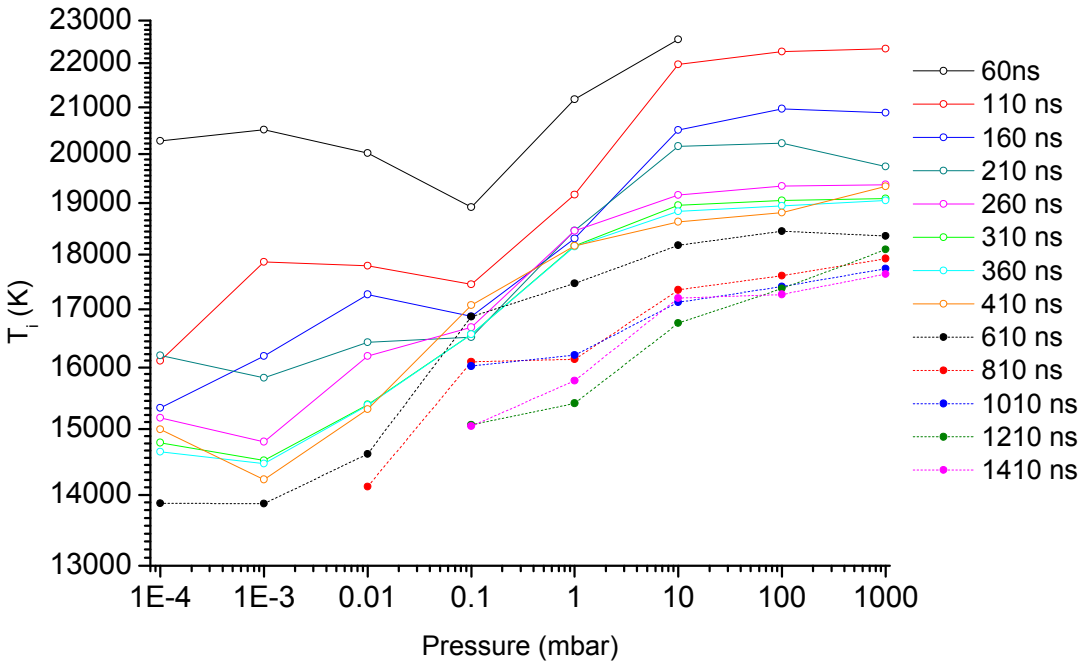

Figure 4-22 Ionic species temperature versus pressure using the Saha-Eggert equation

Figure 4-22 displays the effect of ambient pressure on the singly ionised plasma species temperature. It can be seen that, for a given capture delay time, the ionic species temperature decreases with pressure; the maximum ionic species temperatures were observed at atmospheric pressure. The maximum ionic species temperature T_i recorded was 22551 K, the minimum 13658 K.

LIBS plasmas are traditionally modelled as being in Local Thermal Equilibrium (LTE), wherein the plasma may be treated as having a single temperature, i.e. the free electrons, ions and neutral species comprising the plasma are at the same temperature. Therefore, if the LIBS plasmas observed in this study exhibit LTE, then the calculated electron and ionic species temperatures should be identical. A comparison of the calculated electron and ionic species temperatures is presented in Figure 4-23.

4.3.11 Comparison of Electron and Ion Temperatures

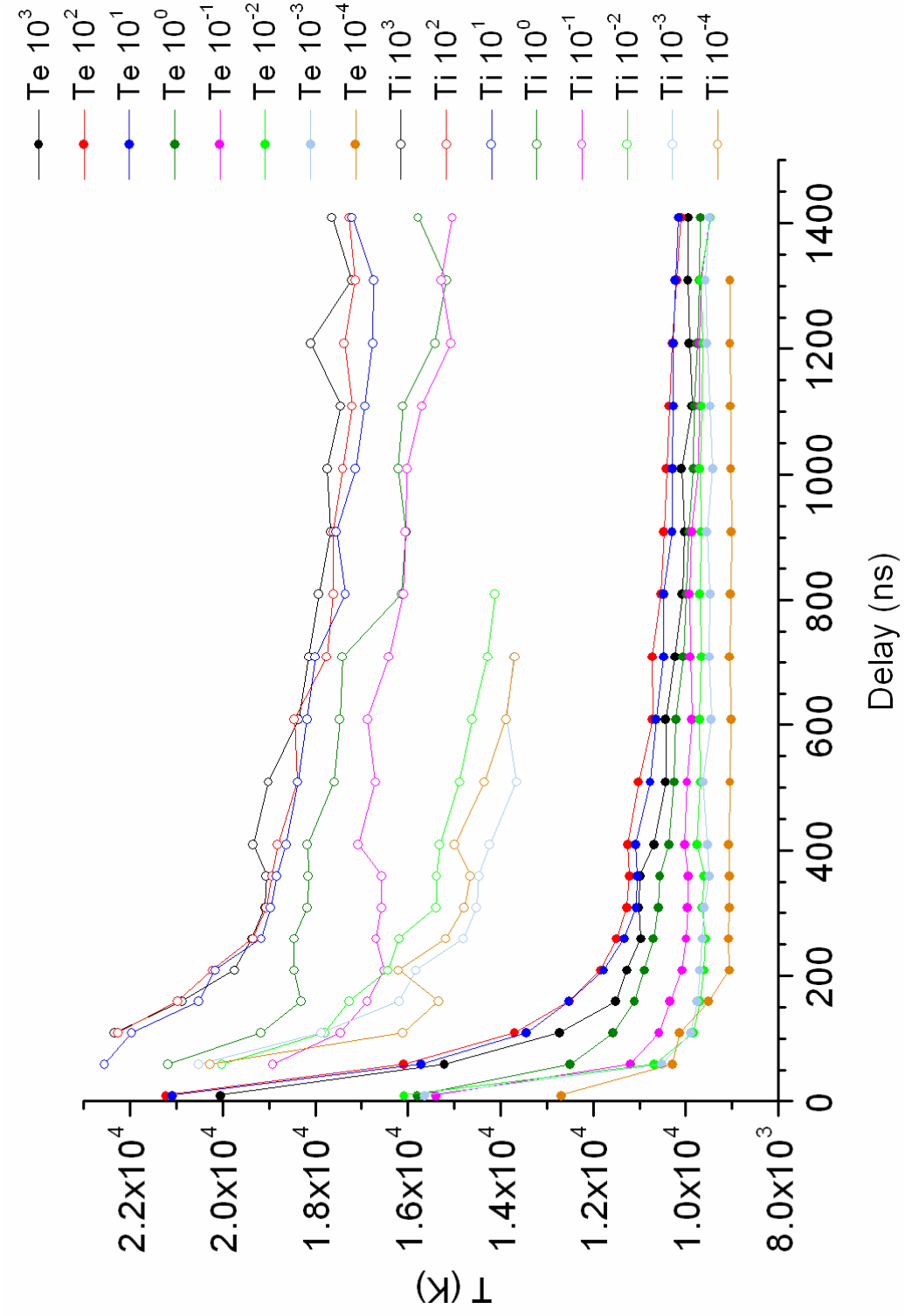

Figure 4-23 Comparison of laser-induced silicon plasma electron and ion temperatures versus time

From Figure 4-23 it is immediately apparent that at no point in the parameter space of this study are the electron and ionic species temperatures identical; the ionic species are observed to have a higher temperature throughout. At each pressure and delay time considered here, the laser-induced silicon plasmas do not exhibit Local Thermal Equilibrium.

4.3.12 Determination of the Electron Impact Broadening Parameter

In order to calculate the plasma electron density using Equation 2.31, the electron impact broadening parameter w must be known (Milan and Laserna 2001, Thorne 1974). The electron impact parameter is generally interpolated for the appropriate temperatures from the tables of Griem (Griem 1964); the Si (I) 288.16 nm emission broadening parameter is not listed in Griem's tables, so interpolation for wavelength must also be conducted.

Figure 4-24 plots Griem's electron impact broadening parameter values as listed for the 297.0353 nm, 252.8509 nm, 245.2120 nm, and 220.7978 nm emission lines (Griem 1964). The dotted lines on the figure represent linear fits of the form: $y = mx + c$ to the w values tabulated at temperatures of 2500, 5000, 10000, 20000, 40000 and 80000 K. The coefficients of determination for the straight line fits shown in Figure 4-24 are given in Table 4-11, and indicate a high level of accuracy; it is therefore reasonable to assume that, for a given plasma temperature, w may be interpolated for wavelength.

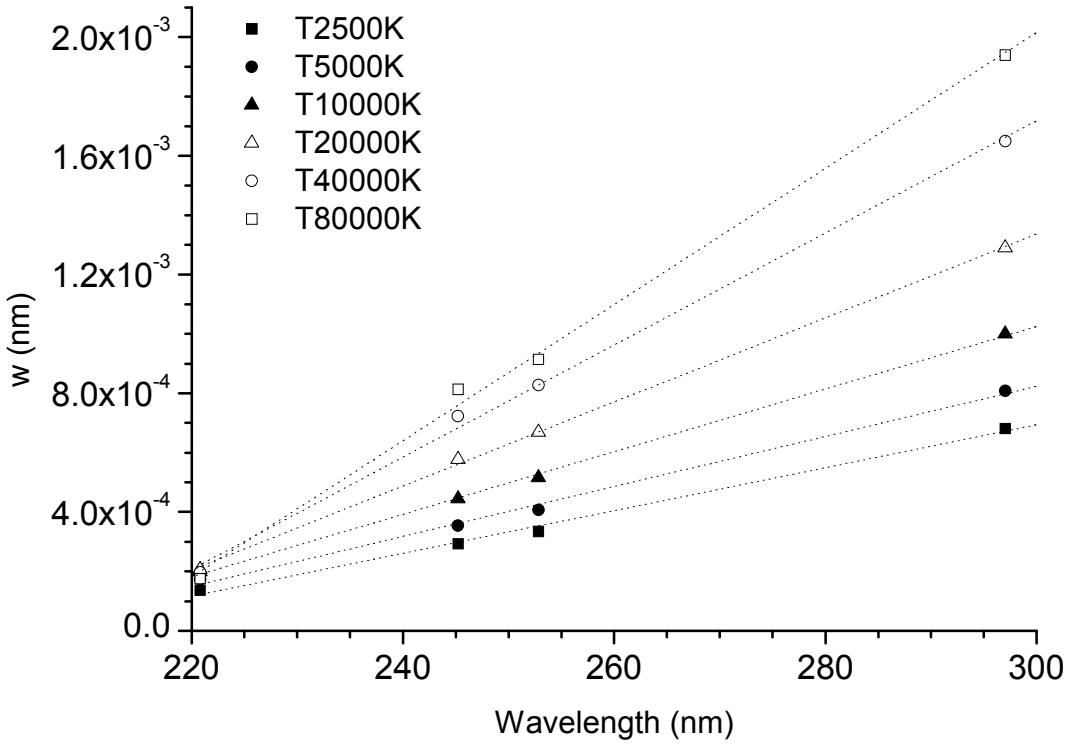

Figure 4-24 Electron impact broadening parameter versus temperature for Si (I) 220.80, 245.21, 252.85, 297.04 nm emission lines

Table 4-11 Coefficients of determination derived from Figure 4-24

Temperature (K)	$y = mx + c$	R^2
2500	$y=7\times10^{-6}x$ -0.0147	0.9957
5000	$y=8\times10^{-6}x$ -0.0170	0.9962
10000	$y=1\times10^{-5}x$ -0.0214	0.9992
20000	$y=1\times10^{-5}x$ -0.0291	0.9994
40000	$y=2\times10^{-5}x$ -0.0395	0.9978
80000	$y=2\times10^{-5}x$ -0.0487	0.9975

.

Assuming then a linear variation of *w* with wavelength, interpolation between Griem's *w* values listed for the Si (I) 252.85 and 297.00 nm emission lines enabled a plot of *w* for the Si (I) 288.16 nm emission line to be constructed, as shown in Figure 4-25. The curve representing the change in the broadening

parameter for the Si (I) 288.16 nm emission line with respect to plasma temperature was found to best fit a double-phase exponential association curve, the general form of which is described by Equation 4.2:

$$y = y_0 + A_1\left(1 - \exp\left(-\frac{x}{t_1}\right)\right) + A_2\left(1 - \exp\left(-\frac{x}{t_2}\right)\right) \qquad (4.2)$$

The coefficient of determination for this fit, and the values derived for the variables in Equation 4.2, are listed in Table 4-12.

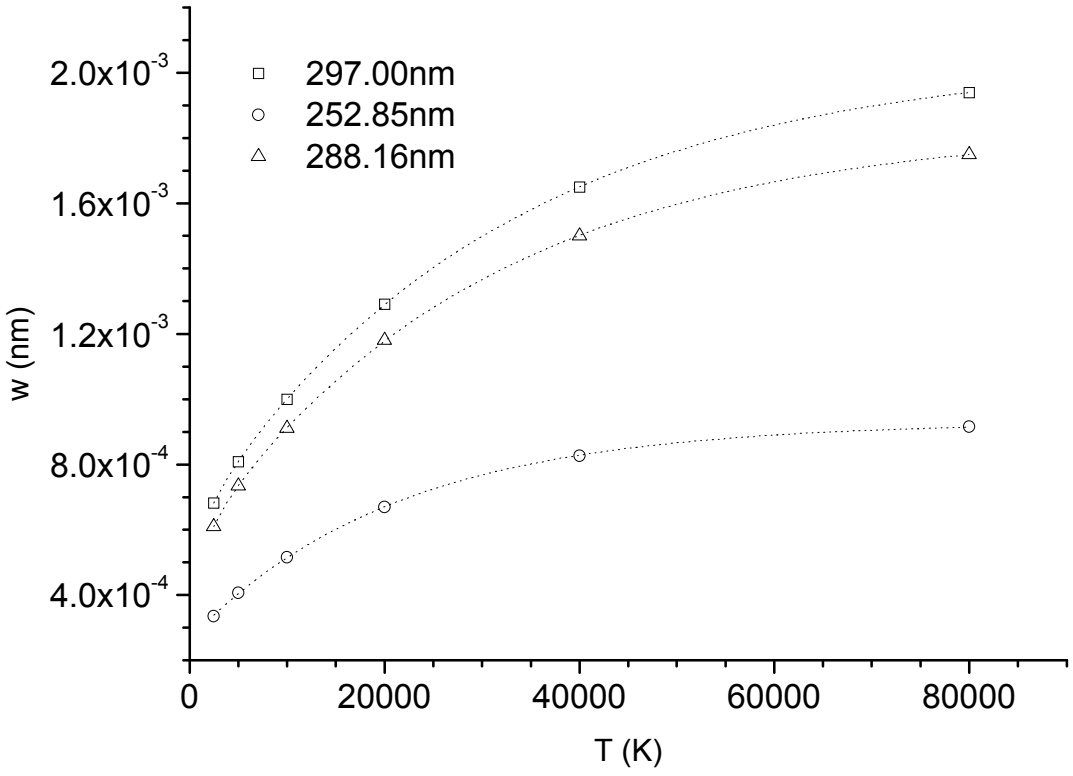

Figure 4-25 Interpolation of the electron impact broadening parameter for the Si (I) 288.16 nm emission line

Table 4-12 Values for the exponential association fit to the 288.16 nm *w* versus temperature curve plotted in Figure 4-25

Term	Value	Error
Y_0	0.00036	± 0.00012
A_1	0.0013	± 7.0946E-6
t_1	29494.5985	± 528.48851
A_2	0.00018	± 0.00011
t_2	1550.23537	± 755.43651
R^2	0.99999	

The values listed in Table 4-12, in conjunction with Equation 4.2, allow the electron impact broadening parameter to be calculated for the Si (I) 288.16 nm emission line at any plasma temperature up to 80000K. Using the minimum and maximum T_e recorded here, w varied from 8.74×10^{-3} to 1.21×10^{-2} nm.

4.3.13 Plasma Electron Density

The electron density of the laser ablation plasma was determined from the Stark broadening of the 288.16 nm Si (I) emission line. The contributions of resonance and Doppler line broadening were deemed insignificant under the conditions of this study. Resonance broadening is negligible as the 288.16 nm Si (I) line is not associated with a resonance state. The Doppler effect will cause a maximum broadening of the Si (I) 288.16 nm emission line, estimated using Equation 2.32 (Page 56), as 0.0059 nm, assuming that the plasma temperature is the maximum measured in this study, $\sim 2.3 \times 10^4$ K.

The emission lines were corrected for the instrumental broadening profile prior to FWHM measurement; the instrumental broadening profile was found to be 0.0178 nm, measured using several narrow emission lines from a cadmium hollow cathode lamp (Appendix 10.2).

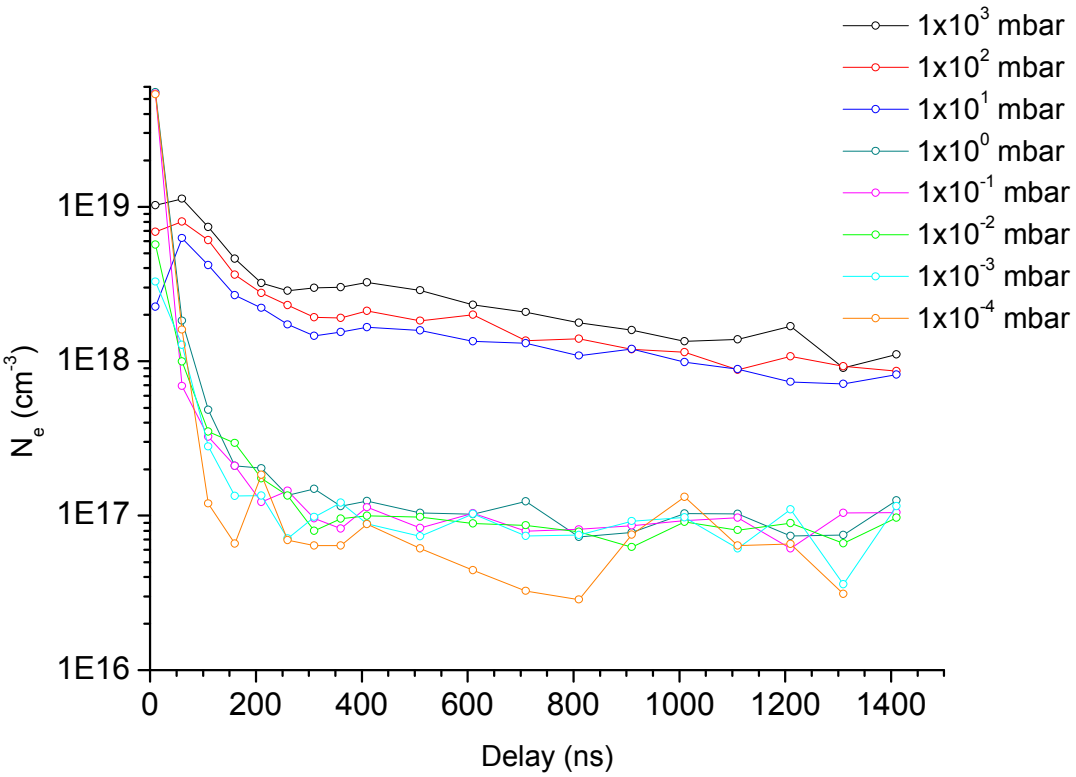

Figure 4-26 Plasma electron number density versus delay

The electron number densities deduced from the Stark broadening of the Si (I) 288.16 nm emission line are plotted in Figure 4-26. At all pressures the electron number density decreases with time, starting in each case from an initial value of the order 10^{19} cm^{-3}.

The electron number density behaviour appears to be separated into two ambient pressure dependent regimes. For ambient pressures $\geq 1 \times 10^{1}$ mbar the electron number density decreases steadily from ~ 10^{19} to ~ 10^{18} cm^{-3} over 1400 ns. For

ambient pressures < 1×10^1 mbar there is a sudden drop in electron number density from ~ 10^{19} to ~ 10^{17} cm^{-3} in the first 200 ns of plume evolution, followed by a much slower decrease over the remainder of the observation period.

At each pressure the electron number density variation with time was found to best be described by a second-order exponential decay; the coefficients of determination for these fits are presented in Table 4-13. The R^2 values in Table 4-13 indicate an accurate fit to the data at each pressure, but the accuracy of the fit appears to drop for ambient pressures of 1×10^1 mbar and above.

Table 4-13 Coefficients of determination, R2, for second-order exponential fits to the electron number density data presented in Figure 4-26

Pressure (mbar)	R^2	Pressure (mbar)	R^2
1×10^3	0.91546	1×10^{-1}	0.99998
1×10^2	0.91369	1×10^{-2}	0.99838
1×10^1	0.96249	1×10^{-3}	0.99488
1×10^0	0.99996	1×10^{-4}	0.99999

Figure 4-27 plots the variation in electron number density with respect to pressure. The highest electron number densities are observed at atmospheric pressure, and drop with decreasing ambient pressure. The step change in electron number density is evident, dropping by approximately an order of magnitude between ambient pressures of 10 and 1 mbar. The maximum recorded electron number density was 5.53×10^{19} cm^{-3}, the minimum 2.86×10^{16} cm^{-3}.

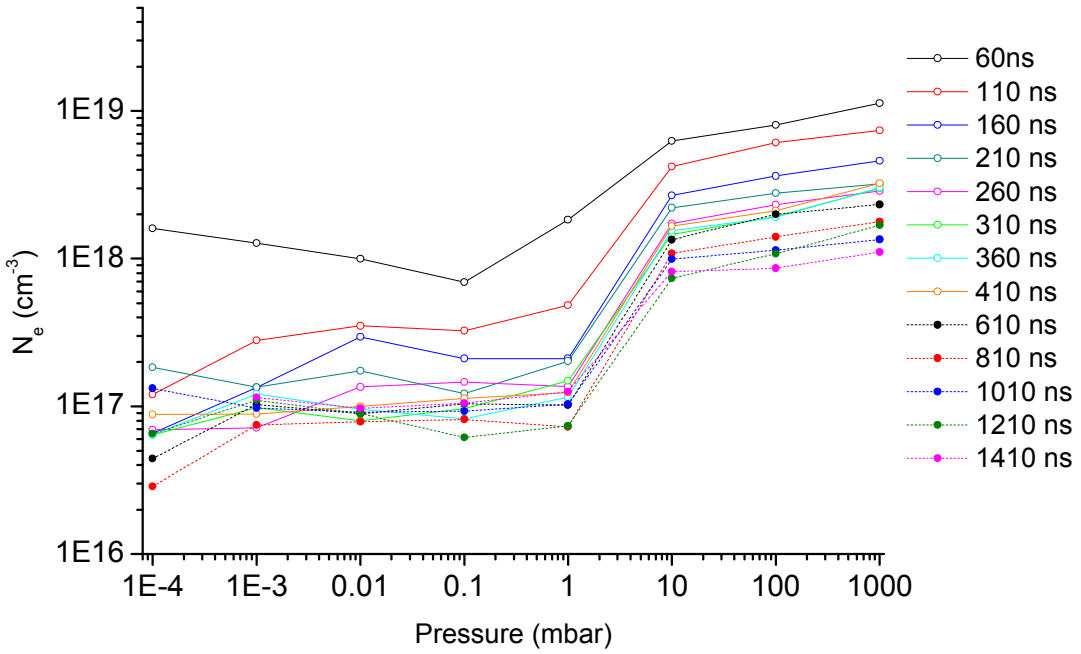

Figure 4-27 Plasma electron number density versus pressure

4.3.14 Local Thermal Equilibrium - Electron Number Density Considerations

For any given plasma to be considered to be in LTE the lower limit for the electron number density N_e must satisfy Equation 4.3 (Thorne 1974, Milan and Laserna 2001):

$$N_e \ (\text{cm}^{-3}) \geq 1.6 \times 10^{12} \ T^{1/2} \ \Delta E^{3} \qquad (4.3)$$

where ΔE (eV) is the energy difference between the upper and lower states and T (K) is the plasma temperature. For the Si (I) 288.16 nm line transition, ΔE = 4.3 eV. Using the highest plasma temperature measured, $T \sim 2.3 \times 10^4$ K yields a minimum electron density of $N_e \geq 1.929 \times 10^{16}$ (cm^{-3}). It can be seen that N_e is greater than the lower limit required for LTE; however N_e is only just greater than this lower limit and the assumption that LTE exists must be treated with

caution. It should also be noted that the criterion outlined in Equation 4.2 is a necessary, but not the only requirement for LTE.

4.3.15 Plasma Morphology

Figures 4-28 to 4-35 show time-resolved, non-dispersed images of the laser–induced silicon plasmas from atmospheric pressure down to $p_a \sim 10^{-4}$ mbar. The laser was operated in single shot mode with each shot on a clean area of the sample; each image is normalized to its maximum intensity. The direction of laser propagation is from the top of each image to the bottom, with the sample surface lying perpendicular to the laser beam i.e the Si sample is at the bottom of the picture with the plasma being generated vertically upwards.

In order to prevent ICCD spot damage from intense plasma emission, a ND 1.2 neutral density filter was placed in front of the spectrometer input slit. The integration time for each capture was 1 ns, and the intensifier gain was set to 200 as in the spectroscopic measurements detailed in previous sections. The plumes appear asymmetrical about the axis of the laser beam propagation due to irregularities in the beam profile. It can be seen that in the early stages of plasma formation, ~ 110 ns, the plasmas generated at atmospheric pressure and at $p_a \sim 10^{-4}$ mbar are comparable in terms of size and luminosity. This similarity is backed up by the spectroscopic measurements of N_e and T_e. The plasma disperses much more rapidly under lower ambient pressure due to free plasma expansion on account of an increased mean free path of the confining ambient gas; this is again supported by the spectroscopic measurements of N_e and T_e.

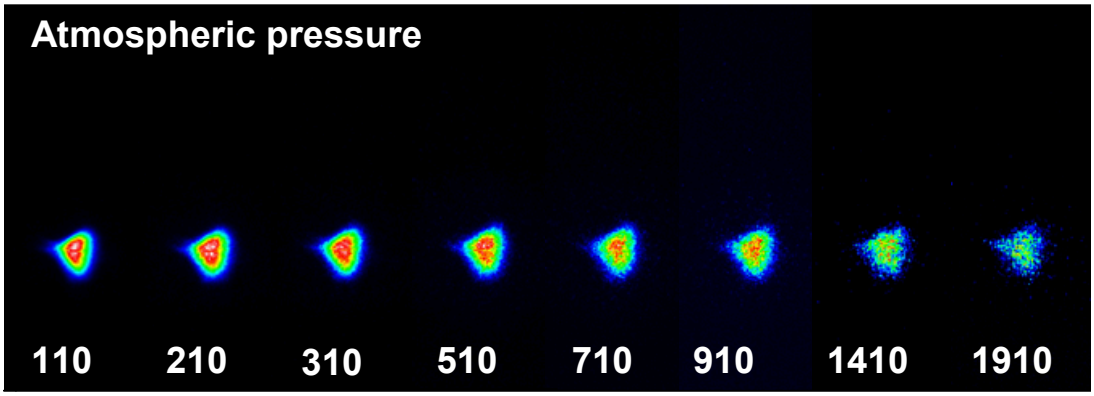

Figure 4-28 Plasma morphology at atmospheric pressure versus time

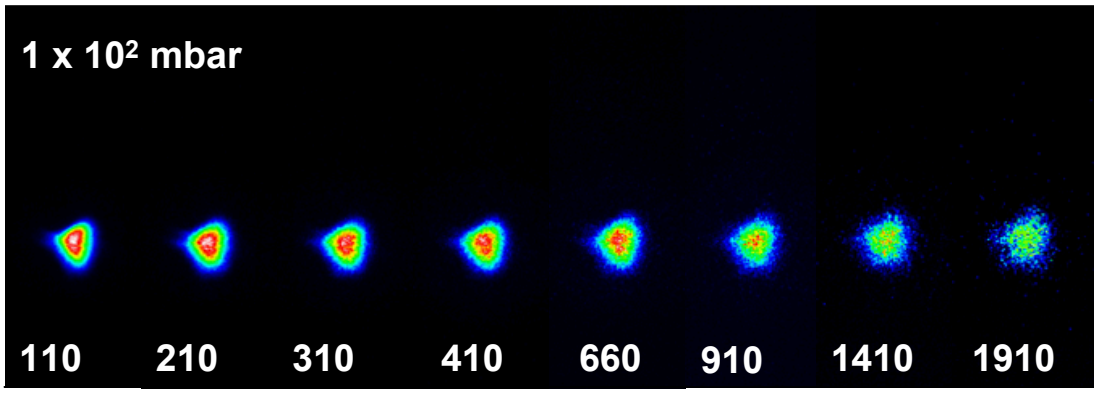

Figure 4-29 Plasma morphology at 1 x 10^2 mbar versus time

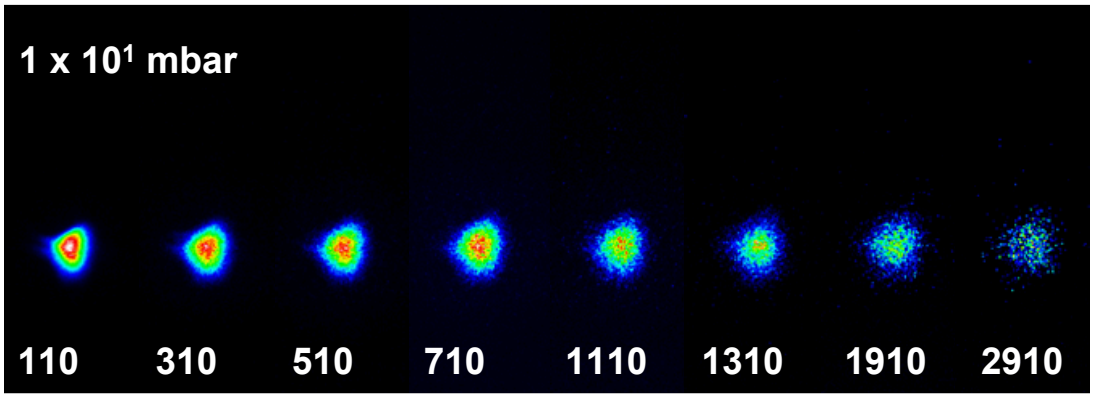

Figure 4-30 Plasma morphology at 1 x 10^1 mbar versus time

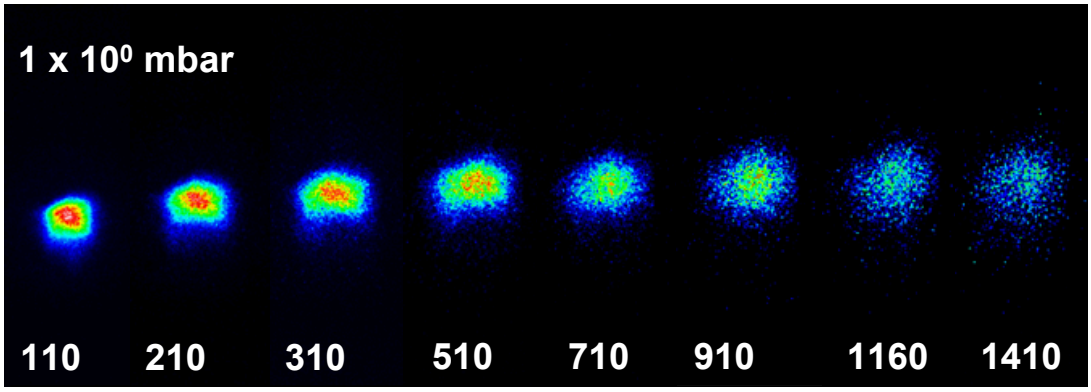

Figure 4-31 Plasma morphology at 1 x 10^{0} mbar versus time

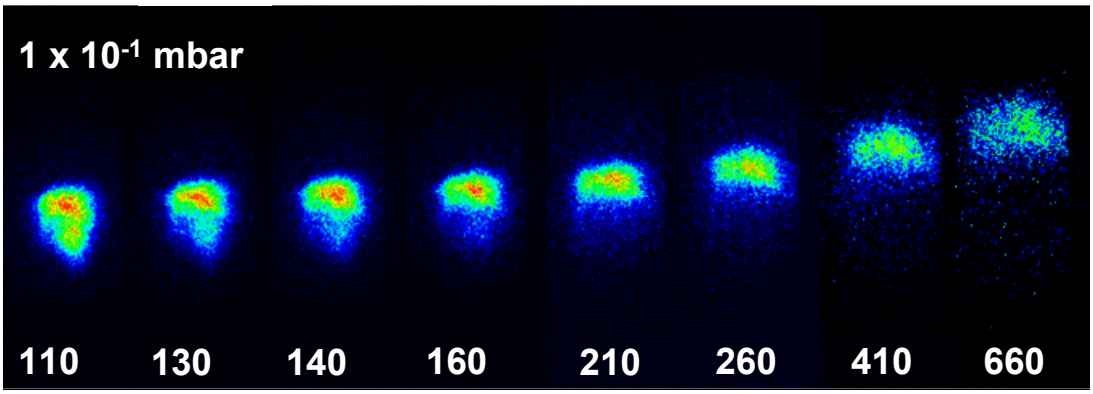

Figure 4-32 Plasma morphology at 1 x 10^{-1} mbar versus time

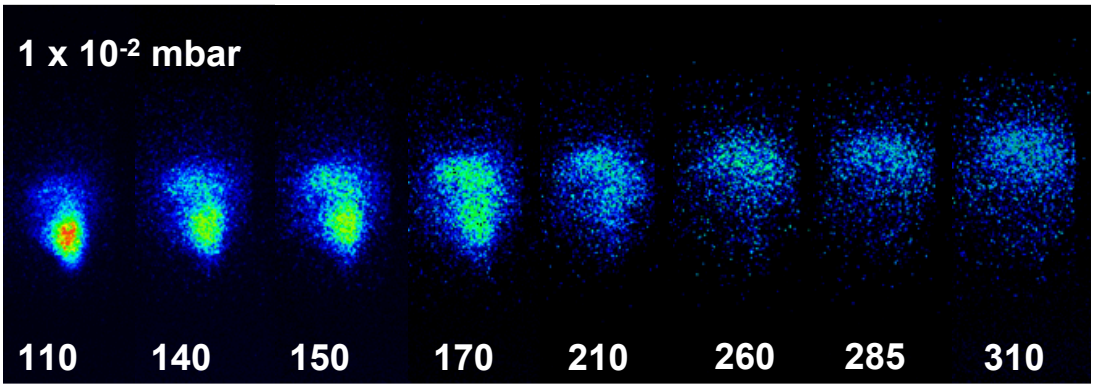

Figure 4-33 Plasma morphology at 1 x 10^{-2} mbar versus time

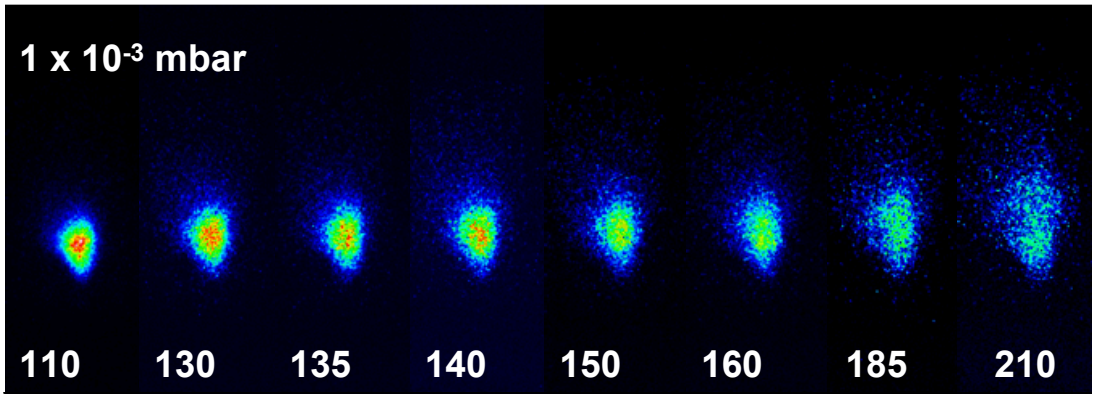

Figure 4-34 Plasma morphology at 1 x 10^{-3} mbar versus time

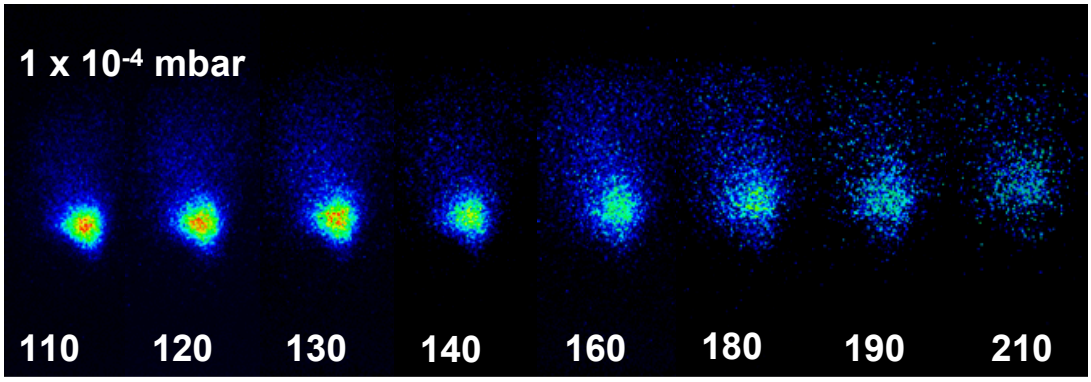

Figure 4-35 Plasma morphology at 1 x 10^{-4} mbar versus time

At atmospheric pressure, 1×10^{2} and 1×10^{1} mbar there is little discernible difference in the shape, size, luminosity or lifetime of the laser induced silicon plasmas. In Figure 4-31, at an ambient pressure of 1×10^{0} mbar the plasma is seen to leave the sample surface as it expands, a trend continued at ambient pressures of 1×10^{-1} and 1×10^{-2} mbar, shown in Figures 4-33 and 4-34.

At ambient pressures of 1×10^{-3} and below the plasma does not leave the sample surface as it expands, as shown in Figures 4-34 and 4-35. Figures 4-28 through to 4-35 indicate that, below an ambient pressure of 1×10^{1} mbar, further pressure decreases show an expected acceleration in the rate of plasma expansion.

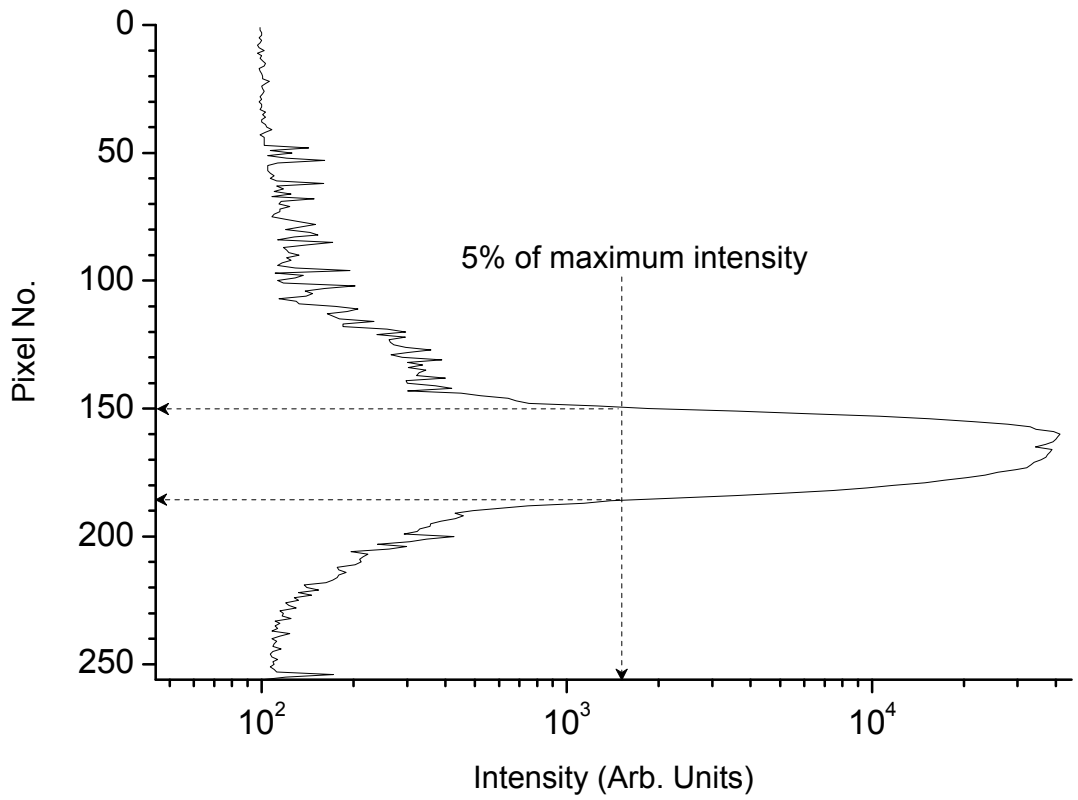

Figure 4-36 Measurement of plasma dimensions

To accurately compare the evolution of the laser-induced silicon plasmas at each pressure considered, a method of consistent plasma length measurement was devised. Figure 4-36 shows the signal intensity profile extracted from a typical CCD readout during single shot LIBS of silicon; this example readout was captured at atmospheric pressure, using a delay of 200ns, with a gate width of 1 ns, and the ICCD gain set to 200. The data shown in Figure 4-36 shows the signal intensity recorded by a vertical column of ICCD pixels on an axis through the centre of the plasma image, and may therefore be used to determine the plasma length. A signal intensity of 5 % of the maximum recorded for each given plasma was set to define the plasma boundary.

The plasma length corresponding to ICCD pixel number was determined. A micrometer movement sample stage was used to move the silicon sample up and down along the direction of plasma expansion, and the subsequent pixel number variations in image position versus micrometer reading noted. It was found that 1 pixel equates to ~0.17 mm of plasma length. Using this conversion factor, and the measurement process detailed above, the plasma expansion versus time for each pressure is presented in Figure 4-37.

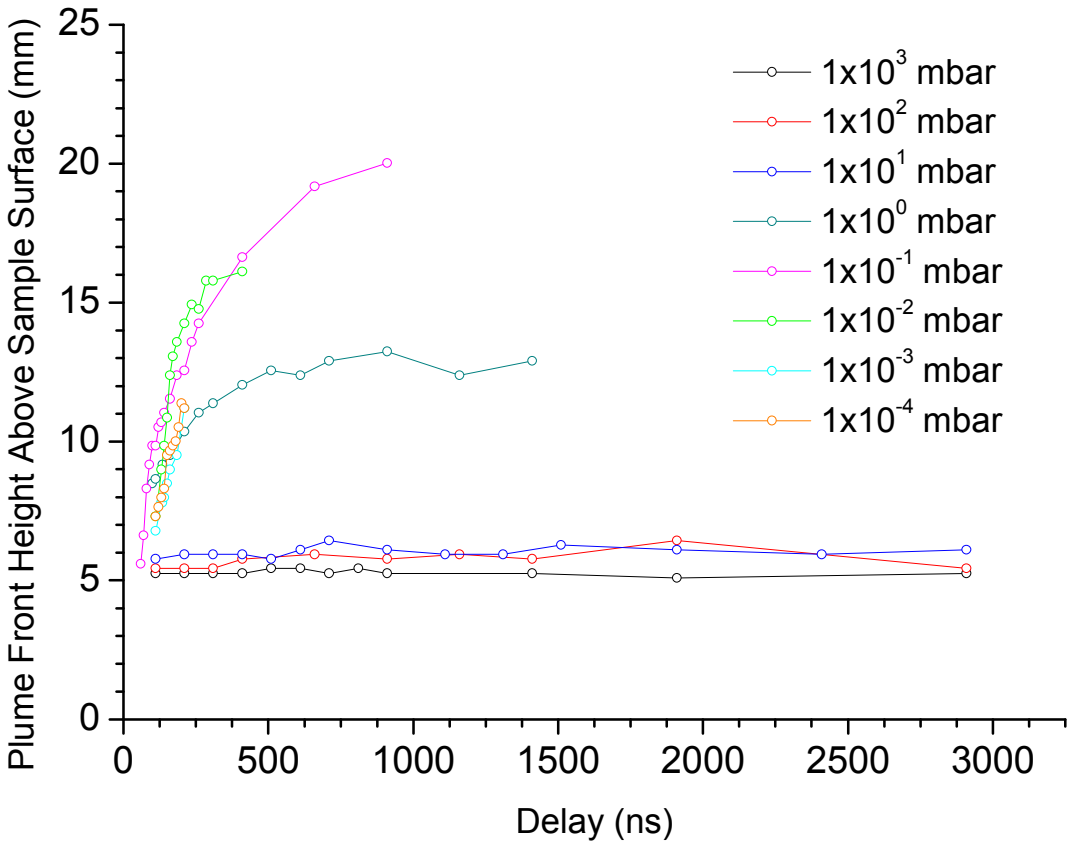

Figure 4-37 Plume front position versus capture delay

Figure 4-37 is a plot of the plasma plume front height above the sample surface versus delay time. Plume confinement is evident at pressures of 1×10^1 mbar and above, with the plasma remaining virtually the same length throughout the

observation period. At ambient pressures of 1×10^{0} and 1×10^{-1} mbar the plasma plume front propagates away from the sample surface, but the traces for these pressures indicate a deceleration of the plume front, and by inference a degree of plasma confinement. At ambient pressures $\leq 1 \times 10^{-2}$ mbar the plume front moves away from the sample surface with a constant velocity, indicating free plasma expansion and little plume confinement.

4.4 Summary

In general, the emission line and plasma continuum intensities are observed to decrease more rapidly with pressure. Figures 4-5 and 4-6 reveal that the coefficient of determination, R^2, of a Lorentz curve fitted to the Si (I) 288.16 nm emission line increases as the plasma evolves. High R^2 values for delays > 200 ns indicate a good fit, better than 99%, to the captured data, and by inference indicate negligible emission line self absorption. At earlier times < 200 ns the broadband continuum emission dominates the signal; as such the emission line may not be clearly resolved leading to a poor fit. In general there is less emission line self-absorption as the ambient pressure decreases. The plasma number density decreases with pressure and as such there are fewer non-emitting species to absorb the optical emission.

The neutral Si (I) 288.16 nm emission line peak intensity, displays a general decrease with decreasing pressure, with the maximum intensities recorded at ambient pressures of 1×10^{2} and 1×10^{1} mbar. From Figures 4-29, 4-30 and 4-37 we observe that at these ambient pressures there is sufficient plasma confinement to give a relatively high plasma density and therefore a high

proportion of emitting species contributing to the emission spectrum. However, Figure 4-37 reveals that the reduced ambient pressure, in the range 1×10^2 to 1×10^1 mbar, allows for a slight plasma expansion, which slightly reduces the plasma particle density; the rate of collisional de-excitations is therefore reduced, leading to an enhanced emission line intensity.

The temporal profile of the Si (II) 413.09 nm also displays a general decrease of intensity with pressure. Again, maximum peak intensities are observed at 1×10^2 and 1×10^1 mbar due to the reduction of collisional de-excitation processes. The Si (II) emission is observed to be shorter lived than that of the neutral species, this is due to free electrons recombining with ions in the early phases of plasma expansion.

The integrated area of an emission line may be taken as a measure of the overall plasma luminosity; the greater the area under the emission line, the higher the plasma luminosity. The integrated area, A, of the Si (I) 288.16 nm emission line displays very complex behaviour, exhibiting different temporal characteristics according to two ambient pressure regimes. For ambient pressures of 1×10^1 mbar and above, the area increases then subsequently decays with respect to plasma lifetime. For ambient pressures of 1×10^0 and below, the integrated area of the Si (I) 288.16 nm decreases steadily with plasma lifetime. Figures 4-5 and 4-6 reveal that in the early stages of plasma evolution, at delay times < 200 ns, the coefficient of determination R^2 is relatively low, indicating a poor Lorentz fit to the captured data. As such, the interpretation of parameters derived from the fit, such as A (the emission line area) should be viewed with caution. Figures 4-

11 and 4-12 show that the maximum values for A are observed at ambient pressures of 1×10^2 and 1×10^1 mbar, indicating an increase in the overall plasma luminosity at these pressures

Figure 4-13 reveals that the plasma continuum emission decays steadily with time, and is sufficiently long lived that it may be resolved above the instrument background throughout the parameter space of this investigation. The continuum emission intensity decay was found to best fit a second order exponential model; the R^2 values for this fit are listed in Table 4-3, and at all ambient pressures are above 99% indicating an extremely accurate fit. The general decrease of the continuum emission with decreasing pressure is ascribed to the lower number density of free electrons at these pressures to contribute to the continuum emission. The decrease of continuum emission intensity with respect to time is due to electron-ion re-combinations reducing the free electron density. The maximum continuum emission intensities are again recorded at ambient pressures of 1×10^2 and 1×10^1 mbar; the reduced level of collisional processes at these pressures leads to higher ion populations which lead to greater continuum emission levels.

The results discussed above highlight a pressure region between 10^0 to 10^1 mbar where there is a distinct change in the plasma characteristics. This is again confirmed when considering the Full Width Half Maxima (FWHM) of the Si (I) emission line shown in Figure 4-15. Two distinct groups of data can be seen, one representing the plasmas that are confined to the substrate surface by the ambient gas pressure, the other representing plasmas that have detached from the

silicon substrate surface and are thus undergoing free expansion. In this second region, results reveal that the FWHM are narrowed, and it is postulated that this is due to a reduced electron density, and an associated reduction in the Stark broadening, due to the plasma expansion.

The Boltzmann plot and two line ratio methods of calculating the electron excitation temperature failed to supply any meaningful data. This is shown clearly in Figures 4-17 and 4-18 and was primarily due to the lack of suitable emission lines that were resolvable using LIBS setup. This is a well known problem (Milan and Laserna 2001).

The evaluation of the electron temperature at atmospheric pressure, using the line-to-continuum ratio method, produced results that were in good agreement with the published data (Le Drogoff et al 2001, Milan and Laserna 2001, Liu et al. 1999, Shaikh et al. 2006). Figure 4-19 reveals a second order exponential decay of temperature at each pressure with an R^2 value in excess of 99%. It is shown that as the ambient pressure decreases the electron temperature and electron number density decrease, which is to be expected. The maximum calculated electron temperatures were observed at ambient pressures of 1×10^2 and 1×10^1 mbar; the pressure region through which the plasma is confined to the substrate surface.

The calculated values of ionic species temperature were not as consistent as the results obtained for electron temperature. This could be due to the fact that ionic populations in the plasma plume are more susceptible to fluctuations of the laser

output. Figures 4-21 and 4-22 show that the ion temperature follows a second-order exponential decay at all pressures.

The existence of Local Thermal Equilibrium (LTE) within the transient laser-induced plasmas has been the subject of debate between a number of researchers over the past two years (personal communication). As previously stated in Chapter 2, many of the models used to describe these transient plasmas assume the existence of LTE, and it was therefore considered that the confirmation or rejection of this notion was of prime importance. Much of the research undertaken in this study was directed towards obtaining sufficient information to resolve this problem. For LTE to exist, the temperatures of the free electrons, the ionic and the neutral species must be identical, that is to say $T_e = T_i = T_{atoms} = T_{molecules}$ (Cremers and Radziemski 2006). This is clearly not the case according to Figure 4-23.

It has also been reported that LTE exists if the electron number density is sufficiently high to collisionally thermalise the plasma (Milan and Laserna 2001, Tognoni et al 2002, Liu et al 1999, Le Drogoff et al 2001). The results presented here reveal that throughout the parameter space of this study the measured electron number densities fulfil the above criterion; however, taken in isolation this condition for the existence of LTE is clearly lacking.

Non-dispersed images of the plasma morphology are shown in Figures 4-28 to 4-35, revealing interesting expansion dynamics that are related to the ambient pressure. At pressures of 1×10^1 mbar and above the plumes are comparable in

terms of their size, luminosity and lifetime, whereas at pressures below 1×10^{1} mbar varying degrees of plasma expansion are observed and the plumes are observed to propagate away from the sample surface. Figure 4-37 is a plot of the plasma plume front height above the sample surface versus delay time. Three pressure-specific behaviour regimes are evident:

1. at pressures of 1×10^{1} mbar and above, the size of the plasma is, to a first approximation, constant throughout the observation period
2. at pressures of 1×10^{0} and 1×10^{-1} mbar the plasma plume front propagates away from the sample surface and is seen to decelerate indicating a degree of plasma confinement
3. at ambient pressures $\leq 1 \times 10^{-2}$ mbar the plume front rapidly moves away from the sample surface with a constant velocity, indicating free plasma expansion and reduced plume confinement.

It is concluded that the spectroscopic measurements obtained throughout this work are dependent on the plasma morphology, which in turn is seen to depend on the ambient pressure. At the initial point of plasma formation, and during the first few nanoseconds of plasma lifetime, the ambient pressure plays little part in dictating the shape, size and properties of the plasma, as seen in Figures 4-28 to 4-35 and confirmed by the spectroscopic measurements. As the plasma front subsequently expands into the ambient gas, the ambient pressure now begins to affect these properties, with differing plasma expansion dynamics observed at different ambient pressures.

Figure 4-38 is a plot of mean free path of the ambient gas versus ambient gas pressure. The shaded area represents the pressure regime at which discontinuities in the plasma characteristics are observed. By extrapolation it is seen that the mean free path relating to this pressure boundary possesses a value that is of the order of the plume dimensions. It is therefore concluded that the plasma expansion dynamics change at the point where the mean free path of the confining ambient gas approaches the dimensions of the plasma. This observation can now explain the three observed pressure-dependent plasma behaviour regions:

1. where the mean free path of the ambient gas is small compared to the plasma dimensions, the plasma is confined
2. where the mean free path is comparable to the plasma dimensions, a 'transition region' exists wherein there is a degree of plasma confinement, but the plasma is observed to propagate slowly away from the substrate surface
3. where the mean free path of the ambient gas is large compared to the plasma dimensions, free expansion of the plasma is observed.

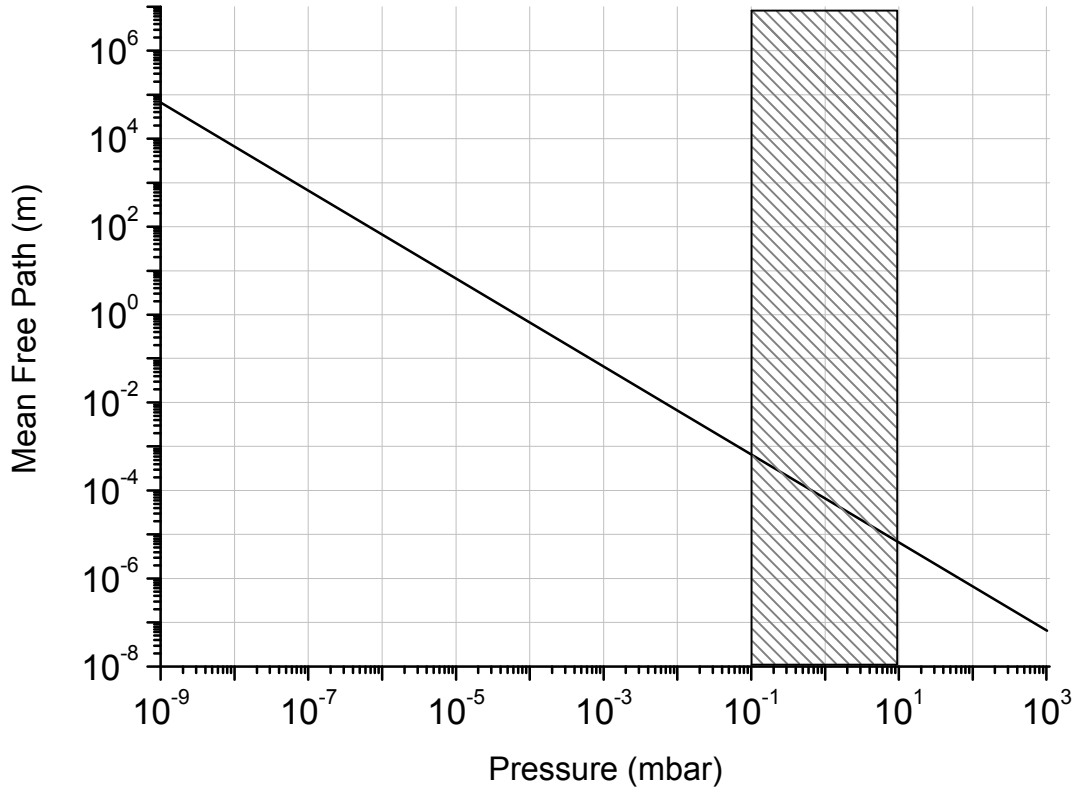

Figure 4-38 Mean free path versus ambient gas pressure

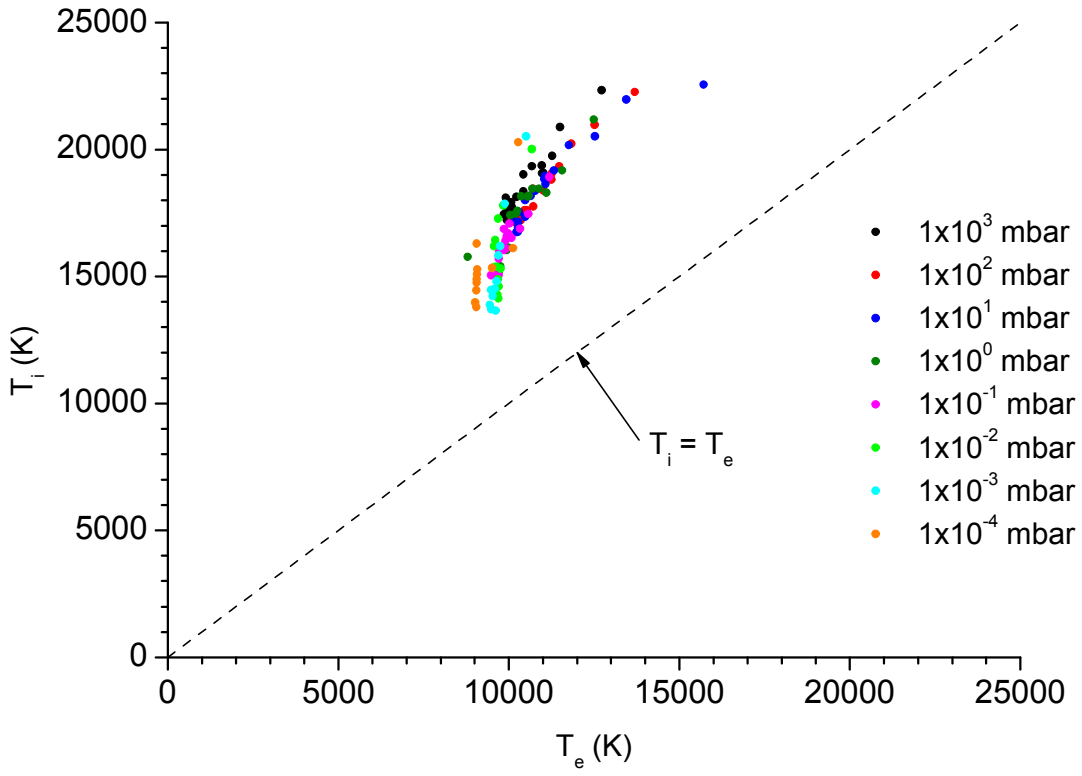

Figure 4-39 Ion temperature T_i versus electron temperature T_e

Figure 4-39 compares the electron and ion temperatures determined over the lifetime of each plasma, produced under the range of ambient pressures reported. The dotted line represents the conditions where LTE can be assumed i.e. at which points $T_i = T_e$. It is clearly shown that none of the points on this graph lie on or close to this line, and therefore it is safe to conclude that LTE does not exist within laser-induced silicon plasmas.

A summary of the important plasma properties, as determined in this study, relating to the applicability of models based on LTE is given in Table 4-14.

Table 4-14 Summary of plasma properties

Plasma property	Minimum	Maximum
Electron temperature T_e (K)	8794	21229
Ionic species temperature T_i (K)	13658	22551
Electron number density N_e (cm^{-3})	2.86×10^{16}	5.53×10^{19}

.

5 Analysis of LIBS Experimental Set-up with Response Surface Analysis

5.1 Introduction

Chapter 4 revealed that the properties of laser-induced plasmas vary markedly with changes in ambient pressure. Instrument parameters optimised to extract useful LIBS spectra at atmospheric pressure may not necessarily provide meaningful data at lower pressures. This chapter describes the optimisation of the LIBS imaging apparatus in order to capture emission spectra of the highest possible quality at atmospheric pressure and under vacuum conditions.

Response Surface Methodology (RSM) was employed to optimise LIBS analysis of single crystal silicon at atmospheric pressure and under vacuum conditions (pressure ~10^{-6}mbar). Multivariate analysis software (StatGraphics 5.1) was used to design and analyse several multi-level, full factorial RSM experiments. A Quality Factor (QF) was conceived as the response parameter for the experiments, representing the quality of the LIBS spectrum captured for a given hardware configuration. The QF enabled the hardware configuration to be adjusted so that a best compromise between resolution, signal intensity and signal noise could be achieved. The effect on the QF of simultaneously adjusting spectrometer gain, gate delay, gate width, lens position and spectrometer slit-width was investigated, and the conditions yielding the best QF determined. A full parametric study of the LIBS hardware configuration was performed to determine the true response of the system; the results of this compare favourably with those yielded from the RSM investigation.

5.2 Initial Comparison of Vacuum and Atmospheric Pressure

For a LIBS spectrum to yield useful information it must have sufficiently high resolution such that overlapping peaks may be resolved, and low background noise ensuring good sensitivity. Many hardware parameters affect the properties of the spectra obtained: laser wavelength, power, frequency and fluence, spectrometer input slit-width, ICCD gate delay and integration time, gain, focal position relative to sample, ambient atmosphere and pressure etc. Initial comparison between LIBS spectra of single crystal silicon captured at atmospheric pressure and at a pressure ~10^{-6} mbar indicates a remarkable difference in both resolution and intensity, as shown in Figure 5-1.

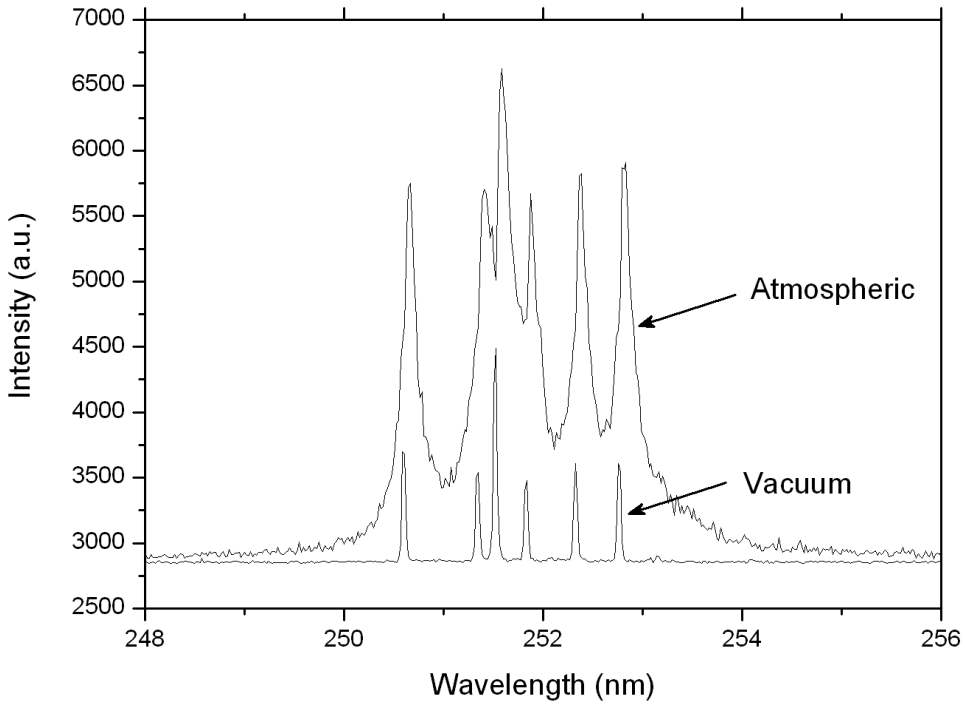

Figure 5-1 Comparison of LIBS spectra obtained from laser ablation of silicon at atmospheric pressure and under vacuum conditions.

If LIBS is conducted under vacuum conditions then the resolving power is greatly improved (Garcia et al. 2001) due to lack of pressure broadening effects. The peak intensity and the background continuum radiation are seen to diminish

due to plasma expansion (Harilal et al. 2003). Hardware optimised to produce usable spectra at atmospheric pressure no longer produces optimal spectra at lower pressures; although resolution has improved, the peak intensity has diminished. The usual method of optimising any experimental set up is to adjust one parameter at a time, keeping all others constant, until the optimum working conditions are found. Adjusting one experimental parameter at a time is necessarily time consuming, and may not reveal all interactions between the parameters. In order to fully describe the response and interactions of any complex system a multivariate parametric study must be conducted.

5.3 Response Surface Methodology

Response Surface Methodology (RSM) is a powerful statistical analysis technique which is well suited to modelling complex multivariate processes, in applications where a response is influenced by several variables and the objective is to optimise this response. Box and Wilson first introduced the theory of RSM in 1951 (Box and Wilson 1951), and RSM is today the most commonly used method of process optimisation (Bas and Boyaci 2007). Using RSM one may model and predict the effect of individual experimental parameters on a defined response output, as well as locating any interactions between the experimental parameters which otherwise may have been overlooked. RSM has been employed extensively in the field of engineering and manufacture where many parameters are involved in a process. Kwak applied RSM to the geometric error in surface grinding processes (Kwak 2005). Choudhury and El-Baradie applied factorial experimental design and RSM when conducting a machinability assessment of Inconel (Choudhury and El-Baradie 1999). Loh et al. used RSM

to optimise the finish in ball burnishing (Loh et al. 1990). Krajnik et al. designed grinding factors based on RSM analysis (Krajnik et al. 2005). RSM has been applied by Noordin et al. in describing the performance of coated carbide tools when turning steel (Noordin et al. 2004). RSM has been employed to optimisation of CNC drilling operations (Onwubolu and Kumar 2006) and in modelling the performance of asphalt pavements (Chavez-Valencia et al. 2005).

RSM is now used widely in such diverse fields as microbiology (Zurera-Cosano et al. 2006, Kalathenos et al. 1995), pharmacology (Belloto et al. 1985), vehicle crash-testing (Forsberg and Nilsson 2006) and food chemistry (Liyana-Pathirana and Shahidi 2005). RSM has been applied to the optimisation of laser welding (Olabi et al. 2006, Lee et al. 2006, Benyounis et al. 2005, Pan et al. 2005) and laser-cutting processes (Matthew et al. 1999), but never before to optimisation of LIBS hardware configuration.

In order to conduct any RSM analysis one must first design the experiment, identify the experimental parameters to adjust, and define the process response to be optimised. Once the experiment has been conducted and the recorded data tabulated, RSM analysis software models the data and attempts to fit a linear or second-order polynomial to this data.

5.3.1 Optimisation of the RSM Experiment

An un-optimised, multi-level full factorial experiment design requires that all possible combinations of the experimental parameters are considered. Increasing

the number of parameters and also the number of levels (the variance of each parameter) will increase the number of analyses required as:

$$(no.\ levels\ factor\ 1) \times (no.\ levels\ factor\ 2) \times \ldots (no.\ levels\ factor\ n) \quad (5.1)$$

The software package used in this RSM study was StatGraphics 5.1, which is a highly specified multivariate statistical analysis package. StatGraphics 5.1 provides the capability to optimise a designed experiment. Optimisation of an experimental design reduces the number of experimental runs required to model the response of a system, whilst retaining a comparable level of model accuracy. Algorithmic logic is used to estimate the minimum number of candidate runs required for the optimised design to adequately describe the system under investigation. The data obtained from the candidate runs is analysed in the same manner as in a full experimental design. The fewer candidate runs one conducts, the less accurately the optimised design models the response of the full design. D-optimality is a criterion calculated by the package and gives a measure of the variability of all the estimated parameters.

5.4 Experimental Set-up

The apparatus shown in Figure 5-2 was designed to be flexible and allow the LIBS analysis of solids, liquids and gases through a range of pressure regimes, from atmosphere down to $<10^{-6}$ mbar. The set-up includes a Nd:YAG laser (Continuum, Surelite), frequency doubled to produce an output at 532 nm, with a 4-6 ns pulse length and a peak energy of 200 mJ. The laser may be operated at repetition rates of up to 10 Hz, but for this investigation was limited to 1 Hz in

order to reduce the gas load on the vacuum pump set. Laser radiation was focused onto the sample using a 300 mm plano-convex glass lens mounted in a micrometer stage allowing positional adjustment along the axis of the laser beam of 30 mm either side of the focal position.

The sample was mounted in the vacuum chamber on an x-y stage such that each LIBS analysis was performed away from previous ablation sites. The laser was focused onto the material under test inside the vacuum chamber through a quartz window mounted in a CF carrier. A Leybold TurboVac 50 turbomolecular pump backed by a Leybold TriVac rotary pump was used to evacuate the chamber to pressures $<10^{-6}$mbar. A molecular sieve foreline trap was employed in order to reduce pump oil contamination back-streaming into the chamber. A schematic of this vacuum system is presented in Figure 5-3.

The main chamber is a stainless steel bell jar of approximate volume 21 litres, with an "L"-shaped elastomer gasket seal at the base. A Leybold TriVAC rotary pump is connected to the chamber via a length of convoluted tubing in order to pump down the chamber to a rough vacuum ($\sim10^{-3}$ mbar). This roughing pump may be isolated from the chamber by the roughing valve to prevent back-streaming when the turbo-molecular pump is in operation. Once a suitable rough vacuum has been obtained, the turbo pump may be turned on, reducing the system to a base pressure of $\sim10^{-6}$ mbar. The turbopump may be isolated from the chamber by a gate valve mounted above its inlet, allowing the pump to remain at full speed whilst the chamber is brought back to atmospheric pressure for sample changes.

Originally it was intended that the TriVAC roughing pump would also be used to back the turbo; however this dictated that the turbo would be momentarily un-backed whilst the chamber open to atmospheric pressure. This ordinarily would not pose a problem for a short period of time, but due to the large chamber volume, and subsequent lengthy pump-down time to reach a pressure suitable for the turbo to operate safely, this was decided against.

It was deemed necessary to introduce a second TriVAC rotary pump to the rig specifically to back the turbo. Using this pumping configuration the chamber may remain at atmospheric pressure indefinitely whilst the turbo remains at full speed operation, thus reducing pump-down time and the time taken for the turbo to spin-up to normal operation with each sample change.

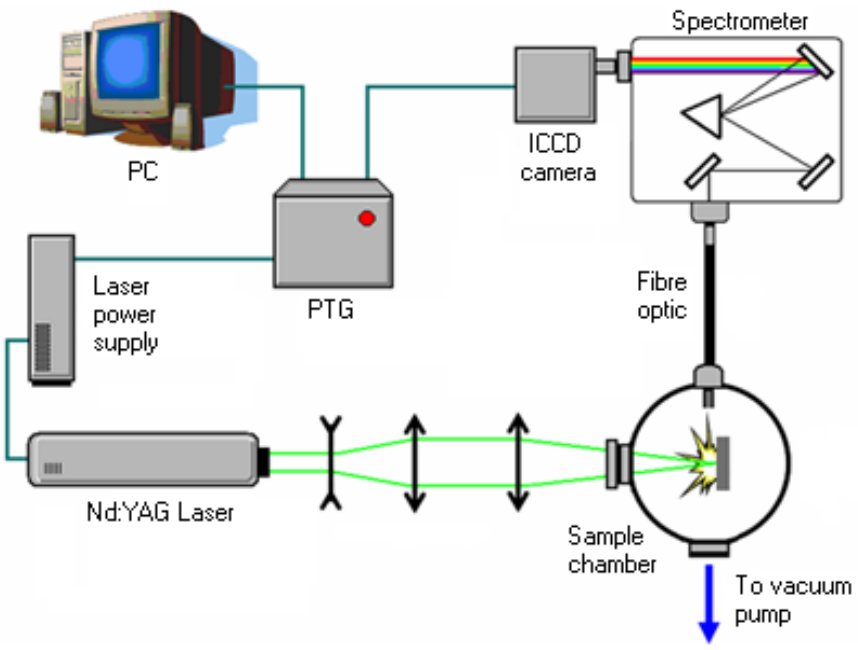

Figure 5-2 Schematic diagram of the LIBS apparatus

Optical emission from the plasma plume was collected through a two metre long fibre-optic cable, manufactured by Roper Scientific, with a wavelength transmission range of 190 to 1100 nm. The fibre-optic cable was inserted into the vacuum chamber using a specially designed, elastomer sealed feed-through, as described in Section 5.4.1., and was coupled to the same imaging spectrometer, ICCD camera and programmable timing generator described in Section 4.2.

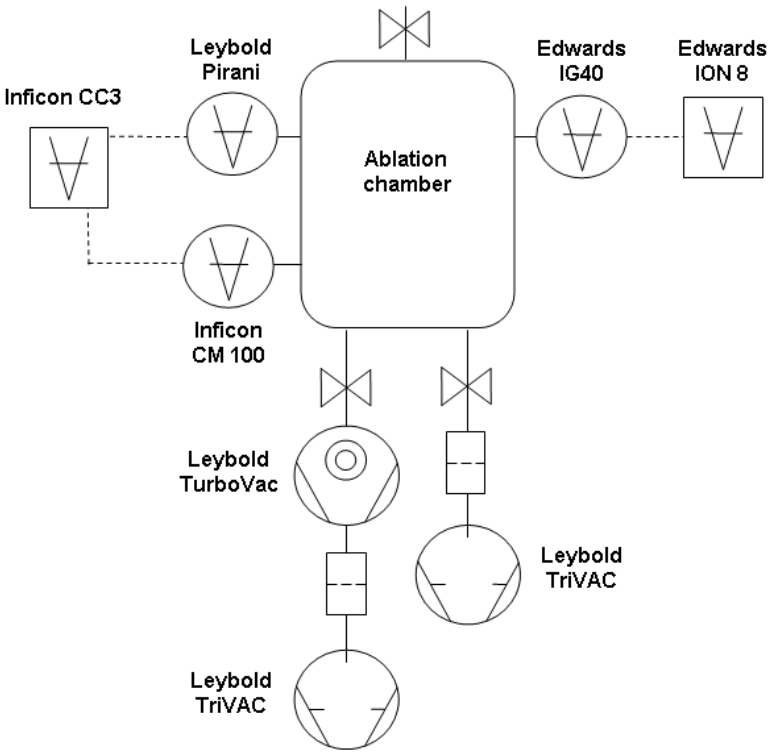

Figure 5-3 Schematic diagram of the ablation chamber vacuum apparatus

As before, the plasma imaging set-up allowed for temporal resolution of the plasma plumes, with the capacity to vary both the gate delay and integration times independently. Roper Scientific's WinSpec/32 spectrum capture and manipulation software enabled both capture of the dispersed plasma emission and identification of any prominent emission lines present.

Table 5-1 Spectroscopic constants of six selected neutral Si (I) emission lines used in the RSM study (CRC Press 1988)

Wavelength (nm)	A ($\times 10^8$ s^{-1})	g_k	E_k (cm^{-1})
250.690	0.4666	5	39955
251.611	1.21	5	39955
251.920	0.456	3	39760
252.411	1.81	1	39683
252.851	0.77	3	39760
253.238	0.26	3	54871

In this RSM study, standard semiconductor grade [111] silicon wafers were analysed. A single sample was used throughout this work and the optimisation process concerned only the silicon emission spectrum. Six Si (I) lines in the 250 - 253 nm wavelength range were monitored using the 2400 lines mm^{-1} grating; the spectroscopic constants for the emission lines analysed in this study are given in Table 5-1. Each data set was the accumulation of ten individual spectra.

5.4.1 Fibre-Optic Feed-through Design

In many vacuum applications light must be coupled through a vacuum envelope for purposes of viewing sample positioning, introducing laser light or analysing optical events occurring within a vacuum chamber etc. This is not always a straightforward affair as there are no commercially available feed-throughs capable of sealing a fibre-optic bundle that passes continuously through a vacuum chamber wall. The most common method employs a pure silica core that is welded into a specific flange with the fibre optic elements being coupled to either end. This is therefore not a true feed-through as the fibre bundle is not continuous through the vacuum envelope. These feed-throughs are difficult to

obtain, are generally expensive, suffer transmission losses (typically of the order 2 dB) and also limit the user to a specific wavelength range, as dictated by the optical properties of the construction materials.

Spectral analysis of the extremely low light levels produced by laser ablation events demands that the maximum possible flux is obtained with minimal transmission losses. In order to investigate LIBS under vacuum conditions, a fibre-optic feed-through must be used that: enables flexible positioning of the fibre collection head to maximise collection efficiency, is continuous ensuring no coupling interface transmission losses, and is also vacuum tight. After an extensive survey of commercially available feed-throughs it was apparent that there were none available that met the above criteria.

Abraham and Cornell describe a Teflon feed-through using a 3.2 mm Swagelok tube fitting connector suitable for UHV applications, but this design is limited to single fibres with diameters of 120 - 160 μm. When they tried to scale this design to a 12.7 mm (½ inch) tube fitting connector they were less successful (Abraham and Cornell 1998). Miller and Moshegov report the design and construction of an all-metal UHV optical fibre feed-through, found to be leak tight to 10^{-9}cm^3/min helium when repeatedly baked to 250°C (Miller and Moshegov 2001). This feed-through design uses unmodified Swagelok tube fitting connectors and is again only suitable for single fibres (400 μm diameter plus aluminium jacket). A machined aluminium plug replacing the forward ferrule of the compression fitting provides the vacuum seal.

Weiss and Stoever (Weiss and Stoever 1985) describe an o-ring and epoxy sealed feed-through for optical fibre bundles. Their design preserves fibre continuity, is deemed to be rugged enough for field use and is easy to construct, but is fairly destructive in that it requires a length of the fibre bundle cladding to be cut away. Testing of this design on a 10 mm diameter fibre bundle yielded a base pressure $\sim 10^{-4}$ mbar.

As there were no suitable feed-throughs in existence, such a device was designed, constructed and tested. The feed-through design was based on standard easily available 'tried and tested' components keeping in mind the design criteria as outlined above. The use of stock parts enabled the feed-through design to be easily tailored for a specific application. The feed-through was constructed using Swagelok Ultra-Torr fittings as shown in Figure 5-4. This simple and effective design used two 12.7 mm diameter unions, one 12.7 mm diameter convoluted tube of length 150 mm and a specially designed threaded aluminium plug (based on a standard fluid tube feed-through) which seals on the outer wall of the chamber with an elastomer o-ring and terminates in a 12.7 mm diameter nipple. All components were ultrasonically degreased in solvent at room temperature prior to assembly.

An Ultra-Torr union connects the aluminium plug to a 150 mm length of 12.7 mm diameter stainless steel convoluted tubing, and a second Ultra-Torr union terminates the convoluted tubing and seals around the end of the fibre-optic cable, shown expanded in Figure 5-5.

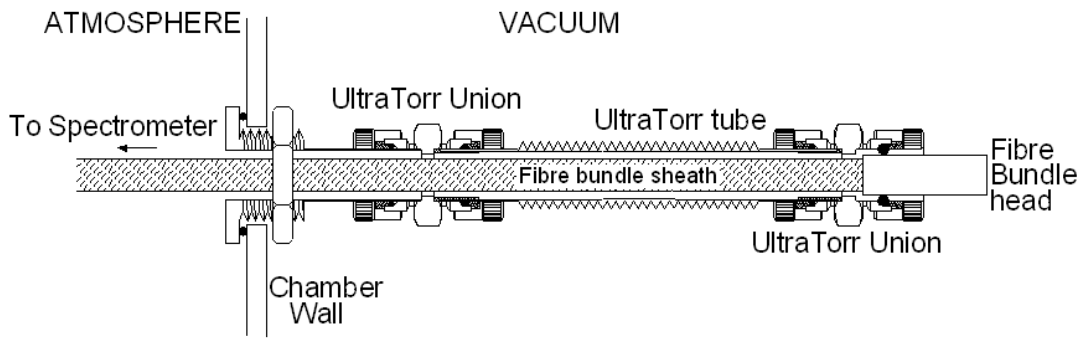

Figure 5-4 Schematic diagram of the fibre-optic feed-through, drawn to scale

The ends of the 12.7 mm convoluted tubing are reinforced with Ultra-Torr 12.7 mm XOA adapter cuffs. The fibres comprising the bundle are sealed in epoxy at the collection head, and the surface of the collection head potted in a protective epoxy coating; as such there is no gas permeation along the fibres or fibre cladding into the vacuum envelope. The Ultra-Torr unions are designed to accept 12.7 mm diameter tubing, whereas the outside diameter of the fibre-optic bundle head measures 10mm. In order to create a vacuum tight seal around the fibre-optic bundle head an o-ring of larger diameter than the stock Ultra-Torr o-ring was inserted; shown in Figure 5-5.

Use of convoluted tubing allows ease of manipulation of the fibre-optic and increases flexibility in accurately positioning the fibre-optic bundle to collect the maximum flux from laser-induced plasma plumes. Replacing the sealing elastomer o-rings with Viton o-rings would enable a gentle baking out of the chamber (maximum 200ºC) to attain base pressures ~10^{-8} mbar.

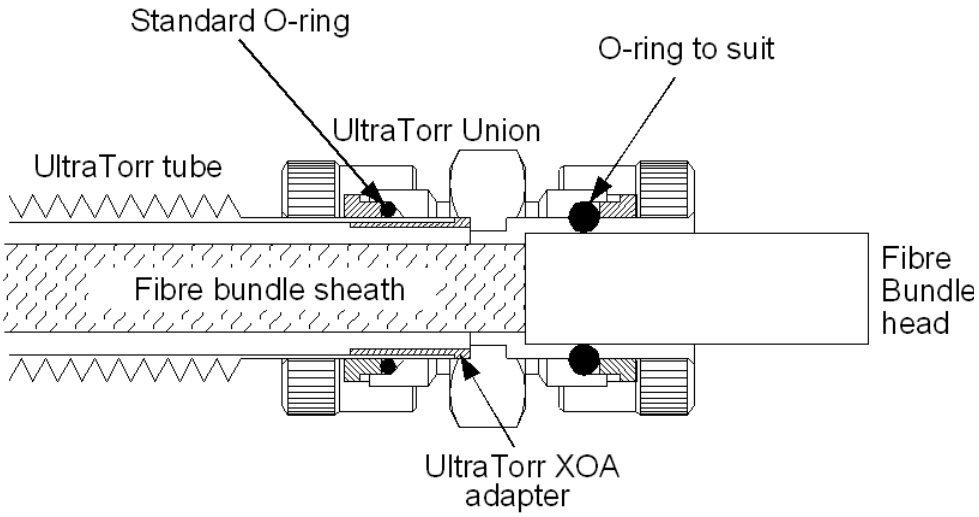

Figure 5-5 Interior view showing the collection end of the feed-through, drawn to scale

Figure 5-6 shows the constructed fibre-optic feed-through in position. The feed-through is secured through the base of the vacuum chamber and clamped in position; the collection end of the fibre-optic can be seen protruding through the clamp.

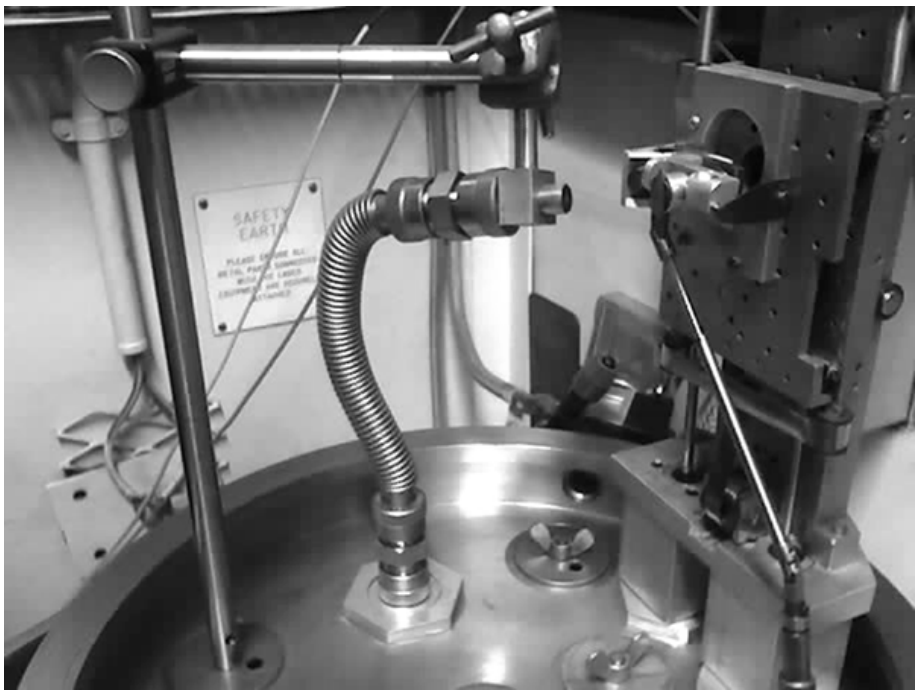

Figure 5-6 Photograph of the feed-through and fibre-optic in-situ

With the feed-through in place the pump-down time and ultimate base pressure of the vacuum chamber are unaltered. A residual gas analyser connected to the chamber was used to helium leak check the feed-through; no leak was found. An up-leak check of the vacuum chamber revealed no discernible change in leak rate with the introduction of the feed-through. The design of the feed-through proved to be extremely successful, enabling LIBS investigations at low pressures.

5.4.2 Analysis Software

This study used experiments that were designed and analysed solely with StatGraphics 5.1, which is a highly specified multivariate analysis package. Using StatGraphics one may design and optimise an experiment, and fit the subsequently gathered data to a first or second-order polynomial model. In order to simplify the analysis of any multivariate system, one must specify the response that is to be optimised. The ultimate aim of this study was to identify the parameters that would produce the best possible compromise of peak signal to background noise ratio, related to the peak resolution. In order to model these two factors as a single system response a Quality Factor (QF) was conceived and defined by Equation 5.2:

$$QF = \frac{net \quad signal}{delta \quad background} \times \frac{0.04}{FWHM} \tag{5.2}$$

where: *net signal* represents the maximum peak value minus the average background signal; *delta background* is the maximum background level minus the minimum background level (i.e. the spread/variance of the background

noise), FWHM is the full-width at half-maximum of the measured peak and 0.04 is the minimum FWHM measurable by the instrument in nm. These parameters are illustrated in Figure 5-7.

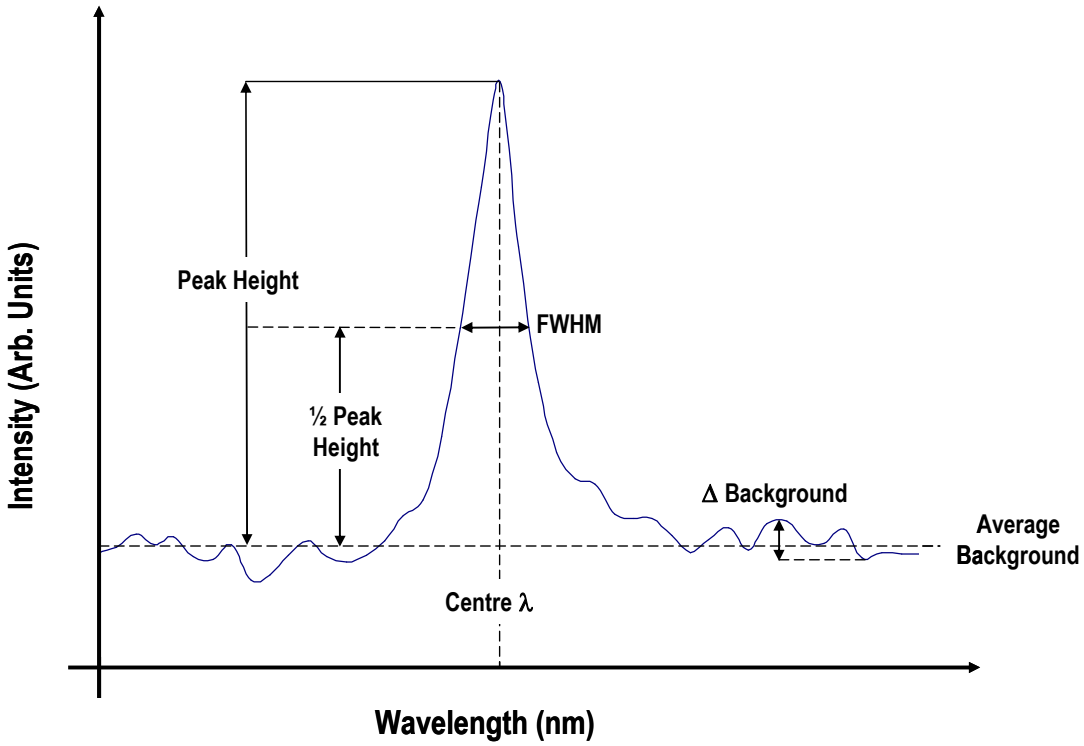

Figure 5-7 Spectral parameters relating to the definition of the Q-Factor

Under certain experimental conditions, i.e. very early gate delays, wide spectrometer input slit settings; the emission lines studied here were not individually resolvable due to peak broadening and their close wavelength proximity. As such, a Lorentz fit could not be successfully applied to all of the captured spectra for the purposes of calculating the peak FWHM. Instead, the FWHM were estimated by counting the number of CCD pixels each peak, or cluster of un-resolved neighbouring peaks, spanned at half maximum height. With each pixel equating to a wavelength resolution of 0.02 nm, the narrowest FWHM that the apparatus may resolve using this method is 0.04 nm, as stated in Equation 5.2.

Table 5-2 Factors and settings for RSM experiment

Factor	Settings			
gain	0	50	100	150
slit-width (μm)	20	70	120	-
lens position (mm)	-15	0	+15	-
gate width (ns)	200	466.67	733.33	1000
gate delay (ns)	100	500	900	1300
ambient pressure	1 (atm)	0 (~10^{-6}mbar)	-	-

The possible parameter settings chosen for this investigation, shown in Table 5-2, represent the *parameter space* of the RSM model. Initially a simple first-order screening experiment was conducted with a large parameter space in order to estimate an overall QF response. With the QF response estimated over a broad parameter space, finer parameter settings were then pinpointed. From initial screening experiments, the spectrometer gain, camera gate delay and gate width were deemed to have greatest impact on QF and as such set to four levels each for a more thorough investigation. The spectrometer input slit-width was varied over three levels: 20, 70 and 120 μm. Three positions of the lens, focusing the laser 15 mm in front of the sample (-15 mm), at the sample surface (0 mm) and 15 mm beneath the surface of the sample (+ 15 mm) were selected to model the general trend. It is well understood that the effect of varying lens position cannot be described by a simple linear or a second order function (Sattmann 1995) and therefore it is desirable to take measurements for a large number of lens positions. However; StatGraphics software has a limitation in the total number of variables that may be handled in any given experimental design, and it was therefore decided to take readings only for the three specified lens positions.

StatGraphics 5.1 demands that all input parameters possess numerical values; as such atmospheric pressure was signified by 1, vacuum conditions by 0 (relating to ~10^{-6} mbar). The finished un-optimised experiment design delivered a proposed 1152 experimental runs. To reduce this impractical number, the experiment design was divided into two. Splitting the design reduces the number of runs required, but necessarily limits the capacity to observe all interactions between all parameters. The parameters judged to have the greatest interactions were grouped together; one experimental design combined lens position, slit-width and gain (36 runs), and the second experimental design combined gate delay, gate width and ambient pressure (32 runs). The run order of both designs was randomised to reduce the effect of any lurking variables such as ambient temperature, humidity, laser power fluctuation etc. Both designed experiments were performed twice to increase accuracy. Initially net signal and FWHM were considered as separate responses before ultimately being combined into the QF to fully describe the response of the LIBS apparatus.

5.5 Results and Discussion

5.5.1 Estimated Response Surfaces- FWHM

Figures 5-8 and 5-9 show the estimated response surfaces generated for FWHM whilst varying spectrometer input slit-width, lens position and gain at atmospheric pressure. Figure 5-8 shows the predicted effects of varying lens position and slit-width at a constant gain of 75; it can be seen that there is a maximum value of FWHM with the lens position focusing the laser at the sample surface, and that FWHM appears to increase linearly with slit-width.

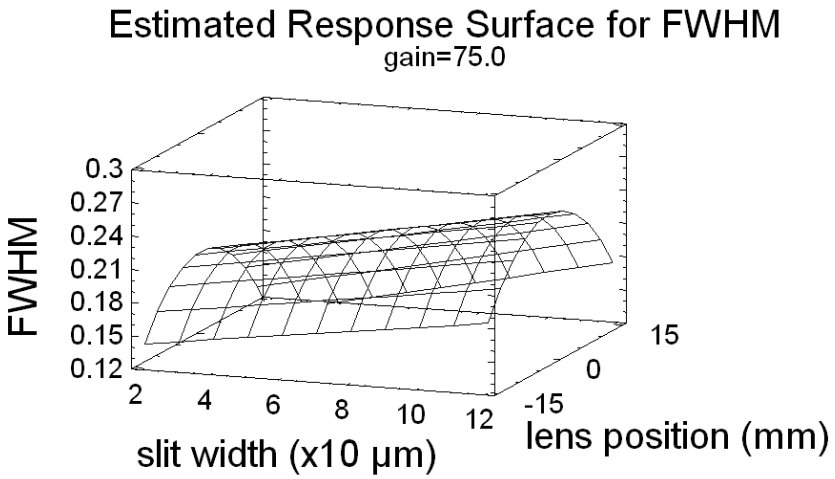

Figure 5-8 Estimated response surface for FWHM varying slit-width and lens position at atmospheric pressure

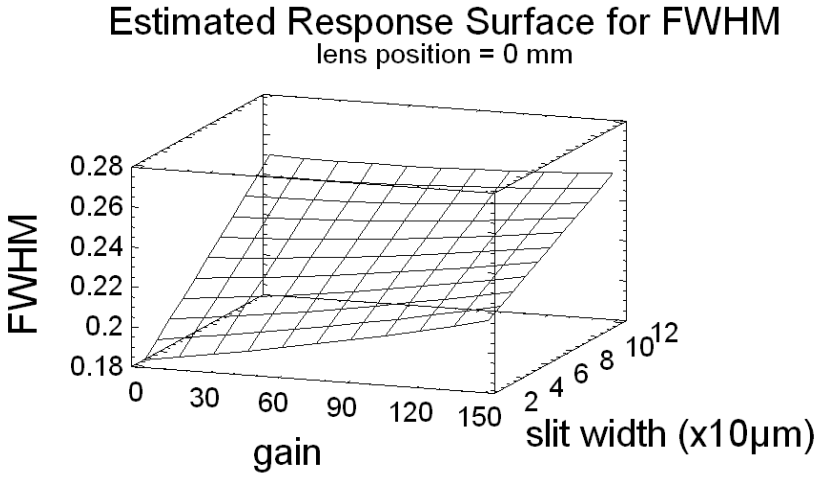

Figure 5-9 Estimated response surface for FWHM varying slit-width and gain at atmospheric pressure

Figure 5-9 shows the effects of varying gain and slit-width at a constant lens position of 0 (focussed at the sample surface); it can be seen that the FWHM increases linearly with both gain and slit-width. If the major concern regarding spectra capture is to minimise FWHM, thus improving resolution, then Figures

5-8 and 5-9 suggest that LIBS analysis should be conducted at low gain, with small slit-width and focusing the laser either in front of or beneath the surface of the sample.

5.5.2 Estimated Response Surfaces- Net Signal

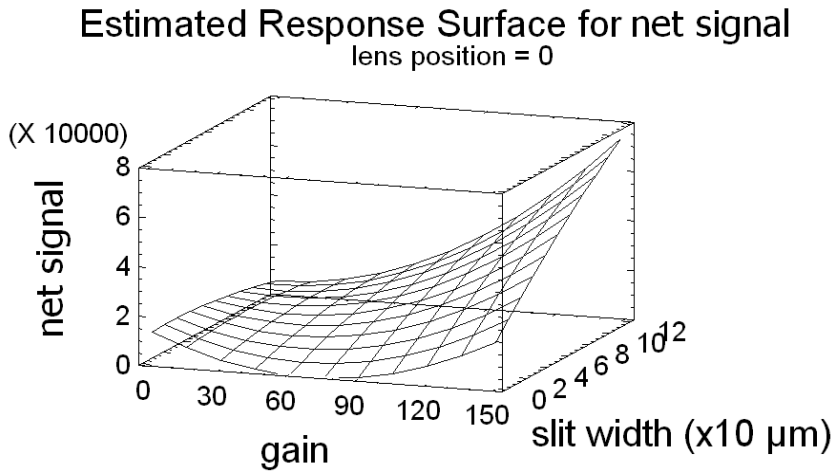

Figure 5-10 Estimated response surface for net signal varying gain and slit-width at atmospheric pressure

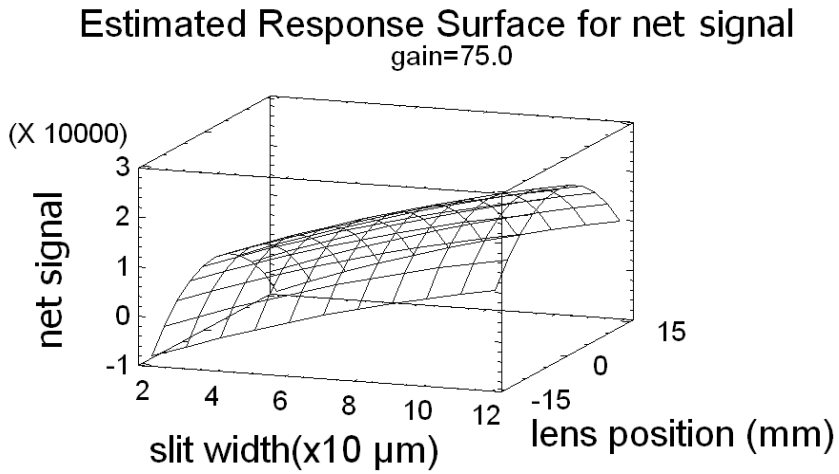

Figure 5-11 Estimated response surface for net signal varying slit-width and lens position at atmospheric pressure

Figures 5-10 and 5-11 display the estimated response surfaces generated for net signal whilst varying spectrometer input slit-width, lens position and gain at atmospheric pressure.

Figure 5-10 predicts the effects of varying lens position and slit-width at a constant gain of 75; it can be seen that 0 is the optimal lens position producing maximum net signal, and that net signal increases linearly with slit-width. Figure 5-11 shows the effects of varying gain and slit-width at a constant lens position of 0; net signal intensity again appears to increase linearly with slit-width.

Net signal appears to vary as a quadratic term with gain. This is not actually the case as the emission line intensity increases exponentially with gain. The erroneous shape of the estimated response surface is due to the fact that StatGraphics is only capable of fitting a first or second order polynomial to the data set. To verify this exponential trend, net signal versus gain was plotted manually at slit-widths of 20, 70 and 120 μm, as shown in Figure 5-12.

Each data point in Figure 5-12 is the average of three readings. An exponential fit to each line has an R-squared value of 0.99; therefore the effect of increasing gain on net signal definitely follows an exponential trend, not a quadratic as implied by StatGraphics. The erroneous shape of the estimated response surface generated in Figure 5-11 warns caution when analysing surface plots, although it does indicate the general trend of an increase of net signal with gain.

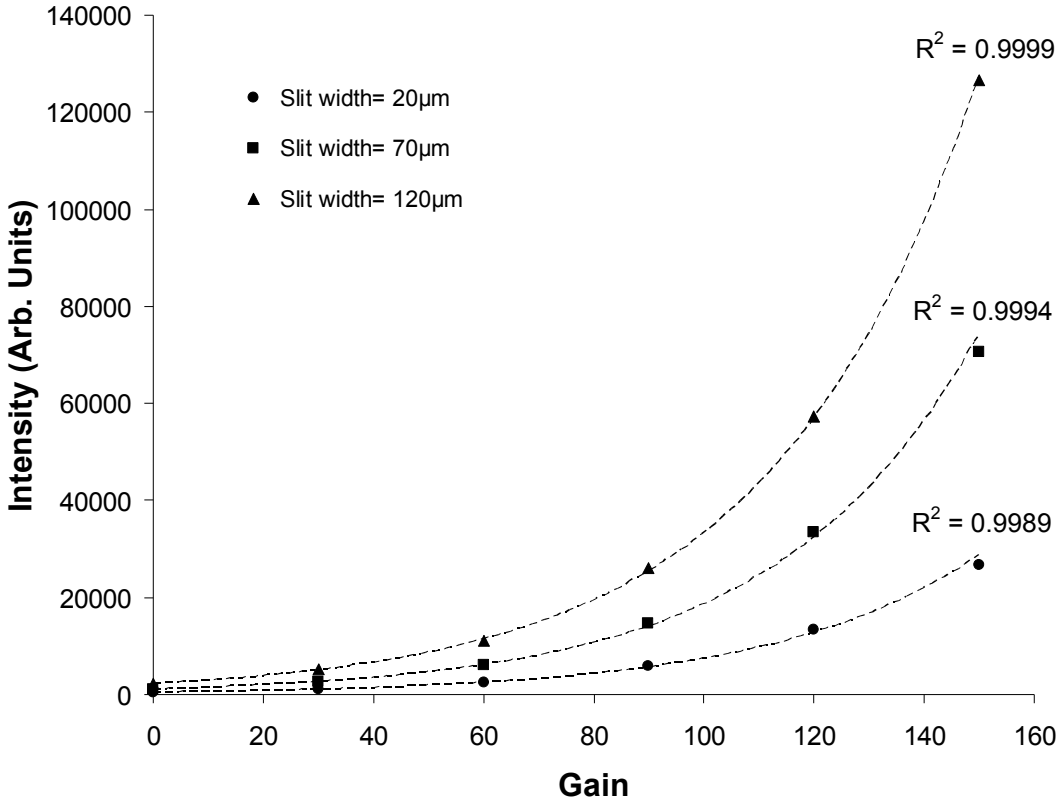

Figure 5-12 Plot to verify RSM model accuracy: measured peak intensity versus gain for spectrometer input slit widths of 20, 70 and 120 µm

Figures 5-10 and 5-11 indicate that if the primary concern regarding spectrum capture is to maximise net signal, and therefore sensitivity, then LIBS analyses should be conducted with high gain, a large slit-width and the laser focused at the surface of the target material.

5.5.3 Estimated Response Surfaces- QF

The two separate responses of net signal and FWHM were combined into the single response of QF, as defined in Equation 5.2. Figures 5-13 and 5-14 show the estimated response surfaces generated for QF whilst varying spectrometer input slit-width, lens position and spectrometer gain at atmospheric pressure.

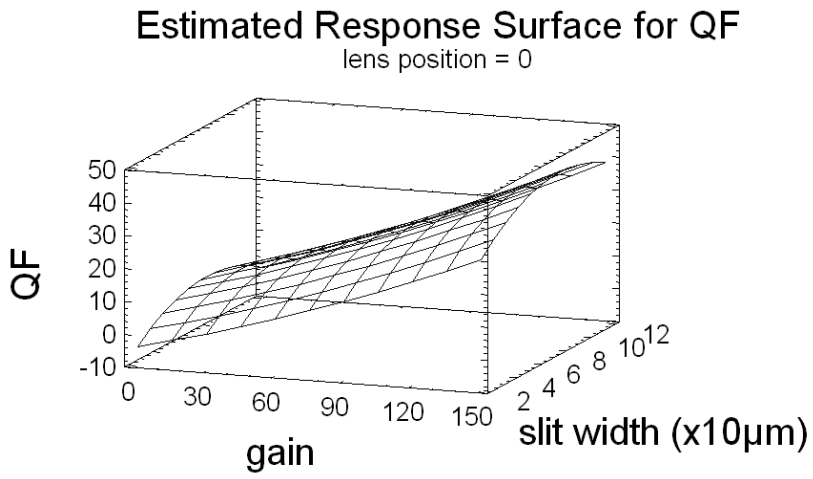

Figure 5-13 Estimated response surface for QF varying slit-width and gain at atmospheric pressure

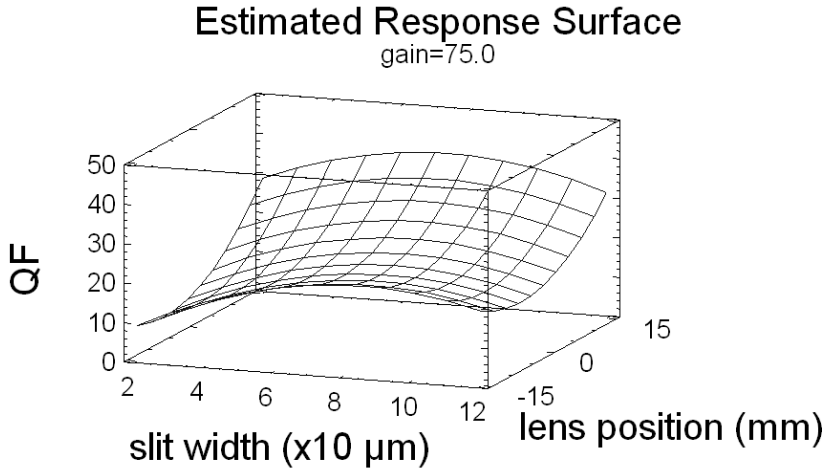

Figure 5-14 Estimated response surface for QF varying slit-width and lens position at atmospheric pressure

Figure 5-13 shows the effect of varying slit-width and gain at a constant lens position of 0, indicating that there is an optimum slit-width at around 90 µm, and that QF increases linearly with gain. Figure 5-14 shows the effect of varying slit-width and lens position at a constant gain of 75, indicating again an optimum slit-

width of 9 µm, and also that QF is optimised at the extremes of lens position, +15 mm and -15 mm. According to the StatGraphics RSM model, if one desires to optimise the LIBS hardware to maximise QF at atmospheric pressure, then LIBS analyses should be conducted at high gain, with a slit-width of 90 µm, and by placing the lens at either of its extreme positions.

5.5.4 Estimated Response Surface- Optimised Experiment

To determine how accurately an optimised experimental design represents the full design, experiment 1 (combining slit-width, lens position and gain with QF as the output response) was optimised and performed again. The original full design required 36 runs (72 with repeat), the optimised design was reduced to 12 runs with a D-optimality of 48.13%.

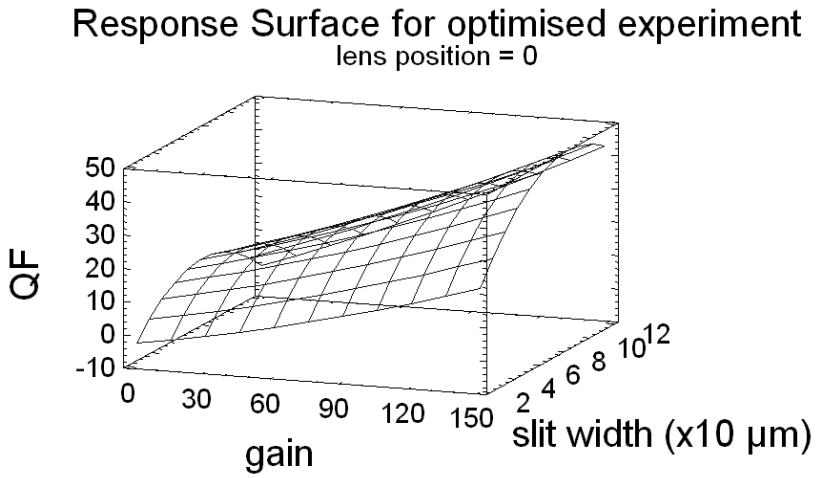

Figure 5-15 Response surface for optimised experiment QF varying slit-width and gain at atmospheric pressure

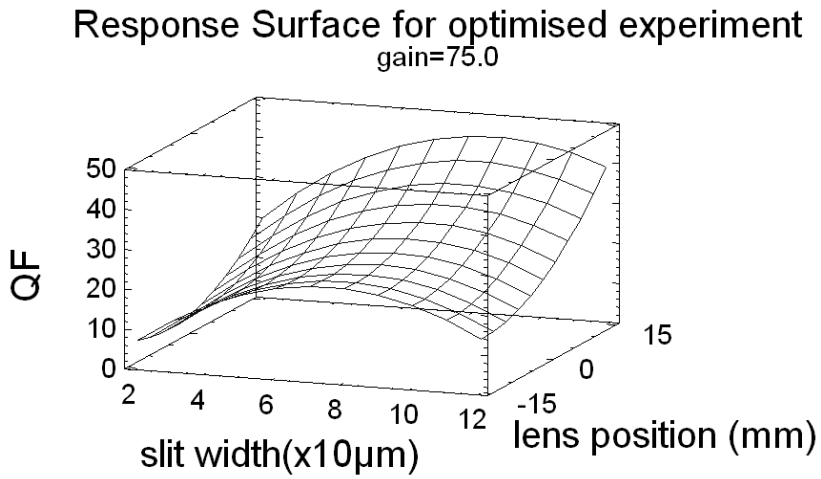

Figure 5-16 Response surface for optimised experiment QF varying slit-width and lens position at atmospheric pressure

The estimated response surfaces generated are shown in Figures 5-15 and 5-16, which may be compared with those generated from the full design in Figure 5-13 and Figure 5-14. It can be seen that although the optimised design estimated response surface does not match exactly that of the full design, the general trend of the QF response is remarkably similar. It appears that optimising an experiment design yields great advantages in terms of the time and effort saved, whilst still maintaining an acceptable level of accuracy in the model.

5.5.5 Comparison of QF Responses

The optimisation of a full experiment design for LIBS at atmospheric pressure has been shown to provide an accurate model of the system; consequently experiment 2 was optimised to reduce the number of runs. Further to this, the experiment was augmented to include a more thorough investigation of five slit-

width settings. The revised parameter space for experiment 2 is shown in Table 5-3.

Table 5-3 Augmented parameter space for experiment 2.

Factor	Setting				
Slit-width (μm)	20.0	80.0	140.0	180.0	260.0
Lens position (mm)	-15	0	+15	-	-
Gate width (ns)	200	466.67	733.33	1000	-
Gate delay (ns)	100	500	900	1300	-

The augmented full design of experiment 2 required 188 (no repeat) runs and was subsequently optimised to 20 candidate runs with a D-optimality of 44.87%. Experiment 2 was performed at atmospheric pressure and also under vacuum conditions; the estimated response surfaces for QF are shown in Figures 5-17 and 5-18 respectively.

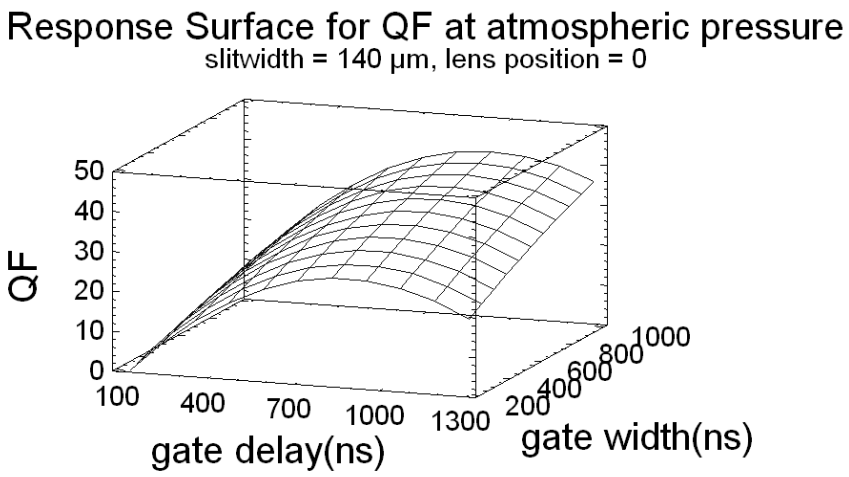

Figure 5-17 Estimated response surface for QF varying gate delay, gate width, lens position and slit-width at atmospheric pressure

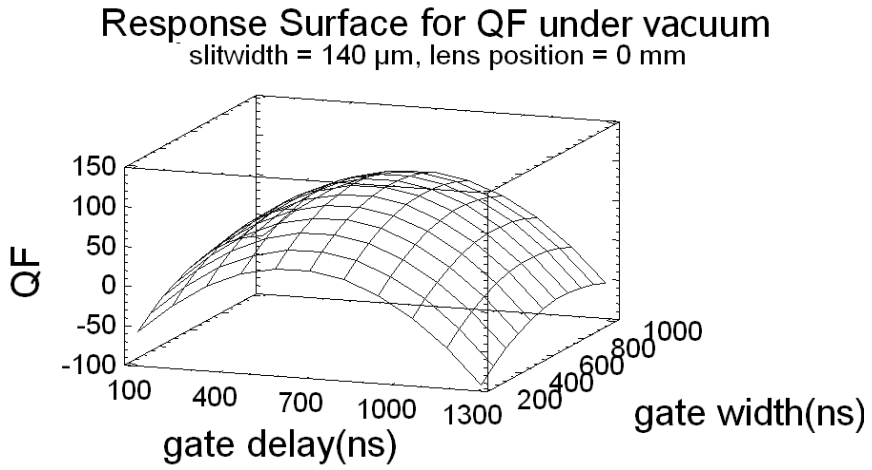

Figure 5-18 Estimated response surface for QF varying gate delay, gate width, lens position and slit-width under vacuum

Figures 5-17 and 5-18 reveal the difference in the response of QF for LIBS conducted at atmospheric pressure when compared to that obtained under vacuum conditions. Figure 5-17 shows the estimated response surface for QF at atmospheric pressure whilst varying gate width, gate delay, slit-width and lens position. It can be seen that QF increases linearly with gate width. The estimated QF response varies as a quadratic term versus gate delay with a maximum value corresponding to a gate delay ~ 900 ns.

Figure 5-18 presents the estimated QF response for vacuum conditions whilst varying gate width, gate delay, slit-width and lens position. It can be seen that the estimated QF displays different behaviour from that presented in Figure 5-17. The QF varies as a quadratic term with respect to gate delay, with a maximum value at gate delay ~ 500 ns. The estimated QF varies as a quadratic function of gate width, displaying a maximum value at gate width ~ 800 ns.

Tables 5-4 and 5-5 show the lowest and highest values assigned to each parameter, under atmospheric pressure and vacuum conditions respectively, used to generate the estimated response surfaces given in Figures 5-17 and 5-18. The optimum values stated are those that StatGraphics predicts will maximise the QF value. When comparing the two sets of results it can be seen that the only parameter that has the same optimum setting is the lens position. All the other optimum parameter settings reveal a unique set of conditions for atmospheric pressure LIBS compared to those under vacuum for maximised QF. Where the optimum value is equal to the high or low setting then the parameter space may not have been sufficiently large enough to locate the true optimum value.

Table 5-4 Optimised response: QF at atmospheric pressure

Factor	Low	High	Optimum
Slit-width (μm)	20.0	260.0	260.0
Lens position (mm)	-15.0	15.0	14.8
Gate delay (ns)	100.0	1300.0	952.9
Gate width (ns)	200.0	1000.0	1000.0

Optimum QF value = 53.7069

Table 5-5 Optimised response: QF under vacuum

Factor	Low	High	Optimum
Slit-width (μm)	20.0	260.0	20.0
Lens position (mm)	-15.0	15.0	15.0
Gate delay (ns)	100.0	1300.0	576.5
Gate width (ns)	200.0	1000.0	745.7

Optimum QF value = 262.32

5.5.6 Summary of the RSM Study Results

Figure 5-19 shows the optimum parameter settings for maximising QF, and the maximum value for the QF, at atmospheric pressure and under vacuum conditions as indicated by StatGraphics. The maximum QF value is seen to be much higher for LIBS conducted under vacuum conditions (262.32) than that obtained for atmospheric pressure LIBS (53.71). Using the definition of QF as given in Equation 5.2, it is predicted that spectra with the highest sensitivity and resolution should be observed when performing LIBS under vacuum conditions and this has been verified experimentally.

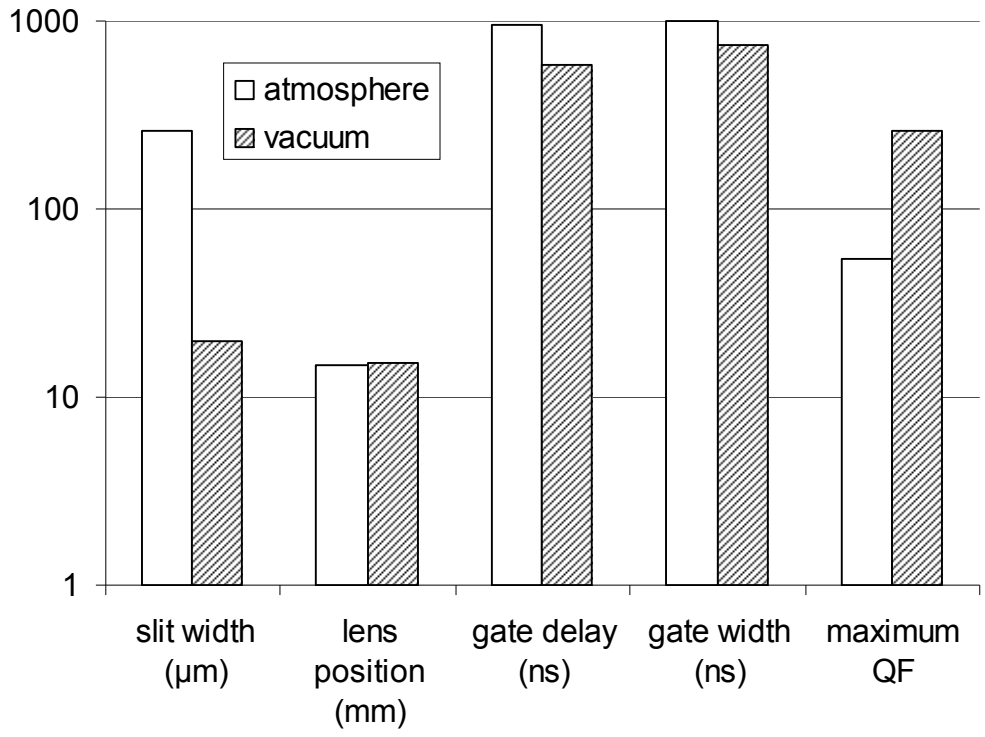

Figure 5-19 Comparison of the optimum settings for vacuum and atmospheric pressure LIBS of silicon, as predicted by the RSM study

Pareto charts generated by StatGraphics were used to graphically summarise and display the relative importance of each parameter with respect to the overall QF

response at both atmospheric pressure and under vacuum conditions. The Pareto charts show all the linear and second order effects of the parameters within the model and estimate the significance of each with respect to maximising the QF response. A Pareto chart displays a frequency histogram with the length of each bar proportional to each estimated standardised effect. The vertical line on the Pareto charts judges whether each effect is statistically significant within the generated response surface model; bars that extend beyond this line represent effects that are statistically significant at a 95% confidence level.

The results obtained under atmospheric conditions, shown in Figure 5-20, predict that there are 4 significant parameters at a 95% confidence level: the linear gate delay; the linear gate width; a negative second order lens position and a linear lens position. These are the major terms in a polynomial fit to the data. The R-Squared statistic indicates that this model as fitted explains 92.78% of the variability in QF.

The results obtained under vacuum conditions, shown in Figure 5-21 predict that there are now only 2 significant parameters with a 95% confidence level: a negative second order gate delay and a negative linear slit-width. The R-Squared statistic indicates that this model as fitted explains 81.23% of the variability in QF.

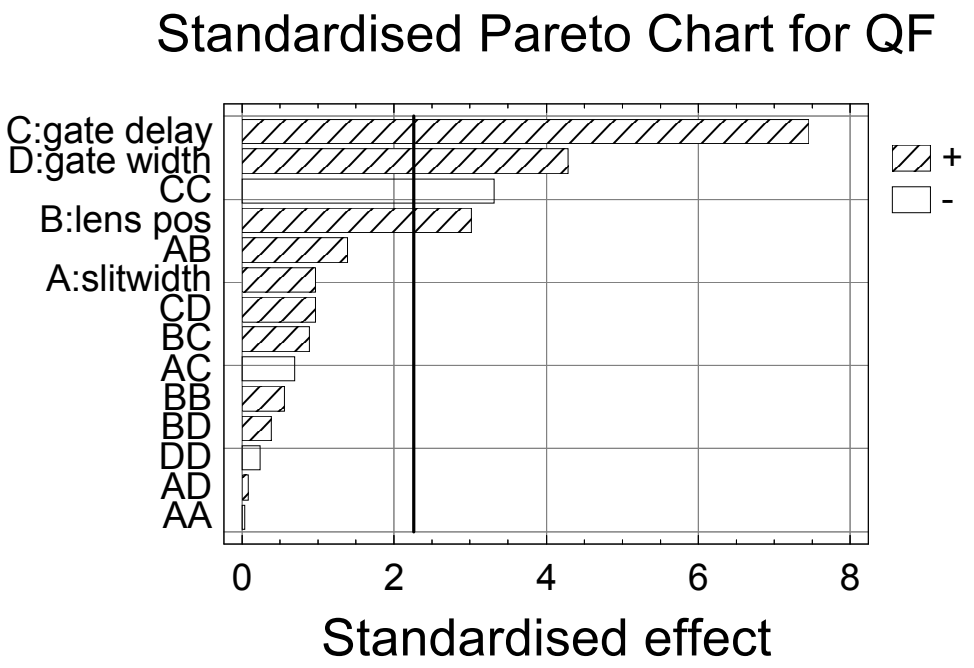

Figure 5-20 Pareto chart for QF response at atmospheric pressure

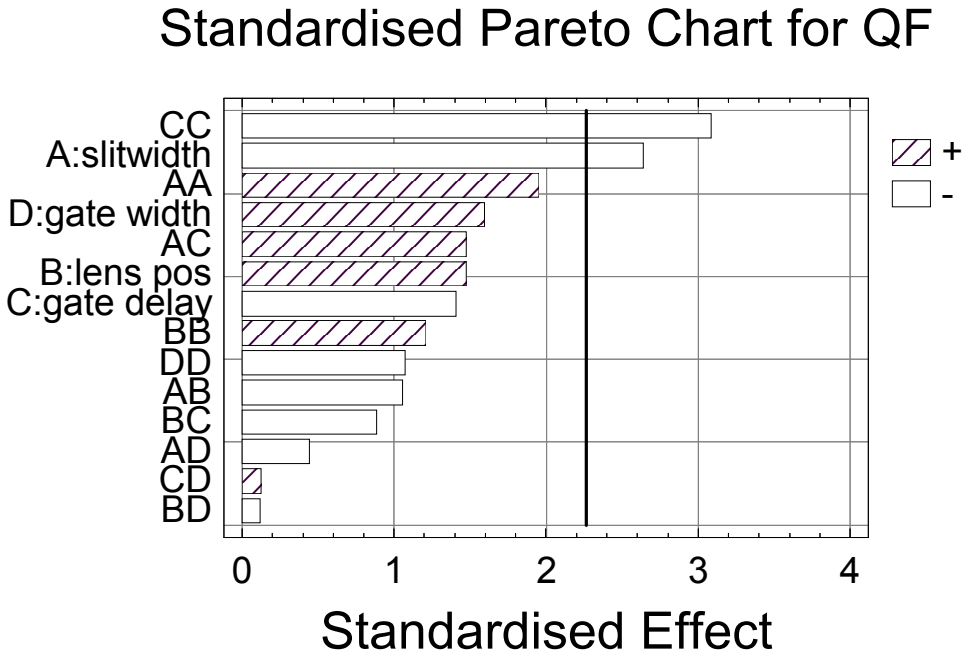

Figure 5-21 Pareto chart for QF response under vacuum

5.6 Manual Optimisation of the LIBS Hardware

Verification of the accuracy of the RSM model was required in order to validate the RSM technique. LIBS spectra of silicon were captured at atmospheric pressure and under vacuum employing the hardware settings that the RSM model suggested should yield the optimum QF. Ten spectra were analysed for QF, and from these an average QF value taken; these average measured values were compared to those predicted by the RSM analysis, as listed in Table 5-6.

Table 5-6 Comparison of RSM -predicted optimal QF, and actual QF as measured at settings suggested by RSM analysis

	Atmosphere	Vacuum
Predicted QF from RSM study:	53.71	262.32
Measured QF at suggested RSM settings:	23.68	750.43

It is evident from Table 5-6 that the RSM analysis does not accurately predict the actual values for the QF responses of the system, although it does predict that the higher QF should be achieved under vacuum, which is indeed the case. To determine the true response of the LIBS apparatus a full parametric investigation of the hardware configuration was performed 'manually'- that is, each individual hardware parameter was adjusted one at a time keeping all others constant. Although a laborious task, this manual investigation of the LIBS system was necessary to validate or refute the accuracy of the RSM model. As in the RSM model, the QF response was monitored whilst independently varying capture delay, integration width, spectrometer input slit-width and focussing lens position. The ICCD gain was set to the maximum used in the RSM study, 150, as higher QF values were observed at higher gain settings for both atmospheric

pressure and vacuum conditions. Setting the ICCD gain to this constant value reduced the number of experimental runs required. The parameter space of the investigation was expanded to be certain of encompassing the optimum values for each parameter, as shown in Table 5-7.

Table 5-7 Parameter space for the manual parametric investigation

Parameter	Range
Gate delay	100 → 2900 ns
Gate width	100 → 2900 ns
Lens position	-20 → + 28 mm
Slit-width	10 → 250 μm
Gain	150

5.7 Manual Optimisation of Gate Delay and Width

Gate delay and gate width were deemed to have the greatest effect on QF and as such were investigated first. Following an initial screening experiment, it was determined that the gate delay and width would each be swept through a range of 100 – 2900 ns, in 200 ns increments. The spectrometer input slit was set to 120 μm, the lens position was set to +15 mm, and the ICCD gain to 150. The repetition rate of the laser was 1 Hz as in the RSM investigation. Each data set was again the accumulation of 10 individual spectra, and each point plotted on the following contour plots is the average of three data sets. As in the RSM investigation 'atmosphere' shall refer to atmospheric pressure and 'vacuum' to an ambient pressure of ~ 10^{-6} mbar. Each contour plot was normalised so as to contain 40 gradient intensity levels evenly spaced between the maximum and minimum values for that given plot. To fully describe the response of the LIBS system QF, Net Signal, FWHM, Average Background and Delta Background (as

defined in Section 5.2.3) were all individually investigated and their contributions to the ultimate QF noted.

5.7.1 Atmospheric Pressure: QF

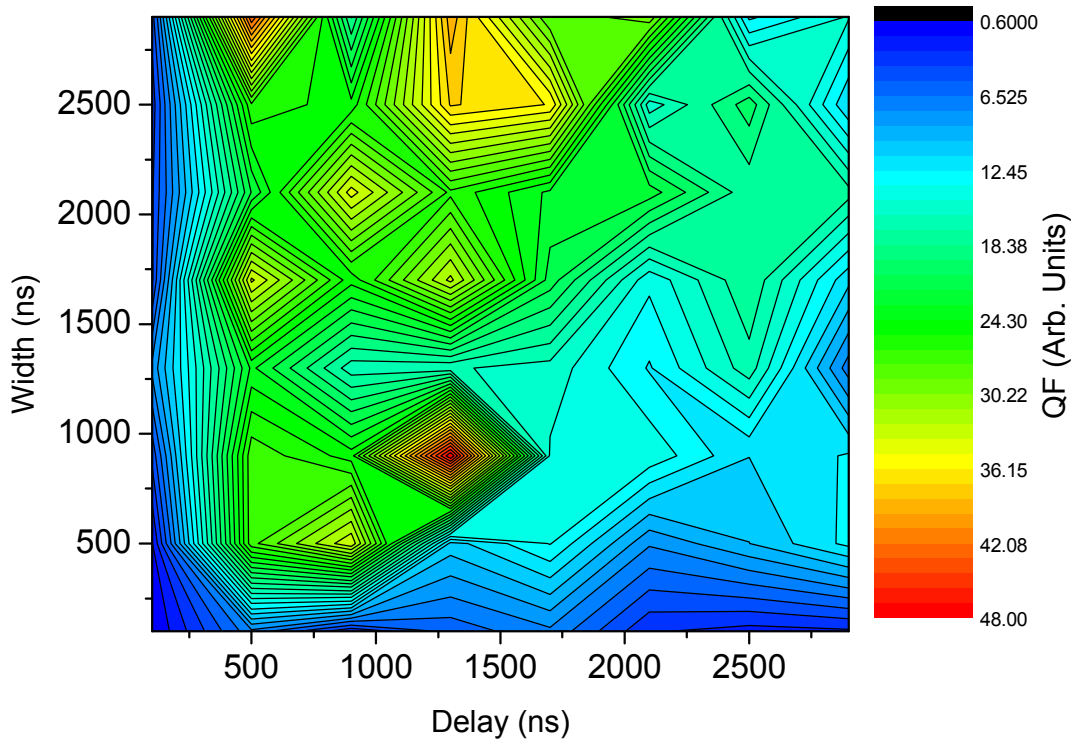

Figure 5-22 QF as a function of gate delay and width: atmospheric pressure

Figure 5-22 shows the variation in QF as measured manually at atmospheric pressure. Even though each data point on the contour plot is the average of three data-sets, in effect an average of 30 individual spectra, the plot is clearly very noisy. There is a large 'plateau' of delay versus width values that appear to yield comparable QF values approximately in the range of 20 to 30, with a maximum QF value of 47.92 observed at a delay of ~ 1300 ns and a width of ~ 900 ns. For delay values shorter than 500 ns the QF is seen to diminish rapidly, due to the

dominance of the continuum radiation over line emission during the early stages of plume evolution.

5.7.2 Atmospheric Pressure: Net Signal

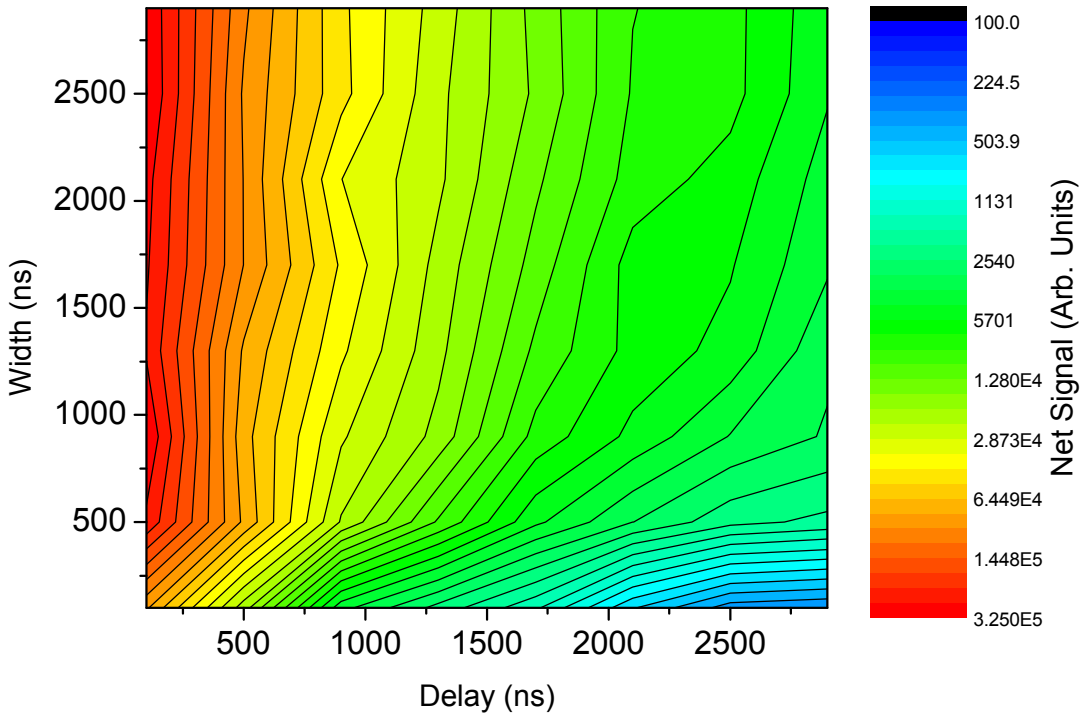

Figure 5-23 Net signal as a function of gate delay and width: atmospheric pressure

Figure 5-23 is a contour plot of net signal intensity as a function of gate delay and width. Due to the large range of net signal values recorded over the parameter space of this experiment, varying from ~100 to 30 000 counts, Figure 5-23 is plotted with a logarithmic net signal scale. It is evident that the intensity of the silicon emission spectra is greatest at earlier delay times, as one would expect to be the case. Net signal increases with longer gate widths due to the collection of more optical emission during the increased integration time. At

delay times greater than ~1000 ns there is a stable plateau region where the net signal intensity is observed to remain more or less constant.

5.7.3 Atmospheric Pressure: FWHM

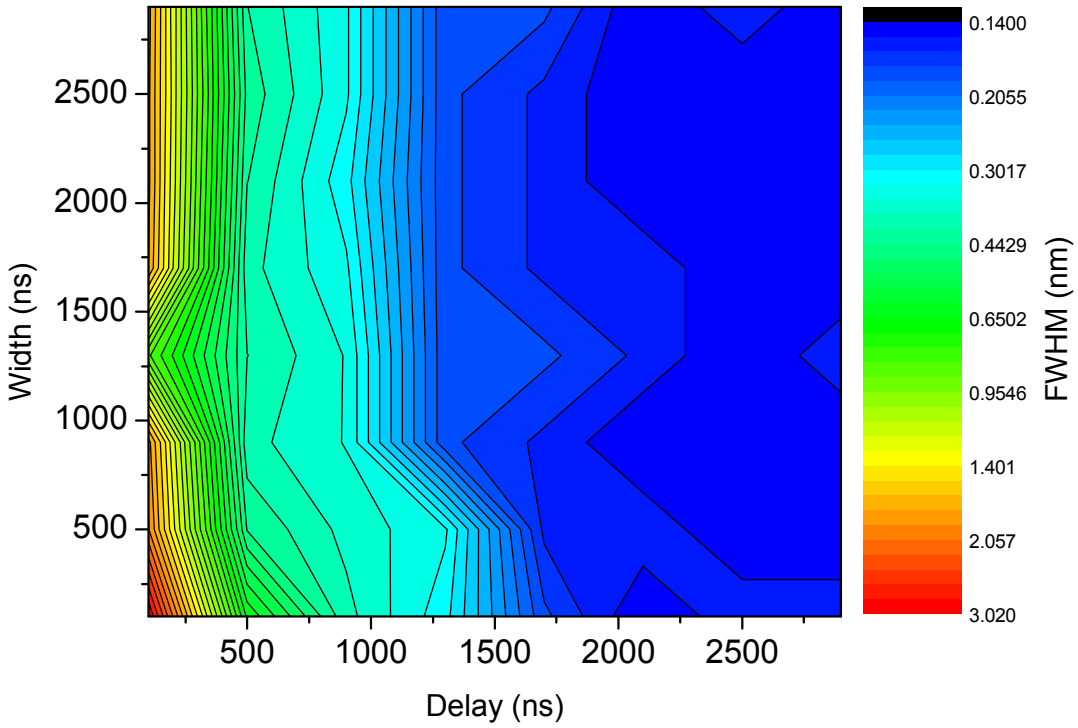

Figure 5-24 FWHM as a function of gate delay and width: atmospheric pressure

Figure 5-24 displays the dependence of emission line FWHM on gate delay and width at atmospheric pressure. The maximum FWHM is evident at delays less than 100 ns, because of the increased plasma continuum contribution to the emission spectra in the early phases of plasma expansion, and Stark pressure broadening of the silicon emission lines. The FWHM diminishes with increasing delay time as the plasma continuum radiation is not integrated into these spectra, and electron-ion recombination events have diminished the electron density of the plasmas, thus reducing Stark line shape broadening.

5.7.4 Atmospheric Pressure: Average Background

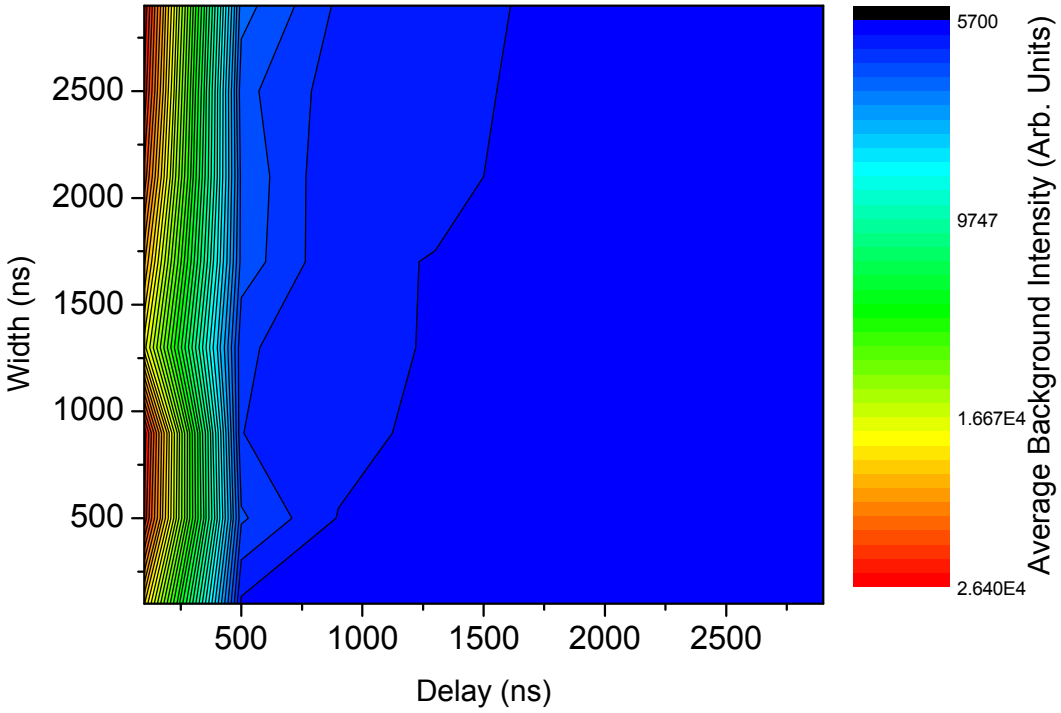

Figure 5-25 Average background level as a function of gate delay and width: atmospheric pressure

Figure 5-25 is a contour plot of the Average Background signals obtained when varying gate delay and width. The background decreases rapidly in the first 500 ns of plasma formation and expansion, falling to a fairly constant level from then onwards. There is a slight increase in background with increasing gate width due to the longer integration time, with a subsequently greater contribution from the ICCD dark charge and stray ambient light leakage. The prominent feature revealed by Figure 5-25 is the lack of change in background level with increasing delay beyond ~ 500 ns. If one wishes to decrease the background to its minimum achievable threshold, it is necessary only to delay spectrum capture until later than ~ 500 ns, thus potentially retaining important spectral data regarding the earlier stages of the plume evolution.

5.7.5 Atmospheric Pressure: Delta Background

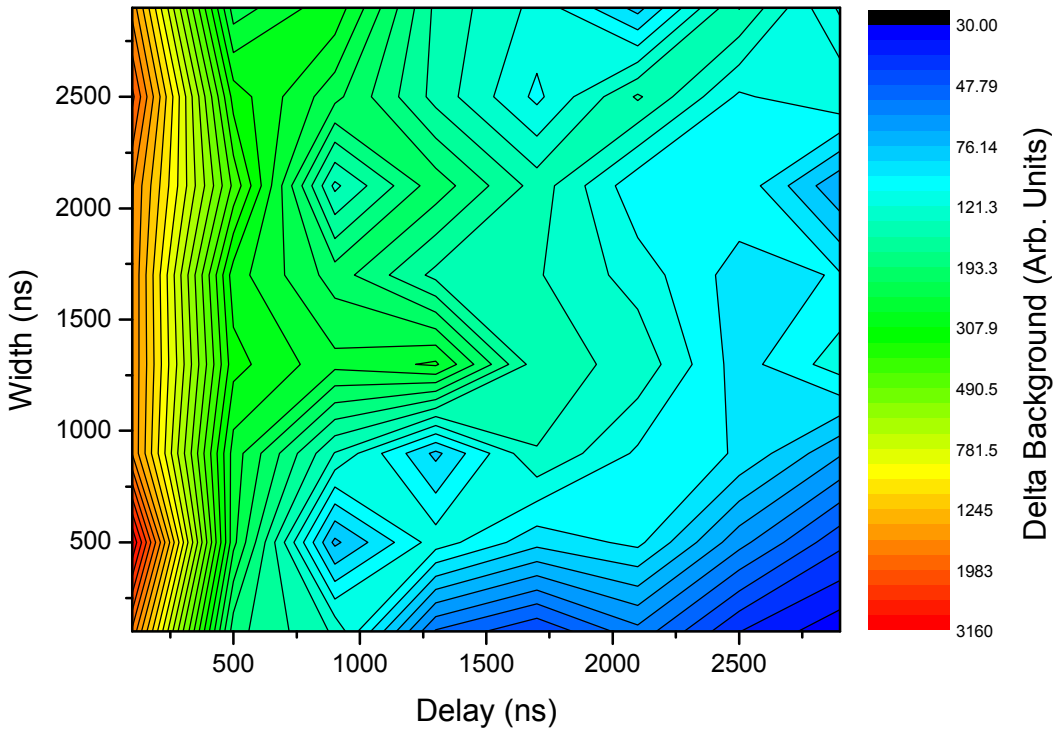

Figure 5-26 Delta background as a function of gate delay and width: atmospheric pressure

Figure 5-26 shows the background variance response, Delta Background, as a function of gate delay and width. There is a large Delta Background value at early delays of less than 100 ns due to the increased contribution from the plasma continuum emission. As the plasma continuum emission level decreases with delay, so too does the Delta Background level. The lowest Delta Background values are obtained for longer delay times and short integration times. If one wishes primarily to reduce the background noise spread when conducting LIBS analyses under the conditions of this particular study, then Figure 5-26 indicates that spectrum capture should be delayed as late as possible after plasma formation.

5.7.6 Vacuum: QF

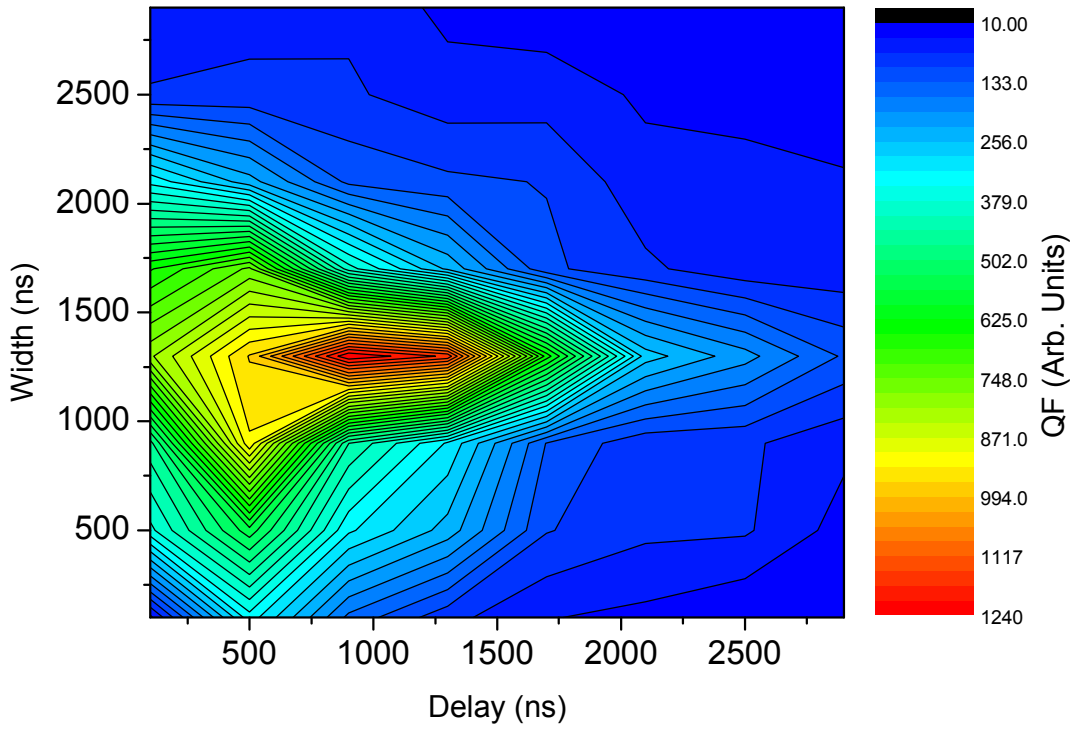

Figure 5-27 QF as a function of gate delay and width: vacuum

Figure 5-27 illustrates the variance in QF versus gate delay and width under vacuum, and clearly shows a dramatically different response to the QF behaviour recorded at atmospheric pressure as displayed in Figure 5-22. In general the QF response is less noisy under vacuum conditions than at atmospheric pressure, and it is evident that there is a much smaller range of delay and width values where a high QF value may be obtained. The maximum QF of 1238 is achieved with a gate delay of approximately 900 ns and a gate width of approximately 1300 ns. Outside of the small range of high QF values the response is very low, on account of the free plasma expansion under vacuum conditions and the correspondingly lower emission intensity in the latter stages of plume evolution under vacuum.

5.7.7 Vacuum: Net Signal

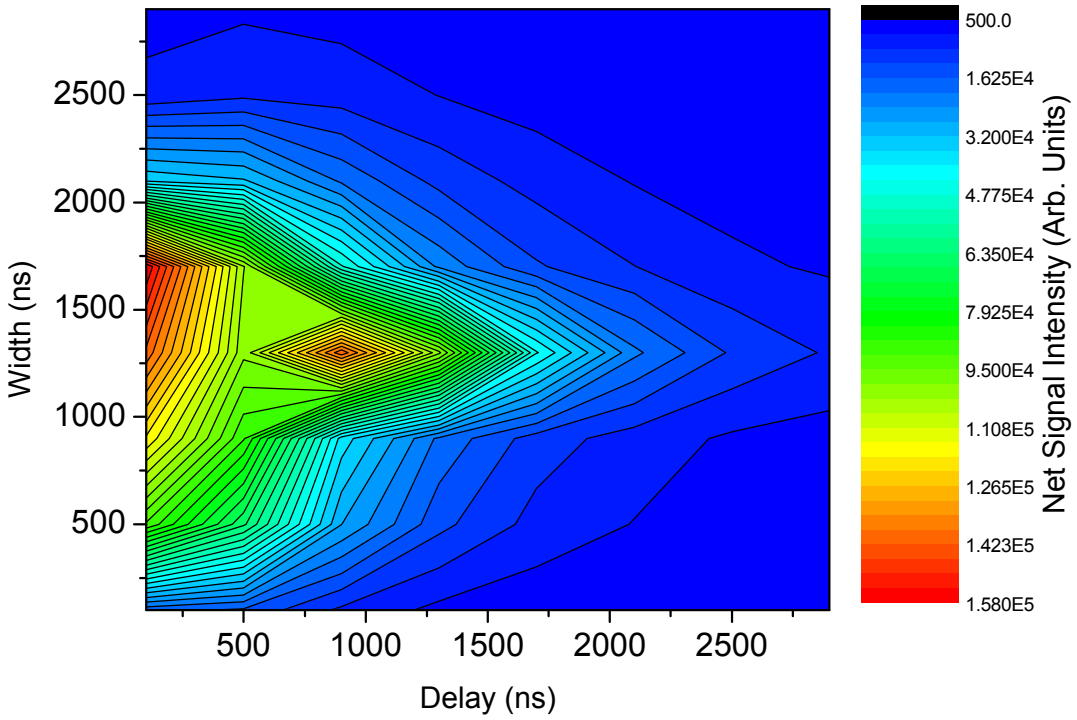

Figure 5-28 Net signal as a function of gate delay and width: vacuum

Figure 5-28 charts the behaviour of Net Signal intensity as a function of both gate width and delay. The Net Signal response under vacuum displays a very different behaviour to that observed at atmospheric pressure in Figure 5-23. There is a clear region of gate versus delay values where the Net Signal intensity is maximised in the region of 5000 to 10000 counts; outside of this region the Net Signal intensity is very low, of the order of 500 - 1000 counts. In order to maximise Net Signal intensity under vacuum conditions one should perform LIBS of silicon with a gate delay less than 1500 ns and a width between 500 and 2000 ns.

5.7.8 Vacuum: FWHM

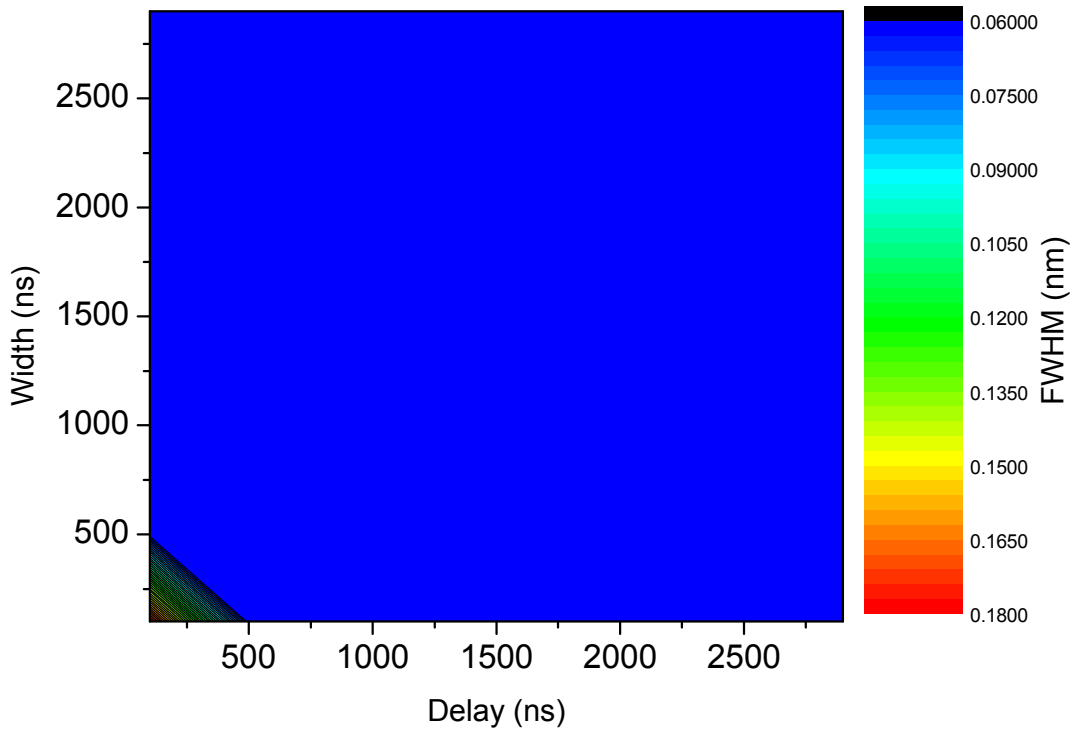

Figure 5-29 Emission line FWHM as a function of gate delay and width: vacuum

Figure 5-29 shows the emission line FWHM response as a function of gate delay and width under vacuum. It is quite clear that, unless delay and gate values less than 500 ns are employed, there is very little variation in FWHM under vacuum throughout the parameter space of this study.

The rapid plasma expansion at an ambient pressure of ~ 10^{-6} mbar reduces the plasma electron density below the threshold at which the pressure broadening Stark effect is noticeable above the instrumental broadening profile in the silicon emission lines.

5.7.9 Vacuum: Average Background

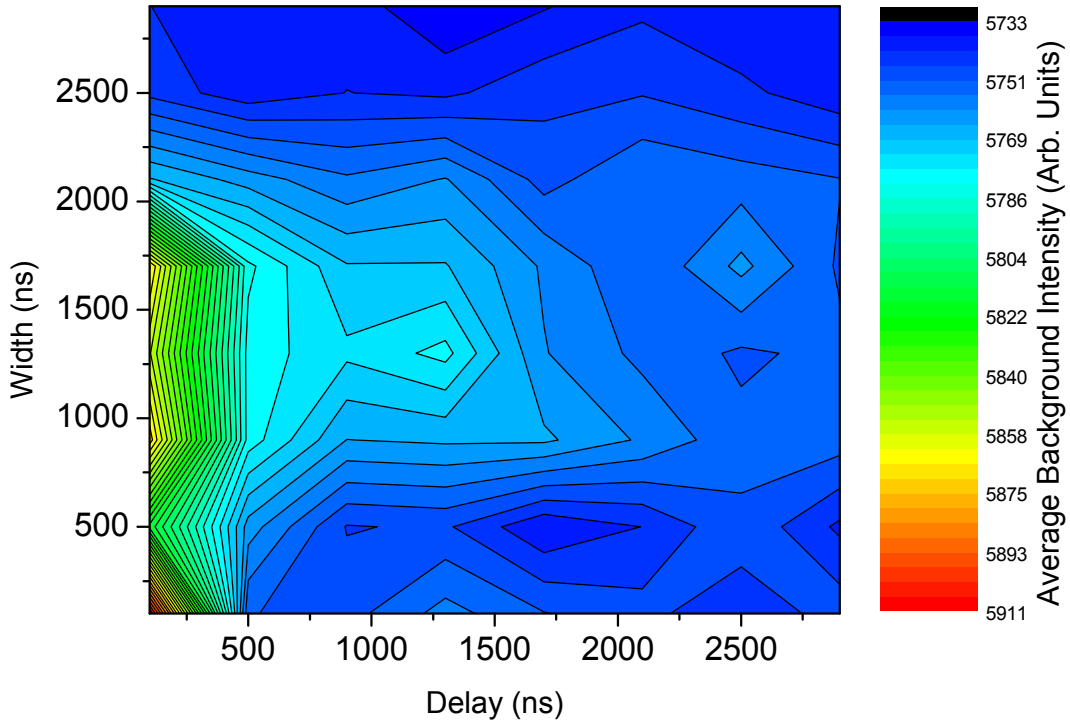

Figure 5-30 Average background level as a function of gate delay and width: vacuum

Figure 5-30 shows the response of the plasma Average Background level under vacuum as a function of gate delay and width The behaviour of Average Background under vacuum is similar to that displayed at atmospheric pressure, the intensity decaying rapidly after delay times greater than 500 ns. The background appears to decrease with delays greater than approximately 2000 ns as the optical emission from the plasma has diminished before the ICCD has finished capture; as such comparatively little optical emission is further integrated into the emission signal with increased gate width. There is in fact evident a small increase in background level with increasing gate width, but this is not apparent due to the scale of the contour plot. If one desires to reduce the Average Background level, thus increasing signal to noise ratio and consequently

instrument sensitivity, then LIBS of silicon should be performed at gate delays of greater than approximately 500 ns under vacuum.

5.7.10 Vacuum: Delta Background

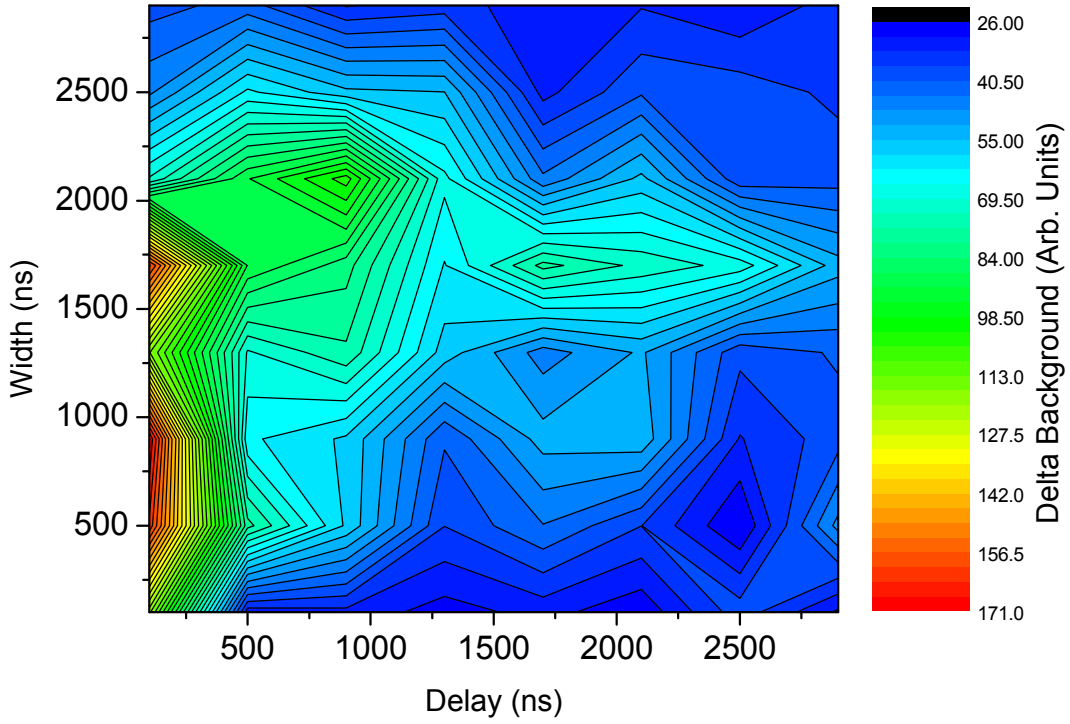

Figure 5-31 Delta background as a function of gate delay and width: vacuum

Figure 5-31 shows the response of Delta Background versus gate delay and width. The behaviour of Delta Background under vacuum is different from that exhibited at atmospheric pressure, as displayed in Figure 5-26. The highest Delta Background level recorded under vacuum is 171, which is much lower than that recorded at atmospheric pressure, 3160. The free expansion of the plasma under vacuum reduces the continuum emission contribution to the spectra, which in turn reduces the background signal variance. Much 'cleaner' spectra in terms of

resolution and background noise are recorded under vacuum than at atmospheric pressure.

5.8 Manual Optimisation of Spectrometer Input Slit-width

With capture gate delay and width values broadly determined for maximum QF, the spectrometer input slit-width was swept from 10 to 250 μm. The ICCD gain remained set to 150, the laser was again operated at a repetition rate of 1 Hz, and the lens position remained fixed at + 15 mm. As previously, each data-set was the accumulation of 10 spectra, and all results are the average of three data-sets. At atmospheric pressure the gate delay and width were arbitrarily set to those giving the optimum QF as suggested by the manual investigation; 1300 ns delay, and 900 ns width. For vacuum conditions the delay and width were again set to those observed to produce the optimum QF; 900 ns delay, and 1300 ns width.

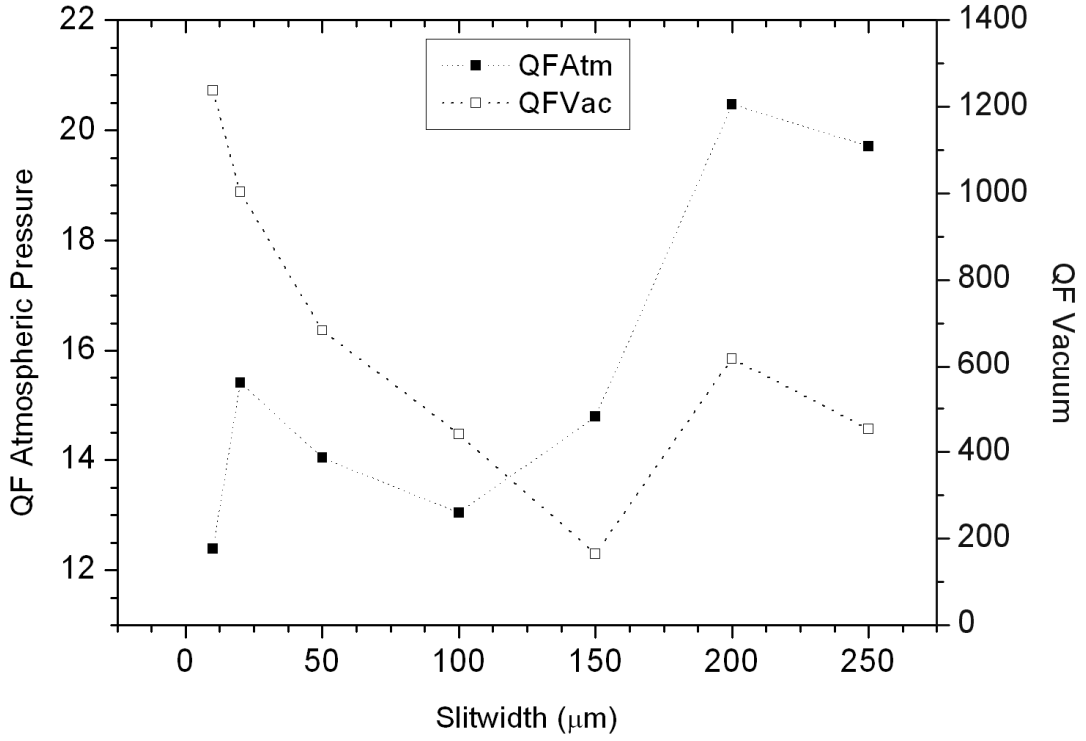

Figure 5-32 QF as a function of slit-width at atmospheric pressure and under vacuum

Figure 5-32 depicts the QF response as a function of varying spectrometer input slit-width. Both the vacuum and atmospheric pressure traces display complex behaviour, indicating that varying the slit-width simultaneously affects several parameters in the QF definition; as the slit-width is narrowed to minimise FWHM, this is to the detriment of the net signal intensity. The maximum QF value here is observed for a slit-width of 200 μm at atmospheric pressure, and a slit-width of 10 μm under vacuum.

5.9 Manual Optimisation of Lens Position

The laser focussing lens position was varied across the entire range permitted by the micrometer mounting, from -20 to +28 mm. All other hardware parameters remained constant and were set to the values stated in the previous Section 5.8. The QF response to varying the lens position is illustrated in Figure 5-33.

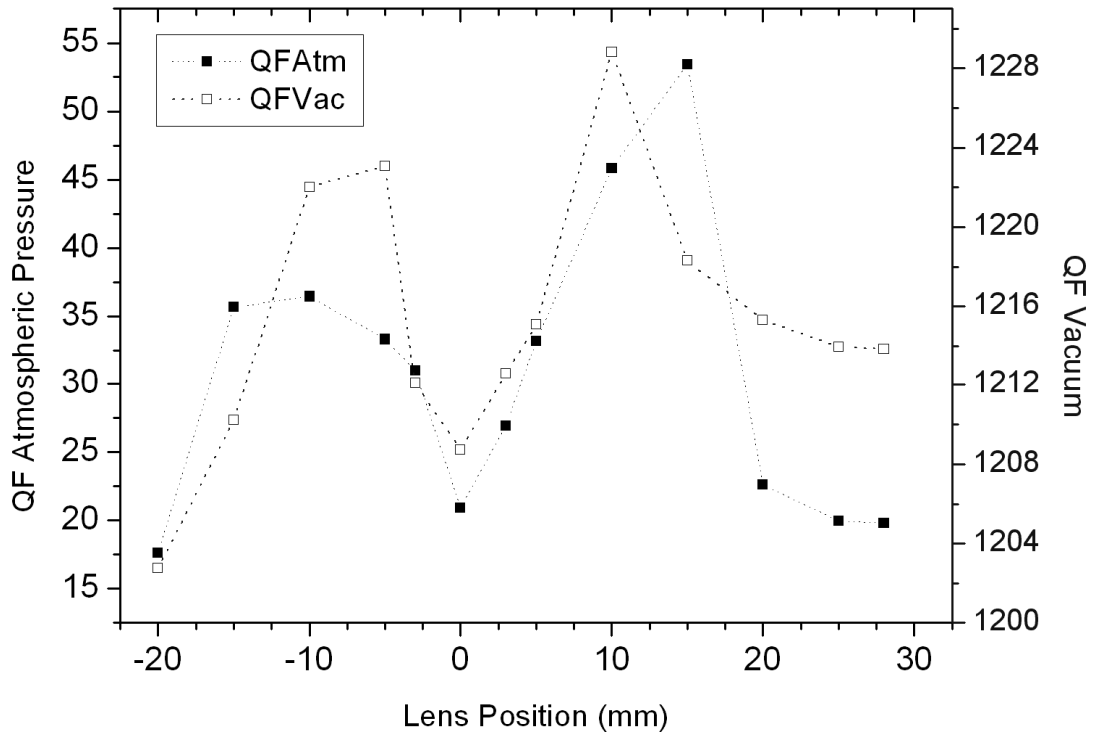

Figure 5-33QF as a function of lens position at atmospheric pressure and under vacuum

It can be seen from Figure 5-33 that the QF in both pressure regimes exhibits broadly similar behaviour with variations in lens position, with minima observed for both pressures at the extremes of the lens travel and at the zero position. The maximum QF at atmospheric pressure, 54, is observed at a lens position of + 15 mm. The maximum QF under vacuum, 1229, is observed at a lens position of + 10 mm. Maximum QF values are achieved for both pressure regimes where the laser beam is focussed beneath the surface of the sample.

Focussing the laser beam beneath the surface of the sample increases the effective spot size; if sufficient fluence is maintained with this enlarged spot to overcome the ablation threshold of silicon, then a greater amount of silicon will be ablated per laser shot. This increased amount of ablated silicon leads to a corresponding increase in the intensity of the optical emission from the plasma, thereby increasing Net Signal level and hence QF. Focussing beneath the sample surface reduces the risk of pre-ablation ionisation in the ambient atmosphere, which reduces the energy in the incoming beam. As an example, lens positions of + 10 mm and – 10 mm produce equal laser spot sizes, but the fluence when focussing at + 10 mm shall be greater as no beam energy is lost to unintentional breakdown in the ambient atmosphere above the sample surface.

Minima in the QF plots are observed at the extremes of lens position as the spot size becomes so large that the laser fluence is reduced, leading to a drop in plasma optical emission. The QF minimum observed for a lens position of zero corresponds to focussing the laser beam at the surface of the sample and hence equates to the smallest spot size. The small spot size leads to a drop in the

volume of ablated material and hence to a drop in Net Signal intensity and consequently QF.

5.10 Manual Optimisation: Comparison of Atmosphere vs. Vacuum QF Measurements

Table 5-8 presents the values of gate width, gate delay, focussing lens position and spectrometer input slit-width determined to give the maximum values of QF at atmospheric pressure and under vacuum, and the measured QF values yielded from those particular instrument settings. It is immediately obvious from Table 5-8 that the maximum attainable QF under vacuum is over 25 times higher than the maximum QF observed at atmospheric pressure. If one desires to maximise QF, as defined in Equation 5.2, then LIBS of silicon should be performed under vacuum.

Table 5-8 Comparison of manually obtained optimum QF and instrument settings under atmosphere and vacuum

	Atmosphere	Vacuum $1x10^{-6}$ mbar
Delay (ns)	1300	900
Width (ns)	900	1300
Lens Position (mm)	15	10
Slit-width (μm)	200	10
Optimum QF	47.92	1238.76

The data presented in Table 5-8 are reproduced graphically in Figure 5-34 for ease of comparison.

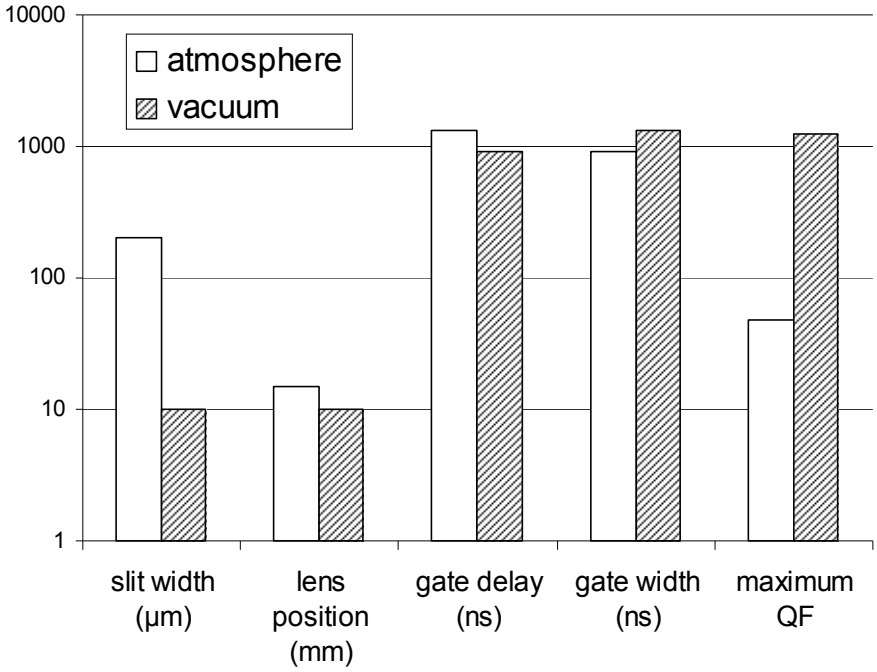

Figure 5-34 Comparison of the maximum QF obtained at atmosphere and under vacuum, and the specific instrument parameter settings yielding these maximum QF values

Figure 5-8 clearly indicates that the settings of lens position, gate delay and gate width yielding the maximum QF value at atmospheric pressure and vacuum are similar. The spectrometer input slit widths leading to the maximum QF values at atmospheric pressure and under vacuum are very different; 10 μm under vacuum and 200 μm at atmospheric pressure. The impact of each instrument parameter on the measured QF values is discussed in the following section.

5.10.1 Impact of Each Hardware Parameter on the QF Response

Figure 5-35 illustrates the impact of each hardware parameter on the QF response at atmospheric pressure and under vacuum. Due to the manner of this study, here slit-width and lens position are considered individually, with gate delay and width combined as a single instrument parameter. The length of each bar in

Figure 5-35 represents the difference between the maximum and minimum QF values recorded whilst varying that particular hardware parameter.

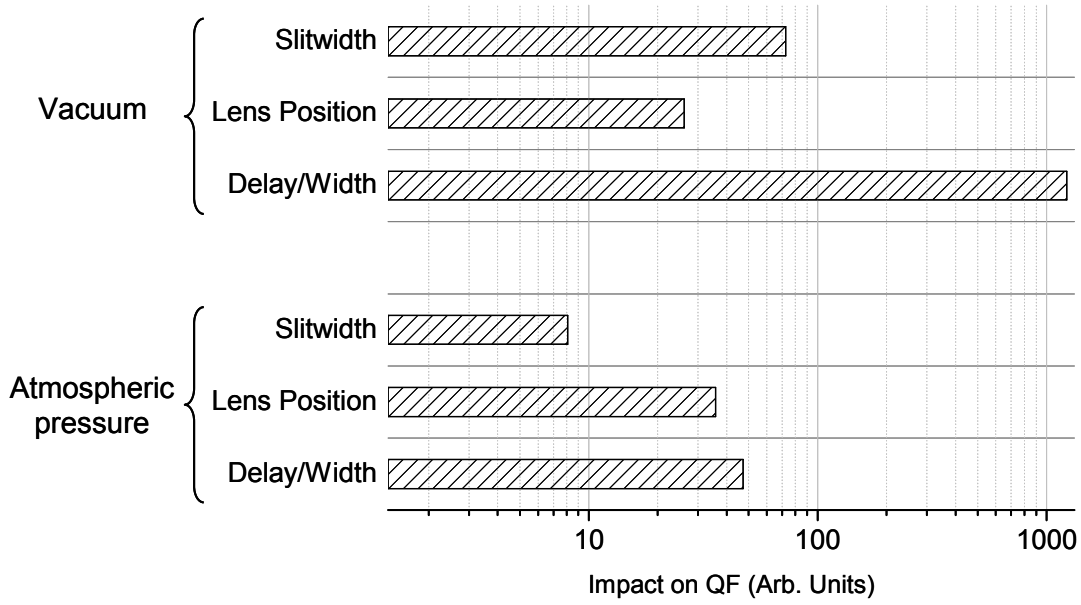

Figure 5-35 Impact on QF of gate delay/width, lens position and slit-width at atmospheric pressure and under vacuum

Figure 5-35 indicates that variations of gate width/delay have the greatest impact on the QF of the LIBS spectra; more so under vacuum as the plasma emission decays more rapidly, leading to a shorter window of opportunity in which to capture useful, intense, well-resolved spectra. Under vacuum the slit-width has a greater bearing on the QF than at atmospheric pressure; at atmospheric pressure variations in the measured FWHM are due to Stark broadening of the emission lines, whereas under vacuum the instrumental broadening profile, i.e. the slit width, dominates. The lens position is seen to have a greater impact on the ultimate QF value at atmospheric pressure rather than under vacuum; pre-

ablation breakdown in the ambient atmosphere when focussing the laser above the sample surface is not an issue under vacuum.

5.11 Comparison of Manual Optimisation and RSM Studies: Atmospheric Pressure

Table 5-9 shows the maximum optimum QF value measured during the manual hardware optimisation and that predicted by the RSM model, and the hardware parameter settings required to produce these maxima at atmospheric pressure.

Table 5-9 Comparison of Manual and RSM Optimisation: Atmospheric Pressure

	Manual	RSM
Delay (ns)	1300	952.953
Width (ns)	900	1000
Lens Position (mm)	15	14.8148
Slit-width (μm)	200	260
Optimum QF	47.92	53.7069

The data listed in Table 5-9 are reproduced graphically in Figure 5-36 for ease of comparison. It is apparent from Figure 5-36 that the QF value predicted by the RSM model is very close to that determined from the manual optimisation of the hardware.

The values of gate delay, gate width, lens position and spectrometer input slit-width predicted by the RSM model to yield the optimum QF value at atmospheric pressure are all similar to those deduced from the manual hardware optimisation.

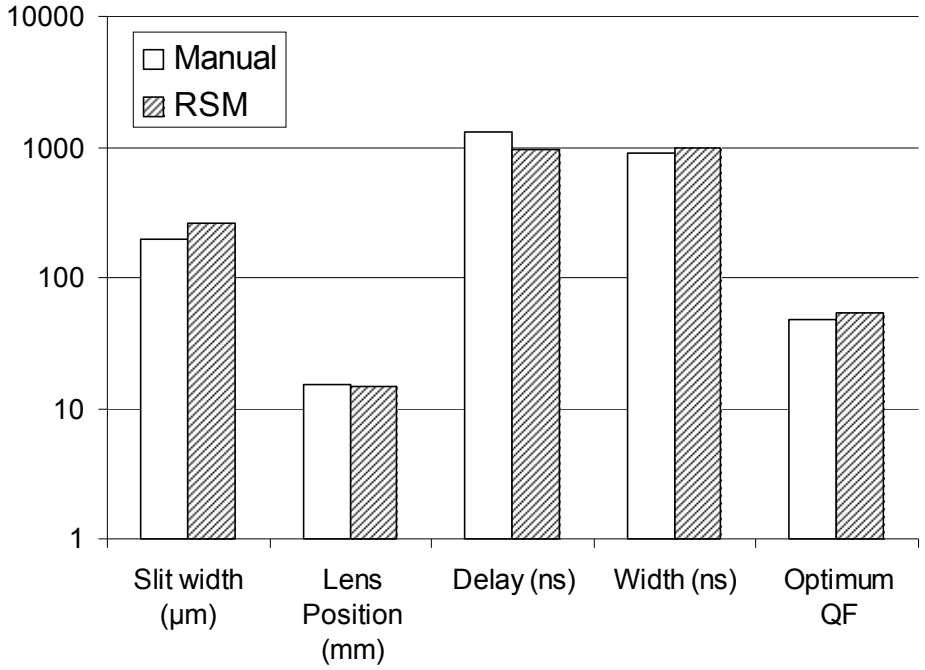

Figure 5-36 Comparison of manual and RSM optimisation: atmospheric pressure. Settings of slit width, lens position, gate delay and gate width yielding the greatest QF are shown.

5.12 Comparison of Manual Optimisation and RSM Studies: Vacuum

Table 5-10 lists the RSM model predicted QF value and that determined from the manual parametric investigation, and the instrument parameter settings required to produce said QF values. The data presented in Table 5-10 are reproduced graphically as Figure 5-37 for ease of comparison.

Table 5-10 Comparison of Manual and RSM Optimisation: Vacuum

	Manual	RSM
Delay (ns)	900	576.513
Width (ns)	1300	745.712
Lens Position (mm)	10	15
Slit-width (µm)	10	120
Optimum QF	1238.76	262.32

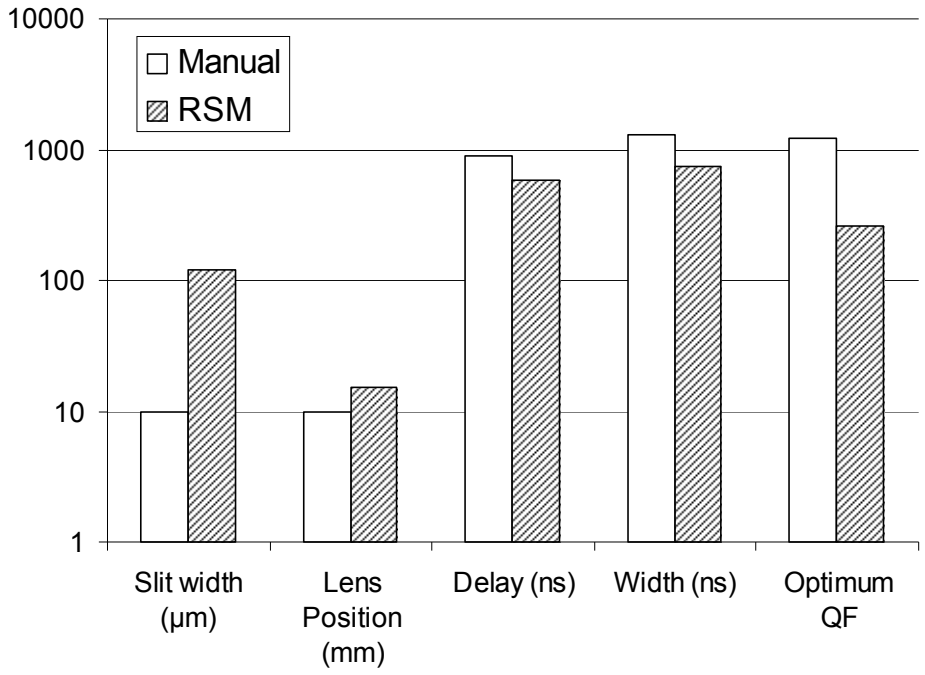

Figure 5-37 Comparison of manual and RSM optimisation: vacuum

It is immediately apparent that the RSM-predicted QF is almost a factor of five lower than the measured value as determined from the manual parametric investigation. The predicted and manually measured optimal instrument setting values differ much more under vacuum than those recorded at atmospheric pressure, as presented in Section 5.11. The RSM model prediction of the optimum slit-width, in particular, is awry.

It has previously been established that the StatGraphics software is only equipped to apply a combination of linear and second order polynomial fits to the data put into the RSM model, and any data following a different trend will be misrepresented. It should also be recalled that the software optimisation of the RSM experimental design necessarily reduces the accuracy of any fit to the input data. Also, each data-set inputted into the RSM model was the average of only

two sets of ten accumulated spectra, so errors in the RSM predictions may well be attributed to erroneous data points.

5.13 Summary

A system was designed and constructed that permitted LIBS investigations of silicon samples at atmospheric pressure and under an ambient pressure of ~ 10^{-6} mbar. Large differences in both the intensity and FWHM of emission lines from laser-induced silicon plasmas were observed with respect to ambient pressure, as indicated in Figure 5-1. The Response Surface Methodology was applied to the optimisation of the instrument parameters in order to yield spectra of the highest potential usefulness at both atmospheric pressure and under vacuum. A quality factor (QF) was conceived as the response for a multivariate parametric analysis of the instrument parameters conducting using the software package StatGraphics 5.1.

Using the StatGraphics software a series of experiments was designed, optimised retaining a moderate level of design accuracy, and performed; and hence the response of the LIBS system predicted. A manually performed parametric study of the LIBS apparatus settings was conducted to characterise the true response of the LIBS system and thus validate, or refute, the accuracy and applicability of the RSM technique in this instance.

The RSM model suggested that spectra displaying higher QF should be observed under vacuum conditions. Furthermore, as indicated by Figure 5-20, the RSM model predicted that there are four crucial instrument parameters governing the

QF behaviour at atmospheric pressure: linear gate delay, gate width and lens position components, and a quadratic gate delay dependent term. Conversely, the RSM model predicted that only two instrument parameters were critical in governing the QF response under vacuum: a linear slit-width term and a quadratic delay component.

The Pareto charts displayed in Figures 5-20 and 5-21 indicated that the RSM model considered the spectrum capture delay to play an important role in governing the QF values at both atmospheric pressure and under vacuum. Indeed, this consideration seems valid as the characteristics of LIBS plasmas have been shown in Chapter 4 to vary markedly with respect to time. The RSM model points to the fact that the laser-focussing lens-position has an important impact on the QF behaviour at atmospheric pressure, which was verified by the manually performed parametric study. The RSM model also hinted at the heightened importance of the spectrometer input slit-width on the QF behaviour under vacuum; again this conclusion was corroborated by the manually performed parametric study.

The RSM study results compared favourably with those arising from the manual parametric study; the RSM predictions correlated more closely with the manually measured data at atmospheric pressure, as evident from Sections 5.11 and 5.12. It was predicted by the StatGraphics model that silicon LIBS spectra displaying the best possible compromise of resolution and sensitivity should be observed under vacuum conditions, which was been confirmed to be the case. Discrepancies between the RSM model and experimental observations are due to

the fact that StatGraphics is only capable of fitting first or second order polynomial models to the input data set. As was shown in Figure 5-12, the input data need not necessarily follow either of these models, but will still be modelled as such. By its nature, and limitations, RSM may never fully describe a complex system, but can offer a useful insight into the general trends and any interactions occurring; in this regard the Response Surface Methodology was proven to be a success in broadly predicting the behaviuor of the LIBS system.

We consider now the outcomes of the manually performed parametric study, which described the true response of the LIBS hardware arrangement. The QF response at atmospheric pressure, as presented in Figure 5-22, featured a large range of gate delay and width values that yielded a broadly similar QF values in the range 20 -30. By contrast, Figure 5-27 shows that a much higher optimum spectrum QF is observed under vacuum, but there is a much smaller range of gate delay and width values that yield an appreciable QF. The rapid plasma expansion under vacuum leads to a smaller temporal window in which to capture plasma emission; the gate delay and width settings are thus more critical in providing useful LIBS spectra under vacuum.

It was seen in Figure 5-34 that the spectrometer input slit-width has a greater impact on the QF under vacuum than at atmospheric pressure. Stark broadening of the emission lines is more prevalent at atmospheric pressure, as plasma confinement by the ambient atmosphere incurs higher plasma electron densities. At atmospheric pressure, Figure 5-24 indicates that varying gate delay may alter the FWHM by up to 3 nm. Therefore, at atmospheric pressure, the dominant

contribution to emission line FWHM measurement is the width of the peaks themselves. Under vacuum conditions, where little Stark broadening is evident, the dominant contribution to the emission line FWHM is the instrumental broadening profile, which depends on the spectrometer input slit-width. Considering Figure 5-29, the FWHM of the LIBS emission lines observed under vacuum is virtually constant throughout the majority of the parameter space.

Comparing Figures 5-26 and 5-31 we observe that the LIBS spectrum background is very much lower under vacuum, in the range 26 -171 arbitrary units, than at atmospheric pressure where a range of 30 -3160 arbitrary units is recorded. The LIBS background noise is due primarily to the plasma continuum emission, which is in turn dependent on the free-electron density of the plasma. Under vacuum conditions, $p_a \sim 10^{-6}$ mbar, the plasma expands freely due to lack of confinement by the ambient atmosphere; this reduces the electron density of the plasma which in turn decreases the emission spectrum background noise.

Figure 5-33 reveals that there is a complex relationship between laser focussing lens position and the observed QF of the emission spectra. Varying the position of the focussing lens alters the spot size of the laser at the sample surface. QF minima are observed under atmospheric pressure and under vacuum when focussing the laser at the sample surface and at either extreme of lens travel. When focussing at the sample surface the spot size is reduced, therefore a smaller volume of material is ablated; this leads to a drop in emission intensity to the detriment of the QF response. At the extremes of lens travel the spot size at the sample surface has become so large that the effective laser fluence is reduced;

this again leads to a lesser volume of target material ablation and lower emission signal intensity. Figure 5-33 also reveals that focussing the laser in front of the sample surface is detrimental to the observed QF response. When focussing the laser above the target surface, breakdown in the ambient atmosphere is induced at the focal volume of the laser beam; this effectively reduces the laser energy available for sample ablation and reduces the plasma emission intensity. The issue of pre-ablation breakdown in the ambient gas is a greater problem at higher ambient pressures, as corroborated by Figure 5-35.

It must be stressed that the parametric investigation conducted here was concerned solely with maximising the emission spectrum QF, as defined in Equation 5.2, with respect to six neutral silicon emission lines in the wavelength range 250 -254 nm. It should also be stressed that the definition of QF was employed solely to permit the LIBS instrument's complex behaviour to be modelled as a single response. The QF definition stated in Equation 5.2 does not allow for LIBS spectrum optimisation in all cases; as it does not, for example, take account for the need to detect minor element emission lines in a complex sample matrix, or the desire to perform quantitative measurements.

The instrument parameters determined herein to maximise QF are certainly not considered to be applicable across all LIBS investigations. The behaviour of laser-induced plasmas is subject to variations in sample composition, laser wavelength and pulse duration, ambient gas composition and pressure etc. (Tognoni et al. 2002). Considering the LIBS apparatus described here, if a different wavelength range of the emission spectrum was monitored, or if singly

or doubly ionised silicon emission lines were considered instead of neutral lines, then the instrument parameters necessary to maximise QF will differ from those presented here.

This is, perhaps, further evidence of one of the major shortcomings of the LIBS technique. Aside from the plasma analysis problems arising from inappropriately applied local thermal equilibrium assumptions, and a lack of a thorough understanding of the physical processes governing laser-induced breakdown emission, there is a lack of standardisation across the LIBS community. With virtually infinite scope for LIBS hardware variations, it is extremely difficult to perform direct comparisons between LIBS results captured by different systems. Indeed, such is the complexity of the typical LIBS set-up that direct comparisons may ultimately be impossible; a LIBS system designed and optimised to perform properly under specific operating conditions may well produce meaningless data when applied to a different situation.

6 Mass Spectrometry

6.1 Introduction

Mass Spectrometry (MS) is an analytical tool employed across a multitude of disciplines; a comprehensive review covering each of the many varied MS techniques lies beyond the scope of this thesis. This section presents a review of the fundamental principles underlying the operation of the mass spectrometer, with a primary focus on the quadrupole mass analyser and the Residual Gas Analyser (RGA) as employed in this work.

Section 6.2 introduces the concept of mass spectrometric analysis and ion separation according to mass to charge ratio. The electron ionisation source is described and the operating conditions and maximum ambient pressure constraints of the MS are considered in terms of the ion free path. The construction and operation of the quadrupole mass analyser are detailed, and the trajectories of ions accelerated through the quadrupole field considered. Finally, a brief description of the RGA and its typical applications is given.

Section 6.3 details the experimental set-up and the results obtained when monitoring laser ablation under vacuum, with the RGA mounted in the traditional chamber 'sniffing' configuration. Section 6.4 details the design and construction of apparatus enabling the RGA to perform direct line-of-sight analyses of the laser-induced plasmas, and the results obtained from this hardware configuration. A summary of the results of these investigations is given in Section 6.5.

6.2 Principle of the Mass Spectrometer

The mass spectrometer separates ions according to their mass to charge ratio, *m/z*.

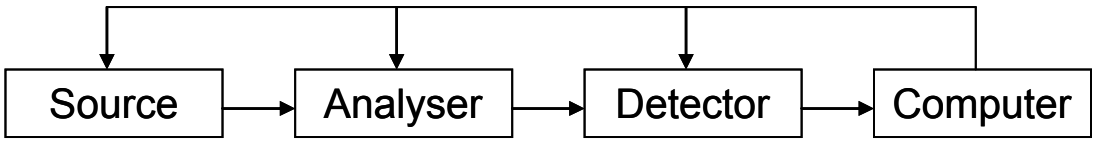

Figure 6-1 Block diagram of a typical mass spectrometer

Figure 6-1 illustrates the main components of a typical mass spectrometer. Upon introduction into the MS, gas-phase analyte ions are generated by the ion source, subsequently extracted via suitable ion optics, and then accelerated towards the mass analyser. Mass separation may occur by exploiting the differences in the ion Time-of-Flight (ToF), or from the variation in trajectories of ions subject to electric and/or magnetic fields. The mass resolved ions are detected and counted, producing a mass spectrum of the relative intensities of each *m/z* considered. Generally the charge state z of the ions produced and analysed in a mass spectrometer is 1, so the ion mass to charge ratio *m/z* may be considered as analogous to the ion mass in amu. A computer is employed to synchronise and control the whole process, and to record and output the obtained data in a user-friendly format.

Scanning mass analysers, such as the quadrupole, transmit ions of different *m/z* successively with respect to time (de Hoffmann and Stroobant 2003) and as such are poorly suited to transient events, such as laser ablation (Kuzuya et al. 1998). Some mass analysers allow for the simultaneous detection of all ions; the ToF

MS is particularly well suited to laser ablation analyses as it requires ions to be formed in pulsed 'packets' (de Hoffmann and Stroobant 2003).

6.2.1 The Electron Ionisation Source

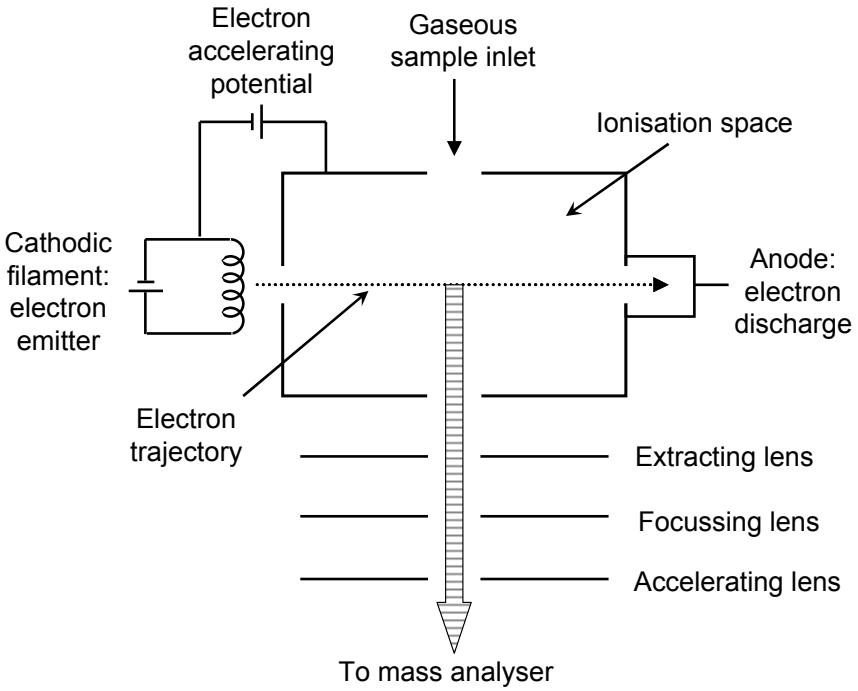

Figure 6-2 Schematic diagram of a typical electron ionisation source

For mass spectrometric analysis, gas-phase ions of the analyte must be created by, for example, electron ionisation (EI):

$$M + e^- \rightarrow M^\bullet + 2e^- \qquad (6.1)$$

The EI source produces ion beams of excellent stability and low energy spread (Farmer 1963), allowing for good repeatability and accuracy. Most modern EI sources are simple devices based on those developed by Bleakney (Bleakney 1929) and Nier (Nier 1939). The EI source comprises of a heated filament,

usually fabricated from tungsten (Elliott 1963, O'Hanlon 2003) or thoriated iridium (Chambers 2005), which emits electrons that are accelerated across the source region to an anode. As the electrons traverse the ionisation space they interact with the gaseous analyte molecules that have been injected via the source inlet. Each electron may be treated as a wave, the wavelength λ of which is given by (de Hoffmann and Stroobant 2003):

$$\lambda = \frac{h}{mv} \tag{6.2}$$

where h is Planck's constant, m is the electron mass (9.12×10^{-31} kg) and v its velocity. When this wavelength approaches the bond lengths of the analyte molecules, complex energy transfer processes take place leading to electronic excitations and subsequently an electron is expelled from the analyte (de Hoffmann and Stroobant 2003).

The ions created in the source are extracted, focussed and accelerated towards the mass analyser by a series of ion optics plates. The ion yield at a given filament electron energy varies from gas to gas. Figure 6-3 shows typical curves for the number of ions produced versus electron energy for N_2 and He. The maximum ion yield for most gases relates to electron energies in the range of ~ 50 to 90 eV; for this reason an electron energy of 70 eV is usually chosen for general analytical work (O'Hanlon 2003, Farmer 1963). The EI source produces ion beams of excellent stability and low energy spread (Farmer 1963), allowing for good repeatability and accuracy. At a given acceleration potential and at a constant temperature the number of ions q produced per time in a volume V is

linked to the source pressure p_a by Equation 6.3 (de Hoffmann and Stroobant 2003):

$$q = \kappa p_a i V \tag{6.3}$$

where κ is a constant of proportionality and i is the electron current. On average one ion is produced per every 1000 analyte molecules entering the ion source under normal operating conditions (de Hoffmann and Stroobant 2003).

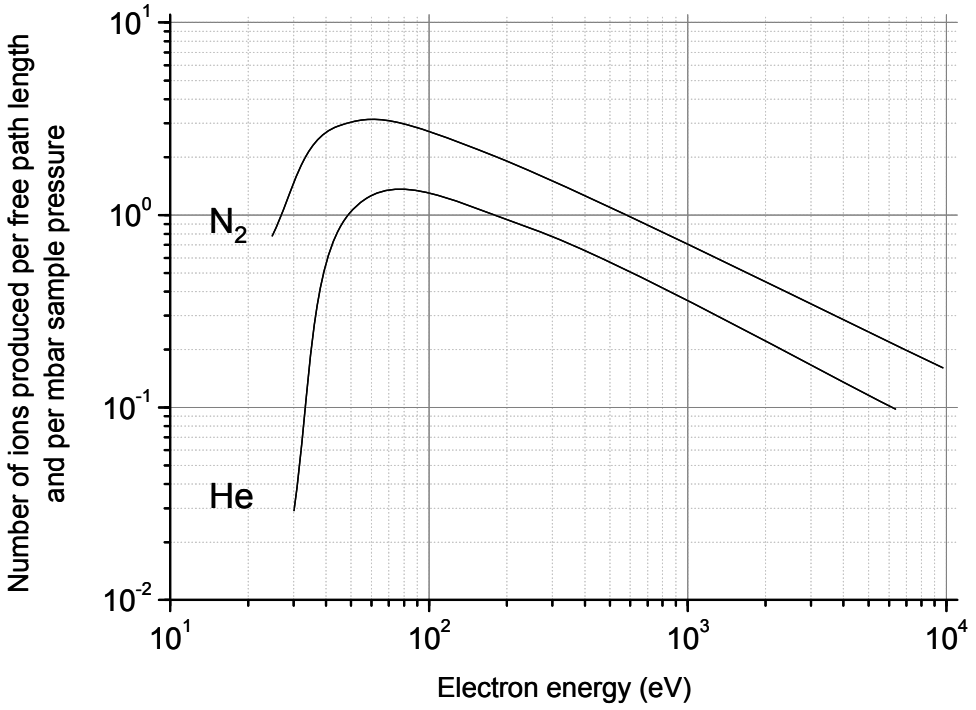

Figure 6-3 Number of ions produced by the EI source as a function of electron energy

6.2.2 Ion Free Path

Mass spectrometers must function under high vacuum to reduce collisions between analyte ions and other residual gas molecules within the instrument (de

Hoffmann and Stroobant 2003, O'Hanlon 2003). Ions colliding with the instrument walls are neutralised, and hence these ions cannot be detected by the mass spectrometer. Ion/molecule collisions may also lead to unwanted reactions inside the MS, increasing the complexity of the resultant mass spectra.

The mean free path L of ions within the mass spectrometer (at a temperature of 300K) may be approximated (de Hoffmann and Stroobant 2003, O'Hanlon 2003) by:

$$L \approx \frac{6.6 \times 10^{-3}}{p_a} \tag{6.4}$$

where p_a represents the pressure inside the instrument measured in mbar, and L is measured in cm. In a mass spectrometer the mean free path should be of the order of 1 metre, leading to a maximum theoretical operating pressure of 6.6×10^{-5} mbar. Mass spectrometers equipped with an EI source must also be operated at high vacuum to protect the EI filament (O'Hanlon 2003). In practice mass spectrometers may be operated at slightly higher pressures; the MKS MicroVision Plus RGA, for example, will function adequately at a maximum pressure of $\sim 1 \times 10^{-4}$ mbar (MKS Instruments Inc. 2004).

6.2.3 The Quadrupole Mass Analyser

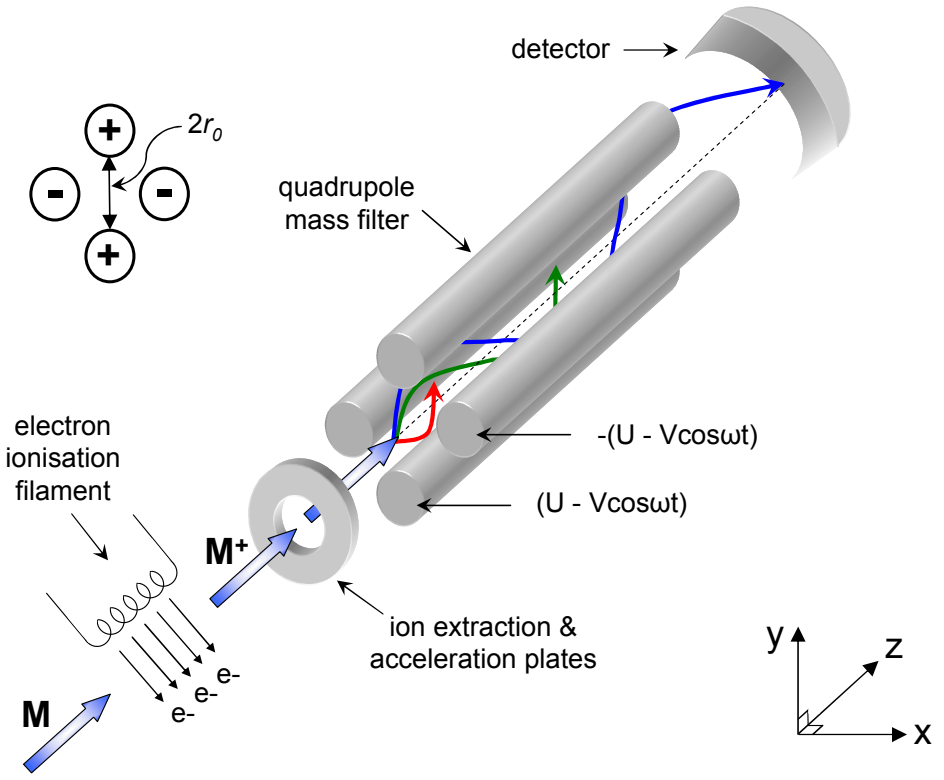

Figure 6-4 Schematic diagram of quadrupole mass analyser

The quadrupole design was first described by Paul and Steinwegen in the 1950s (Dawson 1976). Analyte ions are generated externally to the mass analyser, usually by electron ionisation. The quadrupole mass filter separates ions according to their *m/z* ratios by exploiting the stabilities of ion trajectories in oscillating electric fields (Reuben et al. 1996). The quadrupole analyser is comprised of four perfectly parallel rods having a circular, or preferably hyperbolic, cross-section (de Hoffmann and Stroobant 2003). The rods are arranged symmetrically and all lie a distance r_0 from the central point of the arrangement; the rod separation is therefore $2r_0$.

Ions entering the mass analyser are subject to an electric field generated by the application of a combined radio frequency (RF) and direct potential to the four rods. The ions will follow either a stable or unstable trajectory according to their *m/z* and the rod potential. In Figure 6-4 an example stable ion trajectory is represented by the wavy blue arrow, two unstable trajectories by the red and green arrows. Ions following stable trajectories will successfully traverse the mass analyser; ions following unstable trajectories will collide with the quadrupole rods and are neutralised.

Identical positive and negative potentials Φ_0 are applied to opposite pairs of rods:

$$\Phi_0 = +(U - V\cos\omega t) \quad \text{and} \quad -\Phi_0 = -(U - V\cos\omega t) \tag{6.5}$$

where ω is the angular frequency = $2\pi f$, with f the frequency of the RF signal. U is the magnitude of the direct potential and V is the zero-to-peak amplitude of the RF voltage. Typically U may vary from 500 to 2000 V and V from 0 to 3000 V (de Hoffmann and Stroobant 2003).

6.2.4 Ion Trajectories through the Quadrupole Mass Filter

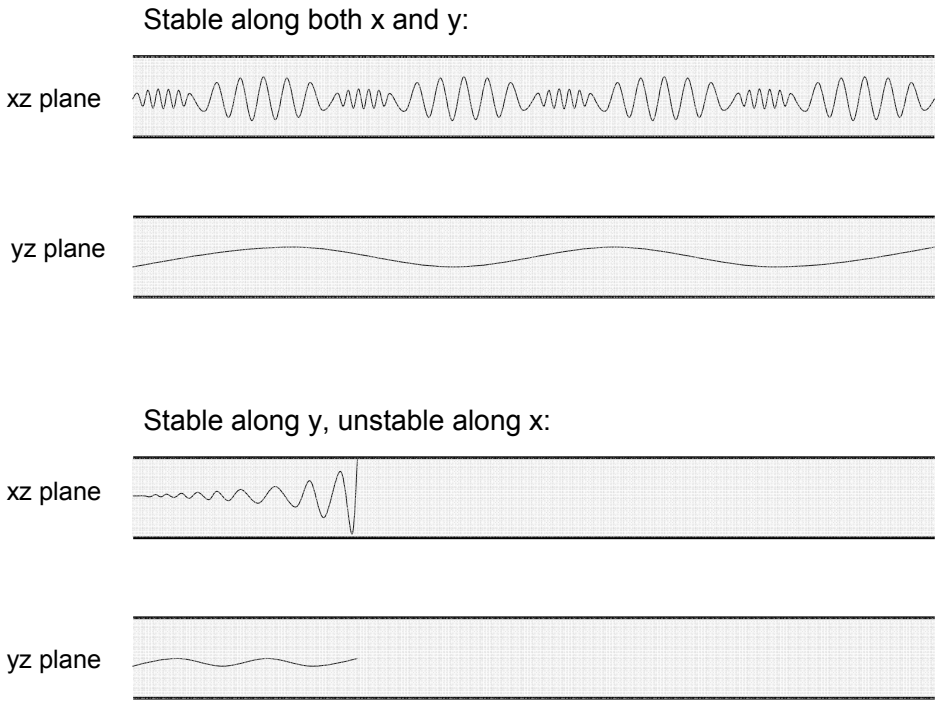

Figure 6-5 Example ion trajectories in quadrupole mass analyser; ion motion from left to right

The trajectory of a given ion entering the quadrupole mass analyser in the *z* direction oscillates in the *x* and *y* directions, and is determined by the *m/z* ratio of the ion and the potentials applied to the rods. For each *m/z* value there exists a set of rod potentials at which the ion trajectory will be stable, allowing the ion in question to traverse the mass analyser and subsequently be detected; ions of any other *m/z* values follow unstable trajectories and will collide with the quadrupole rods. Figure 6-5 shows examples of such ion trajectories. In the upper half of the diagram are shown the *x*-*z* and *y*-*z* components of an ion following a stable trajectory, successfully traversing the mass analyser and going on to the detector. The lower half of Figure 6-5 represents the *x* and *y* motion components of an ion

having a stable *y*-*z* plane trajectory, but an unstable *x*-*z* trajectory; this ion crashes into one of the rods and is neutralised.

The ions are accelerated through a constant potential in the *z* direction by ion optics at the interface of the ion source and the quadrupole, and as such may be considered as maintaining a constant velocity along the *z* axis of the analyser. The forces arising from the rod potentials $+\Phi$ and $-\Phi$ accelerate the ions in the *x* and *y* directions; assuming a uniform quadrupole electric field these forces are described by (de Hofmann and Stroobant 2003):

$$F_x = m\frac{d^2x}{dt^2} = -ze\frac{\partial\Phi}{\partial x}\,, \qquad F_y = m\frac{d^2y}{dt^2} = -ze\frac{\partial\Phi}{\partial y} \tag{6.6}$$

where *m* is the ion mass, *z* is the ionisation/charge state, *e* is the electron charge and Φ is a function of Φ_0:

$$\Phi_{(x.y)} = \frac{\Phi_0\left(x^2 - y^2\right)}{r_0^2} = \frac{\left(x^2 - y^2\right)\left(U - V\cos\omega t\right)}{r_0^2} \tag{6.7}$$

Rearranging Equations 6.6 and 6.7, and considering here only the case for the *x*-component of the ion motion we obtain:

$$m\frac{d^2x}{dt^2} = -ze\frac{\partial}{\partial x}\left[\frac{\left(x^2 - y^2\right)\left(U - V\cos\omega t\right)}{r_0^2}\right] \tag{6.8}$$

Performing the partial derivative in Equation 6.8 we yield:

$$m\frac{d^2x}{dt^2} = -ze\frac{2x(U - V\cos\omega t)}{r_0^2} \tag{6.9}$$

Rearranging Equation 6.9 we obtain the equation of motion for the ion in the *x* direction:

$$\frac{d^2x}{dt^2} + \frac{2ze}{mr_0^2}(U - V\cos\omega t)x = 0 \tag{6.10}$$

Similarly the equation of ion motion in the *y* direction may be derived:

$$\frac{d^2y}{dt^2} - \frac{2ze}{mr_0^2}(U - V\cos\omega t)y = 0 \tag{6.11}$$

An ion's trajectory is considered stable if the ion never touches the quadrupole rods i.e. the values of *x* and *y* never reach r_0 (de Hoffmann and Stroobant 2003). In order to deduce the values of *x* and *y*, Equations 6.10 and 6.11 must be integrated. The *Mathieu Equation* was developed by the physicist Mathieu in 1866 to describe the motion of waves in membranes (de Hoffmann and Stroobant 2003), and is given (Reuben et al. 1996):

$$\frac{d^2u}{d\xi^2} + (a_u - 2q_u\cos 2\xi)u = 0 \tag{6.12}$$

where the suffix *u* may represent either *x* or *y*.

Comparing Equation 6.12 with Equations 6.10 and 6.11, and recalling that the potential along *y* has the opposite polarity to that along *x*, the equations of ion motion in the quadrupole field may be expressed in the form of the Mathieu equation (de Hoffmann and Stroobant 2003, Reuben et al. 1996), using the following substitutions:

$$\xi = \frac{\omega t}{2} \tag{6.13}$$

$$a_u = a_x = -a_y = \frac{8zeU}{m\omega^2 r_0^2} \tag{6.14}$$

$$q_u = q_x = -q_y = \frac{4zeV}{m\omega^2 r_0^2} \tag{6.15}$$

The nature of the Mathieu equation is well understood and is covered in more detail elsewhere (Dawson 1976); only the nature of the solutions is discussed here, and it is sufficient merely to recognise that the equation relates the *x* and y co-ordinates of an ion with time.

For a given quadrupole arrangement r_0 is fixed and ω is maintained constant; *U* and *V* are variables (de Hoffmann and Stroobant 2003). The *x* and *y* co-ordinates of a given ion depend on the values of *U* and *V*; if these values are such that *x* and *y* never reach r_0 then the ion trajectory is stable. For an ion of a given mass, the values of *U* and *V* that promote a stable ion trajectory may be illustrated on an a_u,q_u diagram, as shown in Figure 6-6. The shaded portions of Figure 6-6 represent areas of ion trajectory stability; the upper portion of the illustration represents values of a_u and q_u giving trajectories stable along *x*, the lower portion

those giving rise to stable trajectory along *y*. Where the *x* and *y* stability zones overlap (the regions labelled A, B, C and D), the ion trajectory is stable along both *x* and *y* and the ion successfully traverses the quadrupole to the detector.

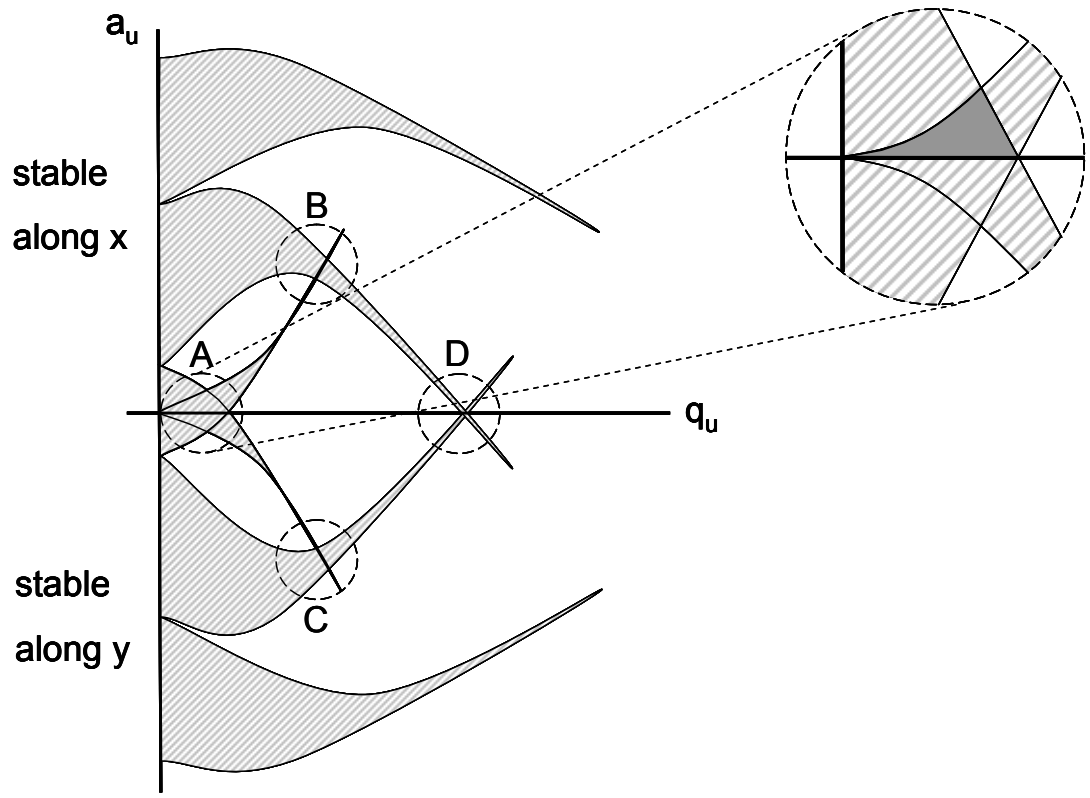

Figure 6-6 Ion stability regions: an a_u,q_u diagram for a given mass

It can clearly be seen from Figure 6-6 that the largest area of *x* and *y* stability overlap is that labelled A; this region is shown expanded inset in Figure 6-6. The upper part of the area A, for positive a_u, is shaded, and is that generally exploited in mass spectrometry. If we recall the relationships given in Equations 6.14 and 6.15 namely:

$$a_u = \frac{8zeU}{m\omega^2 r_0^2} \quad \text{and} \quad q_u = \frac{4zeV}{m\omega^2 r_0^2}$$

then we may deduce that (de Hoffmann and Stroobant):

$$U = a_u \frac{m}{z} \frac{\omega^2 r_0^2}{8e} \tag{6.16}$$

$$V = q_u \frac{m}{z} \frac{\omega^2 r_0^2}{4e} \tag{6.17}$$

The last term in both Equations 6.16 and 6.17 is a constant as the quadrupole mass filter operates at a fixed ω, and r_0 is also constant for a given pole-piece arrangement. From these two equations it is evident that altering the *m/z* value to monitor ions of sequential masses will result in a proportional multiplication of a_u and q_u; therefore the size of the upper half of the stability region labelled A in Figure 6-6 will change from mass to mass (de Hoffmann and Stroobant 2003, Reuben et al. 1996).

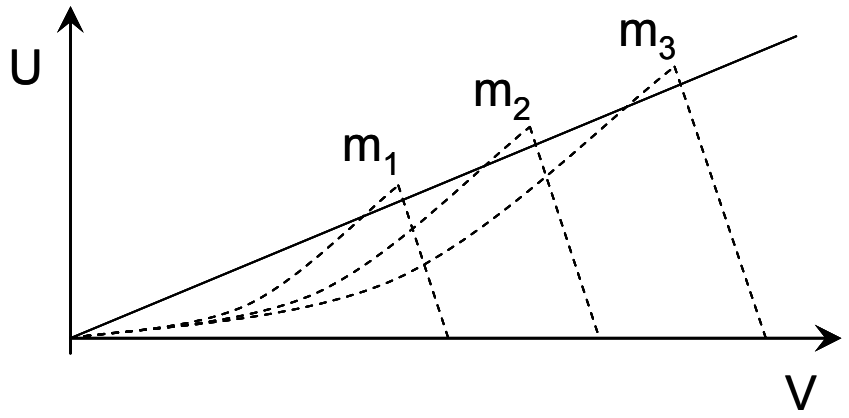

Figure 6-7 Stability regions of U and V for ions of masses $m_1 < m_2 < m_3$

Figure 6-7 represents in a *U*, *V* diagram the areas of the upper portion of the region A for three different masses, $m_1 < m_2 < m_3$. The stability regions of *U* and

V values for each of the masses are represented by the dotted lines. The solid line drawn over Figure 6-7 represents a scan of constant *U*/*V* which allows for the successive detection of different masses. Masses may be unambiguously resolved only if the line of constant *U*/*V* intercepts a single stability region at a given time; the greater the gradient of this line, the better the instrument mass resolution.

6.2.5 Ion Detection

Having created and mass filtered the analyte ions, some method of detection and counting is required. The transmitted ion current may be measured directly using a Faraday cup, or using a more sophisticated means involving multiplication of the ion current (Chambers 2005). The principle of the Faraday cup is shown in Figure 6-8.

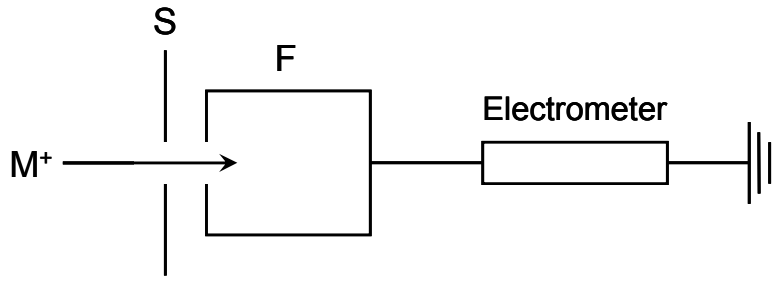

Figure 6-8 The Faraday Cup

The positively charged ions, M^+, exiting the mass filter enter the cup shaped electrode, labelled F, and neutralise on its surface, giving rise to an equal electron current in the circuit which is measured by the electrometer. A suppressor plate, labelled S, repels back into the cup any secondary electrons created from the initial ion impact (Chambers 2005). The ion currents measurable using the

Faraday cup are relatively high; the minimum ion current measurable above noise levels is approximately 10^{-14} A, which corresponds to a minimum detectable partial pressure of approximately 10^{-9} mbar (Chamber 2005). Greater sensitivity may be provided with the use of an electron multiplier, the principle of which is illustrated in Figure 6-9.

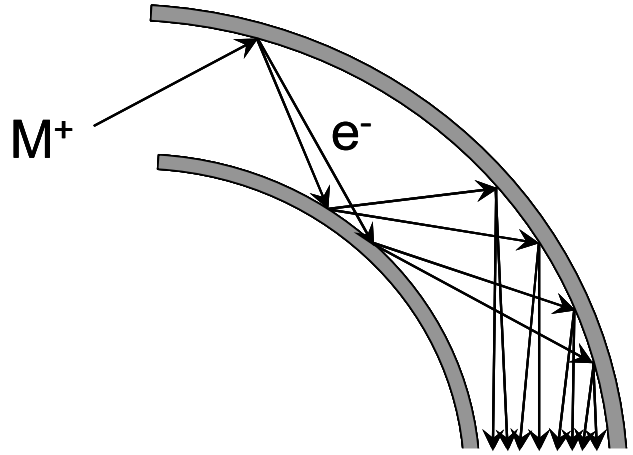

Figure 6-9 The Electron Multiplier

The electron multiplier is typically constructed from a curved glass channel coated with a dynode material that features a high secondary electron emission yield. An ion entering the multiplier channel is incident on the interior surface, liberating secondary electrons. An accelerating potential, generally 1-2 kV (Chambers 2005) is applied across the dynode, accelerating the secondary electrons from the entrance towards the exit.

The secondary electrons then themselves impact the multiplier walls, thus liberating further secondary electrons, and so on. The cascading secondary electrons exit the electron multiplier and the resulting current is measured with an electrometer. The gain of such an electron multiplier may reach 10^7 (de

Hoffmann and Stroobant 2003) but is typically of the order of 10^6 (Chambers 2005, O'Hanlon 2003); the minimum detectable partial pressure using an electron multiplier is of the order 10^{-14} mbar (Chambers 2005).

6.2.6 Instrument Resolution

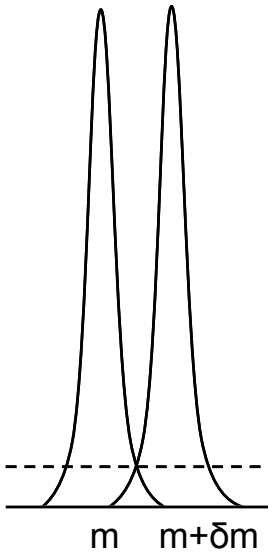

Figure 6-10 The Concept of mass spectrum peak resolution

The resolution of a mass spectrometer is a measure of its ability to discriminate between two adjacent masses m and $m+\delta m$; the smaller the mass difference an instrument may discern, the better its resolution. The concept of mass spectrum peak resolution is illustrated in Figure 6-10. The dotted line represents the fraction of peak height at which the two peaks of masses m and $m+\delta m$ may be clearly resolved.

The American Vacuum Society recommends that two adjacent peaks may only be considered as being clearly resolved when this value is no greater than 5% of the height of the weaker peak (Chambers 2005). If δm represents the smallest

mass difference for which two peaks m and $m+\delta m$ can be resolved, then the resolution of the instrument R is defined by (de Hoffmann and Stroobant 2003):

$$R = \frac{m}{\delta m} \tag{6.18}$$

6.2.7 The Residual Gas Analyser

The Residual Gas Analyser (RGA) is a simple mass spectrometric device, typically consisting of a quadrupole mass filter coupled with an electron ionisation source and a Faraday cup and/or an electron multiplier detector. The RGA is employed primarily to monitor the gaseous composition within evacuated vacuum vessels; the so-called residual gases. Changes in gas composition may be recorded with respect to time, to allow for accurate process control.

The RGA generally operates at unit mass resolution; that is to say it may only resolve integer *m/z* values (Chambers 2005, O'Hanlon 2003). As the RGA is limited to integer *m/z* resolution it cannot discriminate between residual gases of similar mass; for example the RGA will sense both N_2 (28.0061 amu) and CO_2 (27.9949 amu) as an integer mass value of 28 amu. The RGA quadrupole mass filter performs rapid scans of *m/z* values from 1 to typically 100, although commercially available RGA devices may extend this mass range up to *m/z*= 300 (MKS Instruments Inc. 2004). The RGA does not provide the mass range or precision of traditional mass spectrometers found in analytical laboratories, but is relatively inexpensive and easier to operate and deploy in comparison.

Regardless of its precision shortfalls, the versatility, ease of operation and relatively low cost of the RGA have seen it employed extensively in research and industrial applications. Herbert employed several RGAs to monitor the beam line of the Daresbury Synchrotron Light Source (Herbert 1996). RGAs may be found as online process monitoring tools (Dixon 1997), and are commonly employed as vacuum system leak detection instruments (MKS Instruments Inc. 2004).

6.3 LAMS Employing the Traditional RGA Configuration

For routine leak detection or background gas analysis the RGA is generally mounted on a port directly adjacent to the chamber (O'Hanlon 2003). This section details the experimental work and the results obtained when monitoring laser ablation events with the RGA mounted in this traditional configuration: adjacent to the vacuum chamber and not in a direct line-of-sight with the laser-induced plasma plumes. Neutral and ionic species generated during the laser ablation of silicon, copper and Fecralloy (Fe 72.8%, Cr 22%, Al 5%, Zr trace, Y trace) were monitored with the RGA, the effect of laser repetition rate on the resultant mass spectra was quantified, and preliminary materials compositional analyses are reported.

6.3.1 Experimental set up

A set of apparatus was designed and constructed to facilitate simultaneous LIBS and LAMS plasma diagnostics. The MS analyses were performed using a commercially available RGA- the MicroVision Plus supplied by MKS Spectra, which has a mass range of 300 amu and unit mass resolution. The MicroVision

plus employs a quadrupole mass filter coupled to an EI ion source and a combined Faraday cup/electron multiplier ion detection system. The use of this RGA enforced a constraint on the maximum ambient pressure for these investigations; the maximum operating pressure of the RGA is 1×10^{-4} mbar (MKS Instruments Inc. 2004). The apparatus shown schematically in Figure 6-11 allows for the simultaneous LIBS and LAMS investigation of solid or gaseous analytes.

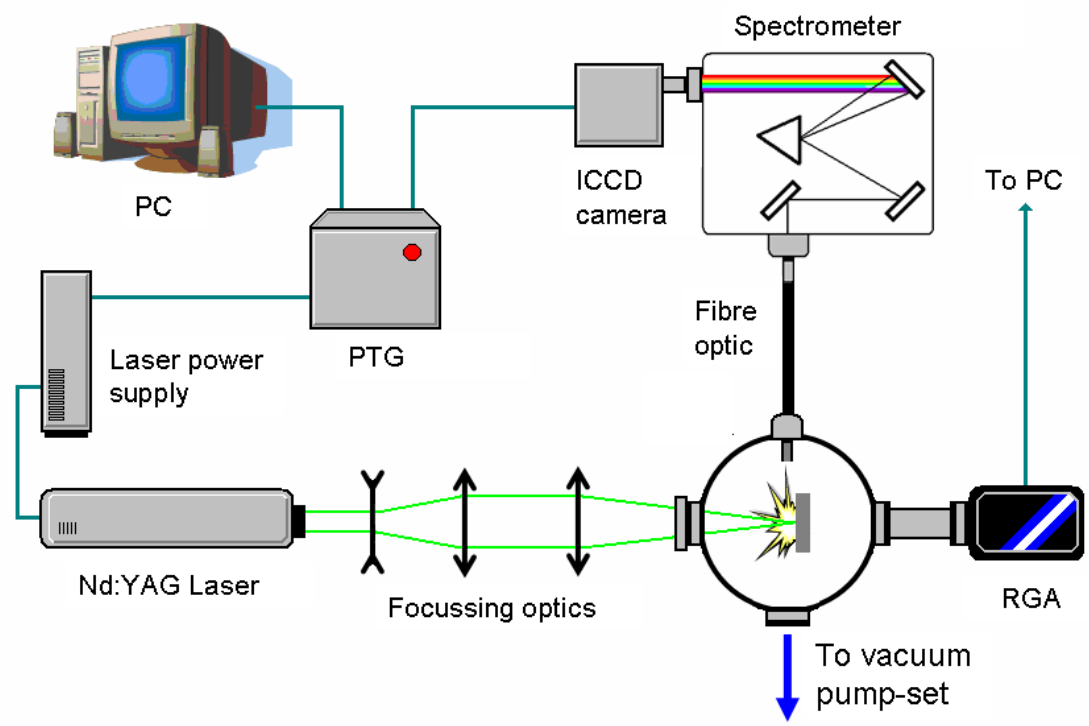

Figure 6-11 Schematic diagram of the combined LIBS / MS apparatus

The chamber, pumping set, gauges, laser, sample stage and optical emission spectroscopy apparatus are identical to those described in Section 5.4. The laser acts as both an excitation source for LIBS and as a sampling method to volatilise the analyte into the gaseous phase for introduction into the RGA. For most of the LIBS/LAMS experiments described here the laser was operated at a repetition

rate of 1Hz unless otherwise specified. In order to maximise the amount of ablated material entering the gas phase the samples were positioned at the focal point of the focussing lens; this improves the sensitivity of any RGA measurements. As previously discussed, the *x*-*y* stage was used to position the samples such that each analysis was performed on a fresh sample surface.

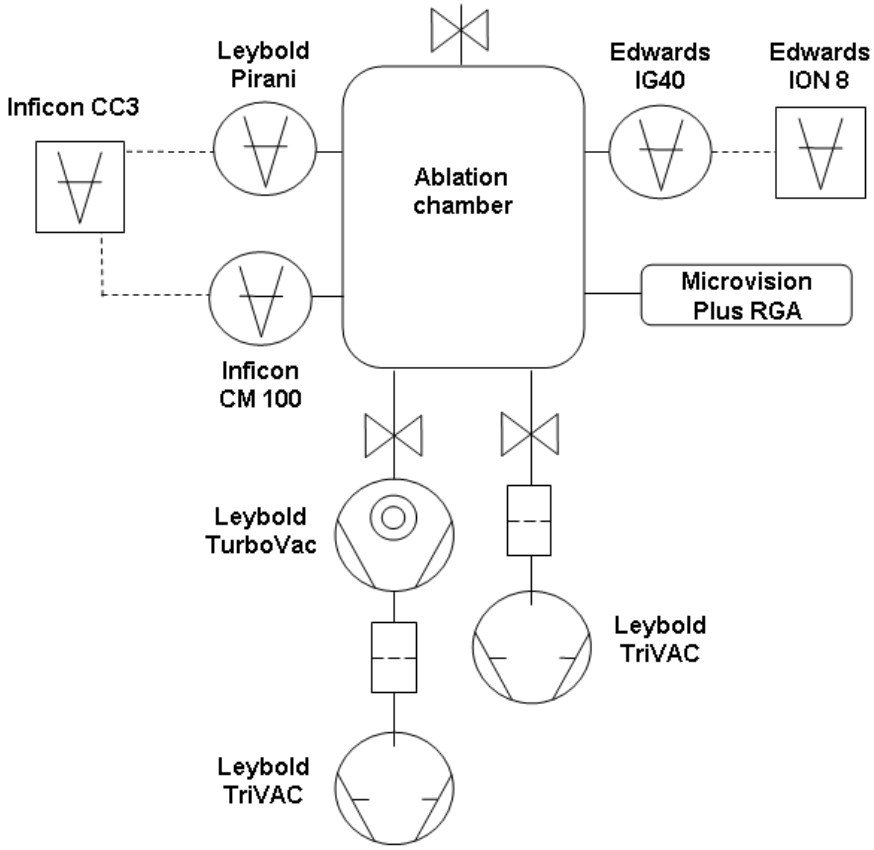

Figure 6-12 Schematic diagram of the ablation chamber vacuum pump-set

Figure 6-12 illustrates the vacuum chamber, pump-set and measurement apparatus with the RGA installed adjacent to the chamber. The RGA was mounted vertically from the base of the vacuum chamber and hence was not in direct line-of-sight of the laser ablation plume; therefore the RGA does not sample the plume directly, but rather analyses the residual gases present in the

chamber and monitors their respective partial pressures. The RGA was controlled using MKS Instruments' Process Eye Professional v5.22.0 software and the data obtained manipulated using MKS Instruments' Recall v5.22.0 software.

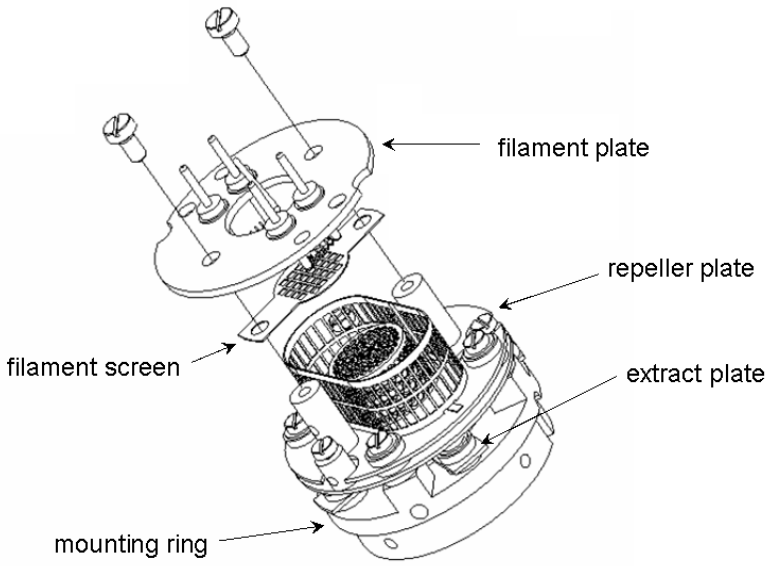

Figure 6-13 The MKS Microvision RGA ion source assembly[†]

The RGA's integral electron ionisation ion source ordinarily ionises neutral gas species for subsequent mass analysis. The MicroVision EI ion source features a repeller plate that accelerates the analyte ions towards the mass filter region, shown expanded in Figure 6-13. Ionic species generated in the laser-induced plasmas cannot be monitored by the RGA using the standard source configuration, as the repeller plate repels any ions generated externally to the ion source. Removal of the EI source repeller plate enables ionic species generated externally to the source to enter the mass filter for analysis; in this way the RGA

[†] Taken from the MicroVision+ RGA manual, Hickson J., MKS Instruments Inc., 2005, page 41.

may be configured to monitor either neutral or ionic plasma plume constituents at any given time.

When recording over large mass ranges the scan time of the RGA is long (10.52 seconds for a 300 amu scan) compared with the transient laser ablation event. To increase the scan frequency only masses known to be of interest were monitored. Initial background mass spectra were obtained before laser ablation of the sample was carried out. It was assumed that the sample materials used were homogeneous and that no compositional change with depth due to laser drilling occurred. All mass spectra were captured using a gain of 20000 on the Faraday cup detector and the electron multiplier active, providing a minimum detectable partial pressure of 2.7×10^{-11}mbar (MKS Instruments Inc 2004).

Preliminary LAMS studies of silicon were performed to determine whether the RGA could detect an increase in the residual chamber gas partial pressures. The vacuum pump-set was used to reduce the chamber pressure below the maximum operating pressure of the RGA, attaining a chamber base pressure of $\sim 10^{-6}$ mbar; all experiments were conducted at this base pressure. The RGA was programmed to scan repeatedly through a range of *m/z* ratios from 1 to 300 amu; an increase in the partial pressures of the gaseous species inside the chamber was observed as the laser was fired. It is inferred that this increased gas load was due to the ablation of the target material, and thus may be analysed to determine the composition of the sample. Initial LIBS/LAMS investigations were conducted in order to determine whether the RGA was able to accurately discern the isotopic ratio of copper and validate the use of the system.

The optimum repetition rate for the laser was found by performing LAMS of copper at various laser pulse frequencies, 1, 2, 5 and 10 Hz. Simultaneous LIBS/LAMS analysis of Fecralloy (Fe 72.8%, Cr 22%, Al 5%, Zr trace, Y trace) was conducted to determine whether either technique can be employed to detect trace amounts of minor elements in a major element matrix. The RGA EI filament was degassed prior to each set of readings.

6.3.2 Results: LAMS of Silicon

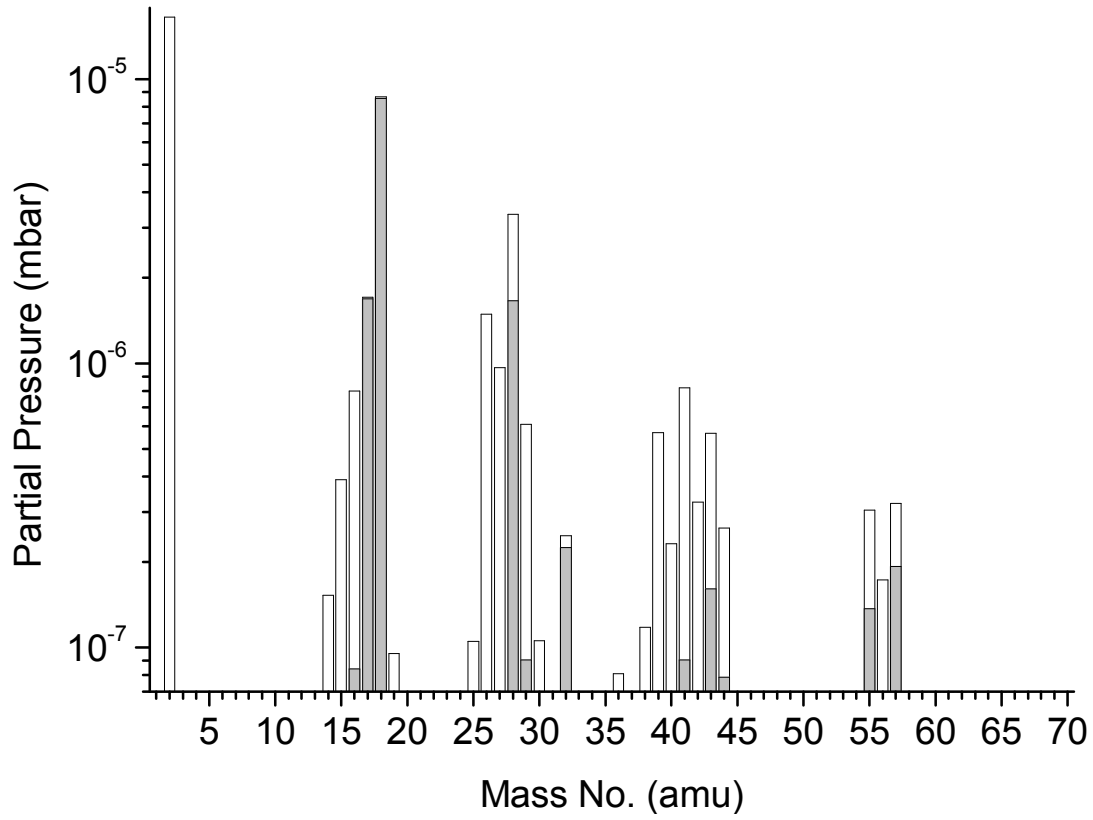

Figure 6-14 Bar chart mass scans taken before and immediately after laser ablation of silicon

Figure 6-14 is a bar chart mass scan illustrating the change in partial pressure of the chamber residual gases during laser ablation of silicon; the grey bars

represent the partial pressures before ablation, the white bars represent the partial pressures recorded immediately after laser ablation. The RGA is operated in its conventional mode, employing the EI source to monitor neutral residual gas species. The bar chart mass scan before laser ablation indicates that the residual gases are those one might expect at an ambient chamber pressure of 10^{-6} mbar. Peaks at 16 (O), 17 (OH) and 18 (H_2O) amu are typical of water contamination, 28 (N_2), 32 (O_2) and 44 amu (CO_2) are indicative of residual air, and the peaks at 41, 43, 55 and 57 amu are characteristic fragments of mechanical vacuum pump oil contamination (O'Hanlon 2003).

Considering the mass scan after laser ablation, it is clearly evident that there is a large contribution to the partial pressures from the pump oil contamination. The large peak at 2 amu is due to the dissociation of hydrogen from the hydrocarbon pump oil molecules. The other partial pressure increases are due primarily to pump oil fragments. Saturated straight chain hydrocarbons are characterised by groups of fragment peaks at centres of 14 amu apart coinciding with the number of carbon atoms in the chain fragment (O'Hanlon 2003). The fragment group for C_1 spans 12 to 16 amu; C, CH, CH_2, CH_3, CH_4. Higher carbon group fragments display similar ranges: C_2 24-30 amu, C_3 36-44 amu, C_4 48-58 amu and so on. As the RGA only has unit mass resolution it is difficult to ascertain whether an increase in *m/z* of 28 is due to the ablated silicon (28.0855 amu) or the pump oil fragment C_2H_4 (28.0538 amu). A molecular sieve foreline trap is employed in order to reduce pump oil contamination, but this is shown to be ineffective in this case, showing the importance of using dry pumps on such systems.

The pump oil contamination was detected when monitoring the neutral residual gas species; it was hoped that if the ionic species from the plasma were generated then this problem may be overcome. Also copper has isotopic peaks at 63 and 65 amu which were found to have a low pump oil contribution.

6.3.3 Simultaneous LIBS and LAMS of Copper

In an attempt to overcome the problem of pump oil contamination corrupting the partial pressure scans, it was decided to analyse a sample of a specific mass that did not display significant partial pressure increase during the laser ablation of silicon as described in the previous section. Copper was chosen as a suitable, vacuum compatible, readily available sample, having isotopes of masses 63 and 65 amu; from Figure 6-14 it can be seen that there is negligible pump oil contribution to these masses, so any change in their partial pressures may be ascribed to an increased copper vapour gas load from laser ablation of the sample.

Prior to the MS analysis of neutral and ionic species, a screening experiment using LIBS was performed to ascertain whether the laser-ablation of copper produced any copper ions under the conditions of this study. The chamber was evacuated to ~10^{-6} mbar and a LIBS spectrum of the copper sample captured, shown in Figure 6-15. The figure is the software accumulation of ten individual spectra, and was captured using the 2400 grooves mm^{-1} grating, using a gate delay of 600 ns, a gate width of 800 ns, an ICCD gain of 150 and a laser repetition rate of 1 Hz.

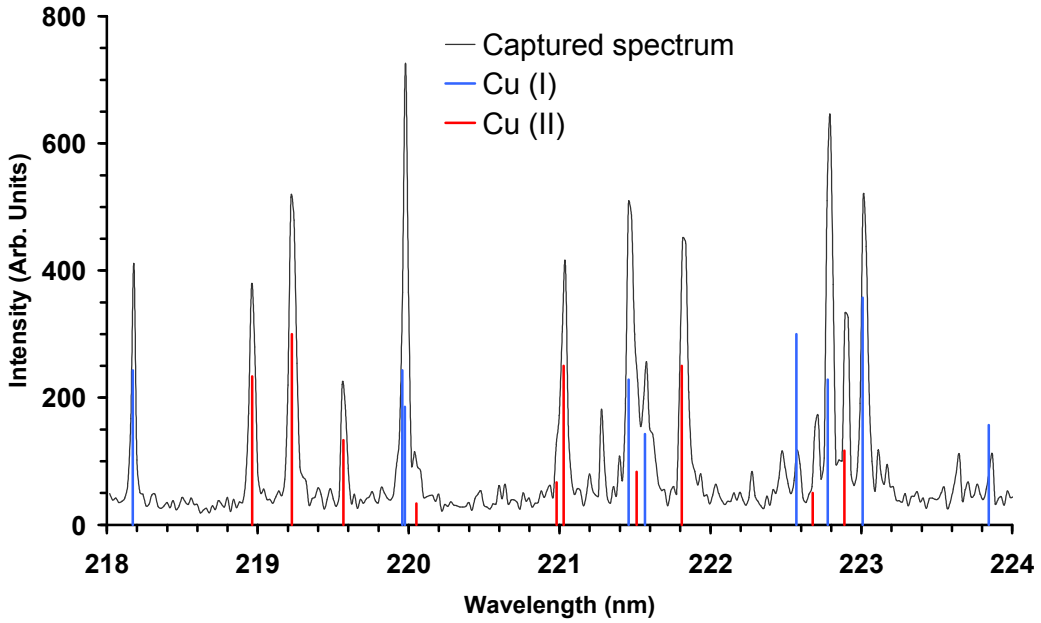

Figure 6-15 LIBS spectrum of copper, wavelength range 218-224 nm

The captured spectrum is given in black, and the predicted neutral (blue) and singly ionised (red) copper emission line wavelengths are overlaid for peak identification (CRC Press 1988). From Figure 6-15 it is seen that there coexist both neutral and ionic species in the copper plasma plume; having established the presence of both neutral and ionic copper species, the laser-induced plasmas were subsequently subject to MS analyses.

Figure 6-16 shows the partial pressure traces for selected *m/z* with respect to time (scan number), observed during laser ablation of copper, and employing the RGA EI source to monitor neutral species. Partial pressures of 32 amu (top trace, red), 16 amu (middle trace, blue) and 63 amu (bottom trace, green) were monitored whilst firing the laser at different repetition rates of 1, 2, and 5 Hz (from left to right).

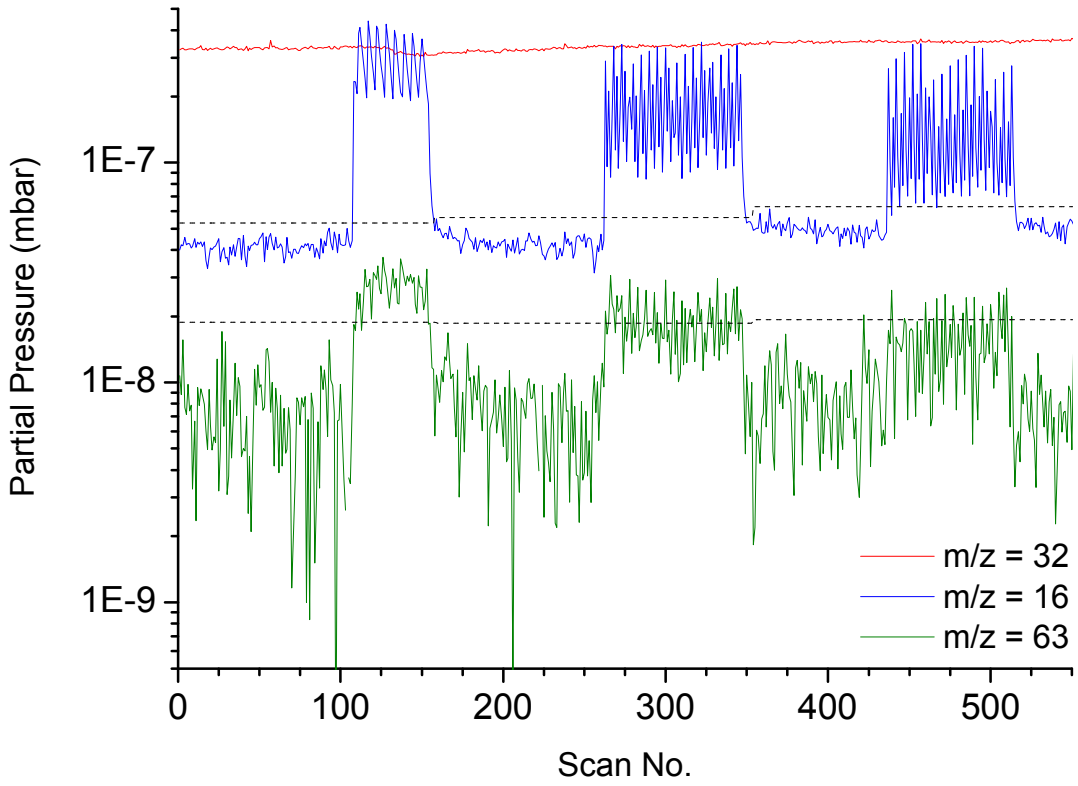

Figure 6-16 Partial pressure trace of m/z = 16, 32, 65 during laser ablation of copper

The laser could not be operated at its maximum repetition rate of 10 Hz using this particular experimental set-up as the gas load from ablated material at this frequency is too great for the turbo pump (pumping speed 55 ls^{-1}) to maintain the chamber pressure below the maximum operating pressure of the RGA (1×10^{-4} mbar). The horizontal dashed lines across the *m/z* = 16 and 63 traces represent the limits of detectable signal (LODS) for the given masses at their respective pressures. A detectable signal is defined as one being greater than 3 times the standard deviation of the background signal when the laser is not firing (Yueh et al. 2000), i.e.:

$$LODS \geq \bar{x} + 3\sigma \qquad (6.19)$$

where $\bar{x}$ is the mean background level and σ is the standard deviation of the background signal. Any signal lower than this LODS cannot be clearly resolved from the background noise. The background steadily rises after each run of laser shots due to the increased amount of gas phase ablated material in the chamber. The LODS was recalculated before each change in laser repetition rate to account for the variance in background level.

In Figure 6-16 the lower trace, mass 63 amu, represents the major naturally abundant copper isotope; the minor isotope mass 65 amu was also monitored but due to overlap is omitted from Figure 6-16 for clarity. The middle trace, mass 16 amu, may represent either atomic oxygen or a mechanical pump oil fragment CH_4 within the resolution of the RGA. The top trace, mass 32 amu, molecular oxygen was monitored to confirm the origin of the 16 amu peak. It can be seen that the 32 amu trend remains at a constant average level while the 16 amu trend increases during the ablation process; therefore the contribution to m/z = 16 from atomic oxygen is negligible which provides further confirmation that pump oil contamination was present within the chamber.

It can be seen that increasing the repetition rate of the laser is detrimental to the m/z = 63 signal obtained. The mean detected partial pressure drops and the relative standard deviation of the signal increases, as shown in Figure 6-17.

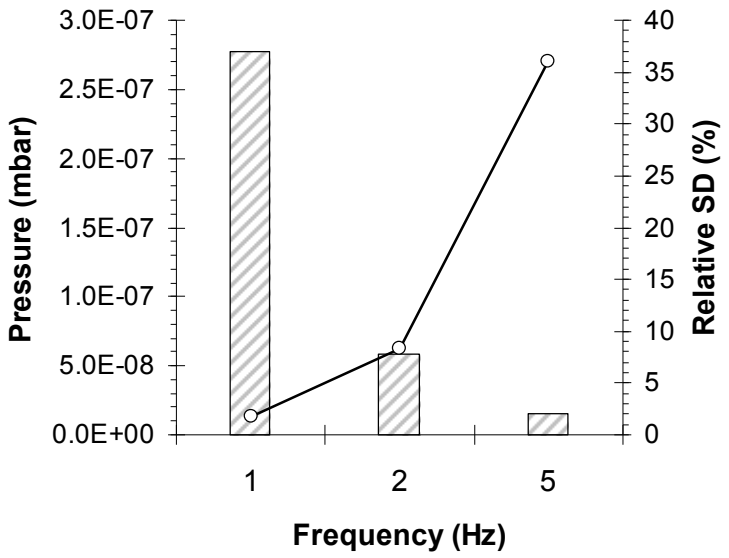

Figure 6-17 Mean detected partial pressure and relative standard deviation versus laser repetition rate

The 63 amu trace (Figure 6-16) is barely resolvable above the defined limit of detection with the laser pulsing at 5 Hz. Operating the laser at higher pulse frequencies effectively lowers the sensitivity of the RGA. The rise in background signal on the 16 and 63 amu traces is due to the increased amount of each respective residual gas within the chamber as a result of the laser ablation process.

The partial pressure of mass 16 features a 'saw tooth' profile which becomes more evident with increased laser pulse frequency. It is believed that this is due to a lack of synchronisation between the short laser pulse and the RGA mass scan (in this case 0.87 s at a minimum detectable partial pressure of 2.0×10^{-11} mbar). A suitable timing and delay generator would solve this mismatch and should produce a steady partial pressure trace (Kuzuya et al. 1998).

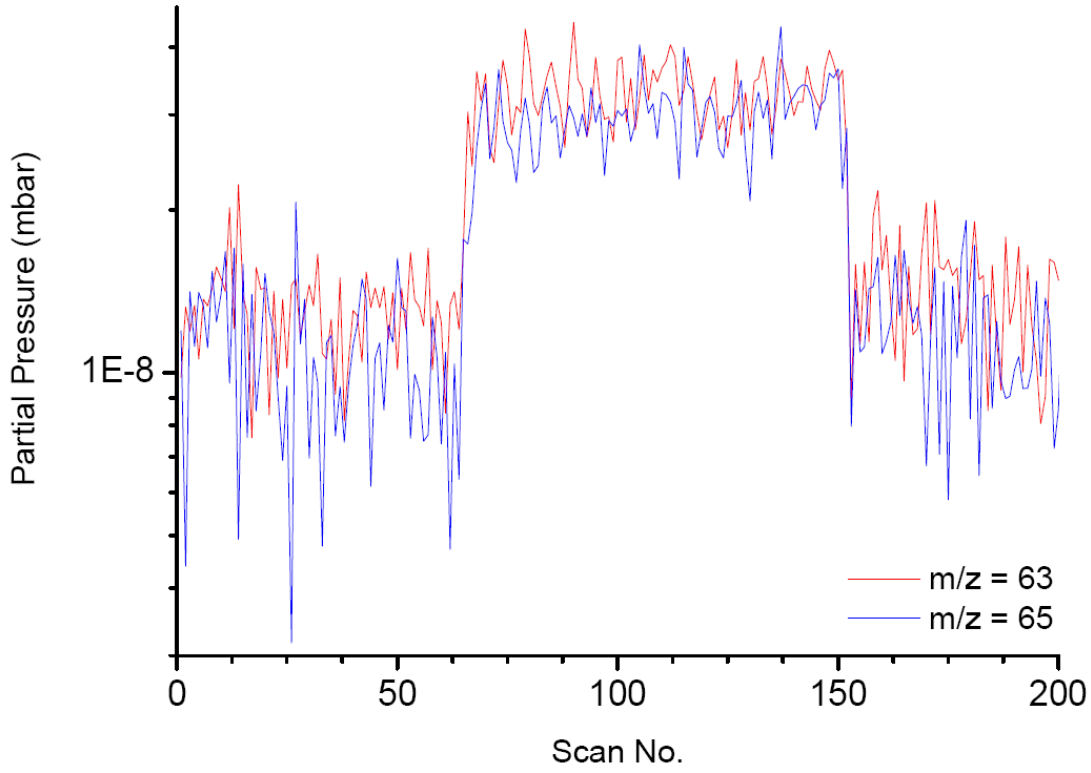

Figure 6-18 Partial pressure of m/z = 63, 65 during laser ablation of copper- analysis of neutral species

Figure 6-18 shows how the 63 and 65 amu partial pressures vary with scan number, with the laser operating at a repetition rate of 1 Hz, and an RGA scan time of 0.70 s. In contrast, Figure 6-19 shows the analysis of ions present within the vacuum chamber, obtained with the RGA ionisation source and ion repeller plate removed, and the maximum potential of 110 V applied to the ion accelerator plate. Figure 6-19 clearly shows the short-lived nature of these ions, and reveals that the analysis of the ablated ions presents a greater problem in terms of synchronising the laser pulse with the RGA mass scan than when analysing neutrals.

At a pressure of $<10^{-6}$ mbar the gas molecules and ions present in the chamber are in the molecular flow regime, which implies that there are no interactions

between the neutrals and ions, ions and ions etc. It should be noted that ion optics were not used to focus the ablated ions into the RGA, and therefore any ions entering the RGA do so in a random fashion. As the RGA was not positioned in direct line-of-sight of the ablated sample, the number of ions entering the RGA is small compared to the number of ions colliding with the chamber walls and subsequently neutralised. This short-lived nature of the ionic species leads to the lower sensitivity of the instrument when configured to monitor ions.

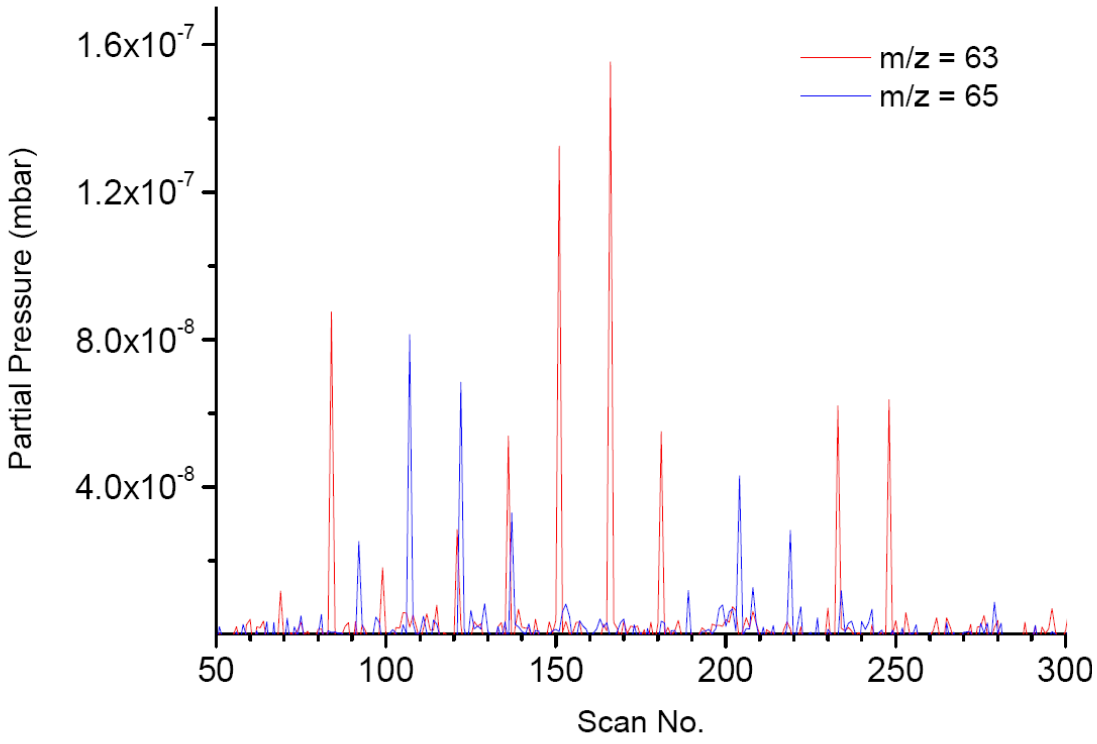

Figure 6-19 Partial pressure of m/z = 63, 65 during laser ablation of copper- analysis of ionic species

Figure 6-20 compares the natural abundance of the two isotopes of copper (de Hoffmann and Stroobant 2003) to the relative percentage of mass 63 amu and mass 65 amu observed when analysing either the neutral or ionic species produced by laser ablation of copper.

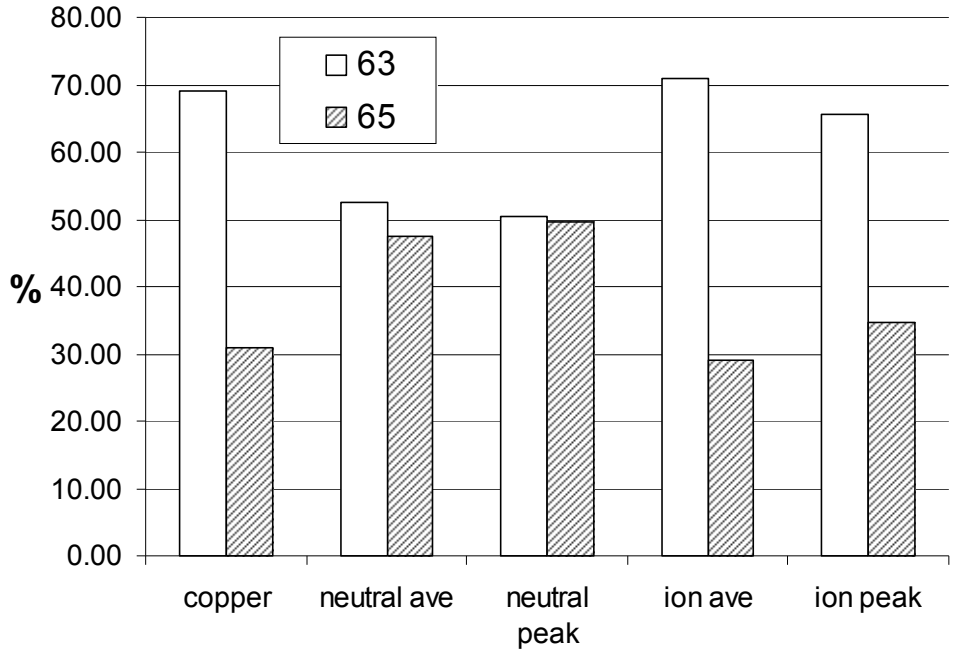

Figure 6-20 Comparison of the measured neutral and ionic species signals to the natural abundance of Cu 63 and Cu 65 isotopes

Two different methods were employed to determine the relative abundance of 63 amu and 65 amu species within the vacuum chamber; measuring the average partial pressure signal of each mass during laser firing, or maximum peak signal for each mass during laser firing. These two methods were applied to the analysis of neutral and ionic species. It can be seen that the average ion signal provides the closest correlation to the natural abundance of the two copper isotopes. A proposed reason for this mismatch in the neutral signals may be that pump oil fragments provide extra contributions to the partial pressures recorded for 63 and 65 amu. As the RGA quadrupole has unit mass resolution it is extremely difficult to ascertain the true nature of the species contributing to the partial pressure scans of 63 and 65 amu with the current experimental configuration.

6.4 RGA Operated in Line-of-Sight of the Plasmas

In order to monitor the laser ablation events directly, an apparatus was designed and constructed that would allow the RGA to be positioned in line-of-sight of the laser-induced plasmas. Using this sampling geometry it was hoped that the effective sensitivity of the system would be improved, by sampling a greater proportion of plasma species rather than any contaminant residual gases present in the chamber. This apparatus is described in Section 6.4.1., and the results obtained are presented in Section 6.4.2.

6.4.1 Experimental Set up

The line-of-sight MS plasma analysis apparatus is illustrated schematically in Figure 6-21, and features the same Nd:YAG laser, MKS Spectra RGA, vacuum pump-set and measurement system and vacuum chamber as described previously in Section 4.2. The RGA was mounted adjacent to the vacuum chamber in a stainless steel housing pumped by a separate vacuum pump-set as shown in Figures 6-22 and 6-23. The RGA housing was attached to the main chamber by an adaptor flange that featured a 20 μm orifice plate, thus restricting the angle of acceptance for particles entering the RGA. The RGA housing may be evacuated to a base pressure of ~ 10^{-7} mbar using a Leybold Turbovac 50 turbomolecular pump backed by a Leybold TriVAC dual stage rotary pump.

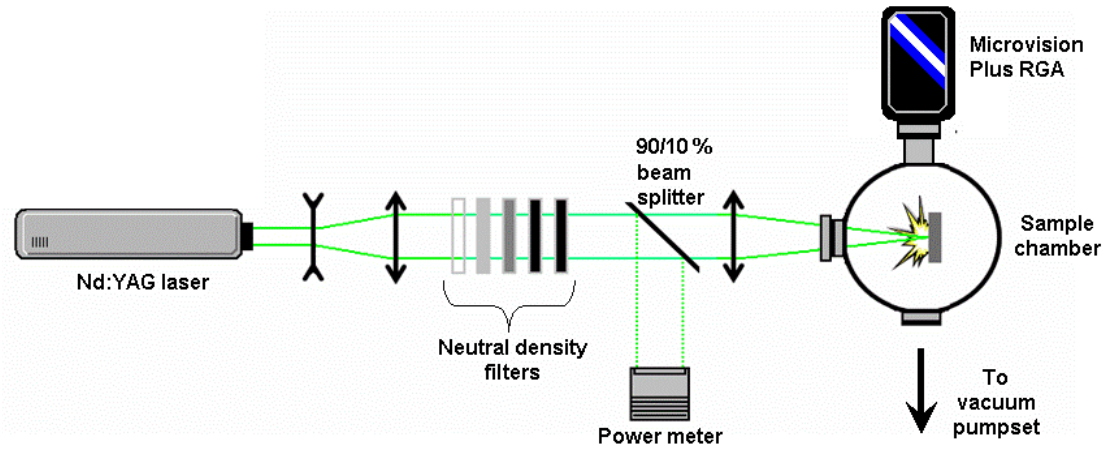

Figure 6-21 Schematic diagram of line-of-sight LAMS instrument

Rough vacuum pressures within the RGA housing were measured with a Varian TC0531 thermal convection gauge operated by a Varian SenTorr gauge controller; this gauge was mounted at the exhaust of the turbomolecular pump so that it may also monitor the pump backing pressure. Chamber pressures ~10^{-3} and below were measured using a Varian CC525 cold cathode gauge, again operated using the Varian SenTorr controller.

A molecular sieve foreline trap was integrated into the pump-set to reduce mechanical pump oil contamination in the RGA housing. The RGA housing may be isolated from the main ablation chamber by means of a quarter-turn Swagelok plug valve, so that the ablation chamber may be vented to atmosphere for sample changing whilst the RGA housing remains under high vacuum, thus reducing pump down time.

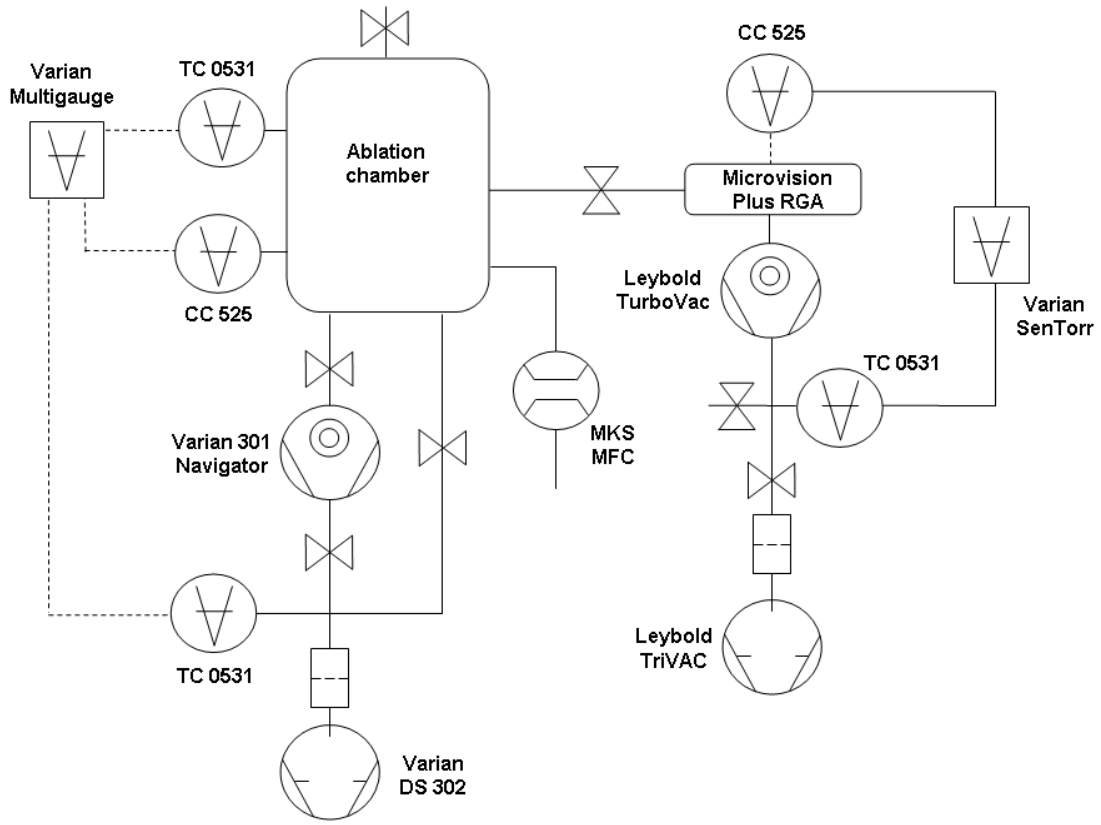

Figure 6-22 Schematic diagram of the line-of-sight LAMS instrument vacuum pump-set

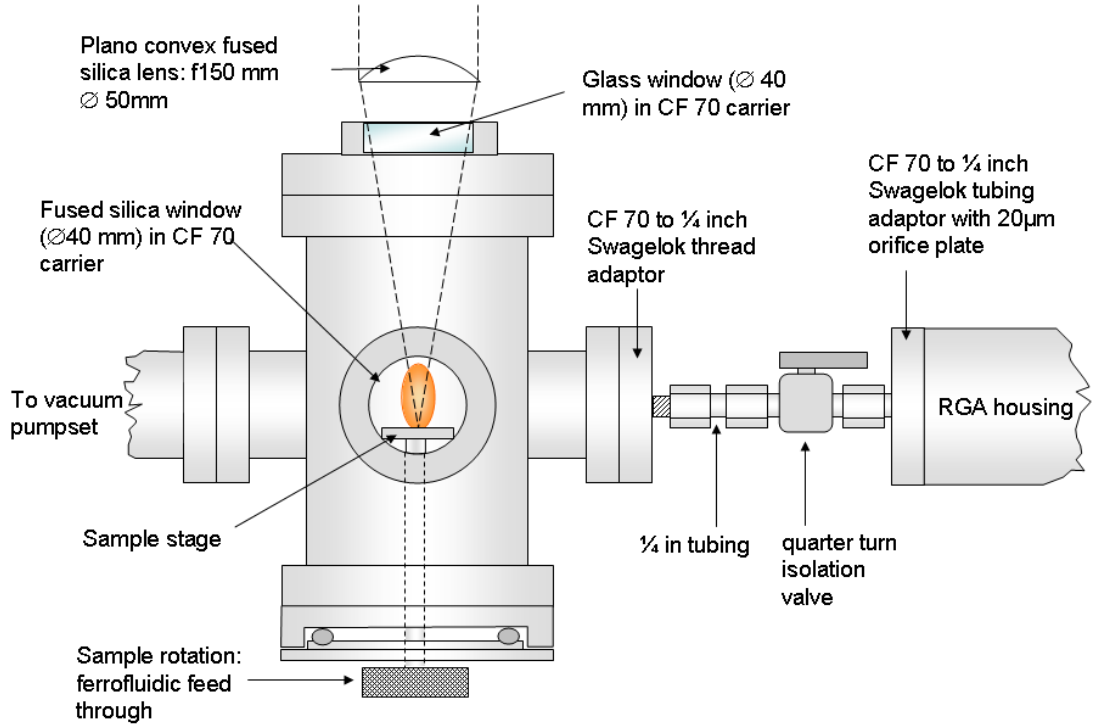

Figure 6-23 Representation of the ablation chamber and RGA housing coupling

Laser pulses were focussed onto the sample surface through a 50 mm diameter, 150 mm focal length glass lens, producing a laser spot size of ~ 400 μm. Laser radiation was admitted to the ablation chamber through a glass window mounted in a CF70 carrier, and the optical plasma emissions were collected through a quartz window mounted similarly. The samples were mounted on a rotating stage enabling each ablation event to be conducted on a fresh area of sample; ten 'cleaning shots' were performed before each data acquisition in order to remove any surface contamination present.

6.4.2 Results: LAMS of Silicon

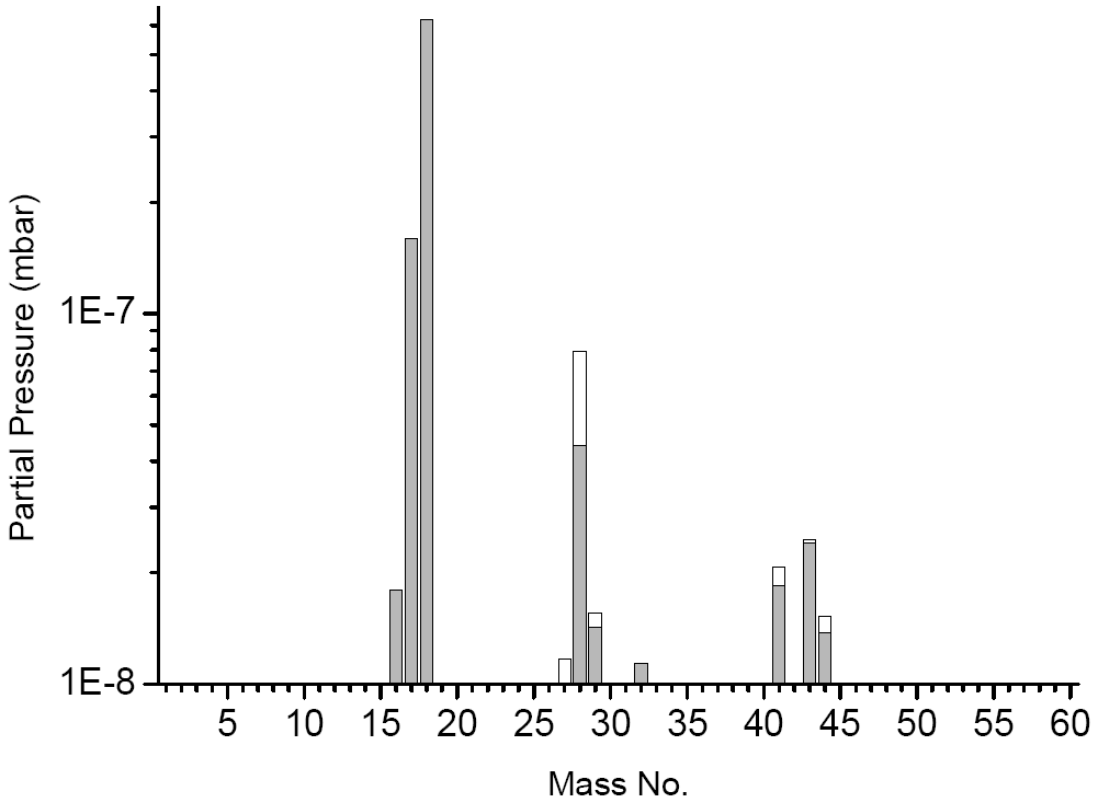

Figure 6-24 Bar chart scan before and during laser ablation of Silicon

An initial background scan of the residual gases present in the ablation chamber and analyser housing was performed, and is presented shown in Figure 6-24 as the grey bars. The main ablation chamber was maintained at a pressure ~ 10^{-6} mbar, with the RGA housing maintained at a pressure ~ 10^{-7} mbar. As before, the RGA filament was de-gassed prior to data acquisition.

It is evident from Figure 6-24, there is far less vacuum pump oil contamination when using the differential pumping arrangement and separate analyser housing. Comparing the background scan in Figure 6-24 to that shown in Figure 6-14 it is striking that the *m/*z values of 55 and 57, indicative of pump oil contamination (O'Hanlon 2003) are absent; the RGA is much less sensitive to chamber contamination in this configuration.

Laser ablation of a silicon sample was performed and the bar-chart scan taken during this process is presented as the white bars in Figure 6-24. Due to the differential pumping arrangement, it was possible to operate the laser at its maximum repetition rate of 10 Hz without the gas load due to sample ablation causing the chamber pressure to rise above the safety threshold of the RGA; all data presented here were performed with a laser repetition rate of 10 Hz. When comparing Figure 6-24 to Figure 6-14 it is apparent there is much less contribution to the mass scan from pump oil fragments.

Figure 6-25 presents a trend mode RGA scan performed whilst monitoring several *m/*z values for neutral species, immediately before, during and after laser ablation of a silicon sample.

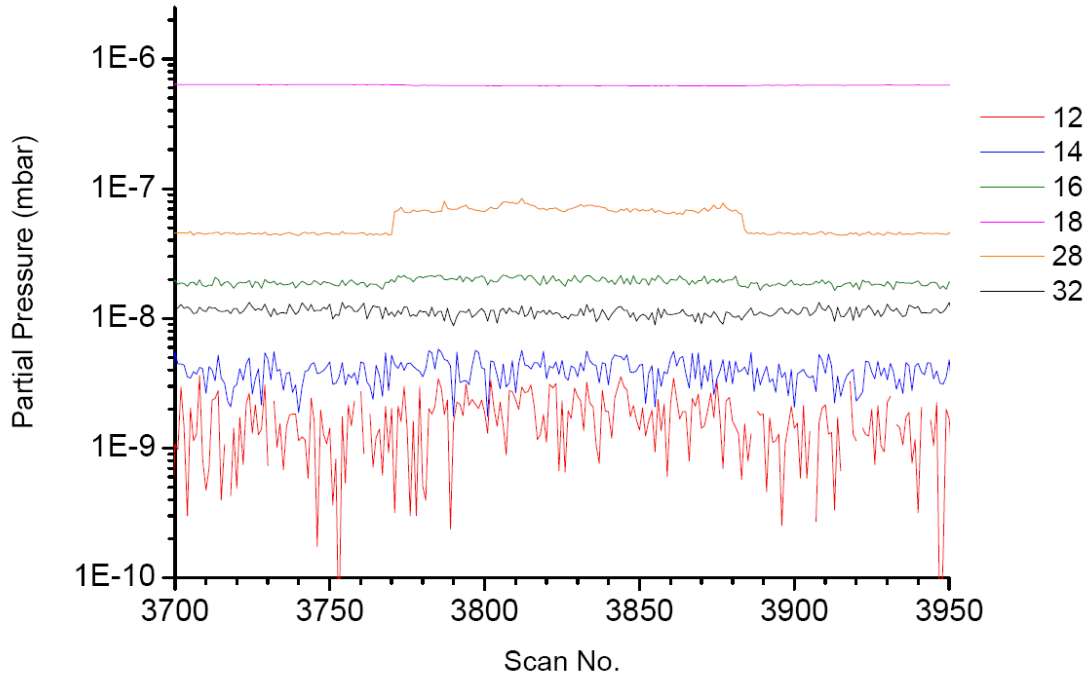

Figure 6-25 Trend mode bar-chart scan of selected neutral species before, during and after laser ablation of silicon

Mass 12, attributed to carbon, was monitored to determine whether contamination form cracked hydrocarbon pump oil fragments would be observed. Masses 14 (atomic nitrogen), 16 (atomic oxygen) and 32 (molecular oxygen), and 18 (water) were monitored to ascertain whether there was any contribution to the RGA signal from the most common chamber residual gases (O'Hanlon 2003).

Mass 28, that of silicon, was monitored during ablation of the silicon sample and was seen to increase throughout the duration of the laser cycle then return to its background level immediately the laser ceased firing; there was a negligible increase in the partial pressures of the other masses recorded.

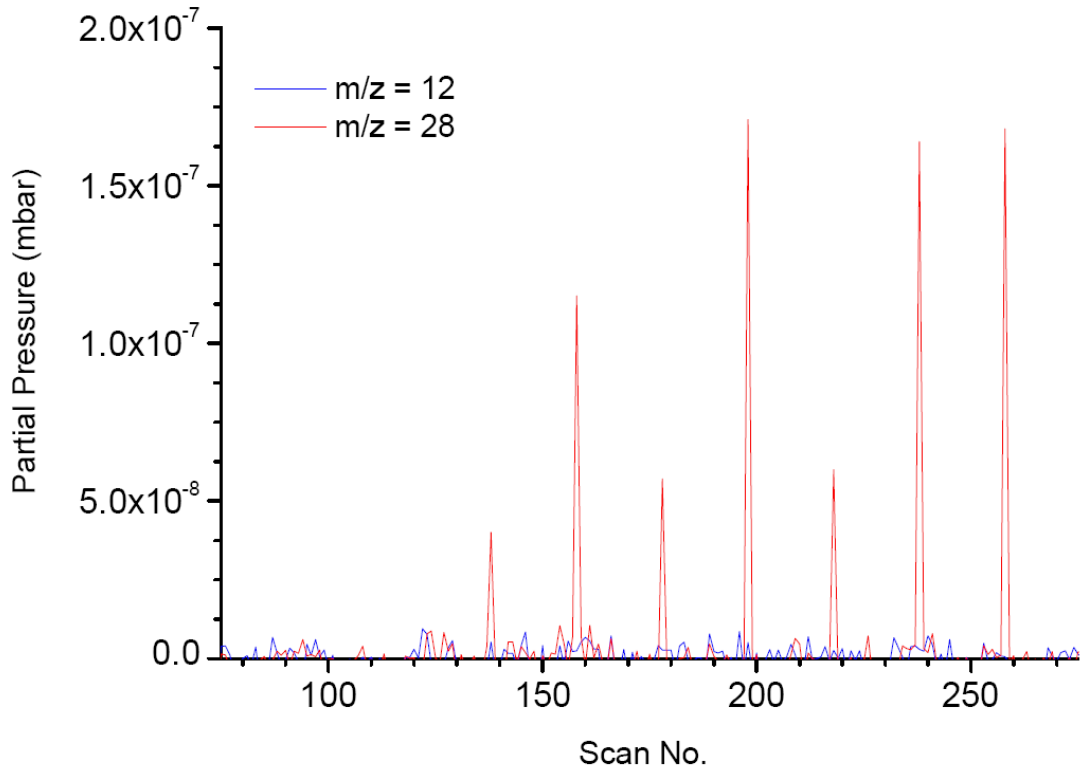

Figure 6-26 Trend mode scan of ionic species having *m/z* of 12 and 28 during laser ablation of silicon

Figure 6-26 presents the RGA trend mode scan data captured during laser ablation of a silicon sample, with the RGA configured to monitor ionic species. Only two masses were monitored here to reduce the RGA scan time and to improve the synchronisation between the RGA scan and the laser pulse. Mass 28, representing silicon, was monitored alongside mass 12, attributed to carbon, to ascertain whether pump oil contamination was evident when employing the RGA to monitor ionic species during laser ablation of silicon. The intensity of the silicon 28 peak is seen to vary with scan number; this is again due to a lack of synchronisation between the laser pulse and the RGA mass scan. There is no discernible variation in the intensity of the m/z = 12 trace, indicating that very few ionic pump oil fragments were able to enter the analyser housing and corrupt

the RGA spectrum. Unfortunately, due to time constraints, no further progress could be pursued on this potentially fruitful avenue of research.

6.5 Summary

Plasma plumes resulting from Nd:YAG laser ablation of copper and silicon were analysed using Laser-Induced Breakdown Spectroscopy (LIBS) and Laser Ablation Mass Spectrometry (LAMS). A commercially available Residual Gas Analyser (RGA) was employed to perform mass spectrometric analysis of the neutral and ionic species created during the laser ablation process. The RGA was mounted in the traditional sampling configuration, adjacent to the ablation chamber. Investigations of the laser repetition rate have shown that increasing the frequency of the laser pulse rate was detrimental to the mass spectra produced; the average detectable partial pressure dropped and the relative standard deviation of the signal increased. The RGA was shown to be susceptible to corruption of partial pressure measurement due to pump oil contamination when monitoring neutral gaseous species generated by the ablation event. Lack of synchronisation between the transient laser pulse and the RGA mass scan resulted in unstable partial pressure readings when analysing both neutral and ionic species.

The RGA was found to be too sensitive to chamber contamination when applied to the analysis of neutral species. Pump oil molecules present within the chamber were ionised by the RGA ion source along with the ablated analyte neutrals. These high molecular weight long chain hydrocarbons have complex cracking patterns that can contribute a significant increase in the partial pressure

signals recorded for a large range of masses. In the case of the two peaks that were monitored during the copper study (63 and 65 amu), it is now believed that the inclusion of $C_5H_3^+$ and $C_5H_5^+$ pump oil fragments has led to erroneous results when using the RGA with its associated hot filament ion source. Even though a fore-line oil filter was incorporated in the system it is known that oil molecules can still backstream into the vacuum chamber. These molecules tend to adsorb on to all the internal chamber surfaces; at a pressure of 10^{-6} mbar, there are approximately 10^6 molecules adsorbed on the walls of the system for each molecule in the gas phase (de Segovia 1996). During the ablation process, the expanding plume promotes electron/ion-stimulated desorption of oil contamination from interior chamber surfaces, and it is these molecules that are subsequently ionised and then analysed by the RGA.

When performing direct line-of-sight mass spectrometric analyses of the laser-induced plasmas, the RGA was found to be less susceptible to measurement corruption by chamber contaminants. Using the line-of-sight RGA sampling configuration, analysis of the neutral and ionic constituents of laser-induced silicon plasmas revealed a much lower contribution to the mass spectra from cracked hydrocarbon pump oil fragments. The use of the 20 μm inlet orifice restricts angle of acceptance for particles entering the RGA to a 'corridor' lying along the line-of-sight from the plasma to the RGA inlet. As such, it is more likely that particles ejected from the expanding laser-induced plasma plumes, rather than residual gas pump oil contaminants, will be recorded by the RGA; this leads to the cleaner RGA spectrum. However, the issue of synchronisation between the RGA mass scan and the laser pulse remained, evident in the variable

partial pressure measurements of both ionic and neutral species; the short-lived nature of the ionic species lead to a lower sensitivity of the instrument when configured to monitor ions. Development of ion optics to extract the ionic species from the plasma plumes and accelerate them towards the RGA may improve instrument sensitivity and reduce the signal background noise.

6.6 Conclusion

The potential for using a commercially available RGA for plasma analysis has been proven. The limitations imposed by the relatively slow scan speed of the quadrupole mass spectrometer could potentially be overcome by using a Time of Flight mass spectrometer, which is particularly suited to laser-ablation mass spectrometry as it requires ions to be produced in pulsed packets (de Hoffmann and Stroobant 2003). The synchronisation of the RGA mass scan to the transient laser pulse has to be addressed if quadrupole LAMS is to be a used as an accurate, reproducible analytical technique (Kuzuya et al. 1998).

7 General Conclusions and Further Work

The goal of this work was to develop a set of apparatus to permit a thorough investigation of the behaviour and properties of laser-induced plasmas, by a combination of optical emission spectroscopy and mass spectrometric methods and to ascertain the validity of the premise that LTE exists within these transient plasmas. In this respect, the project was a success. However, deeper investigation of the laser-induced plasmas has presented as many questions as it has provided satisfactory answers. If nothing else, the work presented in Chapter 4 has cast the shadow of doubt on the commonly held assumption that laser-induced plasmas exhibit LTE. Laser ablation silicon plasmas have been shown to satisfy the minimum electron number density requirement for LTE, but differing measurements of electron temperature and ionic species temperature show that the plasma may not be characterised by a single temperature; it is most definitely not in thermal equilibrium.

LIBS is a developing technology and is growing in popularity amongst research and industrial communities. The acceptance of LIBS as an accurate materials analysis technique relies on the development of a thorough understanding and knowledge of the complex processes governing transient plasma formation and evolution. There is a fundamental lack of understanding regarding the LIBS plasma, manifest in the fact that a wholly inappropriate plasma model has traditionally been applied to the analysis of these plasmas.

Mass Spectrometric (MS) and optical emission spectroscopy diagnostics of Nd:YAG (532 nm) laser-induced plasmas were performed. A set of apparatus were designed, constructed and tested, that permitted analysis of the laser-induced plasmas through a range of ambient pressure regimes. This apparatus facilitated simultaneous LIBS and MS analysis of the laser-induced plasmas through a range of pressure regimes from atmospheric pressure down to 1×10^{-4} mbar. A rigorous optical emission spectroscopy study of single crystal silicon plasmas was performed, combining dispersed spectroscopic measurements with fast-gated photography to characterise the expansion dynamics of the plasmas.

Plasma plumes were characterised in terms of electron excitation temperature T_e, ionisation temperature T_i, and electron density N_e with respect to time at each pressure considered. The Boltzmann plot and 2-line-ratio methods of plasma temperature determination were found to breakdown, giving clearly erroneous results; the lack of suitable emission lines resolvable within the range of the imaging apparatus, and uncertainties in the transition probability data, are believed to cause this problem (Milan and Laserna 2001).

Electron excitation temperatures were obtained from the line to continuum ratio of the Si (I) 288.16 nm line, which yielded temperatures in the range 8000 – 22000 K. Ionic species temperatures were determined from an iterative solution of the Saha-Eggert equation yielding temperatures in the range 13000 – 23000 K. Electron number densities were determined from the Stark broadening of the Si (I) 288.16 nm emission line; number densities in the range of 2.9×10^{16} to 5.5×10^{19} cm^{-3} were observed. These values of electron temperature and number

density are similar to those determined in previous studies (Milan and Laserna 2001, Liu et al. 1999, Le Drogoff et al. 2001, Shaikh et al. 2006).

Work carried out under various ambient pressures consistently produced results that indicated three pressure regimes in which the characteristic behaviour of the plasma expansion dynamics and spectroscopic measurements were markedly different. These results have been linked to the changes in the mean free path of the ambient gas with changing pressure. It has been concluded that the plasma properties are dependent on the plasma morphology, which is in turn dictated by the level of plasma confinement by the ambient gas. The transition region between ambient pressures causing plume confinement or allowing free expansion is characterised by a mean free path that is comparable to the size of the laser-induced plasmas.

The Response Surface Methodology (RSM) was applied to the optimisation of the LIBS hardware. A RSM study of the LIBS hardware setup was performed and compared with a full, parametric investigation of the apparatus. The RSM results compared favourably with those derived from the manually performed parametric investigation. Small discrepancies between the RSM model and the manually collated data are due to the limitations of the RSM analysis software; only first or second order polynomial relationships may be fitted to the collected data. With this limitation in mind, the RSM analysis was shown to be a useful tool when applied to modelling the general response of a complex, multivariate system.

Mass spectrometric results indicated that a commercially available Residual Gas Analyser (RGA) has the potential to be used as a plasma diagnostic tool. The RGA was found to be less susceptible to measurement corruption from chamber contamination when sited in a direct line of sight of the laser-induced plasmas. The accuracy and reproducibility of the RGA partial pressure measurements are limited by the lack of synchronisation between the RGA mass scan and the laser pulse.

The results presented in this work will have implications for the LIBS community in general. This is the first, rigorously performed, analysed and documented study that comprehensively refutes the existence of LTE in transient laser-induced plasmas. The need for a model to explain the behaviour of such plasmas is critical if LIBS is to be accepted as an accurate, reproducible, quantitative analysis technique.

The work presented here shall underpin future research that will enable the development of a model that accurately describes non-LTE transient plasmas.

7.1 Further Work

Perhaps the most obvious starting point for future research is the development of a new model to describe transient, non-LTE plasmas; this is not a trivial task and will require a huge effort, not only from experimental physicists but theoreticians too.

Such is the almost infinite scope for variety in the LIBS set-up; there are a great many investigations that may be pursued with the present LIBS hardware configuration. As a direct continuation of the work presented here, the author wishes to investigate:

- the relationship between laser fluence and the fractional ionisation of the laser-induced plasmas
- changes in the laser ablation and breakdown thresholds versus ambient pressure
- the behaviour of plasmas induced from other single and multi-elemental samples, and the effects of different ambient gas compositions
- spatially resolved plasma diagnostics using the ICCD region of interest to zoom in on different areas of plume; this would enable any spatial variations in electron number density and temperature, and ion temperature, to be mapped
- variations in the amount of material ablated from the sample, and subsequently re-deposited, with respect to ambient pressure

Considering mass spectrometric plasma diagnostics using the Residual Gas Analyser (RGA), there are several avenues of further research that the author wishes to pursue:

- synchronisation of the RGA mass with laser pulse is essential to producing consistent, reproducible partial pressure measurements
- development of an ion optics system to extract ions from the laser-induced plasmas and inject them into the RGA mass analyser should help to improve instrument sensitivity

- investigation the effect of varying the laser fluence on the neutral to ionic ratio of plasma constituent species
- if possible use dry mechanical pumps to reduce pump oil contamination
- perform MS plasma diagnostics using a time-of-flight analyser; this type of mass spectrometer is more suited to the pulsed nature of ion formation encountered in laser-ablation plasmas than the quadrupole based RGA
- the current hardware configuration may be augmented with an electrostatic energy filter to analyse the ion energetics of the plasma (Torrisi et al. 2008), and a capacitance plate to directly perform real-time electron number density measurements (Bredice et al. 2007).

8 References

Abraham E.R.I., Cornell E.A. *'Teflon feed-through for coupling optical fibers into ultrahigh vacuum systems'* Applied Optics 37 (1998) 1762-3.

Acquaviva S., De Giorgi M.L., Marini C., Poso R. *'A support of restoration intervention of the bust of St. Gregory the Armenian: Compositional investigations by laser-induced breakdown spectroscopy'* Applied Surface Science (2005) 248, 218-223.

Alexander M.L., Smith M.R., Hartman J.S., Mendoza A., Koppenaal D.W. *'Laser ablation inductively coupled plasma mass spectrometry'* Applied Surface Science (1998) 127, 225-261.

Almirall J.R., Umpierrez S., Castro W., Gornushkin I., Winefordner J. *'Forensic elemental analysis of materials by laser-induced breakdown spectroscopy'* Sensors (2005) 4, 657-666.

Amador-Hernández J., Fernández-Romero J.M., Luque de Castro M.D. *'Three-dimensional analysis of screen-printed electrodes by laser induced breakdown spectrometry and pattern recognition'* Analytica Chimica Acta (2001) 435, 227–238.

Amoruso S., Bruzzese R., Spinelli N., Velotta R. *'Characterization of laser-ablation plasmas'* Journal of Physics B: At. Mol. Opt. Phys. (1999) 32, R131-R172.

Angeletti R., Giacchini A.M., Seraglia R., Piro R., Traldi P. *'The Potential of Matrix-assisted Laser Desorption/Ionisation Mass Spectrometry in the Quality Control of Water Buffalo Mozzarella Cheese'* Journal of Mass Spectrometry (1998) 33, 525-531.

Applied Physics Laboratory, The John Hopkins University *'A portable Universal Sensor: The Miniature Mass Spectrometer'*, promotional literature, (2006).

Arp Z.A., Cremers D.A., Harris R.D., Oschwald D.M., Parker Jr. G.R., Wayne D.M. *'Feasibility of generating a useful laser-induced breakdown spectroscopy plasma on rocks at high pressure: preliminary study for a Venus mission'* Spectrochimica Acta Part B (2004) 59, 987-999.

Asimellis G., Giannoudakos A., Kompitsas M. *'Phosphate ore beneficiation via determination of phosphorus-to-silica ratios by Laser Induced Breakdown Spectroscopy'* Spectrochimica Acta Part B (2006) 61, 1253–1259.

Badman E.R.; Cooks R.G. *'Special Feature: Perspective – Miniature Mass Analysers'*, Journal of Mass Spectrometry (2000) 35, 659-671.

Balzer H., Hoehne M., Sturm V., Noll R. *'Online coating thickness measurement and depth profiling of zinc coated sheet steel by laser-induced breakdown spectroscopy'* Spectrochimica Acta Part B (2005) 60, 1172-1178.

Barrette L., Turmel S. *'On-line iron-ore slurry monitoring for real-time process control of pellet making processes using laser-induced breakdown spectroscopy: graphitic vs. total carbon detection'* Spectrochimica Acta Part B (2001) 56, 715-723.

Bas D., Boyacı I.H. *'Modelling and optimisation I: Usability of response surface methodology'* Journal of Food Engineering (2007) 78, 836-845.

Becker J.S. *'Applications of inductively coupled plasma mass spectrometry and laser ablation inductively coupled mass spectrometry in materials science'* Spectrochimica Acta Part B (2002) 57, 1805-8120.

Belloto R.J., Dean A.M., Moustafa M.A., Molokhia A.M., Gouda M.W., Sokoloski T.D. *'Statistical techniques applied to solubility predictions and pharmaceutical formulations: an approach to problem solving using mixture*

response surface methodology' International Journal of Pharmaceutics (1985) 23, 195-207.

Bennett J.R.J., Hughes S., Elsey R.J., Parry T.P. *'Outgassing from stainless steel and the effects of the gauges'* Vacuum (2004) 73, 149–153.

Benyounis K.Y., Olabi A.G., Hashmi M.S.J. *'Effect of laser welding parameters on the heat input and weld-bead profile'* Journal of Materials Processing Technology (2005) 164-165, 978-985.

Bi M., Ruiz A.M., Gornushkin I., Smith B.W., Winefordner J. D. *'Profiling of patterned metal layers by laser ablation inductively coupled plasma mass spectrometry (LA-ICP-MS)'* Applied Surface Science (2000) 158, 197-204.

Blain M.G., Riter L.S., Cruz, D., Austin, D.E., Wu G., Plass W.R., Cooks R.G. *'Towards the hand-held mass spectrometer: design considerations, simulation, and fabrication of micrometer-scaled cylindrical ion traps',* International Journal of Mass Spectrometry (2004) 236, 91-104.

Bleakney W. *'A new method of positive ray analysis and its application to the measurement of ionization potentials in mercury vapor'* Physical Review (1929) 34, 157-161.

Bogue R. *'LIBS range extended through the use of a transportable terawatt laser system'* Sensor Review (2005) 25, 105-108.

Boué-Bigne F. *'Analysis of Oxide Inclusions in Steel by Fast Laser-Induced Breakdown Spectroscopy Scanning: An Approach to Quantification'* Applied Spectroscopy (2007) 61, 333-337.

Boumsellek, S., Ferran, R.J. *'Trade offs in Miniature Quadrupole Design'*, Journal of the American Society for Mass Spectrometry (2001) 12, 633-640.

Box G.E.P., Wilson K.B. *'Experimental attainment of optimum conditions'* Journal of the Royal Statistical Society (1951) 13, 1-45.

Brech F., Cross L. *'Optical microemission stimulated by a ruby laser'* Applied Spectroscopy (1962) 16, 59.

Bredice F., Sorbal H., Villagran-Muniz M., Di Rocco H.O., Cristoforetti G., Legnaioli S., Palleschi V., Sa ;vetti A., Tognoni E. *'Real time measurement of the electron density of a laser generated plasma using a RC circuit'* Spectrochimica Acta Part B (2007) 83, 836-840.

Brysbaert A., Melessanaki K., Anglos D. *'Pigment analysis in Bronze Age Aegean and Eastern Mediterranean painted plaster by laser-induced breakdown spectroscopy (LIBS)'* Journal of Archaeological Science (2006) 33, 1095-1104.

Budzikiewicz H., Grigsby D. *'Mass spectrometry and isotopes: a century of research and discussion'* Mass Spectrometry Reviews (2006) 25, 146-157.

Bugoi R., Constantinescu B., Neelmeijer C., Constantin F. *'The potential of external IBA and LA-ICP-MS for obsidian elemental characterization'* Nuclear Instruments and Methods in Physics Research Section B (2004) 226, 136-146.

Bulajic D., Corsi M., Cristoferetti G., Legnaioli S., Palleschi V., Salvetti A., Tognoni E. *'A procedure for correcting self absorption in calibration free-laser induced breakdown spectroscopy'* Spectrochimica Acta Part B (2002) 57, 339-353.

Bustamante M.F., Rinaldi C.A., Ferrero J.C. *'Laser induced breakdown spectroscopy characterization of Ca in a soil depth profile'* Spectrochimica Acta Part B (2002) 57, 303-309.

Cabalin L. M., Romero D., Baena J. M., Laserna J. J. *'Effect of Surface Topography in the Characterization of Stainless Steel Using Laser-induced Breakdown Spectrometry'* Surface and Interface Analysis (1999) 27, 805–810.

Caneve L., Colao F., Fabbri F., Fantoni R., Spizzichino V., Striber J. *'Laser-induced breakdown spectroscopy analysis of asbestos'* Spectrochimica Acta Part B (2005) 60, 1115 – 1120.

Caneve L., Colao F., Sarto F., Spizzichino V., Vadrucci M., *'Laser-induced breakdown spectroscopy as a diagnostic tool for thin films elemental composition'* Spectrochimica Acta Part B, (2005a) 60, 1098-1102.

Carranza J.E., Fisher B.T., Yoder G.D., Hahn D.W. *'On-line analysis of ambient air aerosols using laser-induced breakdown spectroscopy'* Spectrochimica Acta Part B (2001) 56, 851-864.

Carmona N., Oujja M., Gaspard S., García-Heras M., Villegas M.A., Castillejo M. *'Lead determination in glasses by laser-induced breakdown spectroscopy'* Spectrochimica Acta Part B (2007) 62, 94–100.

Chambers A., *'Modern Vacuum Physics'* Chapman and Hall/CRC Press, London, 2005. ISBN 0-8493-2438-6.

Charfia B., Harith M.A. *'Panoramic laser-induced breakdown spectrometry of water'* Spectrochimica Acta Part B (2002) 57, 1141–1153.

Chávez-Valencia L.E., Manzano-Ramírez A., Luna-Barcenas G., Alonso-Guzmán E. *'Modelling of the performance of asphalt pavement using response surface methodology'* Building and Environment (2005) 40, 1140-1149.

Choudhury I.A., El-Baradie M.A. *'Machinability assessment of inconel 718 by factorial design of experiment coupled with response surface methodology'* Journal of Materials Processing Technology (1999) 95, 30-39.

Corsi M., Cristoforetti G., Hidalgo M., Legnaioli S., Palleschi V., Salvetti A., Tognoni E., Vallebona C. *'Application of laser-induced breakdown spectroscopy technique to hair tissue mineral analysis'* Applied Optics (2003) 42, 6133-6138.

Cowpe J.S., Pilkington R.D. *'Swagelok Ultra-Torr based feed-through design for coupling optical fibre bundles into vacuum systems'* Vacuum (2008) 82, 1341-1343.

CRC Handbook of Chemistry and Physics, CRC Press Inc., Florida, 1988.

Cremers D.A., Radziemski L.J., *'Handbook of laser-induced breakdown spectroscopy'* John Wiley and Sons Ltd, Chichester, 2006. ISBN 13 978-0-470-09299-6.

Cyionics Ltd, *'IOTA: changing your expectation of RGA instrumentation'*, promotional literature, 2006.

Debra-Guedon J., Liodec N. *'De l'utilisation du faisceau d'un amplificateur a ondes lumineuses par emission induite de rayonnement (laser a rubis), comme source energetique pour l'excitation des spectres d'emission des elements'* C.R. Acad. Sci (1963) 257, 3336-3339.

de Giacomoa A., Dell'Aglioa M., Colaob F., Fantoni R. *'Double pulse laser produced plasma on metallic target in seawater: basic aspects and analytical approach'* Spectrochimica Acta Part B (2004) 59, 1431– 1438.

de Hoffman E., Stroobant V., *'Mass Spectrometry: Principles and Applications 2nd Ed'* John Wiley and Sons Ltd., Chichester, 2003. ISBN 0-471-48566-7.

de Segovia J.L. '*A review of electron stimulated desorption processes influencing the measurement of pressure or gas composition in ultra high vacuum systems'* Vacuum (1996) 47, 333-340.

de Lucia Jr. F.C., Gottfried J.L., Munson C.A., Miziolek A.W. *'Double pulse laser-induced breakdown spectroscopy of explosives: Initial study towards improved discrimination'* Spectrochimica Acta Part B (2007) 62, 1399-1404.

Diaz J.A., Daley P., Miles R., Rohrs H., Polla D. *'Integration Test of a miniature ExB mass spectrometer with a gas chromatograph for development of a low-cost, portable, chemical-detection system'*, Trends in Analytical Chemistry (2004) 4, 314-322.

Dimov S.S., Chryssoulis S.L. *'Standardization of time-of-flight laser ionization mass spectrometry analysis of minerals'* Spectrochimica Acta Part B (1998) 53, 399-406.

Dixon A. *'RGA for corrosive semiconductor applications'* III-IVs Review (1997) 10, 51.

Dockery C.R., Goode S.R. *'Laser-induced breakdown spectroscopy for the detection of gunshot residues on the hands of a shooter'* Applied Optics (2003) 42, 6153-6159.

Elliott R.M. *'Ion Sources'* in McDowell C.A. (Ed.) Mass Spectrometry, McGraw-Hill Book Company, Inc., New York, 1963, pp. 69-103.

El Sherbini A.M., El Sherbini T.M., Hegazy H., Cristoferetti G., Legnaioli S., Palleschi V., Pardini L., Salvetti A., Tognoni E. *'Evaluation of self-absorption coefficients of aluminium emission lines in laser-induced breakdown spectroscopy measurements'* Spectrochimica Acta Part B (2005) 60, 1573-1579.

El Sherbini A.M., Hegazy H., El Sherbini T.M. *'Measurement of electron density utilizing the H_α-line from laser produced plasma in air'* Spectrochimica Acta Part B (2006) 61, 532-539.

Escoubas P., Quinton L., Nicholson G.M. *'Venomics: unravelling the complexity of animal venoms with mass spectrometry'* Journal of Mass Spectrometry (2008) 43, 279-295.

Farmer J.B. *'Types of Mass Spectrometers'* in McDowell C.A. (Ed.) Mass Spectrometry, McGraw-Hill Book Company, Inc., New York, 1963, pp.7-63.

Forsberg J., Nilsson L. *'Evaluation of response surface methodologies used in crashworthiness optimisation'* International Journal of Impact Engineering (2006) 32, 759-777.

Fortes F.J., Cortés M., Simón M.D., Cabalín L.M., Laserna J.J. *'Chronocultural sorting of archaeological bronze objects using laser-induced breakdown spectrometry*' Analytica Chimica Acta (2005) 554, 136-143.

Garcia-Ayuso L.E., Amador-Hernandez J., Fernandez-Romero J.M., Luque de Castro M.D. *'Characterization [sic] of jewellery products by laser-induced breakdown spectroscopy'* Analytica Chimica Acta (2002) 457, 247-256.

Garcia C.C, Vadillo J.M., Palanco S., Ruiz J., Laserna J.J. *'Comparative analysis of layered materials using laser-induced plasma spectrometry and laser-ionization time-of-flight mass spectrometry'* Spectrochimica Acta Part B (2001) 56, 923-931.

Glumac N., Elliott G. *'The effect of ambient pressure on laser-induced plasmas in air'* Optics and Lasers in Engineering (2007) 45, 27–35.

Gondal M.A., Hussain T. *'Determination of poisonous metals in wastewater collected from paint manufacturing plant using laser-induced breakdown spectroscopy'* Talanta (2007) 71, 73-80.

Griem H.R., *'Plasma Spectroscopy'* McGraw-Hill Inc., New York, 1964, Library of Congress Catalog [sic] Card Number 63-23250.

Griem H.R., *'Principles of Plasma Spectroscopy'* Cambridge Monographs on Plasma Physics 2, Cambridge University Press, 1997. ISBN 0-521-45504-9.

Griesser H.J., Kingshott P., McArthur S.L., McLean K.M. Kinsel G.R., Timmons R.B. *'Review: Surface-MALDI mass spectrometry in biomaterials research'* Biomaterials (2004) 25, 4861–4875.

Gruber J., Heitz J., Strasser H., Bauerle D., Ramaseder N. *'Rapid in-situ analysis of liquid steel by laser-induced breakdown spectroscopy'* Spectrochimica Acta Part B (2001) 56, 685-693.

Haglund R.F., Itoh N. *'Electronic Processes in Laser Ablation of Semiconductors and Insulators'* in Laser Ablation Principles and Applications, Miller J.C. (Ed.), 1994, Springer-Verlag, New York.

Häkkänen H., Houni J., Kaski S., Korppi-Tommola J.E.I. *'Analysis of paper by laser-induced plasma spectroscopy'* Spectrochimica Acta Part B (2001) 56, 737-742.

Harilal S.S., Bindhu C.V., Isaac R.C., Nampoori P.N., Vallabhan C.P.G. *'Electron density and temperature measurements in a laser produced carbon plasma'* Journal of Applied Physics (1997) 82, 2140-2146.

Harilal S.S, Bhindu C.V., Tillack M.S., Najmabadi F., Gaeris A.C. *'Internal structure and expansion dynamics of laser ablation plumes into ambient gases'* Journal of Applied Physics (2003) 93, 2380-2388.

Harmon R.S., De Lucia F.C., Miziolek A.W., McNesby K.L., Walters R.A., French P.D. *'Laser-induced breakdown spectroscopy (LIBS) – an emerging field-portable sensor technology for real-time, in-situ geochemical and environmental analysis'* Applied Geochemsistry (2006) 21, 730-747.

Harmon R.S., DeLucia F.C., Winkel R.J., LaPointe A., Grossman S., McNesby K.L., Miziolek A.W. *'LIBS: a new versatile, field deployable, real-time detector system with potential for landmine detection'* Proceedings of SPIE (2003) 5089, 1065-1077.

Henry C.M. *'Itsy-Bitsy Mass Spectrometers'* Chemical and Engineering News (2002) 80, 34-5.

Herbert J.D. *'Residual Gas Analysis on the Daresbury Synchrotron Light Source'* Vacuum (1996) 48, 755-758.

Hiden Analytical *'Hiden EQP Mass and Energy Analysers for Plasma Diagnostics'* (2007) Technical Information Sheets and Application Notes: 229, 231, 236, 242, 243, 244, 245, 503.

Huba J.D. *'NRL Plasma Formulary'* Plasma Physics Division, Naval Research Laboratory, Washington D.C., 20375.

Ingalls A.E., Anderson R.F., Pearson A. *'Radiocarbon dating of diatom-bound organic compounds'* Marine Chemistry (2004) 92, 91– 105.

Kalathenos P., Baranyi J., Sutherland J. P., Roberts T. A. *'A response surface study on the role of some environmental factors affecting the growth of Saccharomyces cerevisiae'* International Journal of Food Microbiology (1995) 25, 63-74.

Kaminska A., Sawczak M., Komar K., Śliwiński G. *'Application of the laser ablation for conservation of historical paper documents'* Applied Surface Science (2007) 253, 7860-7864.

Karellas N.S., Chen Q.F., De Brou G.B., Milburn R.K. *'Real time air monitoring of hydrogen chloride and chlorine gas during a chemical fire'* Journal of Hazardous Materials (2003) 102, 105–120.

Kelly M.C., Gomlak G.G., Panayotov V.G., Cresson C., Rodney J., Koplitz B.D. *'Energetics of pulsed laser ablation species as determined by quadrupole and time-of-flight mass spectrometry'* Applied Surface Science (1998) 127-129, 988-993.

Keszler A.M., Nemes L. *'Time averaged emission spectra of Nd:YAG laser induced carbon plasmas'* Journal of Molecular Structure (2004) 695, 211-218.

Kim T., Specht Z.G., Vary P.S., Lin C.T. *'Spectral Fingerprints of Bacterial Strains by Laser-Induced Breakdown Spectroscopy'* Journal of Physical Chemistry (2004) 43, 5477-5482.

Kimura T., Nakamura T., Ishikawa K., Kokai F., Koga Y. *'Time-of-flight mass spectroscopic studies of positive ionic species generated by laser ablation of silicon carbide'* Chemical Physics Letters (2001) 340, 296-301.

Kosjek T., Heath E., Petrovic M., Barcelo D. *'Mass spectrometry for identifying pharmaceutical biotransformation products in the environment'* Trends in Analytical Chemistry (2007) 26, 1076-1086.

Krajnik P., Kopac J., Sluga A. *'Design of grinding factors based on response surface methodology'* Journal of Materials Processing Technology (2005) 162-163, 629-636.

Kumar A., Yueh F., Singh J.P., Burgess S. *'Characterisation of malignant tissue cells by laser-induced breakdown spectroscopy'* Applied Optics (2004) 43, 5399-5403.

Kuzuya M., Ohoka Y., Katoh H., Sakanashi H. *'Application of a quadrupole mass filter to laser ionisation mass spectrometry: synchronisation between the laser pulse and the mass scan'* Spectrochimica Acta Part B (1998) 53, 123-129.

Kwak J. *'Application of Taguchi and response surface methodologies for geometric error in surface grinding process'* International Journal of Machine Tools and Manufacture (2005) 45, 327-334.

Kylander M.E., Weiss D.J., Jeffries T.E., Kober B., Dolgopolova A., Garcia-Sanchez R., Coles B.J. *'A rapid and reliable method for Pb isotopic analysis of peat and lichens by laser ablation-quadrupole-inductively coupled plasma-mass spectrometry for biomonitoring and sample screening'* Analytica Chimica Acta (2007) 582, 116-124.

Lawson G. *'Medical and Environmental Applications'* in Dawson P.H. (Ed.) Quadrupole Mass Spectrometry and its Applications, Elsevier Scientific Publishing Company, Amsterdam, pp.307-334. ISBN: 0-444-41345-6.

Lazare S., Guan W., Drillhole D. *'High sensitivity quadrupole mass spectrometry of neutrals sputtered by UV laser ablation of polymers'* Applied Surface Science (1996) 96-98, 605-610.

Lazic V., Barbini R., Calao F., Fantoni R., Palucci A. *'Self-absorption model in quantitative laser induced breakdown spectroscopy measurements on soils and sediments'* Spectrochimica Acta Part B (2001) 56, 807-820.

Lazic V., Rauschenbach I., Jovicevic S., Jessberger E.K., Fantoni R., Di Fino M. *'Laser induced breakdown spectroscopy of soils, rocks and ice at subzero*

temperatures in simulated martian conditions' Spectrochimica Acta Part B (2007) 62, 1546–1556.

Le Drogoff B., Margot J., Chaker M., Sabsabi M., Barthélemy O., Johnston T. W., Laville S., Vidal F., von Kaenel Y. *'Temporal characterization of femtosecond laser pulses induced plasma for spectrochemical analysis of aluminum alloys'* Spectrochimica Acta Part B (2001) 56, 987-1002.

Lee H., Han H., Son K., Hong S. *'Optimisation of Nd:YAG laser welding parameters for sealing small titanium tube ends'* Materials Science and Engineering: A (2006) 415, 149-155.

Lee Y., Song K., Sneddon J. *'Laser Induced Plasmas for Analytical Spectroscopy'* in: Sneddon J., Thiem T.L., Lee Y. (Eds.), Lasers in Analytical Atomic Spectroscopy, VCH publishers Inc., New York, 1997, pp. 197-236.

Liu H.C., Mao X.L., Yoo J.H., Russo R.E. *'Early phase laser induced plasma diagnostics and mass removal during single-pulse laser ablation of silicon'* Spectrochimica Acta Part B (1999) 54, 1607-1624.

Liu Z., Schey K. L. *'Optimization of a MALDI TOF-TOF mass spectrometer for intact protein analysis'* Journal of the American Society for Mass Spectrometry (2005) 16, 482-490.

Liyana-Pathirana C., Shahidi F. *'Optimisation of extraction of phenolic compounds from wheat using response surface methodology'* Food Chemistry (2005) 93, 47-56.

Loh N.H., Tam S.C., Miyazawa S. *'Use of response surface methodology to optimise the finish in ball burnishing'* Precision Engineering (1990) 12, 101-105.

López A.J., Nicolás G., Mateo M.P., Piñón V., Tobar M.J., Ramil A. *'Compositional analysis of Hispanic Terra Sigillata by laser-induced breakdown spectroscopy'* Spectrochimica Acta Part B (2005) 60, 1149-1154.

Makas A.L., Troshkov M.L., Kudryavtsev A.S., Lunin V.M. *'Miniaturised mass-selective detector with atmospheric pressure chemical ionisation'*, Journal of Chromatography B (2004) 800, 63-67.

Mathew J., Goswami G. L., Ramakrishnan N., Naik N. K. *'Parametric studies on pulsed Nd:YAG laser cutting of carbon fibre reinforced plastic composites'* Journal of Materials Processing Technology (1999) 88-90, 198-203.

Melessanaki K., Mastrogianniodu A., Chloveraki S., Ferrence S.C., Betncourt P.P., Anglos D. *'Analysis of Archaeological Objects with LMntI, a New Transportable LIBS Instrument'* Springer Proceedings in Physics (2005) 100, 443-450.

Milán M., Laserna J.J. *'Diagnostics of silicon plasmas produced by visible nanosecond laser ablation'* Spectrochimica Acta Part B (2001) 56, 275-288.

Milan M., Lucena P., Cubalin C.M., Laserna J.J. *'Depth profiling of phosphorous on photonic grade silicon using laser-induced breakdown spectroscopy'* Applied Spectroscopy (1998) 52, 444-448.

Miller D.L., Moshegov N.T. *'All-metal ultrahigh vacuum optical fibre feed-through'* Journal of Vacuum Science and Technology A (2001) 19, 386-7.

MKS Instruments Inc. *'MicroVision Plus: Gas Analysis'* RGA overview, specifications and application notes. (2004) Available online: http://www.mksinst.com/docs/UR/microv.pdf Accessed 20/05/2008.

Molina A., Shaddix C.R., Sickafoose S.M., Walsh P.M., Blevins L.G. *'Effect of temperature and CO2 concentration on laser-induced breakdown spectroscopy*

measurements of alkali fume' Spectrochimica Acta Part B (2005) 60, 1103 - 1114.

Morel S., Leone N., Adam P., Amouroux J. *'Detection of bacteria by time-resolved laser-induced breakdown spectroscopy'* Applied Optics (2003) 42, 6184-6191.

Mowery M.D., Sing R., Kirsch J., Razaghi A., Béchard S., Reed R.A. *'Rapid at-line analysis of coating thickness and uniformity on tablets using laser induced breakdown spectroscopy'* Journal of Pharmaceutical and Biomedical Analysis (2002) 28, 935–943.

Naumenko D., Quadakkers W. J., Galerie A., Wouters Y., Jourdain S. *'Parameters affecting transient oxide formation on FeCrAl based foil and fibre materials'* Materials At High Temperatures (2003) 20, 287–293.

Nier A.O. *'The Isotopic Constitution of Calcium, Titanium, Sulphur and Argon'* Physical Review (1938) 53, 282-287.

Nogar N.S., Estler R.C., *'Laser Desorption/Laser Ablation with Detection by Resonance Ionization Mass Spectrometry'* in Lubman D. (Ed.) 'Lasers and Mass Spectrometry' Oxford University Press, New York, 1990. pp. 67-83. ISBN 0-19-505929-8.

Noll R., Bette H., Brysch A., Kraushaar M., Mönch I., Peter L., Sturm V. *'Laser-induced breakdown spectrometry - applications for production control and quality assurance in the steel industry'* Spectrochimica Acta Part B (2001) 56, 637-649.

Noll R., Mönch I., Klein O., Lamott A. *'Concept and operating performance of inspection machines for industrial use based on laser-induced breakdown spectroscopy'* Spectrochimica Acta Part B (2005) 60, 1070-1075.

Noordin M. Y., Venkatesh V. C., Sharif S., Elting S., Abdullah A. *'Application of response surface methodology in describing the performance of coated carbide tools when turning AISI 1045 steel'* Journal of Materials Processing Technology (2004) 145, 46-58.

O'Hanlon J.F., *'A User's Guide to Vacuum Ttechnology'* John Wiley and Sons, Ins. New Jersey. (2003)

Olabi A.G., Casalino G., Benyounis K.Y., Hashmi M.S.J. *'An ANN and Taguchi algorithms integrated approach to the optimisation of CO_2 laser welding'* Advances in Engineering Software (2006) 37, 643-648.

Onwubolu G. C., Kumar S., *'Response surface methodology-based approach to CNC drilling operations'* Journal of Materials Processing Technology (2006) 171, 41-47.

Palanco S., Alises A., Cunat J., Baena J., Laserna J.J. *'Development of a portable laser induced plasma spectrometer with fully-automated operation and quantitative analyses capabilities'* Journal of Analytical Atomic Spectroscopy (2003) 18, 933-938.

Palanco S., Lopez-Moreno C., Laserna J. J. *'Design, construction and assessment of a field-deployable laser-induced breakdown spectrometer for remote elemental sensing'* Spectrochimica Acta Part B (2006) 61, 88 – 95.

Pan L.K., Wang C.C., Hsiao Y.C., Ho K.C. *'Optimisation of Nd:YAG laser welding onto magnesium alloy via Taguchi analysis'* Optics & Laser Technology (2005) 37, 33-42.

Pedrotti F.L., Pedrotti L.S. *'Introduction to Optics'* Prentice Hall Inc., New Jersey, 1993. ISBN 0-13-016973-0.

Pettke T., Heinrich C.A., Ciocan A.C., Gunther D. *'Quadrupole mass spectrometry and optical emission spectroscopy: detection capabilities and representative sampling of short transient signals from laser-ablation'* Journal of Atomic and Analytical Spectrometry (2000) 15, 1149-1155.

Pierce W., Christian S.M., Myers M.J., Myers J.D. *'Field-testing for environmental pollutants using a briefcase sized portable LIBS system'* Transcript of Oral Presentation given at LIBS 2004, 3rd International Conference on Laser Induced Plasma Spectroscopy and Applications.

Pouli P., Melessanaki K., Giakoumaki A., Argyropoulos V., Anglos D. *'Measuring the thickness of protective coatings on historic metal objects using nanosecond and femtosecond laser induced breakdown spectroscopy depth profiling'* Spectrochimica Acta Part B (2005) 60, 1163-1171.

Radziemski L.J. *'From LASER to LIBS, the path of technology development'* Spectrochimica Acta Part B (2002) 57, 1109-1113.

Radziemski L., Cremers D.A., Benelli K., Khoo C., Harris R.D. *'Use of the vacuum ultraviolet spectral region for laser-induced breakdown spectroscopy-based Martian geology and exploration'* Spectrochimica Acta Part B (2005) 60, 237-248.

Rai N.K., Rai A.K. *'LIBS -An Efficient Approach for the Determination of Cr in industrial wastewater'* Journal of Hazardous Materials (2008) 150, 835-838.

Ready J.F. *'Effects of High-Power Laser Radiation'* Academic Press, New York. 1971.

Reuben A.J., Simth G.B., Moses P., Vagov A.V., Woods M.D., Gordon D.B., Munn R.W. *'Ion trajectories in exactly determined quadrupole fields'* International Journal of Mass Spectrometry and Ion Processes (1996) 154, 43-59.

Rosenwasser S., Asimellis G., Bromley B., Hazlett R., Martin J., Pearce T., Zigler A. *'Development of a method for automated quantitative analysis of ores using LIBS'* Spectrochimica Acta Part B (2001) 56, 707-714.

Rubakhin S.S., Jurchen J.C., Monroe E.B., Sweedler J.V. *'Imaging mass spectrometry: fundamentals and applications to drug discovery'* Drug Discovery Today (2005) 10, 823-838.

Rusak D.A., Castle B.C., Smith B.W., Winefordner J.D. *'Recent trends and the future of laser-induced plasma spectroscopy'* Trends in Analytical Chemistry (1998) 17, 453-461.

Russo R.E., Mao X.L., Liu C., Gonzalez J. *'Laser assisted plasma spectrochemistry: laser ablation'* Journal of Analytical Atomic Spectrometry (2004) 19, 1084-1089.

Salimbeni R., Pini R., Siano S. *'Achievement of optimum laser cleaning in the restoration of artworks: expected improvements by on-line optical diagnostics'* Spectrochimica Acta Part B (2001) 56, 877-885.

Sallé B., Cremers D.A., Maurice S., Wiens R.C. *'Laser-induced breakdown spectroscopy for space exploration applications: Influence of the ambient pressure on the calibration curves prepared from soil and clay samples'* Spectrochimica Acta Part B (2005) 60, 479-490.

Salle B., Lacour J., Vors E., Fichet P., Maurice S., Cremers D.A., Wiens R.C. *'Laser-induced breakdown spectroscopy for Mars surface analysis: capabilities at stand-off distances and detection of chlorine and sulfur elements'* Spectrochimica Acta Part B (2004) 59, 1413– 1422.

Sallé B., Mauchien P., Maurice S. *'Laser-Induced Breakdown Spectroscopy in open-path configuration for the analysis of distant objects'* Spectrochimica Acta Part B (2007) 62, 739–768.

Salzmann D., *'Atomic Physics in Hot Plasmas'* International Series of Monographs on Physics 97, Oxford University Press, New York 1998, ISBN 0-19-510930-9.

Samek O., Telle H.T., Beddows D.C.S. *'Laser-induced breakdown spectroscopy: a tool for real-time, in vitro and in vivo identification of carious teeth'* BMC Oral Health (2002) 1. Published online 2001 December 19. doi: 10.1186/1472-6831-1-1.

Sattmann R., Sturm V., Noll R. *'Laser-induced breakdown spectroscopy of steel samples using multiple Q-switch Nd:YAG laser pulses'* Journal of Physics D: Applied Physics (1995) 28, 2181-2187.

Shaikh N.M., Rashid B., Hafeez S., Jamil Y., Baig M.A. *'Measurement of electron density and temperature of a laser-induced zinc plasma'* Journal of Physics D: Applied Physics (2006) 39, 1384-1391.

Short R.T., Fries D.P., Kerr M.L., Lembke C.E., Toler S.K., Wenner P.G., Byrne R.H. *'Underwater Mass Spectrometers for the in situ Chemical Analysis of the Hydrosphere'* Journal of the American Society for Mass Spectrometry (2001) 12, 676-682.

Sillon N., Baptist R. *'Micromachined mass spectrometer'*, Sensors and Actuators B (2002) 83, 129-137.

Singh S. '*Sensors—An effective approach for the detection of explosives'* Journal of Hazardous Materials (2007) 144, 15-28.

Skinner C.H. *'Efficient ionisation of calcium, strontium and barium by resonant laser pumping'* Journal of Physics B: Atomic and Molecular Physics (1980) 13, 55-68.

Sneddon J., Thiem T.L., Lee I. *'Lasers in analytical atomic spectroscopy'* VCH Publishers Inc, 1997. ISBN 1-56081-907-3, 209-211.

Soler C., Manes J., Pico Y. *'Comparison of liquid chromatography using triple quadrupole and quadrupole ion trap mass analyzers to determine pesticide residues in oranges'* Journal of Chromatography A (2005) 1067, 115–125.

Song K., Kim D., Cha H., Kim Y., Jung E.A., Choi I., Yoo H., Oh S. *'Characterization of laser-induced plasma in a vacuum using laser ablation mass spectrometry and laser-induced breakdown spectrometry'* Microchemical Journal (2004) 76, 95-103.

Sparkman D.O. '*Focus on Field-Portable and Miniature Mass Spectrometers. Presentations from the 12th Sanibel Conference on Mass Spectrometry'*, Journal of the American Society for Mass Spectrometry (2001) 12, 617-618.

Stavropoulos P., Palagas C., Angelopoulos G.N., Papamantellos D.N., Couris S. *'Calibration Measurements in laser-induced breakdown spectroscopy using nanosecond and picosecond lasers'* Spectrochimica Acta Part B (2004) 59, 1885-1892.

Steen R.J.C.A., Freriks I.L., Cofino W.P., Brinkman U.A.Th. *'Large-volume injection in gas chromatography-ion trap tandem mass spectrometry for the determination of pesticides in the marine environment at the low ng/l level'* Analytica Chimica Acta (1997) 353, 153-163.

St-Onge L., Sabsabi M. *'Towards quantitative depth-profile analysis using laser-induced plasma spectroscopy: investigation of galvannealed coatings on steel'* Spectrochimica Acta Part B (2000) 55, 299-308.

St-Onge L., Kwong E., Sabsabi M., Vadas E.B. *'Rapid analysis of liquid formulations containing sodium chloride using laser-induced breakdown*

spectroscopy' Journal of Pharmaceutical and Biomedical Analysis (2004) 36, 277-284.

Suliyanti M.M., Sardy S., Kusowo A. *'Preliminary analysis of C and H on a "sanigiran" fossil using laser-induced plasma at reduced pressure'* Journal of Applied Physics (2005) 98, published online 14th November 2005.

Sun Q., Tran M., Smith B.W., Winefordner J.D. *'Zinc analysis in human skin by laser induced-breakdown spectroscopy'* Talanta (2000) 52, 293–300.

Thomson J.J., *'Rays of positive Electricity and Their Application to Chemical Analysis'* Longmans Green, London, 1913.

Thorne A.P., *'Spectrophysics'* Chapman and Hall Science Paperbacks, London 1974. ISBN 0 412 12510 X, 354-357.

Todd J.F.J. *'Applications in Atomic and Molecular Physics'* in Dawson P.H. (Ed.) Quadrupole Mass Spectrometry and its Applications, Elsevier Scientific Publishing Company, Amsterdam, pp.241-271. ISBN: 0-444-41345-6.

Tognoni E., Palleschi V., Corsi M., Cristoforetti G. *'Quantitative micro-analysis by laser-induced breakdown spectroscopy: a review of the experimental approaches'* Spectrochimica Acta Part B (2002) 57, 1115-1130.

Torrisi L., Caridi F., Margarove D., Borrielli A. *'Characterization of laser-generated silicon plasma'* Applied Surface Science (2008) 254, 2090-2095.

Turner P.G., Dugdale A., Young I.S., Taylor S. *'Portable mass spectrometry for measurement of anaesthetic agents and methane in respiratory gases'* The Veterinary Journal, in press, accepted proof 17th March 2007.

Vadillo J.M., Laserna J.J. *'Laser-induced breakdown spectroscopy of silicate, vanadate and sulfide rocks'* Talanta (1996) 43, 1149-1154.

Vadillo J.M., Laserna J.J. *'Laser-induced plasma spectrometry: truly a surface analytical tool'* Spectrochimica Acta Part B (2004) 59, 147-161.

Vrenegor J., Noll R., Sturm V. *'Investigation of matrix effects in laser-induced breakdown spectroscopy plasmas of high-alloy steel for matrix and minor elements'* Spectrochimica Acta Part B (2005) 60, 1083-1091.

Wang X., Amoruso S., Armenante M., Boselli A., Bruzzese, R. Spinelli N., Velotta R. '*Pulsed laser ablation of borocarbide targets probed by time-of-flight mass spectrometry'* Optics and Lasers in Engineering (2003) 39, 179–190.

Weiss J.D., Stoever J.H. *'Vacuum feed-through for optical fiber cables'* Applied Optics (1985) 24, 2755-6.

Weritz F., Ryahi S., Schaurich D., Taffe A., Wilsch G. *'Quantitative determination of sulfur content in concrete with laser-induced breakdown spectroscopy'* Spectrochimica Acta Part B (2005) 60, 1121-1131.

Whitehouse A.I., Young J., Botheroyd I.M., Lawson S., Evans C.P., Wright J. *'Remote material analysis of nuclear power station steam generator tubes by laser-induced breakdown spectroscopy'* Spectrochimica Acta Part B (2001) 56, 821-830.

Wilsch G., Weritz F., Schaurich D., Wiggenhauser H. *'Determination of chloride content in concrete structures with laser-induced breakdown spectroscopy'* Construction and Building Materials (2005) 19, 724–730.

Wilson J., Hawkes J.F.B. *'Optoelectronics An Introduction (2nd Edition)'* Prentice Hall International, London, 1993. ISBN 0-13-638495-1.

Wood M., Laloup M., Samyn N., Fernandez M., de Bruijn E.A., Maes R.A.A., De Boeck G. *'Review: Recent applications of liquid chromatography–mass*

spectrometry in forensic science' Journal of Chromatography A (2006) 1130, 3–15.

Yaroshchyk P., Body D., Morrison R.J.S., Chadwick B.L. *'A semi-quantitative standard-less analysis method for laser-induced breakdown spectroscopy'* Spectrochimica Acta Part B (2006) 61, 200-209.

Yaroshchyk P., Morrison R.J.S., Body D., Chadwick B.L. *'Quantitative determination of wear metals in engine oils using laser-induced breakdown spectroscopy: A comparison between liquid jets and static liquids'* Spectrochimica Acta Part B (2005) 60, 986 – 992.

Yoon Y.Y., Kim T.S., Chung K.S., Lee K.Y., Lee G.H. *'Application of Laser-Induced Plasma Spectroscopy to the Analysis of Rock Samples'* Analyst (1997) 122, 1223-1227.

Yueh F., Singh J.P., Zhang H. *'Laser-Induced Breakdwon Spectroscopy, Elemental Analysis'* in Meyers R.A. (Ed.) Encyclopedia of Analytical Chemistry pp. 2066-87. John Wiley & Son Ltd., Chichester (2000).

Zurera-Cosano G., García-Gimeno R.M., Rodríguez-Pérez R., Hervás-Martínez C. *'Performance of response surface model for prediction of Leuconostoc mesenteroides growth parameters under different experimental conditions'* Food Control (2006) 17, 429-438.

9 Appendices

9.1 ICCD Region of Interest

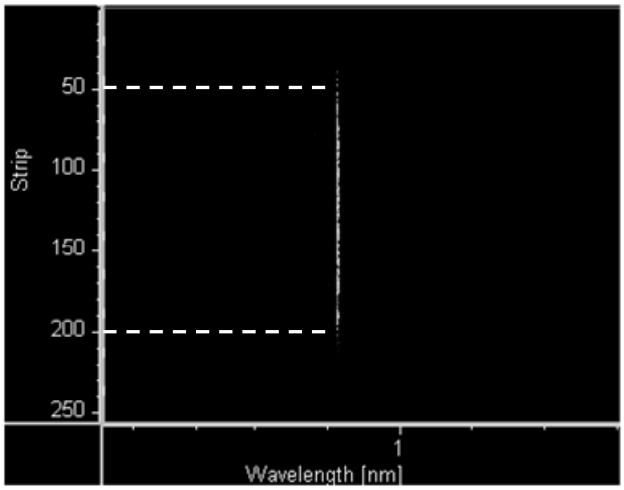

Figure 9-1 Non-dispersed image of spectrometer input slit

Figure 9-1 shows a non-dispersed image of the spectrometer input slit, captured in shutter mode, with gate width 10 μs, gain 200, 1 accumulation. A cadmium hollow cathode lamp imaged onto spectrometer input slit, and 2400 grooves mm^{-1} diffraction grating positioned so as to allow the zero order to propagate through to the ICCD. It can be seen that the input slit image is smaller then the height of the 1024 × 256 CCD array. Any pixels not illuminated by the slit will add noise to the spectra when binned together, so the region of interest is used to ignore these pixels. Strips < 50 and > 200 are disregarded.

Table 9-1 Region of Interest (ROI)

	CCD	ROI
x dimension (pixel)	1 - 1024	150 – 860
y dimension (strip)	1 - 256	50 - 200

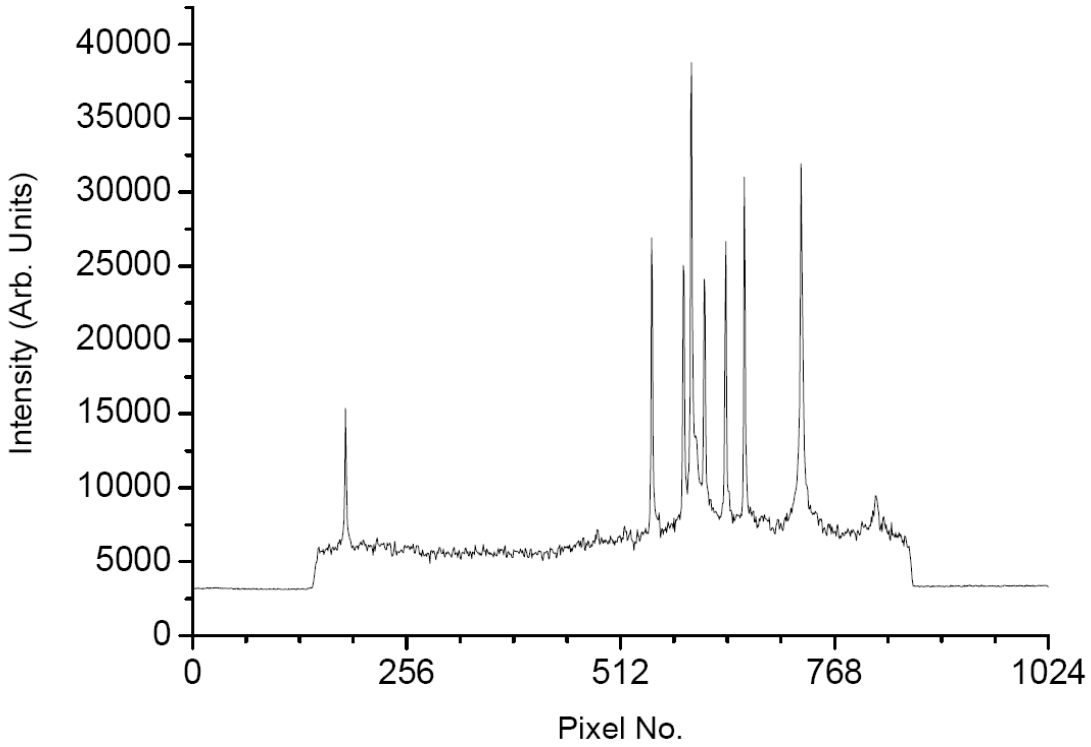

Figure 9-2 Example silicon LIBS spectrum illustrating edges of intensifier

The intensifier does not cover the full width of the CCD array; Figure 9-2 shows an example spectrum of single crystal silicon illustrating this. The spectrum was captured with a gain of 200, gate width 100 ns, gate delay 100 ns, 10 accumulations and at an ambient pressure of $\sim 1 \times 10^{-6}$ mbar. The emission lines are in the 247 to 256 nm range, but here the x axis of the figure is labelled in units of CCD pixel.

The edges of the intensifier are clearly evident, with the captured emission signal dropping in intensity dramatically to either edge of the CCD array. As the un-intensified portions of the CCD will add to background noise, the ROI is used to ignore them. The settings for the x/y ROI are given in Table 9-1, and are shown compared to the physical dimensions of the CCD array.

9.2 Determination of LIBS Instrument Broadening Profile

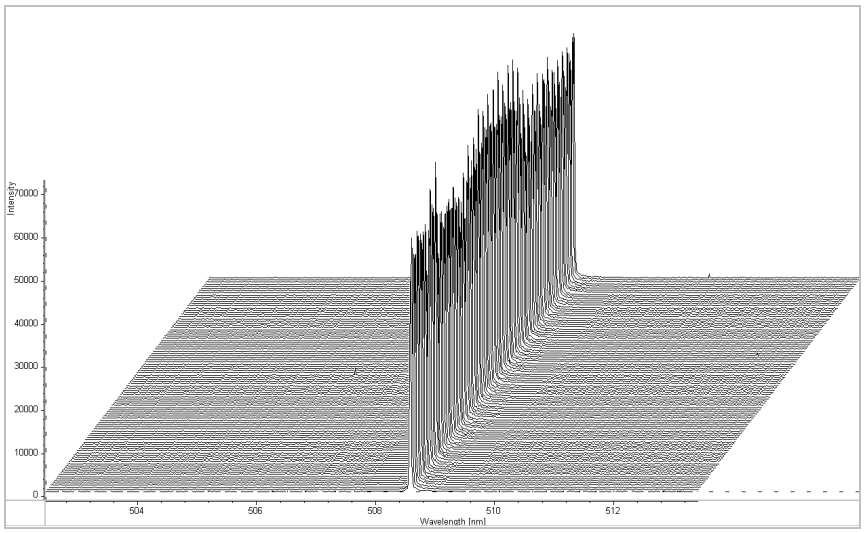

Figure 9-3 Spectra captured for evaluation of instrumental profile

For accurate emission line FWHM measurements, the contribution to the line width from the instrument needs to be determined and subsequently subtracted from the emission spectra. A cadmium hollow cathode lamp was placed at the location of plume generation, and was imaged onto the entrance slit of the spectrometer, just as a typical laser-induced plasma would be.

Using the 2400 grooves mm^{-1} grating positioned so as to allow capture of the 508.582 nm Cadmium (I) emission line, 100 spectra were taken with a gate width of 100 μs, ICCD gain of 200 and 10 software accumulations (shown in Figure 9-3). MicroCal Origin 7.0 was used to fit a Lorentzian curve to each captured spectrum, yielding the FWHM of the emission line and thus the instrumental broadening profile. The average FWHM of 100 such fitted curves, and hence the instrumental broadening profile of the LIBS instrument, was found to be 0.017795 nm.

9.3 Determination of LIBS Instrument Background Level

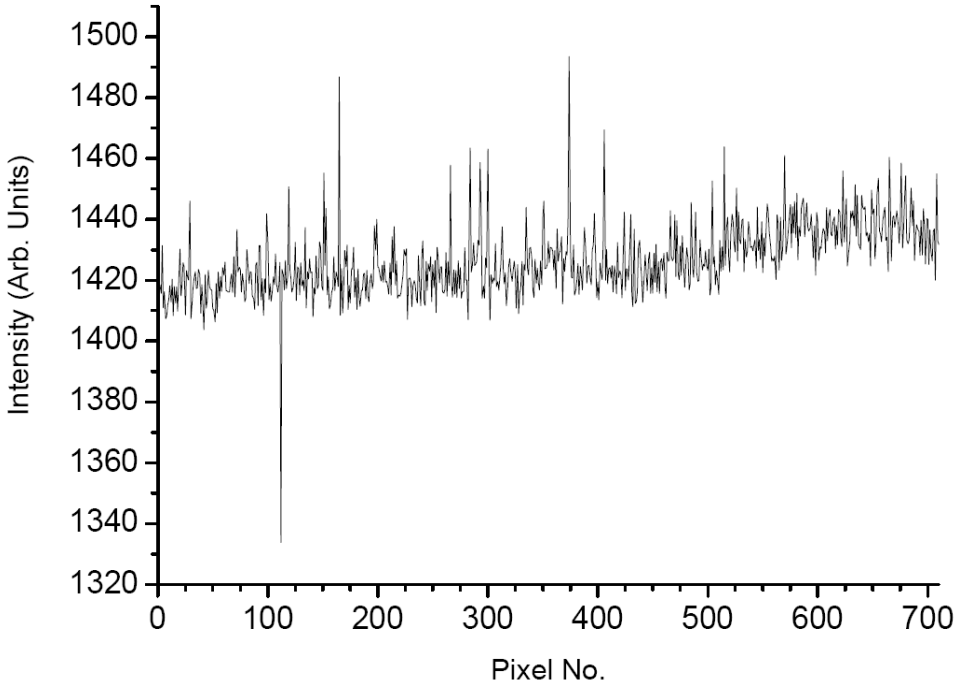

Figure 9-4 LIBS instrument average background level

In order to accurately determine the continuum emission intensity of a given LIBS spectrum it is necessary to first subtract form the spectrum the background level of the LIBS instrument. This background level is due primarily to accumulated ICCD dark charge and stray ambient illumination entering the spectrometer. 100 spectra were captured using the laser as the capture trigger, but with a beam block in the laser path such that no ablation plume was formed. The spectra were captured with a spectrometer input slit-width of 10 μm, ICCD gain of 200, gate width of 50 ns, a gate delay of 500 ns and a laser repetition rate of 10 Hz; all settings exactly as if spectroscopic measurements were being taken, but not allowing any light into the ICCD. The average of the 100 spectra is shown in Figure 9-4, which serves as the instrument background that was subtracted from all spectroscopic measurements.

9.4 Determination of T_e: Iterative Program Listing

```
Dim I As Integer
Dim el As Double
Dim ec As Double
Dim Te As Double
Dim Cr As Double
Dim A21 As Double
Dim g As Integer
Dim Ui As Double
Dim lambda As Double
Dim Ei As Double
Dim E2 As Double
Dim zeta As Double
Dim k As Double
Dim c As Double
Dim x As Double

Private Sub Calculate_Click()

    el = Val(elText.Text)
    ec = Val(ecText.Text)
    Cr = 2.005 * 10 ^ 5
    A21 = 1.9 * 10 ^ 8
    g = 3
    lambda = 288.16 * 10 ^ -9
    Ui = 6.159
    Ei = 8.151
    E2 = 5.028
    k = 5.0286 * 10 ^ -5
    zeta = 1.4
    c = 2.99 * 10 ^ 8
    h = 4.135667 * 10 ^ -15
    x = 1000

   Open "C:\Documents and Settings \JOHN \Desktop
    \Iteration_Lorentz.txt"  For Output As #1

   For i = 1 To 100 Step 1
       x = ((-ec * Cr * A21 * g * lambda * lambda * k *
       Math.Log(x)) * x ^ (-(((Ei - E2) / k) * ((lambda * k) / (h *
       c))))) / (Ei * Ui * ((zeta / x) - zeta + 1))

       Te = -(h * c) / (lambda * k * Math.Log(x))
            Print #1, x
       Next
    Close #1

    TeText.Text = Str$(Te)

End Sub
```

To determine the electron temperature of any given plasma using the line-to-continuum ration method, Equation 2.20 must be solved. As there is no easy analytical solution to this equation (Liu et al. 1999), it must be solved through a series of iterations. The program listing shown on the previous page was written

in Visual Basic Professional 6 to solve Equation 2.20 by successive iteration. The program allows the user to enter values for the line and continuum emission coefficients for the 288.16 nm Si (I) emission line, which are then used with a starting 'guess' of plasma temperature to determine the actual plasma temperature. The program opens a .txt file and stores each successive iteration result for up to 100 steps.

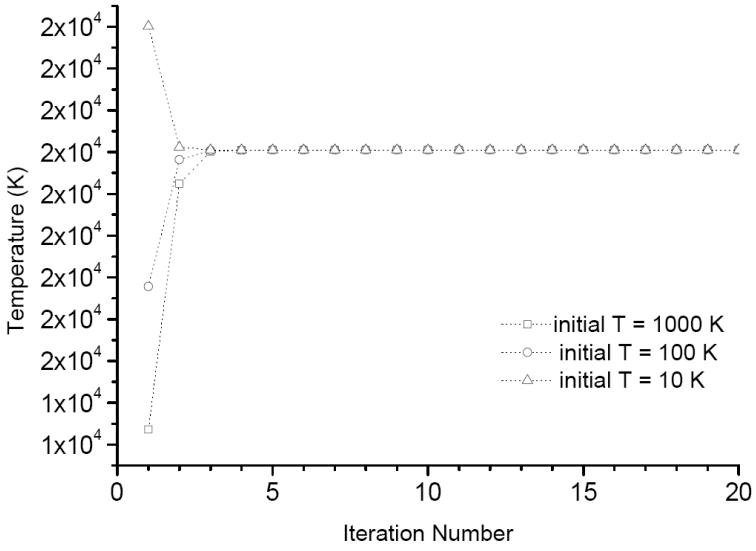

Figure 9-5Converging Temperature from Iterative Program

Figure 9-5 shows the iterative process converging to give a T_e value of 20049.77 K. The series converges to the final value after approximately 5 iteration steps, regardless of the value of the starting guess.

9.5 Invited Papers

Hisek J., Lucas N., Hill A.E., Cowpe J.S., Astin J.S., Pilkington R.D., '*A comparative study of laser induced breakdown spectroscopy and secondary ion mass spectrometry applied to DC magnetron sputtered as-grown copper indium diselenide (CIS)'* Photon 06, Manchester (2006).

Pilkington R.D., Cowpe J.S., Astin J.S. *'Materials analysis by Laser-Induced Breakdown Spectroscopy and Laser Ablation Mass Spectrometry Under Vacuum'* International Symposium on Vacuum Science and Technology, Tata Institute of Fundamental Research, Mumbai, India (2007).

9.6 Poster Presentations

Cowpe J.S., Astin J.S., Pilkington R.D., Hill A.E. *'Application of Response Surface Methodology to Laser-Induced Breakdown Spectroscopy: Influences of Hardware Configuration'* LIBS 06, Montreal, Canada (2006).

Cowpe J.S., Astin J.S., Pilkington R.D., Hill A.E. *'Analysis of Laser Ablation Plumes by Laser-Induced Breakdown Spectroscopy and Quadrupole MS: a Comparative Study'* LIBS 06, Montreal, Canada (2006).

9.7 Publications

Cowpe J.S., Astin J.S., Pilkington R.D., Hill A.E. *'Application of Response Surface Methodology to laser-induced breakdown spectroscopy: Influences of hardware configuration'* Spectrochimica Acta Part B (2007) 62, 1335-1342.

Cowpe J.S., Pilkington R.D. *'Swagelok Ultra-Torr based feed-through design for coupling optical fibre bundles into vacuum systems'* Vacuum (2008) 82, 1341-1343.